2015

An elasto-plastic strain-based approach for analysing the behaviour of ballasted rail track

Qideng Sun
University of Wollongong

UNIVERSITY OF WOLLONGONG

Department of Civil, Mining and Environmental Engineering

An Elasto-plastic Strain-based Approach for Analysing the Behaviour of Ballasted Rail Track

Qideng Sun

This thesis is presented as part of the requirement for the
Award of the Degree of Doctor of Philosophy
of the
University of Wollongong

June 2015

CERTIFICATION

I, Qideng Sun, declare that this thesis, submitted in fulfillment of the requirements for the award of Doctor of Philosophy, in the School of Civil, Mining and Environmental Engineering, University of Wollongong, is wholly my own work unless otherwise referenced or acknowledged. The document has not been submitted for qualifications at any other academic institution.

The following publications are related to the research work conducted in this study:

Sun, Q. D., Indraratna, B. & Nimbalkar, S. (2015). The deformation and degradation mechanisms of railway ballast under high frequency cyclic loading. *Journal of Geotechnical and Geoenvironmental Engineering*, *ASCE* (in press).

Indraratna, B., Sun, Q. D. & Nimbalkar, S. (2015). Observed and predicted behaviour of rail ballast under monotonic loading capturing particle breakage. *Canadian Geotechnical Journal* **52**, No. 1, 73-86.

Sun, Q. D., Indraratna, B. & Nimbalkar, S. (2014). Effect of cyclic load frequency on the permanent deformation and degradation behaviour of rail ballast. *Géotechnique* **64**, No. 9, 746-751.

Sun, Q. D., Indraratna, B. & Nimbalkar, S. (2016). An elasto-plastic method for analysing the deformation of the railway ballast. *3rd International Conference on Transportation Geotechnics*, Sep. 2016, Guimaraes, Portugal (submitted).

Sun, Q. D., Indraratna, B. & Nimbalkar, S. (2016). The deformation and degradation of

granular material under high frequency repeated loading. *Geotechnical & Structural Engineering Congress*, Feb. 2016, Phoenix, Arizona, U.S. (submitted).

Indraratna, B., Sun, Q. D. & Nimbalkar, S. (2015). A critical state based constitutive model for ballast incorporating particle breakage. *15th Pan-American Conference on Soil Mechanics and Geotechnical Engineering*, Nov. 2015, Buenos Aires, Argentina (accepted).

Indraratna, B., Nimbalkar, S., Tennakoon, N. & Sun, Q. D. (2013). From theory to practice in rail geotechnology. Invited KEYNOTE paper, *9th International Conference on the Bearing Capacity of Roads, Railways and Airfields (BCRRA 2013)*, June, 2013, Trondheim, Norway, 1-20.

Qideng Sun

June 2015

ABSTRACT

Due to the recent utilisation of faster and heavier trains, traditional railways consisting of granular media overlying a subgrade or natural formulation have become increasingly overstressed; this may lead to their excessive deformation and degradation and could result in more frequent and increasingly expensive track maintenance. On this basis, an assessment of the stress-strain and degradation of ballast under traffic loading is of paramount significance. Over the past decade, a number of constitutive models that address the behaviour of a wide range of engineering materials under different loading conditions have been developed, and there has also been a rapid expansion in the application of general purpose geotechnical software by practicing engineers, especially for nonlinear analysis. Thus, it is important to develop a reliable and versatile constitutive model for granular soils such as ballast and to incorporate it into finite element analysis.

Large scale triaxial tests have been conducted to evaluate the permanent deformation, stiffness, and degradation of ballast subjected to monotonic and high frequency cyclic loads. Different confining pressures were applied during monotonic testing which revealed that particle breakage has a profound effect on the critical state, the peak state, hardening, and the stress-dilatancy parameters of ballast. In these cyclic loading tests various frequencies, deviator stress magnitudes and confining pressures were utilised to study the combined effect of these load factors on the deformation and degradation of ballast. It was observed that different deformation mechanisms exist for ballast, namely, elastic shakedown, plastic shakedown, ratcheting, and plastic collapse.

An elasto-plastic constitutive model based on the critical state soil mechanics framework was presented to capture the stress-strain behaviour and degradation of ballast and constitutive parameters were determined from large-scale laboratory tests. The model could predict the monotonic shear behaviour of ballast that corroborated with laboratory measurements, after which it was extended to capture important aspects of cyclic loading such as the load frequency and predict plastic deformation under repeated traffic loading.

A numerical integration of the ballast model was executed by using a fully implicit Euler-backward algorithm based on an elastic stress predictor. The tangent operator was derived by consistent linearisation of the updated stress. The finite element model was validated by analyzing the triaxial specimen with a 2-D axisymmetric approach, from which it was found that the stress-strain response from the simulation and experiment matched each other to an acceptable degree. A finite element case study was then carried out where the settlement of a railway track during the passage of a train was simulated.

ACKNOWLEDGMENTS

First and foremost, I would like to express my sincere and profound gratitude to my supervisor Prof. Buddhima Indraratna for his erudite guidance, invaluable suggestions and constructive criticisms throughout the study. His diligent, analytical and methodical way of working has inspired me and under his guidance I have learned a lot.

Grateful appreciation is also expressed to my co-supervisor, Dr. Sanjay Nimbalkar for his assistance and constant encouragement in the last three and half years. His patience and availability for any help whenever needed is appreciated.

Thanks to the technical staff at the University of Wollongong, Alan, Ritchie, and Cameron, for their continuous help with the initial set-up of equipment and during the laboratory work. I would also like to give thanks to fellow postgraduate friends for their discussions, support, and social interaction. My appreciation is also extended to all past and present members of the department of CME, UOW for keeping the study atmosphere enjoyable and pleasant. The financial support of the CSC is greatly appreciated.

Gratitude is also expressed to all my brothers and sisters in Sydney and Wollongong for their continuous company, embracing and encouragement.

Last but not the least, I would like to give thanks to my beloved parents Zhaoquan and Kelian for all their sacrifice, encouragement and moral support.

TABLE OF CONTENTS

LIST OF FIGURES

LIST OF TABLES

LIST OF NOTATION

a	model parameter linking particle breakage to the specific volume
A	material constant
A_d	dilatancy parameter
b	model parameter linking particle breakage to the specific volume
B	Skempton's coefficient
BBI	Ballast Breakage Index
B_g	Marsal's breakage index
B_m	parameter controlling hyperbolic stiffness relationship
c	empirical constant
C	cohesion of soil
CASR	Cyclic Axial Strain Ratio
CPPM	closest point projection method
CSDZ	compressive stable degradation zone
CSL	critical state line
C_u	coefficient of uniformity
CVSR	Cyclic Volumetric Strain Ratio
D	dilatancy
d	empirical constant
d_{50}	median particle size
d_{95i}	95% of largest sieve size
DAF	dynamic amplification factor
D_C	dilatancy under cyclic loading condition
d_f	model parameter reflecting the effect of frequency on dilatancy
d_{max}	maximum particle size
d_{min}	minimum particle size
dN	the increment of load cycle
DSC	disturbed state concept
DUDZ	dilatant unstable degradation zone
$d\varepsilon_{ij}^{p}$	infinitesimal increment of plastic strain
$d\varepsilon_{s}^{e}$	elastic deviatoric strain increment
$d\varepsilon_{vol,c}^{p}$	plastic volumetric strain increment due to cyclic compaction
$d\varepsilon_{v}^{e}$	elastic volumetric strain increment
$d\kappa^{p}$	increment of plastic distortional strain
E	elastic modulus
e	void ratio
e_0	initial void ratio
e_i	pre-shear void ratio
F	bounding surface
f	cyclic loading frequency
FEM	Finite Element Method
G	shear modulus
h	empirical constant
H	granular layer thickness
H	hardening modulus
h_0	model parameter

H_C plastic hardening modulus
H_f parameter capturing the effect of frequency f on the plastic modulus H_C
H_k parameter controlling the shakedown behaviour of ballast
$\boldsymbol{I}$ the second order identity tensor
j empirical parameter
K elastic bulk moduli
k empirical constant
k_d model parameter
k_p model parameter
K_p plastic modulus
L loading index
LVDT linear variable differential transformer
$\boldsymbol{m}$ the direction of $\dot{\varepsilon}^p$
m unit vector along plastic flow
m_{ij}^f flow directions for frictional sliding
m_{ij}^c flow directions for volumetric compaction
M_c critical state stress ratio with breakage
M_{c0} critical state stress ratio without breakage
M_d phase transformation state stress ratio
M_p peak stress ratio
M_R resilient modulus
N number of cycles
n unit vector normal to loading surface
$\boldsymbol{n}^*$ stress gradient direction
NCL Normal Compression Line
ODZ optimum degradation zone
$Ø_{peak,sta}$ peak friction angle
p' mean effective stress
p_c allowable subgrade pressure
p'_{cs} the value of p' on the critical state line at the current void ratio
$p'_{cs(i)}$ initial value of p'_{cs} at the start of shearing
p_i initial p'
$p'_{i,max}$ the maximum value of p_i'
p_m the vertical stress applied onto the ballast
PSD particle size distribution
q deviator stress
q_d measured dynamic deviator stress
q_m membrane correction
$q_{max,cyc}$ maximum deviator stress magnitude
$q_{min,\,cyc}$ minimum deviator stress magnitude
$\boldsymbol{q_n}$ plastic internal variable
$q_{peak,sta}$ static peak deviator stress
q_{sta} static deviator stress
q_* hardening variable
RCSL Reference Critical State Line
$\boldsymbol{r}_n$ the direction of $\dot{q}_n$

s	the stress deviator
S22	stress component in vertical direction
t	empirical constant
U2	displacement component in vertical direction
V	train speed
v_c	Rayleigh wave speed
W_E^P	effective work
W_R^P	used for particle rearrangement work
W_T^P	total plastic work
α	model parameters to cater effect of particle breakage
α_f	parameter capturing the effect of frequency on the plastic modulus
β	model parameters to cater effect of particle breakage
γ	membership function
γ_b	bulk unit weight
Δq_{cyc}	deviator stress amplitude
$\Delta\boldsymbol{\varepsilon}$	the incremental total strain
$\delta\varepsilon_p$	strain corresponding to the stress p'
$\delta\varepsilon_q$	strain corresponding to the stress q
$\delta\varepsilon^p$	plastic strain increment
$\delta\varepsilon_s^p$	plastic deviatoric strain increment
$\delta\varepsilon_v^p$	plastic volumetric strain increment
$\delta\varepsilon^e$	elastic strain increment
ε_{11}	component of strain vector
ε_{12}	component of strain vector
ε_{22}	component of strain vector
ε_{23}	component of strain vector
ε_{31}	component of strain vector
ε_{33}	component of strain vector
ε_a	cyclic axial strain
$\varepsilon_{a,\,sta}$	static axial strain
$\varepsilon_{a,cyc}$	cyclic axial strain
$\varepsilon_{a,rec}$	resilient axial strain
ε_r	radial strain
ε_s	deviatoric strain
ε_s^p	plastic deviatoric strain
ε_v	cyclic volumetric strain
$\varepsilon_{v,\,sta}$	static volumetric strain
$\varepsilon_{v,cyc}$	cyclic volumetric strain
ε_{s0}^p	accumulated plastic deviatoric strain at the current state
η_{in}	the value of η at initiation of a loading process
θ	bulk stress
θ_b	particle breakage parameter
κ	the swelling/recompression constant
μ	non-linear CSL parameter on q-p' plane
π	empirical constant
ρ	mass density

$\boldsymbol{\sigma}^*$	conjugate image stress state
σ_1'	principal stresses
σ_{11}	component of stress vector
σ_{12}	component of stress vector
σ_2'	principal stresses
σ_{22}	component of stress vector
σ_{23}	component of stress vector
σ_3'	confining pressure
σ_3'	confining pressure
σ_3'	principal stresses
σ_{31}	component of stress vector
σ_{33}	component of stress vector
λ	slope of CSL on υ-lnp' plane
$\dot{\lambda}$	plastic multiplier
η	stress ratio ($\eta = q/p'$)
η_s	hardening law
τ	empirical constant
Γ	specific volume on the CSL at $p' = 1$ kPa
Γ_{ref}	specific volume on the RCSL at $p' = 1$ kPa
υ	specific volume
υ_c	critical state volume
ϕ	friction angle
ϕ_{cs}	critical state friction angle
ϕ'_p	peak angle of friction
Φ_a	Cyclic Axial Strain Ratio
Φ_v	Cyclic Volumetric Strain Ratio
ν	Poisson's ratio
ν_b	particle breakage parameter
ω	non-linear CSL parameter on q-p' plane
ω_b	particle breakage parameter
χ	the material constant defining the rate of ballast breakage
Ψ	cyclic stress ratio
ψ	state parameter

CHAPTER 1

INTRODUCTION

1.1 Background

Railways are one of the most preferred modes of transportation for heavy freight and fast passenger trains, but increasing competition from other modes of transportation drives rail transport to increase its performance while keeping low operating costs. This demands higher train speeds, larger capacity, lower maintenance costs, greater comfort, better safety levels and lower energy consumption. Over the past few decades, the railway industries have considered most of the issues mentioned above, particularly increasing rail capacity, but this can only be achieved by increasing train speed.

While the use of heavier axle loads and higher train speeds have recently been their key priority, higher dynamic wheel loads are transmitted to the track structure with more repetitions (Li and Selig, 1998a). Consequently, railway track is subjected to higher repeated stresses, which may in turn lead to excessive deformation and degradation that greatly increases the cost of the maintaining the track substructure (ballast, subballast and subgrade). For instance, in New South Wales, Australia, millions of dollars are spent each year quarrying the 800,000 tonnes of the coarse aggregate needed to maintain the ballast profile.

Unfortunately, ballast is subjected to particle degradation which in turn affects its strength under cyclic loading, and often results in excessive settlement of rail track. Therefore the key challenges often faced by railway engineers when designing railway

lines can be listed as:

(1) How is excessive settlement and lateral spreading of ballast associated with train speeds?

(2) How does particle breakage influence track instability?

(3) How do different deformation modes of the ballast affect the load bearing capacity of track?

These questions demand an accurate assessment of the stress-strain and degradation behaviour of ballast under traffic (repeated) loading. Over the past decade, constitutive models have been developed to address the behaviour of a wide range of engineering materials under different loading conditions; indeed this decade has also witnessed a rapid expansion in the application of general purpose geotechnical software by practicing engineers, especially for nonlinear analysis. These together with elaborate and attractive graphical user interface (GUI) schemes, and user-friendly ways of performing three-dimensional modelling have added to the sense of confidence among users. Thus, it is important to develop reliable and versatile constitutive models for granular soils such as ballast.

Within the framework of classical plasticity theory, isotropic hardening can simulate the stress-strain of ballast under monotonic loading, but to mimic the reversible plastic flow and retain the load history, kinematic hardening or mixed hardening (isotropic and kinematic hardening) is normally used. However, kinematic hardening models are complicated and often too difficult to implement in constitutive drivers in reliable finite element codes, mainly because most of them were designed and validated for specific

stress paths, such as, conventional triaxial compression, so they were not validated or made useful for the other loading paths that occur in general boundary value problems of geotechnical engineering and structure-soil interaction.

In addition to basic modelling challenges, the remaining issues are how to model the effect of train speed on the mechanical behaviour of ballast (strength, dilatancy, stiffness, degradation) in a simple and systematic way, so a comprehensive, simple, and robust constitutive model is needed to relate to the strength, breakage, and deformation of ballast and to derive an implicit integration scheme to implement into finite element analysis.

1.2 Objectives and Scope of This Research

The current research focuses on the development of a constitutive model for ballast, including its calibration, validation, and its numerical integration into the Finite Element Method (FEM) to analyse the mechanical response of rail track under traffic loading. Large scale triaxial tests have been conducted to evaluate the permanent deformation, stiffness, and degradation of ballast subjected to monotonic and high frequency cyclic loads. Various confining pressures (i.e. σ_3' = 10 kPa to 570 kPa) were applied during monotonic testing, while in the cyclic loading tests, the load frequency f was varied from 5 to 60 Hz to simulate train speeds of 40 to 400 km/h. Two sets of deviator stress magnitude ($q_{max,cyc}$ = 230 and 370 kPa) were applied to resemble axle loads of 25 and 40 t, respectively. The effect of three levels of confining pressure (σ_3' = 10, 30 and 60 kPa) was examined. The constitutive model is based on the critical state concept, so the influence of particle breakage on the critical state parameters was studied and its effect was then incorporated into the model. The model was further extended into a cyclic model based on the bounding surface concept. A return-mapping algorithm was used to

integrate the constitutive model into FEM. A static analysis was then conducted using FEM to consider the dynamic effect of train speed in terms of a Dynamic Amplification Factor (DAF).

The specific objectives of this research are summarised below:

(1) An experimental investigation into the effect of particle breakage on the critical state, peak state, hardening and stress-dilatancy parameters of ballast.

(2) Development of a monotonic constitutive model for ballast based on the critical state concept, which incorporates the effect of particle breakage.

(3) An experimental investigation of the effects of key parameters such as, frequency, deviator stress magnitude, confining pressure, and number of loading cycles on fundamental ballast responses such as, permanent deformation (axial and volumetric strain), resilient modulus, and particle degradation.

(4) Development of empirical relationships that linked the load frequency f with the dynamic amplification factor (DAF).

(5) Extension of the monotonic model into a cyclic model while incorporating the effect of cyclic load frequency.

(6) Development of UMAT that is a user-defined module in ABAQUS for material properties, including its implication in ABAQUS. Validation of UMAT by making a comparison between FEM modelling predictions with the experimental and field data.

1.3 Thesis Outline

This thesis is divided into 6 chapters including this Introduction. A summary of the remaining Chapters is given below.

Chapter 2 provides an overview of the current state of research regarding the laboratory and numerical studies of ballast. An emphasis is placed on the deformation and degradation of ballast under monotonic and cyclic loading conditions, the recent developments of isotropic/kinematics hardening soil models, constitutive integration schemes, and finite element implementation.

Chapter 3 describes the large-scale triaxial experiments carried out to evaluate deformation and degradation under monotonic and cyclic (high frequency) loading. The stress-strain-volume response of ballast under monotonic loading and the permanent (axial and volumetric) and resilient modulus variations during cyclic loading are presented, including the nonlinear expressions of the critical state lines (CSL), definitions of cyclic strain ratio (CSR) and dynamic amplification factor (DAF). The empirical relationships are also derived to associate the frequency, state of stress, and number of cycles to axial strain, and the volumetric strain and resilient modulus.

Chapter 4 presents an elasto-plastic constitutive model based on the critical state soil mechanics framework that captures the salient aspects of stress-strain behaviour and degradation of ballast. Constitutive parameters are conveniently determined from large-scale laboratory tests. The model is used to predict the monotonic shear behaviour of ballast that corroborates with the laboratory measurements. The proposed model is further validated using experimental results available from previous independent studies. The monotonic model is also extended into a cyclic model that is also

introduced in this chapter. The cyclic model could capture the effect of frequency on the dilatancy of ballast under cyclic loading.

Chapter 5 presents the implication of the model in the finite element method (FEM). A return-mapping algorithm is included. The UMAT is validated by comparing the model prediction with the tests data. A railway track FEM model is established and the track response is analysed using the UMAT.

The conclusions of the study are presented in Chapter 6, together with recommendations for further research. The Appendices with additional details on constitutive modelling are provided at the end.

CHAPTER 2

LITERATURE REVIEW

2.1 Introduction

This chapter outlines the background of this study, including description on the response of granular materials (sand, rockfill and ballast) to monotonic and cyclic loads, recent developments in constitutive modelling, numerical integration schemes, and finite element studies of ballasted rail track.

2.2 Behaviour of Granular Material under Monotonic Loading

The deformation and degradation of ballast are profoundly depends on its loading characteristics, while the confining pressure, previous load history, current stress state, number of load cycles, frequency and magnitude (amplitude) of cyclic loading are the key parameters that govern track deformation. The response of granular materials under monotonic and cyclic loading conditions is discussed in the following sections.

2.2.1 Stress-strain Response

Numerous studies (Bishop, 1966; Vesic and Clough, 1968; Marsal, 1967; 1973; Billam, 1971; Ponce and Bell, 1971; Marschi et al., 1972; Raymond and Davies, 1978; Penman, 1978; Miura and O'Hara, 1979; Charles and Watts, 1980; Barton and Kjaernsli, 1981; Al-Hussaini, 1983; Jeffs, 1989; Indraratna et al., 1993; 1998; Yamamuro and Lade, 1996; Mirghasemi et al., 1997; Sitharam, 1999; Maeda and Miura, 1999) of granular materials subjected to monotonic loads under application of range of confining

pressures σ_3' have been carried out, so it is an established fact that as σ_3' increases:

(1) The volumetric strain changes from dilation to compression, and particle movement and rearrangement is largely restrained at higher confining pressures, which limits dilation.

(2) The axial strain at failure increases and the behaviour becomes increasingly ductile.

(3) The friction angle ϕ (strength) decreases because of reduced inter-particular friction, particle crushing, and the inability of specimens to dilate (Figure 2.1), where ϕ_p is the peak friction angle, ϕ_{max} is the maximum friction angle, ϕ_{fb} is the apparent friction angle including the effect of particle breakage, but excluding dilatancy and ϕ_f is the basic friction angle at aero rate of breakage.

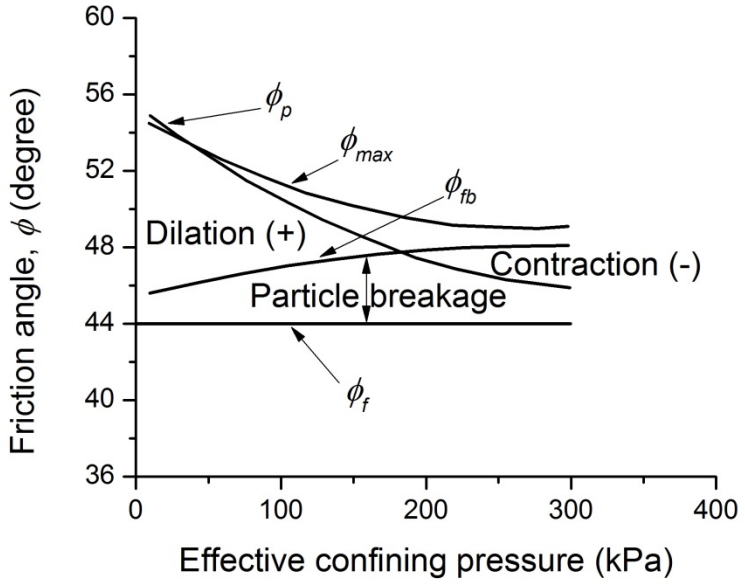

Figure 2.1 Effect of particle breakage and dilatancy on friction angle (modified after Indraratna and Salim, 2002)

(4) The peak deviator stress increases due to the limited horizontal particle displacement and subsequent increase in load carrying capacity, and the stress required to attain a particular strain increases with σ_3'.

(5) The degradation of particles increases because dilation is suppressed and the magnitudes of deviator stress increase.

(6) The initial stiffness of the specimen (modulus) increases.

2.2.2 Particle Breakage

The most important mechanical behaviour of granular materials such as stress-strain and strength, the change volume and development of pore pressure, as well as variations in permeability, depend largely on the strength of the individual particles or the amount of particle breakage that occurs from the change in stress (Lade et al., 1996). All granular aggregates subjected to stresses above normal geotechnical ranges exhibit a great deal of particle breakage (Bishop, 1966; Marsal, 1967; Lee and Farhoomand, 1967; Lee and Seed, 1967; Vesic and Clough, 1968; Billam, 1971; Miura and O'Hara, 1979; Hardin, 1985). Some researchers indicated that particle breakage can even occur at low confining pressure (Miura and O'Hara, 1979; Lade et al., 1996; Indraratna and Salim, 2002). The significance of particle degradation on the mechanical behaviour of granular aggregates has been recognised by many researchers (Marsal, 1967; Vesic and Clough, 1968; Billam, 1971; Miura and O'Hara, 1979; Hardin, 1985; Indraratna et al., 1998; Ueng and Chen, 2000, Indraratna and Salim, 2002). In the following section, the effect of particle breakage on the mechanical behaviour of ballast is discussed.

2.2.3 Effect of Particle Breakage on the Mechanical Behaviour of Granular Materials

The breakage of particles influences the strength and deformation of rail ballast (Indraratna et al., 1998; Indraratna and Salim, 2002; Lackenby et al., 2007; Nimbalkar et al., 2012), and when grain breakage occurs in granular media, the internal angle of friction and associated dilation angle decreases, which facilitates further compression

(Marsal, 1967; Marschi et al., 1972; Chales and Watts, 1980; Lade et al., 1996; Ueng and Chen, 2000; Indraratna et al., 2011; Indraratna and Nimbalkar, 2013). Larger particle with high grain angularity increase the extent of particle breakage during dilation (Lee and Farhoomand, 1967; McDowell and Bolton, 1998; Indraratna and Salim, 2002; Lackenby, 2006; Lackenby et al., 2007), while highly angular aggregates break easily at the corners even at small confining pressures, which reduces the friction angle quite considerably (Marsal, 1967; Marschi et al. 1972; Indraratna et al., 2011). The presence of micro-fissures in blasted and quarried aggregates also exacerbates breakage during shearing (Marsal 1967; Lade et al. 1996). Indraratna et al. (1998) provided the non-linear empirical relationship $\phi'_p = j(B_g)^k$, from their extensive large scale triaxial testing of latite basalt aggregate where ϕ'_p is the peak angle of friction, B_g is Marsal's breakage index (Marsal, 1967), j (64.84 to 73.19) and k (-0.13 to -0.18) are the empirical parameters. This empirical equation was derived at relatively large axial strains (@ 20-25%) and it represents a reduction in the friction angle with increasing particle breakage. For example with latite basalt, the increase in Marsal's breakage index from 5% to 10% was associated with a reduction of about 7-12° in the friction angle depending on the initial particle size distribution (PSD), where a PSD containing larger aggregates indicated greater vulnerability to breakage (Figure 2.2). At large axial strains exceeding say 20-25% (i.e. approaching a state of little or no volume change), the continual breakage of particles reduces angularity which in turn reduces the critical state friction angle. This is associated with a corresponding change in the critical state parameter M_c ($M_c = 6sin\phi_{cs}/(3-sin\phi_{cs})$). Others have reported that this reduction in the value of M_c can be mainly attributed to the confining pressure and particle breakage (Chavez and Alonso, 2003; Cheng et al., 2005) (Figure 2.3), but this result may conflict with previous studies (Coop, 1990; Mooney et al., 1998; Coop et al., 2004; Bandini and

Coop, 2011). The studies by Coop (1990), and Bandini and Coop (2011) conducted on much finer granular materials compared to rail ballast indicated that in spite of excessive particle breakage, the critical state stress ratio M_c remained relatively constant at high confining pressure, and very large amounts of breakage in shearing had almost no effect on M_c (Coop et al., 2004). However, as described earlier and observed in other studies, the rate and extent of breakage of very coarse and highly angular particles such as rail ballast should not be compared directly with much finer grained materials such as sand, which may require higher applied stresses to initiate significant breakage (e.g. Lade et al., 1996; Russel and Khalili, 2004). Also, ballast has very different physical and mechanical properties (size and shape of particles, surface texture, inter-particulate friction, micro-fractures (due to blasting) etc.).

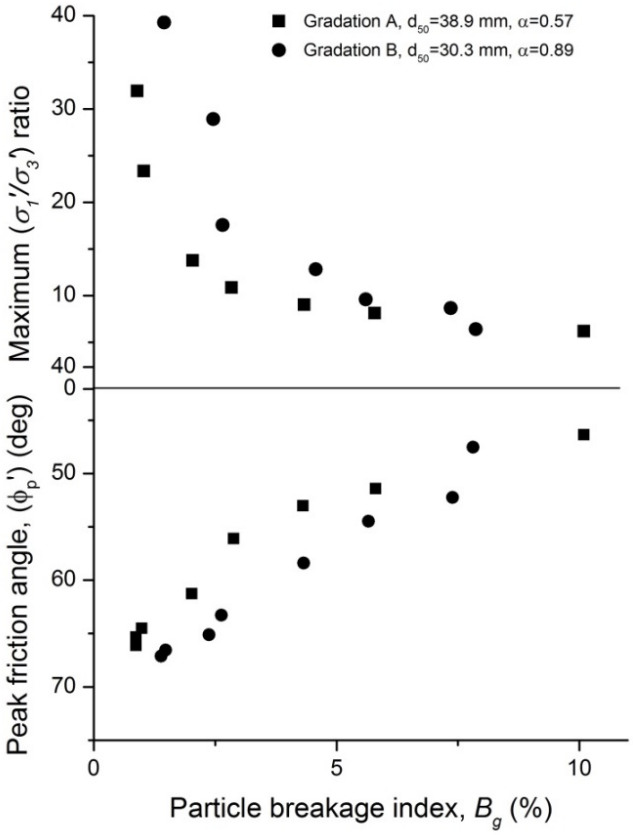

Figure 2.2 Influence of particle breakage on principal stress ratio and friction angle (adopted from Indraratna et al., 1998)

Been et al. (1991) investigated the critical state of sands for a wide range of confining stresses and proposed a bilinear critical state line (CSL). Russell and Khalili (2004) described the behaviour of crushable granular materials using a non-linear CSL (three-segment CSL) within a boundary surface constitutive model (Figure 2.4). Bedin et al. (2012) observed a highly non-linear shape of CSL during a series of monotonic triaxial tests on gold tailings and stated that the curvature was due to particle breakage. Daouadji et al. (2001) represented the position of the CSL in terms of the amount of energy needed for grain breakage, and showed that the CSL in the *e-lnp'* domain descends according to the evolution of particle gradation. Muir Wood and Maeda (2008) proposed a constitutive model for sands where a series of critical state lines in the *e-lnp'* plane were related to the current grading of the soil. As particle breakage occurs, the grading index I_g increased, shifting the CSL towards its limiting value at the limiting grading. The downward shift of the CSL on the *e-lnp'* plane could be attributed to the smaller broken grains which then rearranged themselves into a more compact state attaining a lower void ratio, *e* (e.g. Russel and Khalili, 2004; Bedin et al., 2012). Banidi and Coop (2011) also suggested that the influence of the newly created small fragments on CSL was very small because the latter was insensitive to the new grading, as assumed in the study by Muir Wood and Maeda (2008). Significant concentrations of stress and attrition in coarse and highly angular particles of ballast caused considerable breakage of asperities and sharp corners at relatively low stresses (Lackenby et al., 2007; Indraratna et al., 2014a). Even though the overall volume of breakage of relatively softer materials (e.g. carbonate sands, weathered sandstone) can be higher, the effect of degradation on the properties of ballast is mainly governed by the sharp drop in angularity after breakage (Indraratna et al., 2011). Therefore, the findings on carbonate sand reported by Coop et al. (2004) and Bandini & Coop (2011) may not be directly

applicable to ballast, particularly the behaviour implied at the critical state.

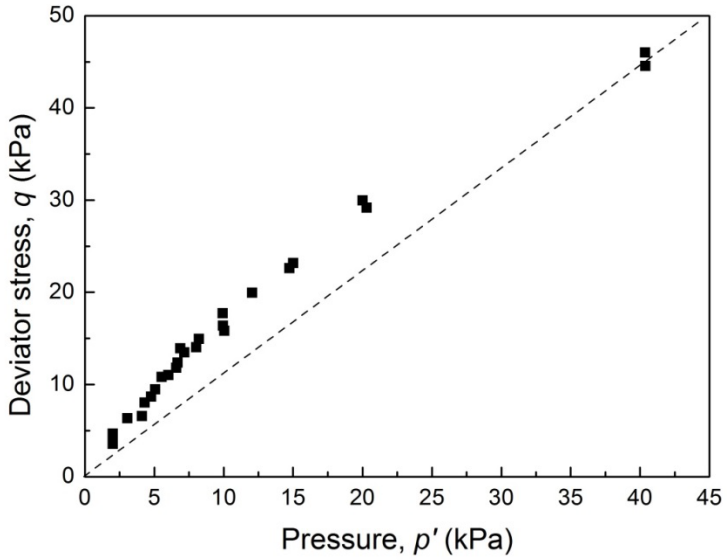

Figure 2.3 Deviator stress against pressure at final states (adopted from Cheng et al., 2005)

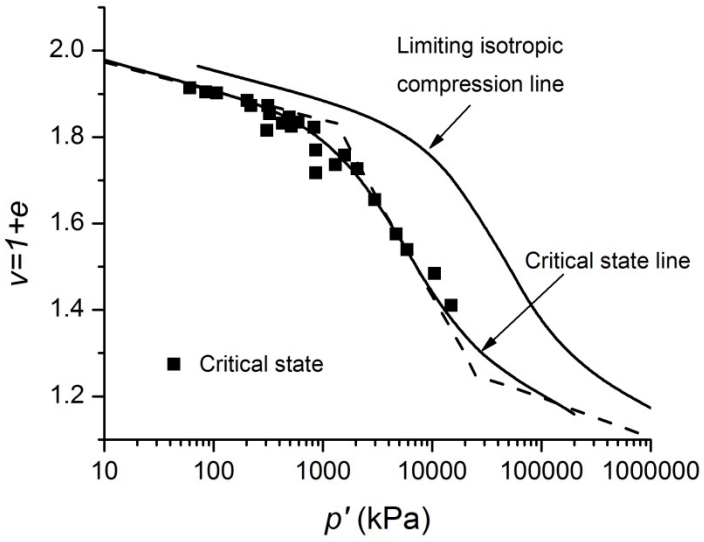

Figure 2.4 Critical state line and limiting isotropic compression line in the υ-lnp' plane and drained and undrained triaxial tests results (adopted from Russell and Khalili, 2004)

2.3 Behaviour of Granular Material under Cyclic Loading

2.3.1 Permanent and Resilient Response of Granular Material

The deformation of ballast under cyclic loading results from three main mechanisms:

densification or dilation, distortion, and degradation, all of which are characterised by a permanent (plastic) and a resilient (elastic) component. The densification or dilation mechanism is where ballast assemblies change in shape and compressibility; the distortion mechanism is characterised by individual particles sliding and rolling, and the degradation mechanism is a change in particle sizes due to attrition and breakage.

When material is subjected to cyclic loading, its stress-strain response can be characterised by the shakedown concept, as described by Werkmeister et al. (2001) and illustrated in Figure 2.5.

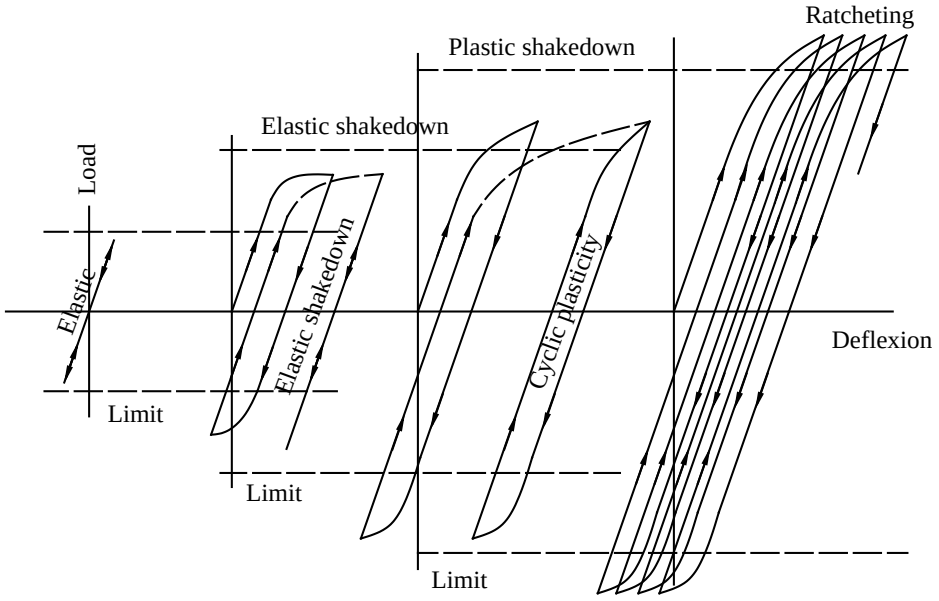

Figure 2.5 Schematic illustration of material behaviour under shakedown (adopted from Werkmeister et al., 2001)

(1) Purely elastic: this is the zone where the repeated stress is small enough so that no element of the material enters the yield condition. From the first stress-strain load cycle, all the deformations recovered completely and the response was termed purely elastic.

(2) Elastic shakedown: this is the zone where the repeated stress is slightly less than that

required to produce plastic deformation, and the material response is plastic for a finite number of stress-strain loadings. The ultimate response is elastic. The material is said to have 'shakedown' and the maximum stress level where this condition is achieved is termed the 'elastic shakedown limit'.

(3) Plastic shakedown: this is the zone where the repeated stress is slightly less than that required to produce a rapid incremental collapse, and where the material achieves a long-term steady state and there is no accumulation of plastic strain, and each response is hysteretic. This implies that a finite amount of energy is absorbed by the material on each stress-strain loading. Once a purely resilient response has been obtained the material is said to have undergone 'shakedown' and the maximum stress level at which this condition is achieved is termed 'the plastic shakedown limit',

(4) Ratcheting: this is the zone where the repeated stress is quite large, and where most of the material is in a yield condition and the plastic strains accumulate rapidly with failure occurring in a relatively short term.

The resilient modulus M_R describes the long-term elastic behaviour of materials under repetitive traffic loading (Ozel and Mohajerani, 2001). M_R can be calculated according to Equation (2.1), where Δq_{cyc} is the amplitude of cyclic loading and $\varepsilon_{a,rec}$ is the recoverable axial strain during unloading. An increasing M_R signifies increasing stiffness. After a large number of cycles, most deformation is essentially elastic (the material has undergone 'shakedown'), hence the use of recoverable strain to portray the long-term response to cyclic loading (Zaman et al., 1994).

$$M_R = \frac{\Delta q_{cyc}}{\varepsilon_{a,rec}} \tag{2.1}$$

Numerous studies have been carried out to characterise the resilient behaviour of granular materials. Hicks (1970) reported that the frequency *f* had almost no effect on the resilient behaviour of granular materials, while Lekarp et al. (2000) stated that under undrained conditions of finer materials, M_R showed a reduction with increasing *f* due to the development of pore pressure. It has also been reported that the moduli of subgrade soils under drained conditions increased almost linearly as a function of the logarithm *f* (Kim et al., 2001). Lackenby et al. (2007) highlighted that for rail ballast, an increase in M_R occurred with the number of load cycles *N*, a confining pressure σ_3' and a cyclic load magnitude $q_{max,cyc}$. Indraratna et al. (2009) investigated the influence of particle breakage on M_R and found that M_R increased with particle breakage as a result of increased packing density.

2.3.2 Assessment of Ballast Breakage

Many researchers (Lee and Farhoomand, 1967; Marsal, 1967; 1973; Hardin, 1985; Indraratna et al., 2005) attempted to quantify particle breakage upon loading and proposed their own computation/graphical techniques while others focused primarily on the probability of particle fracture (McDowell et al., 1996; McDowell and Bolton, 1998; McDowell and Daniell, 2001). In most of these techniques, different empirical indices or parameters were proposed as indicators of particle breakage. All breakage indices are based either on change in a single particle size or on changes in overall grain-size distribution. Lade et al., (1996) summarised the most widely used breakage indices for comparison. In this thesis, all the particle breakage of ballast was measured and represented by the ballast breakage index BBI that was proposed by Indraratna et al.

(2005) specifically for railway ballast. An evaluation of the ballast breakage index (BBI) (Equation 2.2) used the change in the fraction passing a range of sieve sizes. Figure 2.6 illustrates the definition of BBI.

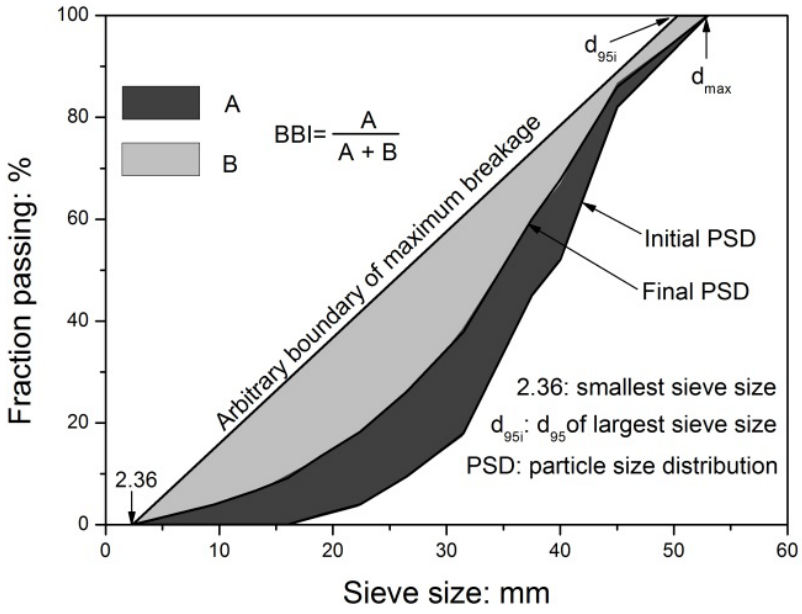

Figure 2.6 Ballast breakage index (BBI) calculation method (after Indraratna et al., 2005)

$$BBI = \frac{A}{A+B} \tag{2.2}$$

where *A* is the area traced out by the shift in the initial particle size distribution towards smaller particle sizes, where the maximum size was unchanged before and after loading (e.g. Indraratna et al., 1998), and *B* is the potential breakage or the area between the arbitrary boundary of maximum breakage and the final particle size distribution (Figure 2.6).

The breakage of ballast under cyclic loading can be categorised into three zones: the dilatant unstable degradation zone (DUDZ), the optimum degradation zone (ODZ), and the compressive stable degradation zone (CSDZ) (Indraratna et al., 2005; Lackenby et al., 2007). These zones depend on the level of confining pressure and maximum

deviator stress acting on the specimen, as shown in Figure 2.7, and are described below.

(1) *Dilatant unstable degradation zone (DUDZ).* Specimens that are subjected to low σ_3', and which experience overall volumetric dilation caused by rapid and considerable axial and expansive radial strains, are characterised in the DUDZ (Figure 2.7). Degradation in the DUDZ is considered to be the most significant of the three zones, with breakage occurring predominantly at the onset of loading when the axial strain and dilation rates are at a maximum (Lackenby et al., 2007). They further reported that most of the degradation in this zone was due to the breakage of angular corners or projections, rather than particle splitting, and also indicated that this was due to internal deformation mechanisms such as sliding or rolling, that inhibit the formation of permanent inter-particle contacts and prevent splitting due to excessive stresses.

(2) *Optimum degradation zone (ODZ).* Lackenby et al. (2007) reported that as a result of a small increase in confining pressure, an optimum internal contact stress distribution and increased inter-particle contact area occurred in the ODZ, and therefore the tensile stresses within particles diminished and breakage reduced significantly. Besides, the coordination number was expected to have increased slightly (compared to the DUDZ specimens) owing to the reversal of volumetric strain from dilation to compression.

(3) *Compressive stable degradation zone (CSDZ).* Indraranta et al. (2005) mentioned that in the CSDZ, particle movement and dilation were largely suppressed owing to the considerable level of confinement. The most significant differences between the ODZ and CSDZ were the reduced mobility of particles and the highly stressed but relatively secure contact points (Lackenby et al.,

2007). Although corner degradation is still the foremost kind of breakage, some particle splitting takes place through planes of weakness such as micro-cracks and other flaws, and particle fatigue becomes more prominent in the CSDZ (Indraratna et al., 2005). They further postulated that particles were highly stressed and contact forces were more isotropic under increasing confining pressure.

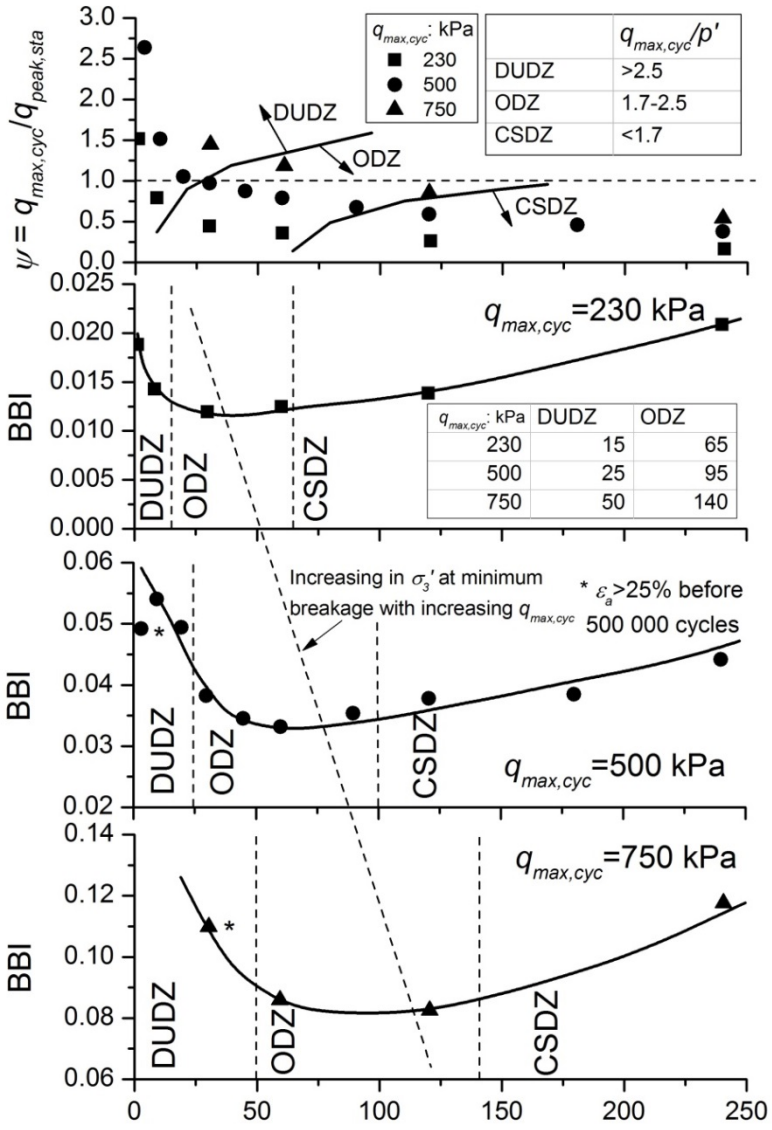

Figurer 2.7 Effect of confining pressure σ_3', and maximum deviator stress $q_{max,cyc}$ on ballast breakage index BBI, and effect of $q_{max,cyc}$ on DUDZ, ODZ and CSDZ zones (adopted from Lackenby et al., 2007)

2.3.3 Effect of Load Frequency on Ballast Behavior

The results of in-situ tests and numerical studies indicated that the train speed V has a significant influence on the track response (i.e. Luo et al., 1996; Kemfert and Hu, 1999; Priest and Powrie, 2009; Banimahd et al., 2013; Indraratna et al., 2014b). Field investigations by Kemfert and Hu (1999) (Figure 2.8) and Indraratna et al. (2014a) indicated that vertical stresses increased with the train speed V. Luo et al. (1996) investigated the dynamic response of railway ballast due to the passage of trains moving at different values of V based on finite element analysis, and concluded that three different regimes of ballast settlement exist, namely, (i) an insignificant displacement region, (ii) a rapidly increasing displacement region, and (iii) an attenuated increase in the displacement region corresponding to $V < 180$ km/h, 180 km/h $\leq V \leq$ 300 km/h and $V >$ 300 km/h, respectively (Figure 2.9). Only limited experimental data was available to quantify the effect that high train speeds had on a ballasted track.

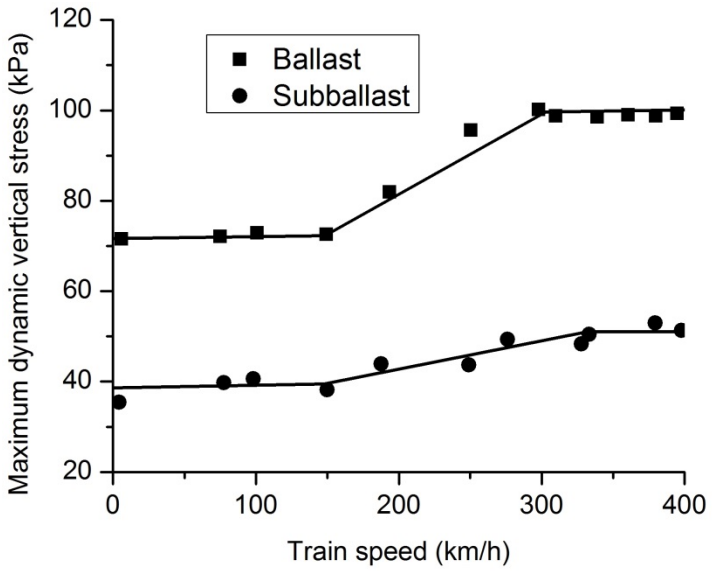

Figure 2.8 Effect of train-speed on dynamic stress (adopted from Kemfert and Hu, 1999)

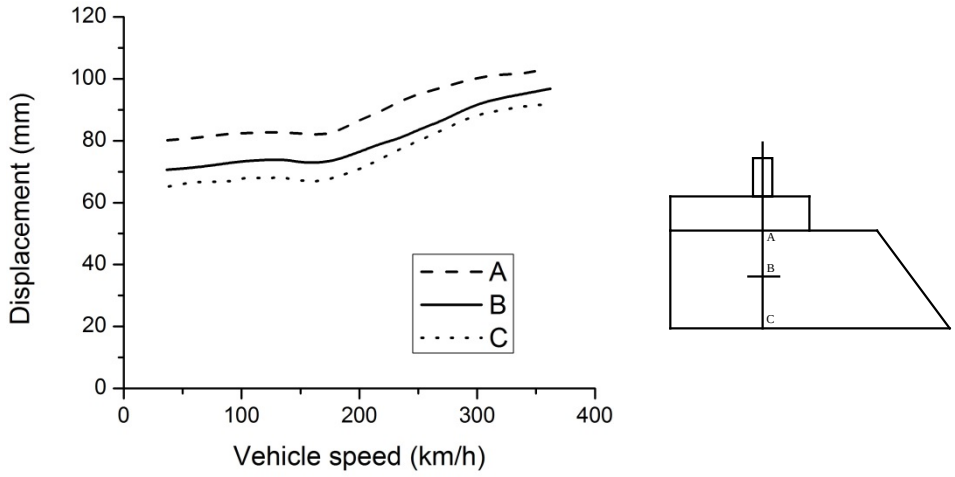

Figure 2.9 Response of displacement (maximum value) (adopted from Luo et al., 1996)

2.3.4 Effect of Load Magnitude and Confining Pressure on Ballast Behaviour

Previous researchers have studied the effects of cyclic load magnitude $q_{max,cyc}$ and confining pressure σ_3' on the permanent deformation of ballast extensively (Raymond and Williams, 1978; Suiker and de Borst, 2003; Lackenby et al., 2007). Suiker and de Borst (2003), for instance, divided the stress domain (in q-p' space, where q is the deviator stress and p' is the mean effect stress) of ballast under cyclic loading into four different response regimes: (i) shakedown, (ii) cyclic densification, (iii) frictional failure, and (iv) tensile failure. Cyclic triaxial data on ballast from Lackenby *et al*. (2007) is replotted in Figure 2.10 to highlight the existence of at least four regimes of permanent deformation based on the applied stress ratio ($q_{max,cyc}/p'$). These regimes are: (i) the zone of elastic shakedown exhibited by no accumulation of plastic strain, (ii) the zone of plastic shakedown characterised by a steady state response with a small accumulation of plastic strain, (iii) a ratcheting zone that shows a constant accumulation of plastic strain (Alonso-Marroquín *et al*., 2004), and (iv) a plastic collapse zone where the plastic strains accumulate rapidly and failure occurs in a relatively short time (Sloan *et al*., 2008). Indraratna et al. (2010a) and Thakur et al. (2013) applied different deviator stress $q_{max,cyc}$ corresponding to the selected frequencies *f*, so their study could not

properly distinguish between the individual effects of $q_{max,cyc}$ and f on the deformation and degradation of ballast.

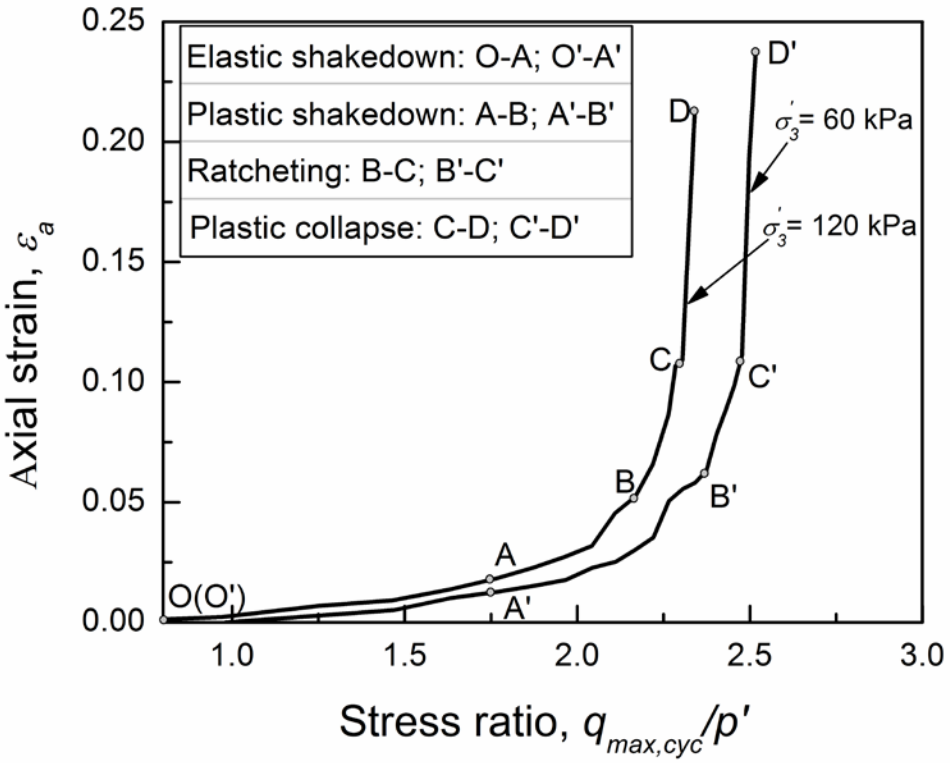

Figure 2.10 Axial strain versus stress ratio (data sourced from Lackenby *et al*., 2007)

2.4 Constitutive Modelling of Granular Material

The literature related to conventional incremental isotropic/kinematic or mixed hardening elasto-plastic theory is vast and the readers are referred to The Mathematical Theory of Plasticity by Hill (1950), Plasticity for Structural Engineers by Chen and Han (1988), Plasticity Theory by Lubliner (1990), Computational Inelasticity by Simo and Hughes (1998), Plasticity: Mathematical Theory and Numerical Analysis by Han and Reddy (1999), and Plasticity for Engineers: Theory and Applications by Calladine (2000), etc. The following discussion focuses on isotropic/kinematic hardening models.

2.4.1 Critical State Models

In the late 1950's and 1960's, Roscoe and his co-authors developed a critical state model based on the theory of plasticity and soil behaviour at the critical states (Roscoe et al., 1958; 1963; Roscoe and Burland, 1968; Schofield and Wroth, 1968). Roscoe and his co-researchers were the first to successfully model plastic shear deformation and the associated change in volume of soils during shearing. The mathematical model developed for the plastic deformation of clay is known as 'Cam-clay' (Roscoe et al., 1963; Schofield and Wroth, 1968), and later models are known as 'modified Cam-clay' (Roscoe and Burland, 1968).

The 'critical state' has been defined as the state at which soil continues to deform at constant stress and constant void ratio (Roscoe et al., 1958). The main features of the critical state model are:

(1) All the possible states of a soil form a stable state boundary surface (SSBS), as shown in Figure 2.11(a),

(2) Deformation of soil remains elastic until its stress state reaches the stable state boundary surface, i.e. soil begins to yield when the stress path meets the SSBS,

(3) At the critical state all the energy transmitted to a soil element across its boundary is dissipated within the soil element as frictional heat loss, without changing its stress or volume. Thus, at the critical state, $q=Mp'$ (Figure 2.11 (b)), where, M is the coefficient of friction at the critical state,

(4) The projection of the critical state line (CSL) on e-p' plane is parallel to the Normal Compression Line (NCL) obtained under isotropic compression (Figure 2.11 (c)).

The NCL and the projection of CSL become parallel straight lines when plotted in a semi-logarithmic *e-lnp'* scale (Figure 2.11 (d)). The swelling and recompression are also assumed to be linear in the *e-lnp'* plane.

Been et al. (1991) studied the critical state/steady state of sands and concluded that the critical state line is approximately bilinear in the *e-lnp'* plane, as shown in Figure 2.12. They found an abrupt change in the slope of the critical state line for Leighton Buzzard sand and Erksak sand at about 1 MPa, which they attributed to grain breakage.

Although the original critical state model (Roscoe et al., 1958; 1963) was based on extensive laboratory tests of remoulded clay, some researchers attempted to model the deformation of sands and gravels similar to the critical state (Cam-clay) model. Schofield and Wroth (1968) presented a critical state model for gravels (Granta-gravel) by omitting the elastic component of the volumetric strain.

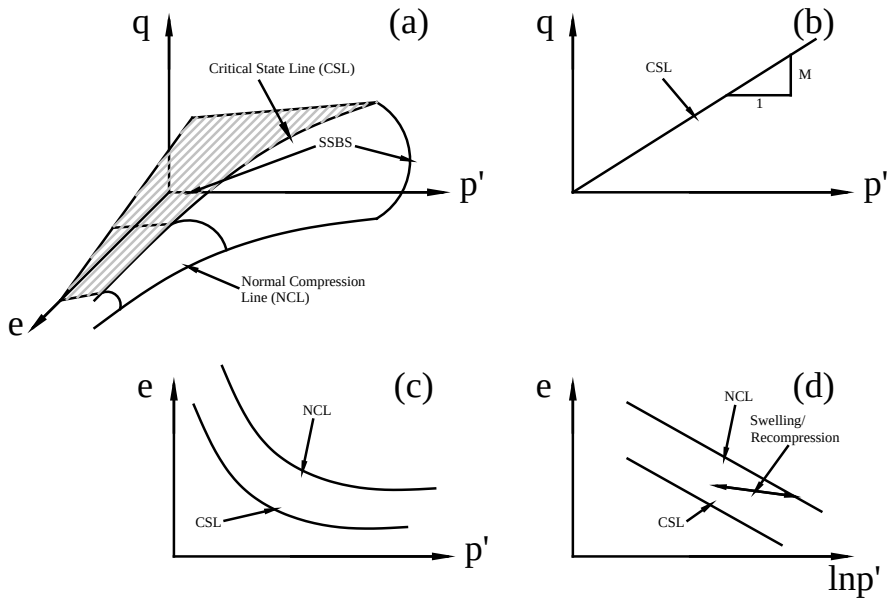

Figure 2.11 Critical state model, (a) state boundary surface, (b) projection of CSL in *q-p'* plane, (c) projection of CSL and NCL on *e-lnp'* plane, and (d) CSL and NCL plotted in *e-lnp'* plane (adopted form Indraratna et al., 2011)

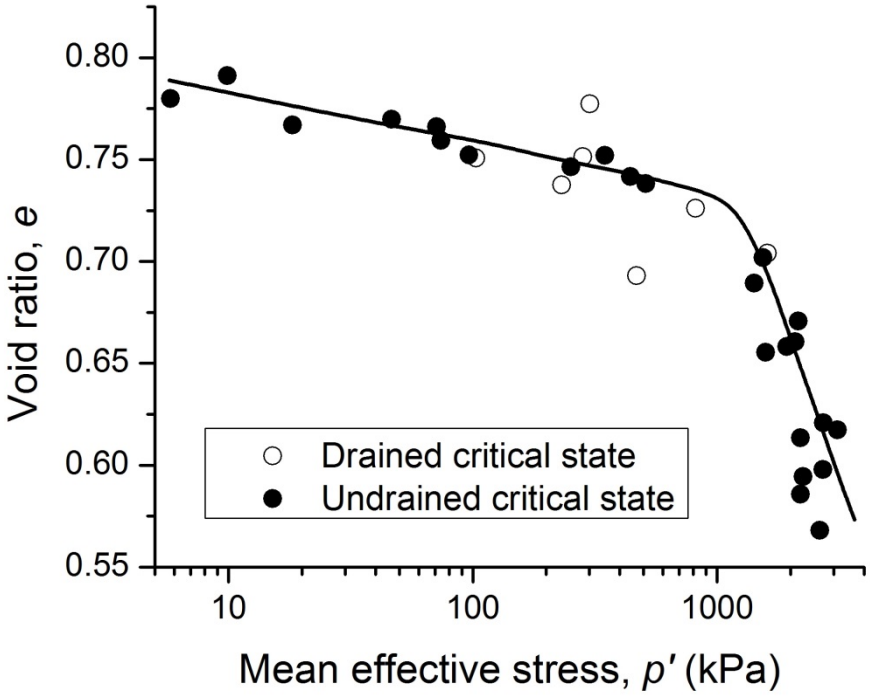

Figure 2.12 Bi-linear critical state line of sands (after Been et al., 1991)

Jefferies (1993) stated that the Cambridge type models could not reproduce the softening and dilatancy of sands, which are on the dense (dry) side of the critical state line. He pointed out that the inability of Cambridge models to dilate is a large deficiency in modelling the behaviour of sand, because virtually all sands are practically denser than the critical state and dilate during shearing. He proposed a critical state model for sand by assuming the associated flow and infinity of the isotropic normal compression line (NCL). The initial density of sand was incorporated through the state parameter ψ, as defined by Been and Jeffries (1985). Jefferies (1993) used the following dilatancy rule:

$$D = \frac{M - \eta}{1 - N} \tag{2.3}$$

where D (= $\delta\varepsilon_p/\delta\varepsilon_q$) is a dilatancy function, $\delta\varepsilon_p$ and $\delta\varepsilon_q$ are strains corresponding to the stresses p' and q, M is the critical state friction coefficient, η is shear stress ratio (=q/p')

and N is a density dependent material property.

Using Equation (2.3) and the normality condition, Jefferies (1993) formulated the yield surface for Nor-sand as given by:

$$\eta = \frac{M}{N}\left[1+\left(N-1\right)\frac{P^{'N/(1-N)}}{p_i^{'}}\right] \quad \text{if } N\neq 0 \tag{2.4a}$$

$$\eta = M\left[1+ln\left(\frac{p_i^{'}}{p^{'}}\right)\right] \quad \text{if } N=0 \tag{2.4b}$$

where p_i' is the mean stress at the image state defined by the condition $\delta\varepsilon_p$=0. A simple hardening rule was used by Jefferies (1993), as given below:

$$\frac{dp_i^{'}}{d\varepsilon_q} = h\left(p_{i,max}^{'} - p_i^{'}\right) \tag{2.5}$$

where h is a proportionality constant and $p'_{i,max}$ is the maximum value of p_i'.

The Nor-sand (Jefferies, 1993) adequately modelled the behaviour of sand including dilatancy, post-peak strain softening, and the effects of confining pressure and initial density. Recognising the limitation associated with the use of normality (associated flow) in sand, most other researchers used non-associated flow in their formulations (Lade, 1977; Pender, 1978; Morz and Norris, 1982; Daffalias and Herrmann, 1980; 1982). Muir Wood et al. (1994) incorporated a state parameter concept for sand modelling where the proposed hardening rule links the change in location of yield locus with distortional strain, and Rowe's stress-dilatancy flow rule is used. Manzari and Dafalias (1997) presented a model within the framework of critical state soil mechanics. Here the two-surface bounding surface plasticity model was coupled with the state

parameter which was used to define the peak and dilatancy stress ratio of sands. The model can simulate the behavior of sand under monotonic and cyclic, and drained and undrained loading conditions. Both isotropic and kinematic hardening rules were used to describe the evolution of yield surface. Isotropic hardening is related to plastic volumetric strain while kinematic hardening is similar to the non-linear kinematic hardening rule put forward by Armstrong and Frederick (1966).

2.4.2 Bounding Surface Plasticity Models

Bounding surface plasticity was originally introduced by Dafalias and Popov (1975), and independently by Krieg (1975), in conjunction with an enclosed yield surface for metal plasticity. Since then the bounding surface plasticity has been developed and implemented by numerous researchers, mainly to model clay soils. Bardet (1985) proposed a bounding surface plasticity model for sands where the model describes strain-softening, stress-dilatancy, drained and undrained behavior, the dissipation of hysteretic energy, and irreversible strain during a cyclic loading test. Anandarajah (1994) presented a bounding surface plasticity model for granular materials under monotonic loading where combined isotropic hardening that includes density, deviatoric and shape hardening was also proposed. An associated flow rule was used to produce a symmetric stiffness matrix, which allows finite element analysis to be carried out in an efficient manner.

The development of a bounding surface concept was motivated by the results of some monotonic and cyclic uniaxial tests where it was found that the stress strain response curve eventually converged with ‘bounds’ in the stress strain space. These bounds cannot be crossed, but may change position during the loading process, but within this framework the plastic strain can occur for stress states within the bounding surface.

Also, it is possible for the plastic modulus to have a very flexible and smooth variation during straining, unlike the multi-surface plasticity model which assumed a piecewise constant plastic moduli.

The role of the bounding surface given by Dafalias and Hermann (1982) is summarised as follows: for any stress point inside the surface, a unique 'image' point is defined on the surface by means of a specific rule. The value of the plastic modulus depends on the distance between the stress point and its 'image', while the gradient of the bounding surface at the 'image' point defines the loading-unloading direction.

A bounding surface (F=0) and its stress gradient direction ($\boldsymbol{n}^*$), as shown in Figure 2.13, are defined by

$$F = F\left(\boldsymbol{\sigma}, q_n\right) \tag{2.6}$$

$$\boldsymbol{n}^* = \frac{\partial F}{\partial \boldsymbol{\sigma}} \tag{2.7}$$

Unlike classical plasticity, the plastic strain rate, for bounding surface plasticity theory, is determined by

$$\dot{\boldsymbol{\varepsilon}}^p = \langle L \rangle \boldsymbol{m} \tag{2.8}$$

and the evolution of the plastic internal variable is given by

$$\dot{\boldsymbol{q}}_n = \langle L \rangle \boldsymbol{r}_n \tag{2.9}$$

where $\boldsymbol{m}$ and $\boldsymbol{r}_n$ are the direction of $\dot{\boldsymbol{\varepsilon}}^p$ and $\dot{\boldsymbol{q}}_n$, respectively. $\boldsymbol{m}$=$\boldsymbol{n}$ if the associated flow rule is applied, and L is the loading index defined by

$\langle L \rangle = L$ when L>0 (2.10a)

$\langle L \rangle = 0$ when L≤0 (2.10b)

where

$$L = \frac{1}{K_p} \boldsymbol{n} : \dot{\boldsymbol{\sigma}} \tag{2.11}$$

K_p is the plastic modulus.

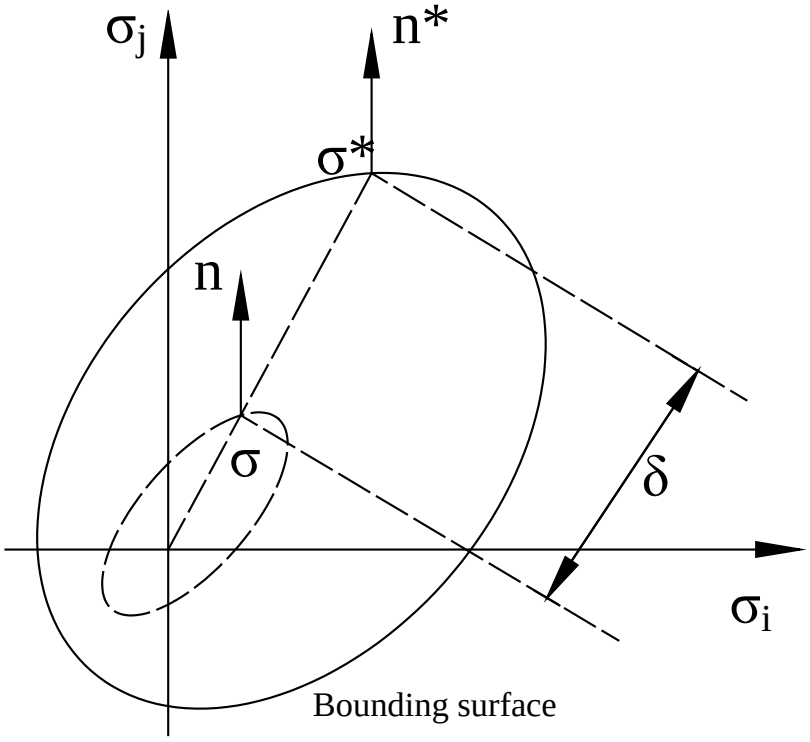

Figure 2.13 Schematic illustration of bounding surface concept (adopted from Dafalias and Hermann, 1982)

For any $\dot{\boldsymbol{\sigma}}$ such that $L \geq 0$, a corresponding $\dot{\boldsymbol{\sigma}}^*$ occurs at the images stress point due to the change of $\dot{\boldsymbol{\sigma}}$ and the hardening of F=0. Since $\boldsymbol{\sigma}^*$ must always remain on F=0, the use of Equations (2.6), (2.7), (2.9) and (2.11) in the consistency condition $\dot{F} = 0$ yields

$$L = \frac{1}{K_p}\boldsymbol{n} : \dot{\boldsymbol{\sigma}} = \frac{1}{K_p^*}\boldsymbol{n}^* : \dot{\boldsymbol{\sigma}}^* \tag{2.12}$$

$$K_p^* = -\frac{\partial F}{\partial q_n}\boldsymbol{r}_n \tag{2.13}$$

The actual plastic modulus K_p is related to K_p^* via the distance δ between $\boldsymbol{\sigma}^*$ and $\boldsymbol{\sigma}$, i.e.

$$\delta = \sqrt{\left(\boldsymbol{\sigma}^* - \boldsymbol{\sigma}\right)\left(\boldsymbol{\sigma}^* - \boldsymbol{\sigma}\right)} \tag{2.14}$$

and an expression of the general form of K_p is given by

$$K_p = K_p\left(K_p^*, \delta, \boldsymbol{\sigma}, \boldsymbol{q}_n\right) \tag{2.15}$$

2.4.3 Disturbed State Model

The disturbed state concept (DSC) model was first proposed by Desai (1974), and its basic concept is that the material is assumed to transform continuously and randomly from a relatively intact (RI) state to the fully adjusted (FA) state under external excitation such as mechanical or thermal forces. The transformation of the material from RI to FA states is defined by the disturbance function. Figure 2.14 shows a schematic of the RI to FA states. Shao and Desai (2000) presented a DSC model to simulate the cyclic behaviour of saturated clay. They showed a simplified approach for modelling the unloading and reloading behaviour without the need to introduce complex functions to describe the motion of the yield surfaces.

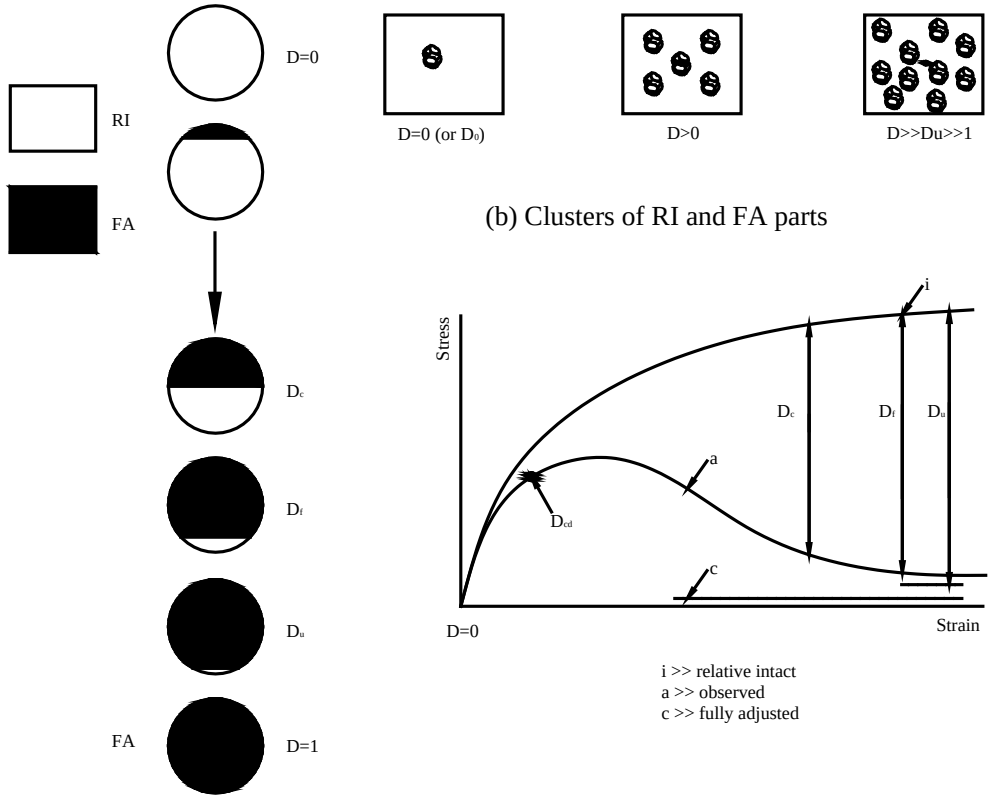

Figure 2.14 Disturbed state concept: schematic representation (adopted from Desai 2007)

2.4.4 Single and Double Hardening Models

Koiter (1953) discussed the concept of multiple yield functions, while Iwan (1967) extended Koiter's work by adding kinematic hardening to each of the yield surfaces. Independently, Mroz (1967) developed an anisotropic hardening model for metals based on the concept of a field of work-hardening moduli. Prevost and Hoeg (1975), Prevost (1977), and Prevost et al. (1981) adopted the work by Mroz in order to study the behaviour of clays under monotonic and cyclic loading conditions and the anisotropic effect of initial consolidation. Mroz et al. (1978) proposed an anisotropic hardening model for soils by applying the concept of a field of hardening moduli. Besides the yield surface, a set of nesting surfaces in a stress space specifies the variation of hardening moduli during the deformation process. Both drained and undrained soil

behaviours under cyclic loading were simulated.

Sture et al. (1982) described details of the analysis and application of the multi-surface anisotropic hardening model. The instantaneous configuration of the field of yield surfaces was established by computing the parameters and equations that govern the translation, expansion or contraction of individual surfaces during proportional as well as non-proportional loading and unloading. The surfaces change size with plastic volumetric strain, and the motion of the active yield surface and all the interior surfaces is governed by Mroz's kinematic rule. Stress induced anisotropy is captured because the sizes and initial positions of the nesting yield surfaces reflect the past stress-strain history of the soil.

Vermeer (1982) presented a five-constant model based on isotropic hardening for both cone and cap yield surfaces. A close approximation of Rowe's stress-dilatancy equation was used to describe the shear dilatancy, and a hyperbolic relationship was assumed between the shear strain and the shear stress. Bardet (1995) proposed a new modelling concept for soil called scaled memory, which transforms the nonlinear plastic modulus into a piecewise-linear distribution, and then used this simplified distribution to generate the plastic modulus during cyclic loadings. Only a one-dimensional case was considered, a multi-dimensional format was not presented.

A large number of researchers have modelled elasto-plastic deformation of sand and other granular media under both monotonic and cyclic loadings, but the research dealing with the development of an elasto-plastic deformation model to simulate the behaviour of ballast, including plastic deformation and particle breakage is limited.

2.4.5 Existing Ballast Models

Until today, the vast majority of railway engineers have regarded ballast as an elastic media. Although the accumulation of plastic deformation under cyclic traffic loading is evident, most researchers are primarily interested in modelling the dynamic resilient modulus of ballast. Limited research has been conducted on modelling the plastic deformation of ballast associated with cyclic loading, although some researchers have attempted to simulate plastic deformation empirically (Indraratna et al., 2011).

Suiker (2002) developed a plastic deformation model for ballast where the plastic 'frictional sliding' and 'volumetric compaction' mechanisms were considered during cyclic loading. He called it the 'Cyclic Densification Model', where the plastic flow rule was decomposed into a frictional contribution and a compaction component, as given by:

$$\frac{d\varepsilon_{ij}^{p}}{dN} = \frac{d\kappa^{p}}{dN} m_{ij}^{f} + \frac{d\varepsilon_{vol,c}^{p}}{dN} m_{ij}^{c} \tag{2.16}$$

where, $d\varepsilon_{ij}^{p}$ is the infinitesimal increment of plastic strain, $d\kappa^{p}$ is the increment of plastic distortional strain, $d\varepsilon_{vol,c}^{p}$ is the plastic volumetric strain increment due to cyclic compaction, m_{ij}^{f} and m_{ij}^{c} denote the flow directions for frictional sliding and volumetric compaction, respectively, and dN is the increment of load cycle.

Suiker (2002) classified the stress domain into four regimes:

(1) The shakedown regime where the cyclic response of ballast is fully elastic,

(2) The cyclic densification regime where progressive plastic deformation occurs under

cyclic loading,

(3) The frictional failure regime where frictional collapse occurs because the cyclic stress level exceeds the static maximum strength, and

(4) Tensile failure regime where non-cohesive granular materials disintegrate due to induced tensile stresses.

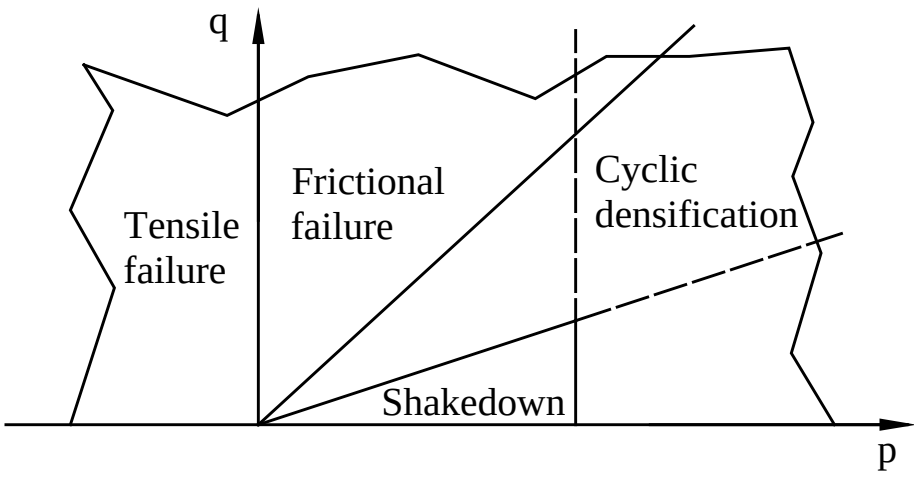

Figure 2.15 Four response regimes during cyclic loading (after Suiker, 2002)

These regimes are shown in Figure 2.15 in the q-p' plane, where, p' and q are the mean effective normal stress and deviator stress (invariants), respectively.

Suiker's (2002) cyclic densification model is an advanced step in modelling the plastic deformation and plastic compaction of ballast under cyclic loading. However, particle breakage associated with cyclic loading, an important factor governing the plastic deformation and cyclic compaction of ballast, is not considered in Suker's (2002) model.

Ge (2003) developed a cyclic constitutive model for ballast based on fuzzy set plasticity. Unlike conventional elasto-plastic hardening models, the fuzzy set model is physically intuitive and easy to visualize, and it can describe repeated load cycles, dilatancy,

material memory, drained and undrained behaviour, features of critical state soil mechanics, density and mean effective stress dependence, and long-term cyclic effects (shakedown). The basic concept assumes that a fuzzy surface exists which resembles a bounding surface. At each point within the fuzzy surface, the value of the membership function ($\gamma=\gamma(\boldsymbol{\sigma})$) is given by a specified assignment, i.e. a real member $\gamma(\boldsymbol{\sigma})$ on the interval [0,1] is assigned to each stress point $\boldsymbol{\sigma}$ in the region $F \leq 0$ as shown in Figure 2.16. The value of the membership function is used to determine the plastic moduli. It is also assumed that for the stress state ($\boldsymbol{\sigma}$) at loading/active surface ($f=f(\boldsymbol{\sigma}, q_*)$), a conjugate image stress state ($\boldsymbol{\sigma}^*$) exists on the fuzzy surface ($F=F(\boldsymbol{\sigma}^*, q_*)$), where the gradients for the loading and fuzzy surfaces have the same direction, as shown in Figure 2.17.

The ingredients of fuzzy set plasticity are the fuzzy surface $F(\boldsymbol{\sigma}^*, q_*)=0$, loading/active surface $f(\boldsymbol{\sigma}, q_*)=0$, plastic flow rule $\dot{\varepsilon}^p = \dot{\lambda} m$, hardening rules $\dot{q}_* = \dot{\lambda} r_*$, consistency condition on the fuzzy surface $\dot{F} = \boldsymbol{n}^* \dot{\boldsymbol{\sigma}}^* - \dot{\lambda} H_p^* = 0$, consistency condition on the loading/active surface $\dot{f} = \boldsymbol{n}\dot{\boldsymbol{\sigma}} - \dot{\lambda} H_p = 0$, and the plastic modulus $H_p = H_p^* + h(\gamma)$. In the above equations, q_* is the hardening variable, $\dot{\lambda}$ is the plastic multiplier, $\boldsymbol{m}$ is the direction of the plastic strain increment, and $\boldsymbol{n}$ is the gradient of the loading/active surface, which is equal to $\boldsymbol{n}^*$, the gradient of the fuzzy surface. Here, the plastic modulus is a function of the value of the membership function, which is determined at any stress state. Plastic deformation occurs when the following condition $n\dot{\gamma} = n^*\dot{\gamma} \geq 0$ $n\dot{\gamma} = n^*\dot{\gamma} \geq 0$ is satisfied, but because there was no database for cyclic traixial experiments, the fuzzy set model developed by Ge (2003) was not validated and the model did not capture the effect of particle breakage.

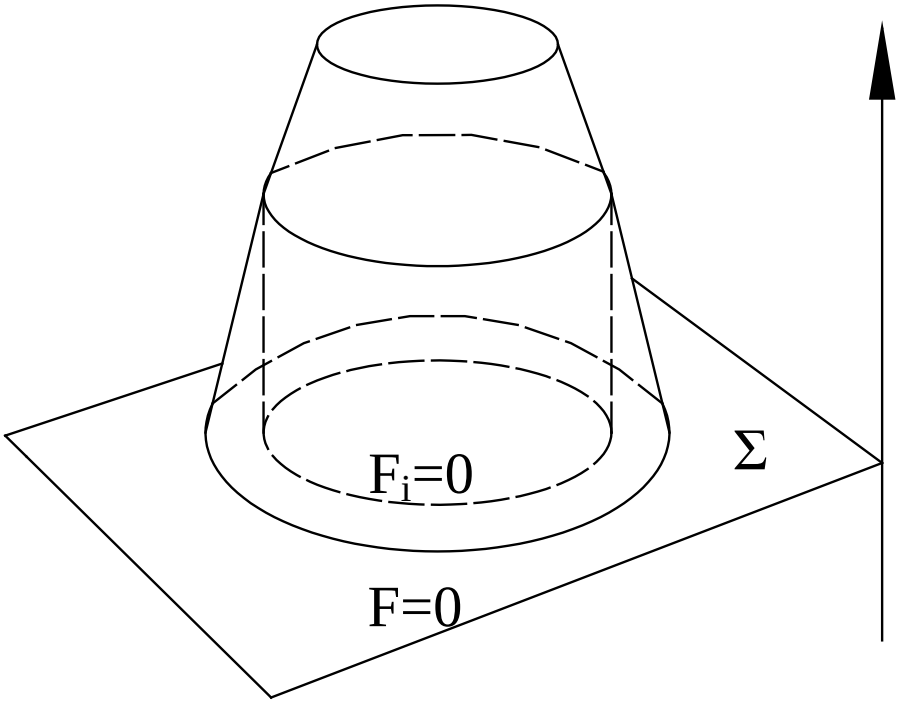

Figure 2.16 The loading/active surface specified by a given constant value of the membership function (after Klisinski,1988)

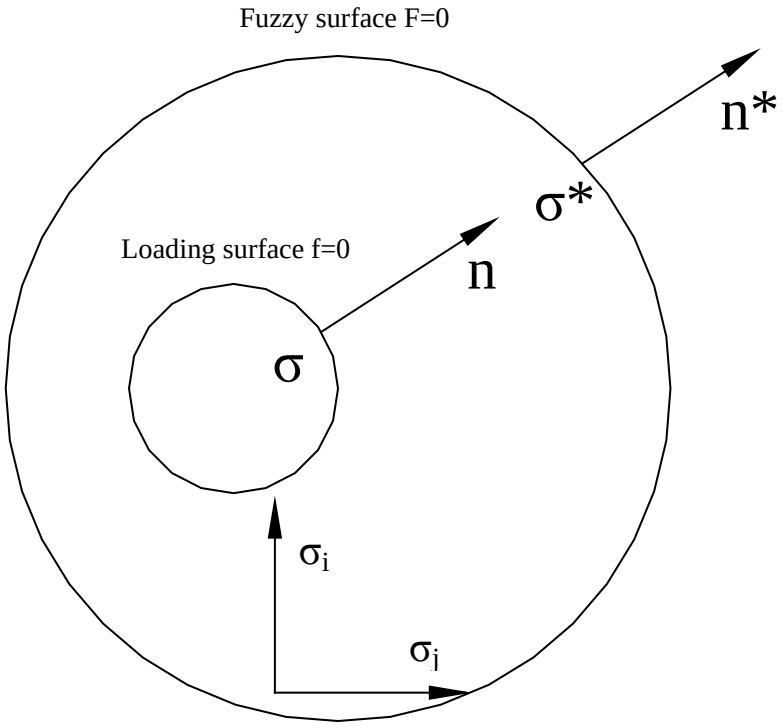

Figure 2.17 Schematic illustration of the gradient at a point on the loading surface and its conjugate image point on the fuzzy surface (adopted from Ge, 2003)

Salim and Indraratna (2004) proposed a new stress-strain and particle breakage constitutive model for ballast based on the critical state framework. A non-associated

flow and kinematic type yield locus (constant stress ratio) was adopted in the model, while particle breakage was modelled by a single non-linear function of distortional strain and the initial state of ballast and then incorporated into a plastic flow rule. The following equations were proposed to calculate the incremental plastic shear and volumetric strain.

$$d\varepsilon_s^p = \frac{2\alpha\kappa\left(\frac{p'}{p'_{cs}}\right)\left(1-\frac{p'_{o(i)}}{p'_{cs(i)}}\right)\left(9+3M-2\eta^* M\right)\eta d\eta}{M^2\left(1+e_i\right)\left(\frac{2p'_o}{p'}-1\right)\left\{9\left(M-\eta^*\right)+\frac{B}{p'}\left[\chi+\mu\left(M-\eta^*\right)\right]\right\}} \tag{2.17}$$

$$\frac{d\varepsilon_v^p}{d\varepsilon_s^p} = \frac{9\left(M-\eta\right)}{9+3M-2\eta^* M}+\left(\frac{B}{p'}\right)\left[\frac{\chi+\mu\left(M-\eta^*\right)}{9+3M-2\eta^* M}\right] \tag{2.18}$$

Where $d\varepsilon_s^p$ is the plastic deviatoric strain increment, $d\varepsilon_v^p$ is the plastic volumetric strain increment, α is related to the initial stiffness of the ballast, κ is the swelling/recompression constant, p' is the mean stress, p'_{cs} is the value of p' on the critical state line at the current void ratio, p'_o is the value of p' at the intersection of the undrained stress path and the initial stress ratio line, $p'_{o(i)}$ and $p'_{cs(i)}$ are the initial value of p'_o and p'_{cs} at the start of shearing, M is critical stress ratio, η is stress ratio, $\eta^*=\eta(p'/p'_{cs})$, e_i is the initial void ratio at the start of shearing, χ and μ are the material constants defining the rate of ballast breakage, and B is a constant given by:

$$B = \frac{\beta}{ln\left(p'_{cs(i)}/p'_i\right)}\left[\frac{\left(9-3M\right)\left(6+4M\right)}{\left(6+M\right)}\right] \tag{2.19}$$

where β is the slope of the rate of energy consumption versus the rate of particle breakage curve, and p'_i is the initial value of p'. Although this model considered the

effect of particle breakage, it did not give an explicit expression of particle breakage, so it cannot predict the value of particle breakage at a particular load stage.

2.5 Numerical Integration Schemes

Iterations for finite-element analysis of material nonlinear can generally be separated into two levels. The first (local) level is tied to the constitutive equations where, for a given strain increment, the algorithm iterates in stress and internal variable space until a convergence criterion is met. The second (global) level involves iterations to achieve a balance of internal stresses with external loads. The techniques for integrating the constitutive equations at the local level directly control the accuracy and stability of the overall numerical solution. These techniques generally fall into explicit (forward Euler) and implicit (backward Euler) categories. Explicit schemes (Zienkiewicz et al., 1969; Nayak and Zienkiewicz, 1972; Owen and Hinton, 1980) were widely used until Simo and Taylor (1985) proposed the implicit closest point projection method (CPPM) which is a type of 'returning mapping' algorithm. Return mapping involves integrating the elastic equations with the total strain increments to obtain an elastic predictor and then the elastically predicted stresses are then relaxed onto a suitably updated yield surface by iteratively correcting the plastic strain increments.

2.5.1 Return-Mapping Algorithms

In the CPPM method, the increments of plastic strain calculated at the end of the step and the yield condition are enforced at the end of the step, so the integration scheme is written as

$$\{\varepsilon_{n+1}\} = \{\varepsilon_n\} + \{\Delta\varepsilon\} \tag{2.20}$$

$$\left\{\varepsilon_{n+1}^{p}\right\} = \left\{\varepsilon_{n}^{p}\right\} + \Delta\lambda_{n+1}\left\{a_{n+1}\right\} \tag{2.21}$$

$$\left\{\sigma_{n+1}\right\} = \left[D^{e}\right]\left\{\left\{\varepsilon_{n+1}\right\} - \left\{\varepsilon_{n+1}^{p}\right\}\right\} \tag{2.22}$$

$$F_{n+1} = F\left(\left\{\sigma_{n+1}\right\}\right) = 0 \tag{2.23}$$

Given the set $\left(\left\{\varepsilon_{n}\right\},\left\{\varepsilon_{n}^{p}\right\},\left\{\Delta\varepsilon\right\}\right)$ at step *n*, Equations (2.20)-(2.23) are a set of nonlinear algebraic equations in $\left(\left\{\sigma_{n+1}\right\},\left\{\varepsilon_{n+1}^{p}\right\}\right)$.

The strain $\{\varepsilon_{n+1}\}$ is obtained from the solution of the system of equations at step *n+1*. If stresses are predicted based on the previous load step, it is understood that $\{\varepsilon_{n+1}\}$ is the total strain after the last iteration of the implicit solution scheme.

First note that from Equation (2.21), the plastic strain increment is given by

$$\left\{\Delta\varepsilon_{n+1}^{p}\right\} = \left\{\varepsilon_{n+1}^{p}\right\} - \left\{\varepsilon_{n}^{p}\right\} = \Delta\lambda_{n+1}\left\{a_{n+1}\right\} \tag{2.24}$$

Substituting this expression into Equation (2.22) gives

$$\begin{aligned}
\left\{\sigma_{n+1}\right\} &= \left[D^{e}\right]\left(\left\{\varepsilon_{n+1}\right\} - \left\{\varepsilon_{n}^{p}\right\} - \left\{\Delta\varepsilon_{n+1}^{p}\right\}\right) \\
&= \left[D^{e}\right]\left(\left\{\varepsilon_{n+1}\right\} - \left\{\varepsilon_{n}^{p}\right\} - \Delta\lambda_{n+1}\left\{a_{n+1}\right\}\right) \\
&= \left[D^{e}\right]\left(\left\{\varepsilon_{n}\right\} + \left\{\Delta\varepsilon\right\} - \left\{\varepsilon_{n}^{p}\right\} - \Delta\lambda_{n+1}\left\{a_{n+1}\right\}\right) \\
&= \left[D^{e}\right]\left(\left\{\varepsilon_{n}\right\} - \left\{\varepsilon_{n}^{p}\right\}\right) + \left[D^{e}\right]\left\{\Delta\varepsilon\right\} - \Delta\lambda_{n+1}\left[D^{e}\right]\left\{a_{n+1}\right\} \\
&= \left\{\sigma_{n+1}^{trial}\right\} - \Delta\lambda_{n+1}\left[D^{e}\right]\left\{a_{n+1}\right\}
\end{aligned} \tag{2.25}$$

where $\left\{\sigma_{n+1}^{trial}\right\} = \left\{\sigma_n\right\} + \left[D^e\right]\left\{\Delta\varepsilon\right\}$ is the trial stress of the elastic predictor and – $\Delta\lambda_{n+1}[D^e]\{a_{n+1}\}$ is the plastic corrector which returns or projects the trial stress onto the yield surface along a direction specified by the plastic flow direction at the end point. The elastic predictor phase is driven by the increment in total strain while the plastic corrector phase is driven by the plasticity parameter $\Delta\lambda_{n+1}$. Thus, during the elastic-predictor stage, the plastic strain remains fixed, and during the plastic-corrector stage, the total strain is fixed. If the normality rule is enforced at the end of this step we have

$$\left\{\Delta\sigma_{n+1}\right\} = -\left[D^e\right]\left\{\Delta\varepsilon_{n+1}^p\right\} = -\Delta\lambda_{n+1}\left[D^e\right]\left\{a_{n+1}\right\} \tag{2.26}$$

The solution of the set of nonlinear Equations (2.20)-(2.23) based on the concept of closed point projection is typically obtained by a Newton procedure involving a systematic linearisation. This results in a plastic corrector returning stresses to the yield surface. During the plastic-corrector stage of the algorithm, the total strain is constant and linearisation is with respect to the increment of $\Delta\lambda$ of the plasticity parameter.

As an example, in order to linearise the equation g($\Delta\lambda$)=0 using the Newton procedure with $\Delta\lambda^{(0)}$=0, at the *kth* iteration it can be written as:

$$g^{(k)} + \left(\frac{dg}{d\Delta\lambda}\right)^{(k)} \delta\lambda^{(k)} = 0$$

$$\Delta\lambda^{(k+1)} = \Delta\lambda^{(k)} + \delta\lambda^{(k)} \tag{2.27}$$

where $\delta\lambda^{(k)}$ is the increment in $\Delta\lambda$ at the *kth* iteration. For the sake of clarity, we will usually omit the load subscript *n+1* so unless indicated otherwise, all the quantities are evaluated at step *n+1*.

The plastic updates and yield condition can be written in the form of Equation (2.28), suitable for Newton iteration, thus defining $\{r\}$ as

$$\{r\} = -\{\varepsilon^p\} + \{\varepsilon_n^p\} + \Delta\lambda\{a\} = 0$$

$$F = F(\{\sigma\}) = 0 \tag{2.28}$$

Linearisation of these equations gives

$$\{r^{(k)}\} + [D]^{-1}\{\Delta\sigma^{(k)}\} + \Delta\lambda^{(k)}\{\Delta a^{(k)}\} + \delta\lambda^{(k)}\{a^{(k)}\} = 0$$

$$F^{(k)} + \left(a^{(k)}\right)^T\{\Delta\sigma^{(k)}\} = 0$$

(2.29)

where

$$\{\Delta a^{(k)}\} = \left[\frac{\partial a^{(k)}}{\partial\sigma}\right]\{\Delta\sigma^{(k)}\} \tag{2.30}$$

Equations (2.29) are a set of two equations which can be solved for $\{\Delta\sigma^{(k)}\}$ and $\delta\lambda^{(k)}$. Substituting Equation (2.30) into the first equation of Equations (2.29)

$$\{\Delta\sigma^{(k)}\} = -[R^{(k)}]\{r^{(k)}\} - \delta\lambda^{(k)}[R^{(k)}]\{a^{(k)}\} \tag{2.31}$$

where

$$[R^{(k)}] = \left[[I] + \Delta\lambda^{(k)}[D^e]\left[\frac{\partial a^{(k)}}{\partial\sigma}\right]\right]^{-1}[D^e] \tag{2.32}$$

and substituting Equation (2.31) into the second of Equation (2.29) and solving for $\delta\lambda^{(k)}$

we get

$$\delta\lambda^{(k)} = \frac{F^{(k)} - \left\{a^{(k)}\right\}^T \left[R^{(k)}\right]\left\{r^{(k)}\right\}}{\left\{a^{(k)}\right\}^T \left[R^{(k)}\right]\left\{a^{(k)}\right\}} \tag{2.33}$$

Thus the update of the plastic strain and the plasticity parameter is

$$\left\{\varepsilon^{p(k+1)}\right\} = \left\{\varepsilon^{p(k)}\right\} + \left\{\Delta\varepsilon^{p(k)}\right\} = \left\{\varepsilon^{p(k)}\right\} - \left[D^e\right]^{-1}\left\{\Delta\sigma^{(k)}\right\}$$

$$\Delta\lambda^{(k+1)} = \Delta\lambda^{(k)} + \delta\lambda^{(k)} \tag{2.34}$$

With the increments given in Equations (2.31) and (2.33), the Newton procedure is continued until convergence to the updated yield surface is achieved to within an acceptable tolerance.

Equation (2.20) shows that CPPM is inherently path independent, so if the stresses are predicted based on the previous iteration, we have

$$\left\{\sigma^{(k+1)}\right\} = \left\{\sigma^{(k)}\right\} + \left[D^e\right]\left\{\Delta\varepsilon_{n+1}^{(i)}\right\} \tag{2.35}$$

where *i* is the global iteration counter, $\{\sigma^{(k)}\}$ is the convergent value of stress at the local iteration, and $\left\{\Delta\varepsilon_{n+1}^{(i)}\right\}$ is the strain increment predicted using a global stiffness operator such as the consistent or continuum elasto-plastic modulus. The complete stress update algorithm (Belytschko et al. 2000) is given as below, and the stress return terms corresponding to CPPM are shown in Figure 2.18.

(1) Initialisation: set initial values of plastic strain to converged values at end of previous load step, zero the incremental plasticity parameter, and evaluate the

elastic trial stress

$$k = 0 : \left\{\varepsilon^{p(0)}\right\} = \left\{\varepsilon_n^p\right\}, \Delta\lambda^{(0)} = 0$$

$$\left\{\sigma^{(0)}\right\} = \left[D^e\right]\left(\left\{\varepsilon_{n+1}\right\} - \left\{\varepsilon^{p(0)}\right\}\right)$$

(2) Check yield condition and convergence at *kth* iteration

$$F^{(k)} = F\left(\left\{\sigma^{(k)}\right\}\right), \left\{r^{(k)}\right\}$$

If $F^{(k)} < TOL_1$ and $\|\{r^{(k)}\}\| < TOL_2$, converged else go to 3.

(3) Compute increment in plasticity parameter

$$\left[R^{(k)}\right] = \left[\left[I\right] + \Delta\lambda^{(k)}\left[D^e\right]\left[\frac{\partial a^{(k)}}{\partial\sigma}\right]\right]^{-1}\left[D^e\right]$$

$$\delta\lambda^{(k)} = \frac{F^{(k)} - \left\{a^{(k)}\right\}^T\left[R^{(k)}\right]\left\{r^{(k)}\right\}}{\left\{a^{(k)}\right\}^T\left[R^{(k)}\right]\left\{a^{(k)}\right\}}$$

(4) Obtain stress increments

$$\left\{\Delta\sigma^{(k)}\right\} = -\left[R^{(k)}\right]\left\{r^{(k)}\right\} - \delta\lambda^{(k)}\left[R^{(k)}\right]\left\{a^{(k)}\right\}$$

(5) Update plastic strain

$$\left\{\varepsilon^{p(k+1)}\right\} = \left\{\varepsilon^{p(k)}\right\} + \left\{\Delta\varepsilon^{p(k)}\right\} = \left\{\varepsilon^{p(k)}\right\} - \left[D^e\right]^{-1}\left\{\Delta\sigma^{(k)}\right\}$$

$$\Delta\lambda^{(k+1)} = \Delta\lambda^{(k)} + \delta\lambda^{(k)}$$

$$\left\{\sigma^{(k+1)}\right\} = \left\{\sigma^{(k)}\right\} + \left\{\Delta\sigma^{(k)}\right\}$$

k=k+1, go to(2).

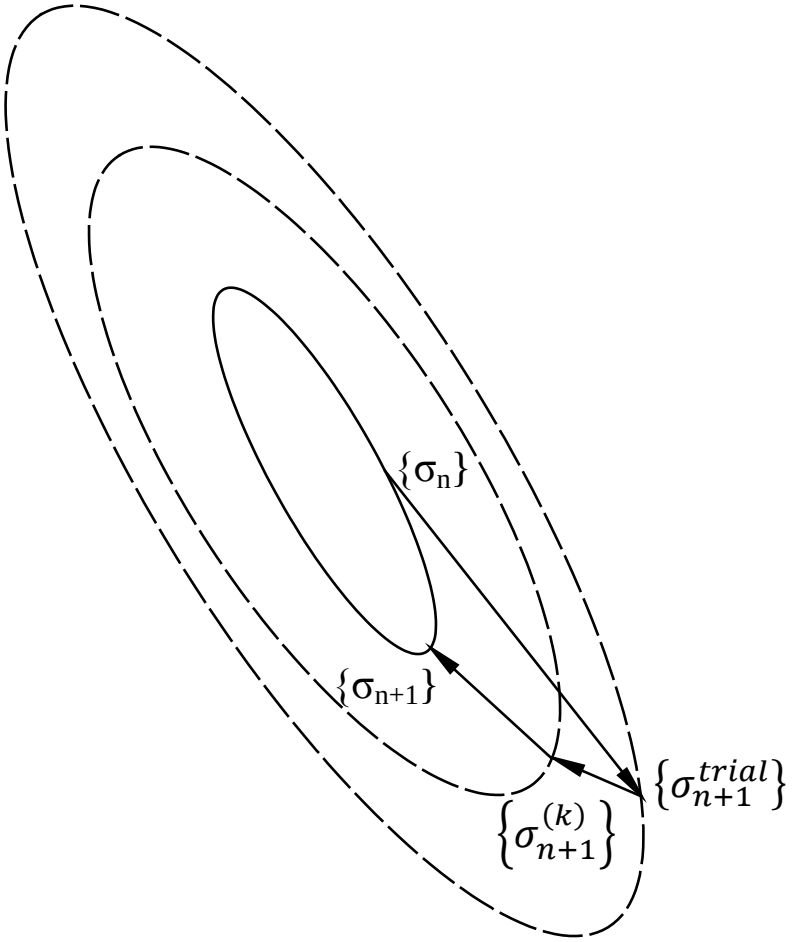

Figure 2.18 Stress return corresponding to CPPM (adopted from Simo and Taylor, 1985)

2.5.2 Newton-Raphson Iteration Procedure

The Newton-Raphson iteration method is described as following such that the typical problem gives N functional relations to be zeroed, and it involves variables x_i, *i=1,2,...,n*:

$$F_i\left(x_1, x_2, ..., x_N\right) = 0 \quad i=1,2,\ldots,N. \tag{2.36}$$

We let *x* denote the entire vector of values x_i and *F* denote the entire vector of functions F_i. In the neighborhood of *x*, each of the functions F_i can be expanded in Taylor series

$$F_i\left(x+\delta x\right)=F_i\left(x\right)+\sum_{j=1}^{N}\frac{\partial F_i}{\partial x_j}\delta x_j+o\left(\delta x^2\right) \tag{2.37}$$

The matrix of partial derivatives appearing in Equation (2.37) is the Jacobian matrix *J*:

$$J_{ij}\equiv\frac{\partial F_i}{\partial x_j} \tag{2.38}$$

In matrix notation Equation (2.37) is

$$F\left(x+\delta x\right)=F\left(x\right)+J\cdot\delta x+o\left(\delta x^2\right) \tag{2.39}$$

By neglecting terms of order δx^2 and higher and by setting $F(x+\delta x)=0$, we obtain a set of linear equations for the corrections δx that move each function closer to zero simultaneously, namely

$$J\cdot\delta x=-F \tag{2.40}$$

The corrections are then added to the solution vector,

$$x_{new}=x_{old}+\delta x \tag{2.41}$$

And the process is iterated to convergence. It is a good idea to check the degree to which both functions and variables have converged because once either of them reaches convergence, the other will not change.

2.6 Bearing Capacity of Shallow Foundation Using the Numerical Method

Studies of the bearing capacity of layered soils have been conducted using theoretical and experimental approaches, and a combination of both. Many empirical equations have been developed from the correlation between in situ data and/or laboratory data in

order to understand how soil deforms when subjected to loading. But its complex behaviour could not be understood just with raw/input data obtained from site investigations or correction equations. Thus with help from numerical modelling, the stress-strain behaviour of soil can be predicted, designed and interpreted using the appropriate model. Indeed the finite element method becomes a powerful tool in geotechnical modelling where soil bodies are discretised into small finite elements. The FEM deals with complex geometry, mixed boundary conditions and material nonlinearity.

Griffith (1982) described techniques used to analyse bearing pressure that could be done in a finite element package. The techniques used in the finite element method were load control or displacement control. For a perfectly flexible foundation, the load control allows the applied stresses to be adjusted closely by the application of nodal forces and where failure under this technique requires a number of iterations per load step and time consuming, unlike the rationale for choosing displacement control due to numerical control and physical reality. Displacement control was applicable for perfectly rigid footings where the equilibrium and yield were satisfied with small iterations even after failure had been reached. This technique was used in the ABAQUS and FLAC studies conducted by (Zhu, 2004; Bandini and Pham, 2011) and Han and Jiang (2011).

A few studies were carried out to estimate the bearing capacity failure of a rough strip footing resting on two layers of clay, this included a parametric study of the effect of the ratio between the thickness of the top layer and the width of the footing, the cohesion ratio of the top to bottom soil layer, and the influence of the inclined bedrock and footing embedment (Zhu, 2004; Merifield and Nguyen, 2006; Bandini and Pham, 2011; Han and Jiang, 2011).

The failure mechanism is defined where the line of discontinuous velocity and the soil mass above that undergoes unrestricted flow at failure in comparison to the rest of the soil mass (Manoharan and Dasgupta, 1995). The modes of failure (Merifield and Nguyen, 2006) for clay layered soils can be categorised as: i) general shear, ii) partial punching shear, and iii) full punching shear. These failure mechanism modes depend on ratio between strength and thickness.

Banimahd and Woodward (2006) used the finite element approach to evaluate the bearing capacity of footings resting on granular soils, because it was based on an advanced multi-surface kinematic constitutive model. Unlike elastic-perfectly plastic models which are often applied to granular foundation problems, the multi-surface model realistically accounted for the stress dependency of the friction angle, and strain softening-hardening and non-associativity. The research showed that the finite element solution can clearly represent the counteracting mechanisms of progressive failure that have an important effect on the bearing capacity of granular foundations.

2.7 Finite Element Study of Ballasted Rail Track

A comprehensive knowledge of the complex mechanisms associated with track deterioration is essential in an accurate prediction of a typical track maintenance cycle. Various simplified analytical and empirical design methods have been used to estimate settlements and stress transfer between the track layers, but they are based on the linear elasticity approach, and they often give only relatively crude estimates (Li and Selig, 1998a). Given the complex behaviour of a composite track system consisting of rail, sleeper, ballast, sub-ballast and subgrade under repeated (cyclic) traffic loads in a real track environment, the current design techniques used by rail industries worldwide are often over simplified.

To understand this complex mechanism of track deformation and then evaluate track degradation, a comprehensive finite element method (FEM) analysis is imperative. Suiker and de Borst (2003) developed a cyclic densification model for ballast and then used the model in a finite-element analysis of track deterioration (Figure 2.19). The dynamic effect of a moving axle load on the track is thought to be represented by a quasi-static line load. The level of deformation corresponding to shakedown was predicted reasonably well by the FEM model, but shakedown in this model occurred faster than in the test track. The difference in response between the test track and the FEM model may be due the plane strain assumption used in the study not representing the deformation in the longitudinal direction of the track. In this respect, the model could be improved by expanding it to 3D and replacing the line load with a set of static point loads at a given intermediate distance. Suiker and de Borst's model did not consider the dynamic effects. Actually, there is a relationship between track dynamics and track deterioration.

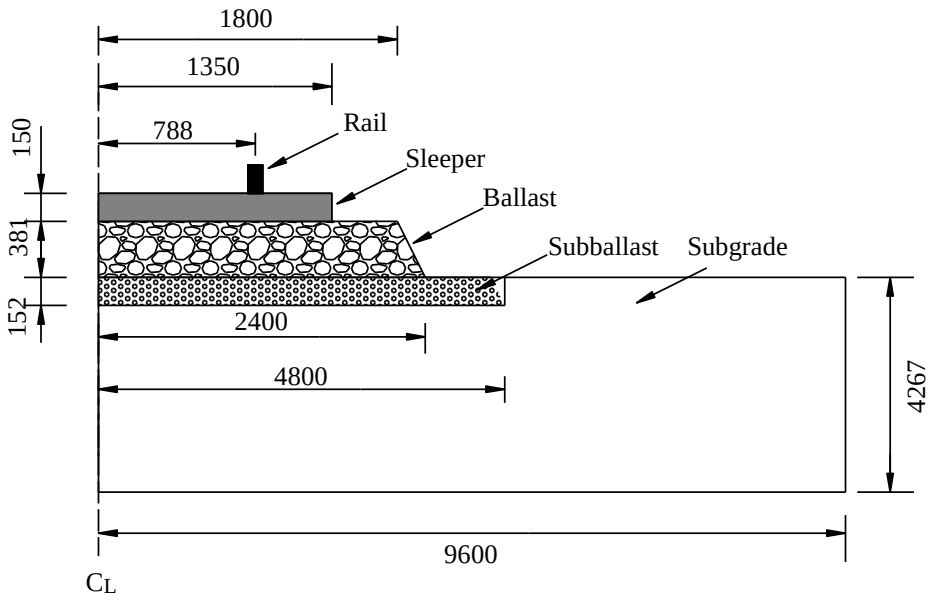

Figure 2.19 Dimensions configuration of track model (adopted form Suiker and de Borst, 2003)

Powrie et al. (2007) reported the results of finite element analyses carried out to investigate the stress changes experienced by an element of soil beneath a ballasted railway track during train passage (Figure 2.20). The location of the elements, the initial in situ stress state of the soil, and the elastic parameters used to characterise its behaviour were investigated, and the modelling of the stress paths in a cyclic hollow cylinder apparatus was discussed. Powrie et al. established a static model using geomaterials as linear elastic materials, but their dynamic effects were not considered.

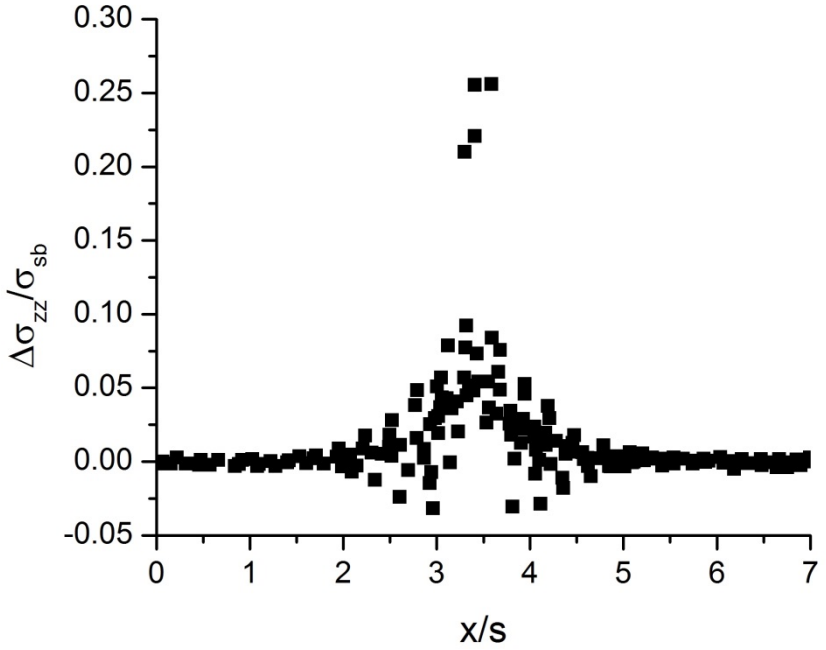

Figure 2.20 The influence of wheel load location on vertical stress at different depths (adopted from Powrie et al., 2007)

Yang et al. (2009) studied the effect of train speeds, acceleration/braking, rail surface shape, and unsupported sleepers on the stress paths experienced by elements of soil in the subbase and the underlying natural ground during train passage using a two-dimensional dynamic finite-element analysis. The results indicated that dynamic effects became apparent when the train speed was more than 10% of the Rayleigh wave speed v_c, of the subgrade. At a train speed of $0.5v_c$, the shear stresses will be underestimated by 30% in a static analysis, and at train speeds greater than v_c the stresses due to

dynamic effects increased dramatically (Figure 2.21).

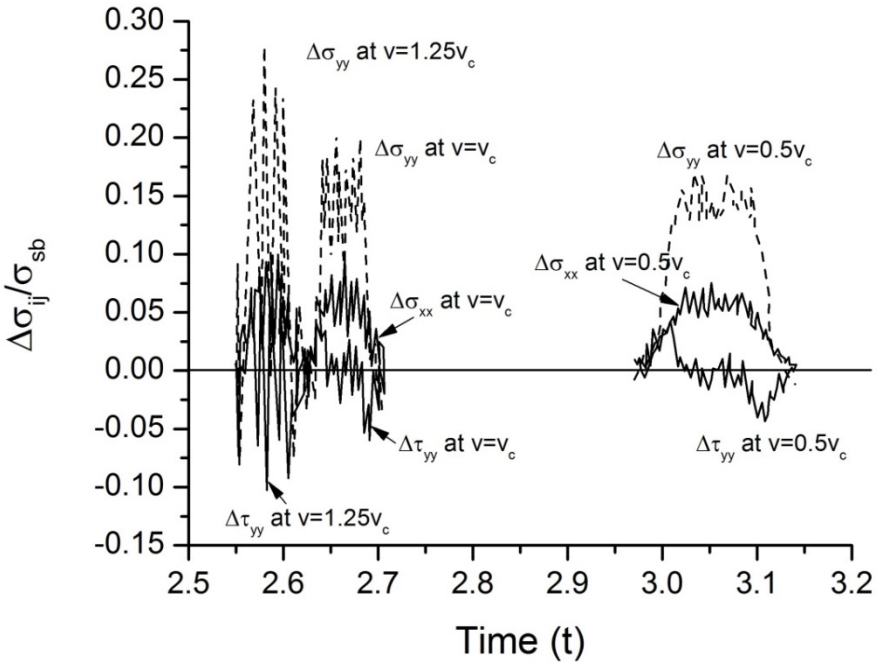

Figure 2.21 Stress on natural ground surface at different train speeds during passage of pair of adjoining bogies (adopted form Yang et al., 2009)

Leshchinsky and Ling (2013) investigated the effectiveness of geocell confinement on the integrity of the substructure by conducting a series of embankment model tests with different configurations of geocell placement and a numerical simulation of these tests by using finite element procedures. The results, which matched reasonably well, were then used to validate a parametric study, observe the effects of less competent geocell material, gravel, and foundations, including their implications. The tests and numerical simulations indicated that geocell confinement increased the stiffness and strength of a gravel embankment while reducing vertical settlement and lateral spreading. Moreover, the parametric study by Leshchinsky and Ling (2013) showed that geocell provides a composite mattressing effect that distributes subgrade stress more uniformly than without reinforcement, increases the bearing capacity and reduces settlement, especially on soft foundations.

CHAPTER 3

LABORATORY INVESTIGATIONS

3.1 Introduction

In order to understand the mechanical behavior of ballast under traffic loads, both static and cyclic triaxial tests are necessary. Previous laboratory testing has yielded much knowledge in this research area (Brown, 1974; Raymond and Davies, 1978; Alva-Hurtado, 1980; Stewart, 1986; Selig and Waters, 1994; Indraratna et al., 1998; Anderson and Key, 2000; Indraratna and Salim, 2002; Indraratna et al., 2005; Lackenby et al., 2007), though there are still some major issues that need attention, for example, the critical state behaviour of ballast and the associated implications due to particle breakage. Comprehensive information on the overall mechanical response of ballast under several loading combinations (i.e. varying f, $q_{max,cyc}$ and σ_3') is not available. In the view of this, a large-scale laboratory testing program was performed to assess static and cyclic behavior of ballast material at stress levels relevant for railway structures. Details on the experimental set-up, the test procedure and the test results and interpretations for both static and cyclic loading are presented below.

3.2 Experimental Set-up and Test Material

Current standards for railway ballast (e.g. Standards Australia, 1996) specify the physical and durability requirements of the parent rock. In Australia, fresh latite basalt, a quarried igneous aggregate is commonly used as railway ballast in New South Wales, Australia. Therefore this material is used for experiments. It was thoroughly cleaned,

dried and sieved through a set of 12 standard sieves (aperture size 53: 2.36 mm). Figure 3.1 shows the particle size distribution (PSD) curve adopted here representing the current Australia practices (Standards Australia 1996). A large-scale triaxial apparatus which could accommodate a 300 mm diameter by 600 mm high specimen was utilized (Figure 3.2 and 3.3). Particles from each size range were weighed separately and mixed thoroughly, before placing them inside a 6 mm thick rubber membrane in four separate layers, where each layer was compacted with a plate vibrator to a density of 1530 kg/m^3 (Table 3.1). Compaction was facilitated by a split cylindrical mould which was removed before the specimen was placed inside the cell pressure chamber. Prior to testing, each specimen was subjected to an upward flow of water from the bottom plate under a back pressure of 10 kPa. The specimen was allowed to saturate overnight until a Skempton's B value of 0.97-0.98 was achieved for typical compacted ballast with an initial void ratio of around 0.76.

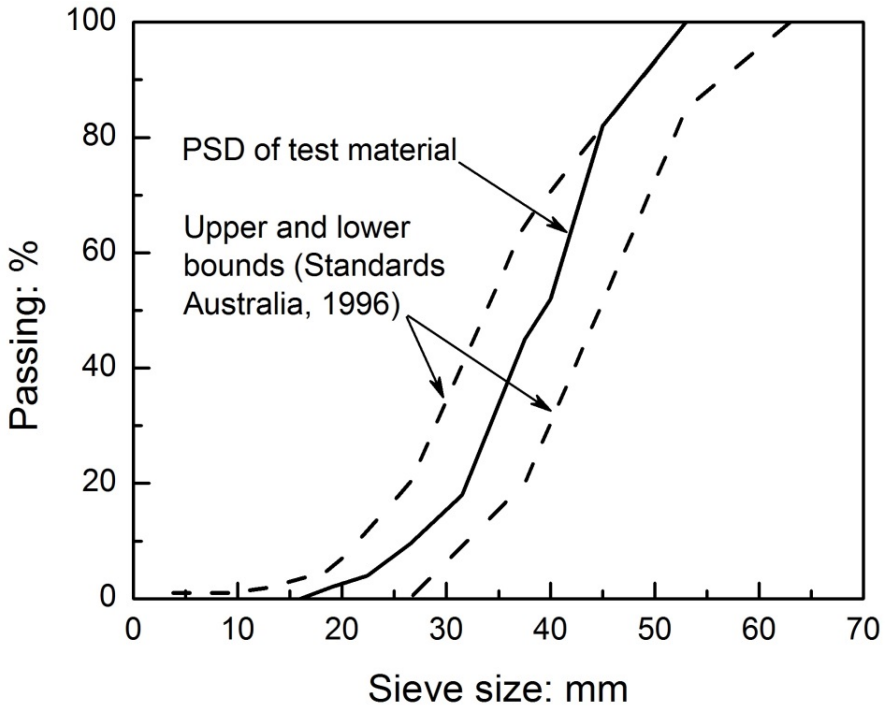

Figure 3.1 Particle size distribution of tested ballast, including the upper and lower bounds from Standards Australia (1996)

Table 3.1 Ballast specimen characteristics used in the tests

d_{max} (mm)	d_{min} (mm)	C_u	d_{50}	γ_b (kN/m^3)	e_0
53	16	1.53	39.5	15.3	0.76

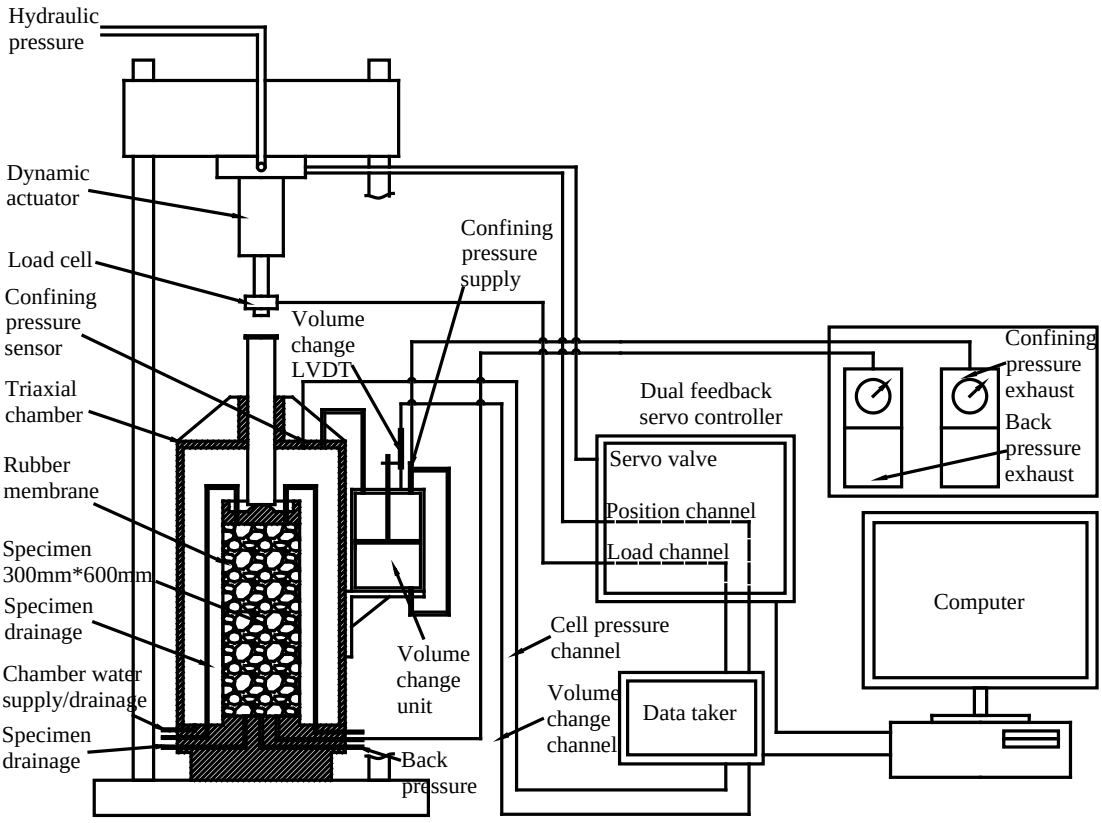

Figure 3.2 Schematic illustration of large-scale triaxial testing system

Figure 3.3 Photograph of large-scale triaxial testing system

3.3 Static Triaxial Tests

After setting up the test apparatus, the confining pressure was increased in several steps to a preselected constant value (Table 3.2), and the corresponding change in volume of the specimen was then recorded. Fully drained compression tests were conducted at an axial strain rate of 3 mm/min, which prevented any build-up of excess pore water pressure. The load cell, pressure transducers and linear variable differential transformer (LVDT) were connected to a computer-controlled data acquisition system. Shearing was continued until the samples either reached their critical states or until the vertical strain reached the maximum strain capacity of 30%. Membrane correction was applied to the

current stress measurements, in accordance with the hoop stress theory discussed by Henkel and Gilbert (1952). The additional radial stress due to membrane confinement was considered in correcting the measured deviator stress and mean stress. Upon completion of each test, the specimens were sieved to determine the extent of breakage using BBI. In order to study the state-dependent dilatancy relationship for ballast, ballast specimens with different bulk unit weights (i.e. γ_b = 15.3 kN/m^3 and 11.2 kN/m^3 separately) were used.

Table 3.2 Summary of the static triaxial tests

Test name	Confining pressure, σ_3' (kPa)	Bulk unit weight, γ_b (kN/m^3)
S1	30	15.3
S2	60	15.3
S3	180	15.3
S4	240	15.3
S5	300	15.3
S6	360	15.3
S7	420	15.3
S8	570	15.3
S9	60	11.6

3.3.1 Stress-strain-volume Behaviour of Ballast

Figure 3.4(a) shows the measured deviatoric stress q versus the deviatoric strain at the range of confining pressures adopted in the present study. It is observed that q initially increases with increasing deviator strain until it reaches the peak value. Apparently, for a higher confining pressure, the peak value of q becomes higher. In Figure 3.4(b), the

deviatoric strain is depicted versus the volumetric strain. It is seen that at relatively low confining pressure ($\sigma_3' \leq 60$ kPa), the volumetric strain is initially compressive but it swiftly becomes dilative with the increasing deviatoric strain. As the confining pressure increases, the rate and magnitude of dilation diminish, as expected. At elevated confining pressure ($\sigma_3' \geq 240$ kPa), the overall volumetric response is compressive. Unlike fine-grained materials such as sand and clay, no distinct shear plane could be observed in coarse aggregates such as rail ballast when tested in large-scale triaxial apparatus, even at low confining pressure. The failure was accompanied by specimen 'bulging' (Lackenby et al. 2007) and subsequent gradual strain softening over a large axial strain up to 30% (limit of the equipment), with many samples reaching a critical state (i.e. almost constant volumetric strain).

3.3.2 Critical State of Ballast Considering Particle Breakage Effect

Triaxial tests were conducted at relatively large axial strain (maximum strain reached 30%) to investigate the critical state of railway ballast under a wide range of confining pressure ($30 \leq \sigma_3' \leq 570$ kPa). Figure 3.4(b) shows that 'constant volume' values corresponding to the critical state were observed for the tests conducted at $\sigma_3' \geq 180$ kPa. For specimens subjected to $\sigma_3' = 30$ and 60 kPa testing could not be continued until the critical state due to the actuator's displacement limitation, hence, extrapolation of the stress-dilatancy data to the critical state was carried out, based on the technique proposed by Carrera et al. (2011) (Appendix A). Figures 3.5(a) and 3.5(b) show the critical states for ballast on q-p' and υ-lnp' plots, and the corresponding BBI at these critical state points are indicated in Figure 3.5(c). As observed in Figure 3.5 (a) and 3.5(b), at relatively higher confining pressure ($\sigma_3' \geqslant 180$ kPa), particle breakage is more pronounced compared with the one at relatively lower confining pressures, which

causes a shift of the location of critical state line on the *q-p'* and *υ-lnp'* planes.

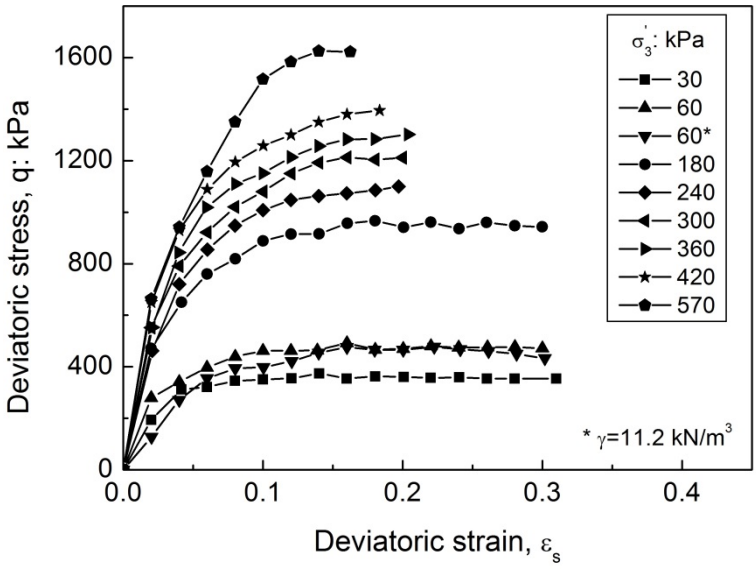

(a)

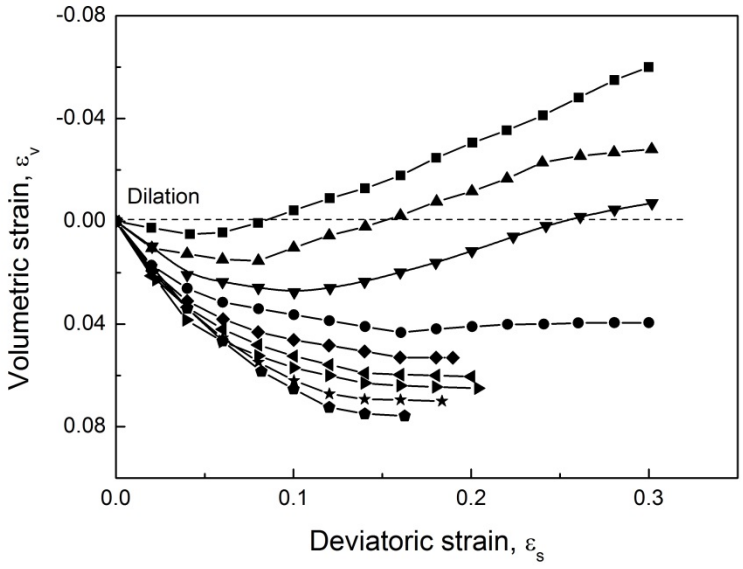

(b)

Figure 3.4 Static response of ballast: (a) variation of deviatoric stress q with deviatoric strain ε_s and (b) variation of volumetric strain ε_v with deviatoric strain ε_s

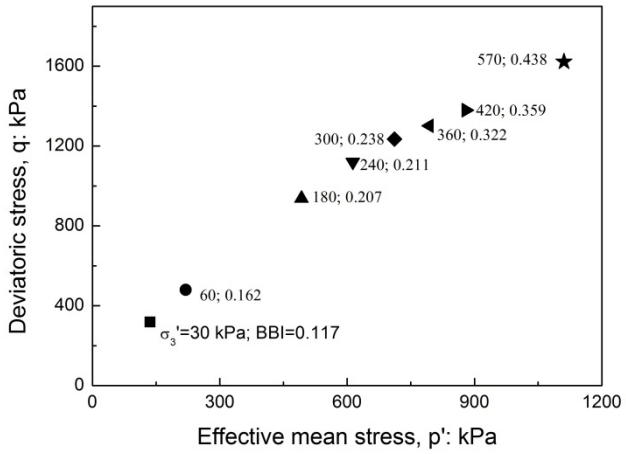

(a)

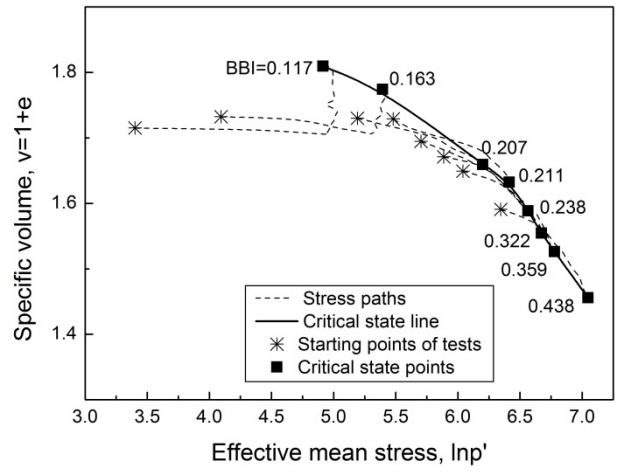

(b)

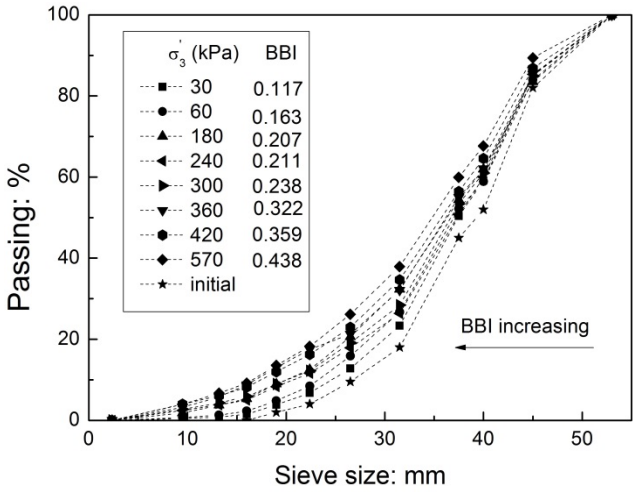

(c)

Figure 3.5 Monotonic triaxial tests on ballast: (a) ctitical state points on *q-p′* plane, (b) critical state points on *υ-lnp′* plane and (c) shift of PSD after triaxial shearing

The CSL in the *q-p′* plane is non-linear as shown in Figure 3.6(a) in comparison with that without breakage set as a Reference Critical State Line (RCSL). RCSL can be approximately determined by drained triaxial compression tests under low confining pressures when particle breakage is insignificant. As expected, the extent of breakage is greater with increasing *p′*, and the drop in *q* is more pronounced as *p′* increases. The CSL in *q-p′* plane can be expressed as:

$$q = \omega \cdot p'^{\mu} \tag{3.1}$$

where ω and μ are material constants.

The critical state stress ratio $M_c = (q/p')_c$ is not a constant for ballast and it is plotted as a function of the confining stress σ_3' and BBI in Figure 3.6(b) and 3.6(c), respectively. The data plotted in Figure 3.6 show that the changes in the critical state stress ratio (M_c) with confining stress can be attributed to particle breakage. The particle breakage could be associated with internal work (plastic work) induced by the applied stress. The total plastic work (W_T^P) involved in the monotonic shearing process includes two parts: (i) W_R^P utilised during particle rearrangement, and (ii) W_E^P accounting for particle breakage (effective plastic work). The critical state stress ratio (M_c) evolves mainly in relation to the increase in effective plastic work (W_E^P), which is defined as the excess of total plastic work (W_T^P) over the plastic work associated with particle rearrangement (W_R^P). Salim and Indraratna (2004) stated that the increment of energy consumption due to particle breakage per unit volume is proportional to the increment of breakage index. The test data in this study showed similar results (i.e. $W_E^P = \beta \cdot BBI$, where β is the

constant of proportionality). As particle breakage increases, M_c decreases as shown earlier in Figure 3.6(c), and can be represented by the following expression:

$$M_c = M_{c0} - \left[1 - \exp\left(-\alpha \cdot BBI\right)\right] \tag{3.2}$$

where α is the model parameter, and M_{c0} = critical state stress ratio for BBI = 0.

The CSL is traditionally written in the υ-*lnp´* plane as:

$$\upsilon_c = \Gamma - \lambda \ln p' \tag{3.3}$$

where Γ and λ are two constitutive parameters which define the local position of the CSL in terms of the specific volume υ_c and the effective mean stress *p'*.

The specific volume and effective mean stress obtained by the tests were plotted earlier in Figure 3.5(b). The results indicate that the CSL for ballast was no longer a straight line, and that the location of CSL would change in the compression plane with the increase of BBI. It can be proposed that this is actually a two-dimensional projection of the three-dimensional information. The CSL in the υ-*lnp'* plane becomes a critical state surface when the extra dimension of BBI is added (Figure 3.7). The CSL, in the form of a dashed line in Figure 3.7, corresponding to the current value of BBI, is assumed to have a constant slope. As the effective mean stress increases, the particles will break and BBI will rise. The critical state surface cannot exist for stress levels above a certain limit which will depend on the current value of BBI. The occurrence of breakage does not necessarily place the material in a critical state, but changes the critical state to which the material would approach as it is subsequently sheared (Muir Wood and Maeda, 2008). Figure 3.7 shows the three-dimensional nature of this critical state surface.

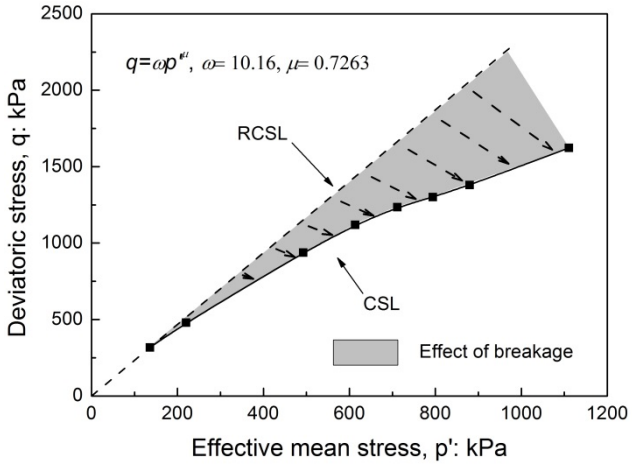

(a)

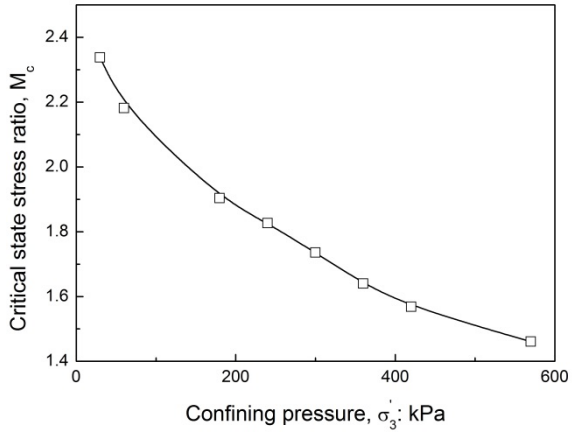

(b)

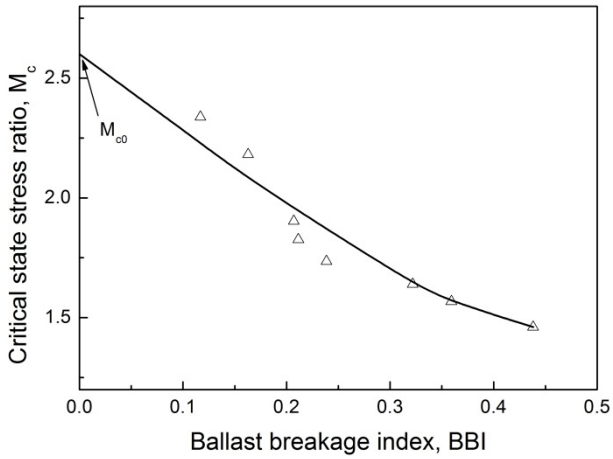

(c)

Figure 3.6 Critical states for ballast: (a) critical state line on *q-p′* plane, (b) variation of M_c with σ_3' and (c) evolution of M_c with BBI

In this study, it is proposed that the critical state surface in the *υ-lnp'-BBI* space might be extended from the rather traditional *υ-lnp'* relationship of Equation (3.3) by considering:

$$\upsilon_c = \Gamma(BBI) - \lambda \ln p' \tag{3.4}$$

where Γ*(BBI)* decreases as BBI increases. Based on the drained compression test data, a hyperbolic relation could be derived for Γ*(BBI)* as:

$$\Gamma(BBI) = \Gamma_{ref} - a \cdot \exp(b \cdot BBI) \tag{3.5}$$

where Γ_{ref} is the reference value to Γ*(BBI)*, *a* and *b* are material constants controlling the evolution rate of the CSL with particle breakage.

The above concept is based on the model of Muir Wood and Maeda (2008) which is supported to some extent by ballast data in this study. In Figure 3.7, the plotted data for ballast indicates that with increasing *p'*, ballast breakage increases and the corresponding specific volume (*v = 1+e*) decreases, which is in line with the hypothesis of the model suggested by Muir Wood and Maeda (2008). It is true that finer grained materials such as sands may require ring shear equipment to reach terminal grading (Coop et al., 2004; Sadrekarimi and Olson, 2011). Bandini and Coop (2011) used a biogenic carbonate sand with weak particles and found that the movement of CSL was small, even for large amounts of breakage. Coarser ballast underwent significant breakage in the large-scale triaxial equipment as shown in Figures 3.5 and 3.7. There is no doubt that the current experimental data for ballast indicates that a downward shift of the CSL is caused by ballast breakage (Figure 3.5(b)), although this downward shift may not be as pronounced as predicted by the Muir Wood and Maeda (2008) model.

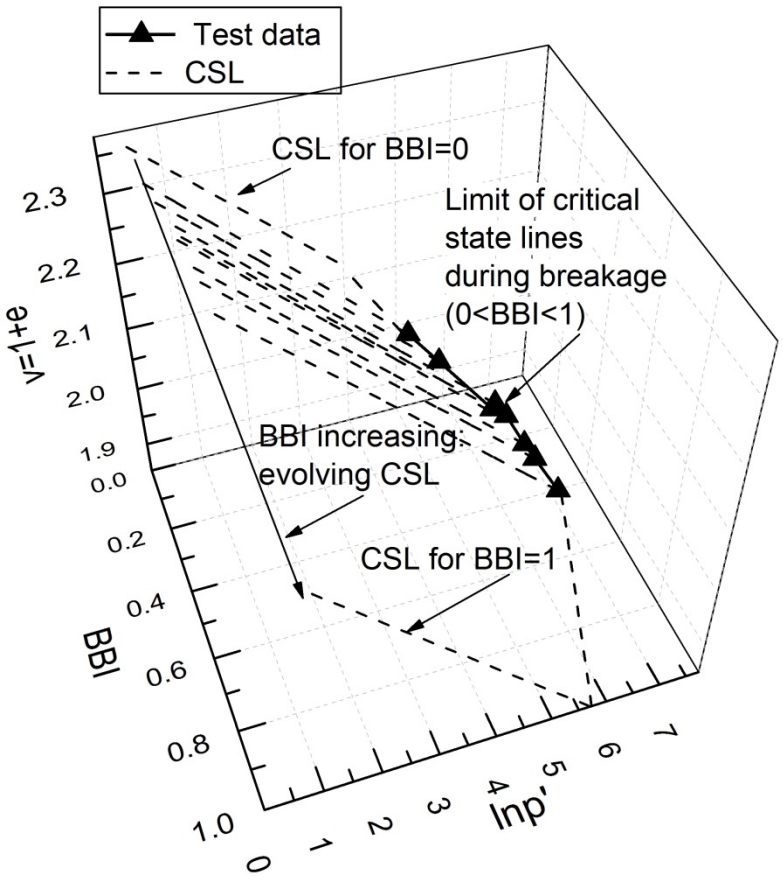

Figure 3.7 Critical state surface in compression-breakage space (modified after Muir Wood and Maeda, 2008)

3.3.3 Static Failure Behavior

During static triaxial testing of ballast it is customary for loading to continue until a certain predetermined value of axial strain ε_a has been obtained, for example 20%. Specimen failure is defined at the peak deviator stress $q_{peak,sta}$, and this value corresponding to the maximum load carrying capacity of the specimen. The magnitude of $q_{peak,sta}$ is dependent on specimen loading conditions, in particular the effective confining pressure σ_3', the applied strain rate, and drainage characteristics. Unlike small-grained materials such as sand, no distinct failure plane or shear band is observed in large granular specimens. Instead, failure is usually accompanied by specimen 'bulging' (Indraratna et al., 1998) (Figure 3.8). The specimen response was measured at

three different confining pressures: σ_3' = 10, 30 and 60 kPa. Figure 3.9(a) depicts the measured stress-strain-volumetric response at the three selected confining pressures. As expected, for a higher confining pressure, the peak strength becomes higher and the amount of dilation produced during testing decreases. Figure 3.9(b) shows the measured values of peak strength in the *p'*-*q* plane. A linear regression line has been constructed by requiring that it passes the origin, thus characterizing cohesionless nature of ballast. The slope of the regression line is $(q/p')_{peak,sta}$ = 2.29. In agreement with the Mohr-Coulomb criterion, this value corresponds to a friction angle $Ø_{peak,sta}$ = 56°.

(a) (b)

Figure 3.8 Comparison of the specimens before and after test: (a) before cyclic test, (b) after test (bulging)

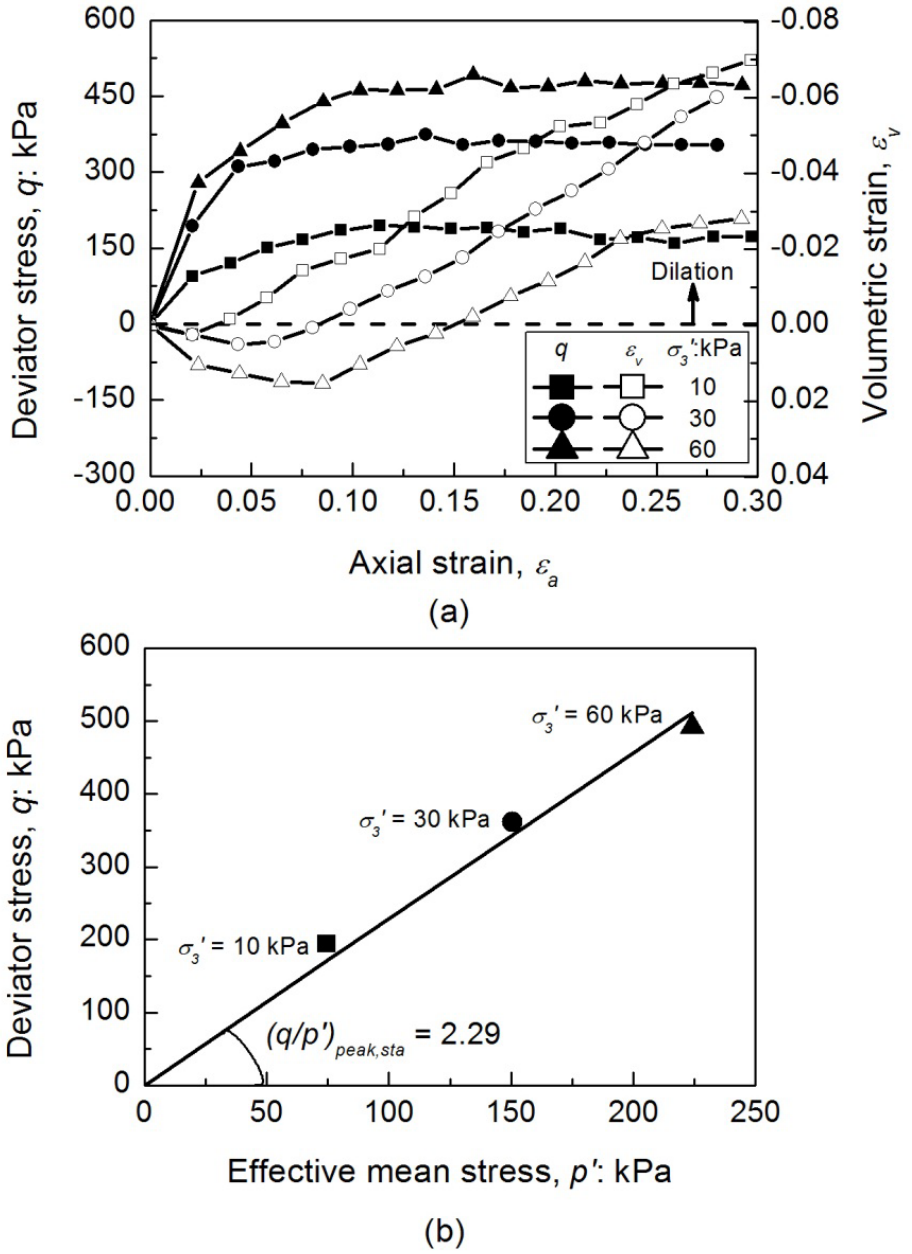

Figure 3.9 Static response of ballast material: (a) stress-strain-volumetric response for various confining pressure σ_3'; (b) measured values of peak strength in the p'-q plane

3.4 Cyclic Triaxial Tests

A total of twenty-three cyclic triaxial tests (Table 3.3) were conducted to investigate the effects of f, $q_{max,cyc}$, σ_3' and N on the permanent strains, M_R, and breakage of ballast.

To each specimen, an initial static load at a rate of 1 mm/s was applied to produce the sum of the minimum cyclic deviator stress $q_{min,cyc}$ and membrane correction q_m.

Membrane correction was calculated following the method proposed by Henkel and Gilbert (1952), and an additional 10 kPa was added to the cyclic deviator stress. The applied load was cycled between the two compressive stress states, ($q_{min,cyc}$ + q_m) and ($q_{max,cyc}$ + q_m), where $q_{min,cyc}$ was set to about 45 kPa for each test to represent the 'in situ' pressure at the top of ballast layer in an unloaded track (Lackenby et al., 2007). $q_{max,cyc}$ is the maximum deviator stress defining the magnitude of cyclic loading. Most tests utilised $q_{max,cyc}$ of 230 kPa and 370 kPa to represent a vertical load from a static train with a 25 t and 40 t axle load, respectively. Two tests incorporated loading magnitudes of 276 kPa and 460 kPa, approaching the peak strengths to study the cyclic failure of ballast with high frequency (i.e. f = 40 Hz). The load frequency of a train is expressed as $f = V/L$, where V is train speed and L is the characteristic length. Previous studies (Zhou and Gong, 2001; Liu and Xiao, 2010; Ni et al., 2013) considered L to be the length of a typical freight wagon, passenger car or a bogie, which results in a lower value of frequency for a given train speed. However, a typical freight wagon often has multiple axles (e.g. four axles) that impart individual load cycles (Figure 3.10). As the axle distance is much smaller than the bogie distance, two rear axles of a leading wagon and two front axles of a trailing wagon induce maximum frequency (Indraratna et al., 2014c). Therefore, considering an axle distance of 2.02 m, frequency f is obtained as 0.138 V. The value of f was varied from 5 Hz to 60 Hz to simulate a range of train speeds from about 40 km/h to 400 km/h. It was necessary to have 1 Hz frequency phase at the commencement of the loading regime to prevent any loss of actuator contact with the specimen during rapid vertical deformation.

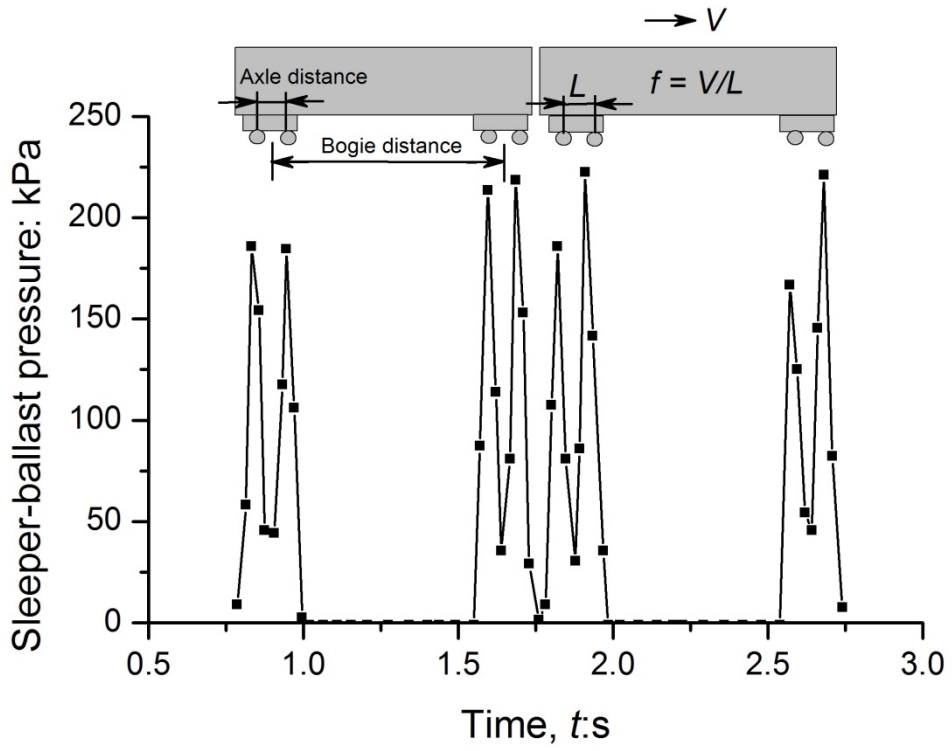

Figure 3.10 Schematic illustration of axles and bogies and record of pressure under the sleeper due to the passage of a coal train (25 t axle load) (data sourced from Indraratna et al., 2010b)

Table 3.3 Summary of cyclic triaxial tests

$q_{max,cyc}$: kPa	σ_3' : kPa	f : Hz	N
230	10	5,10,20,40*	500,000
230	30	5,10,20,30,40,50*,60*	500,000
230	60	5,10,20,30,40,60	500,000
370	60	5,10,20,40	500,000
276	30	40*	1010
460	60	40*	500

Note: *ε_a > 30% before 500,000 cycles.

Details of the cyclic loading procedure are illustrated in Figure 3.11. Field studies of typical Australian railway tracks have indicated that lateral confinement provided by the sleepers, shoulder, and crib ballast rarely exceeds 60 kPa (Indraratna et al. 2010b), so the specimen was subjected to confining pressures of 10, 30, and 60 kPa. A permanent deformation response was recorded periodically during testing, and bursts of data (sampling frequency = 1250 Hz) were recorded at specific cycles to investigate the resilience. Loading was suspended after 500,000 cycles or until vertical deformation had reached the limit of the equipment (@ 30% axial strain). In railway practice a maintenance period may span more train passages than the equivalent of 500,000 load cycles (i.e. 5,000,000). Because the performance of a 5,000,000 load cycles test is time consuming, N = 500,000 was used in this study. After each test was completed, the specimens were sieved to determine the extent of breakage by BBI.

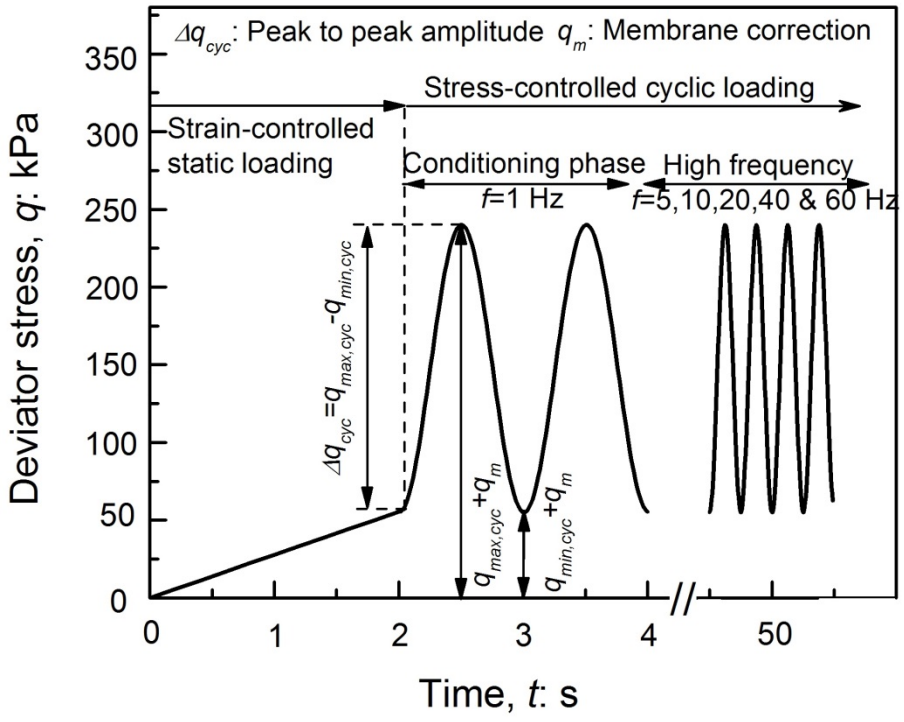

Figure 3.11 Details of cyclic loading procedure

3.4.1 Permanent Deformation Behaviour

Unlike static failure, specimen failure under drained stress controlled cyclic loading at a constant $q_{max,cyc}$ was difficult to ascertain owing to the absence of a peak stress; so it was better to define it by an arbitrary level of strain accumulation, such as $\varepsilon_a \geq 30\%$ (Lackenby et al., 2007). Using this failure criterion, those specimens marked with an asterisk in Table 3.3 are said to have 'failed' before reaching 500,000 load cycles.

The importance of $q_{max,cyc}$ and σ_3' along with f in characterising the deformation mechanisms (axial strain, ε_a and volumetric strain, ε_v) is shown in Figures 3.12(a) to 3.12(h). As discussed earlier by Sun et al. (2014) (i.e. $q_{max,cyc}$ = 230 kPa, σ_3' = 30 kPa), three different deformation mechanisms were observed for ballast in response to f, namely, in Range I: plastic shakedown at $f \leq 20$ Hz, in Range II: plastic shakedown and ratcheting at 30 Hz $\leq f \leq$ 50 Hz, and in Range III: plastic collapse at $f \geq 60$ Hz. The effects of $q_{max,cyc}$ and σ_3' along with f in these different ranges are discussed in detail below.

Range I: plastic shakedown. Specimens which were subjected to a low f (i.e. $f \leq 30$ Hz), where the permanent ε_a stabilised to a relatively steady value as N increased, were characterised as plastic shakedown as shown in Figures 3.12(a, c, e & g). Figure 3.13 shows the data plotted as permanent axial strain rate versus permanent axial strain for the selected specimens (i.e. f = 5, 50 and 60 Hz for Range I, II, and III, respectively). It is illustrated that the plastic axial strain rate progressively decreases (O-A) for Range I specimen, which effectively halts further accumulation of axial strain leading to an asymptotic final value (i.e. plastic shakedown). At relatively lower level of σ_3' (σ_3' = 10 kPa), the specimens experienced an overall volumetric dilation when f was also low ($f \leq$

10 Hz) as shown in Figure 3.12(b). For a given $q_{max,cyc}$ of 230 kPa, as shown in Figures 3.12(c) and 3.12(d). the upper boundary for f during Range I mechanism was 20 Hz at σ_3' = 30 kPa, but when σ_3' increased to 60 kPa, f increased to 30 Hz (Figures 3.12(e) and 3.12(f)). A granular material under Range I condition would eventually stabilise in response to cyclic loading, achieving a state of 'shakedown,' and this is acceptable in design, provided that the accumulated axial strain is small enough.

Range II: plastic shakedown and ratcheting. At higher values of f (i.e. 30 Hz ≤ f ≤ 60 Hz shown in Figures 3.12(a)-3.12(g), the specimens initially experienced shakedown, but as the loading continued, the permanent strains (i.e. ε_a and ε_v) increased again, and they would eventually fail due to ratcheting. In Figure 3.13, the permanent strain rate line for Range II indicates that during the first load cycles (O'-A'), the high level of plastic strain rate decreases to a relatively low, nearly constant level (A'-B'). Thus, a near-linear increase of permanent deformation was observed (i.e. ratcheting). The lower boundary for f during Range II behaviour was 30 Hz at σ_3' = 30 kPa (Figures. 3.12(c) and 3.12(d)), but when confinement increased to 60 kPa, f increased to 40 Hz (Figures 3.12(e) and 3.12(f)). In summary, a critical frequency range (or critical train speed) exists, above which specimen failure in the form of ratcheting may occur. The critical frequency range is 20-30 Hz (145 km/h ≤ V ≤ 220 km/h) and 30-40 Hz (220 km/h ≤ V ≤ 300 km/h) for σ_3' = 30 and 60 kPa, respectively. This indicates that increased confining pressure would result in decreased track settlement.

Range III: plastic collapse. For those specimens with a very high frequency (f ≥ 60 Hz), specimen failure could occur in the form of plastic collapse within a small number of load cycles. This mechanism was defined as Range III: plastic collapse (Figure 3.12(c)). Moreover, at a certain value of f = 40 Hz with $q_{max,cyc}$ approaching the equivalent

monotonic failure load could also lead to plastic collapse (i.e. $q_{max,cyc}$ = 276 kPa and 460 kPa in Figures 3.12(c) and 3.12(g), respectively). This can be illustrated by the strain rate curve representing Range III specimen in Figure 3.13. The curve plots concavely outward (O"-A"), indicating continuing incremental plastic deformation with each load cycle, and the strain rate decreases gradually compared with Range I and II, or not at all. Range III behaviour in a track could result in apparent failure by excessive settlement, hence should not be tolerated in design.

Figure 3.14(a) plots the axial strain ε_a after 500,000 cycles as a function of *f* at different $q_{max,cyc}$ and σ_3' values. For the same *f* and σ_3' (i.e. *f* = 5 Hz and σ_3' = 60 kPa), a larger $q_{max,cyc}$ (i.e. $q_{max,cyc}$ = 370 kPa in comparison with $q_{max,cyc}$ = 230 kPa) generates higher axial strain as expected. For a constant σ_3' (i.e. σ_3' = 60 kPa), the differences between the values of axial strain under different load magnitudes (i.e. $q_{max,cyc}$ = 230 and 370 kPa) increase with *f*. This indicates that the frequency has a more profound effect on axial strain for the specimen with a higher load magnitude. For given values of *f* and $q_{max,cyc}$ (i.e. *f* = 5 Hz and $q_{max,cyc}$ = 230 kPa), increasing σ_3' produces a smaller axial strain. Distinct deformation mechanisms (i.e. Range I and II) exist with a specific stress states while varying *f* from 5 Hz to 60 Hz. A reasonable value of critical train speed (or critical frequency) could be determined by using Figure 3.14(a) for both passenger train (i.e. $q_{max,cyc}$ = 230 kPa) and heavy haul (i.e. $q_{max,cyc}$ = 370 kPa) at various track confinements. It is also shown that the critical train speed decreases with the increasing accumulated deformation. For a track with heavy haul, the value of critical train speed is smaller than that for passenger trains. An increase in the confinement would increase the critical train speed.

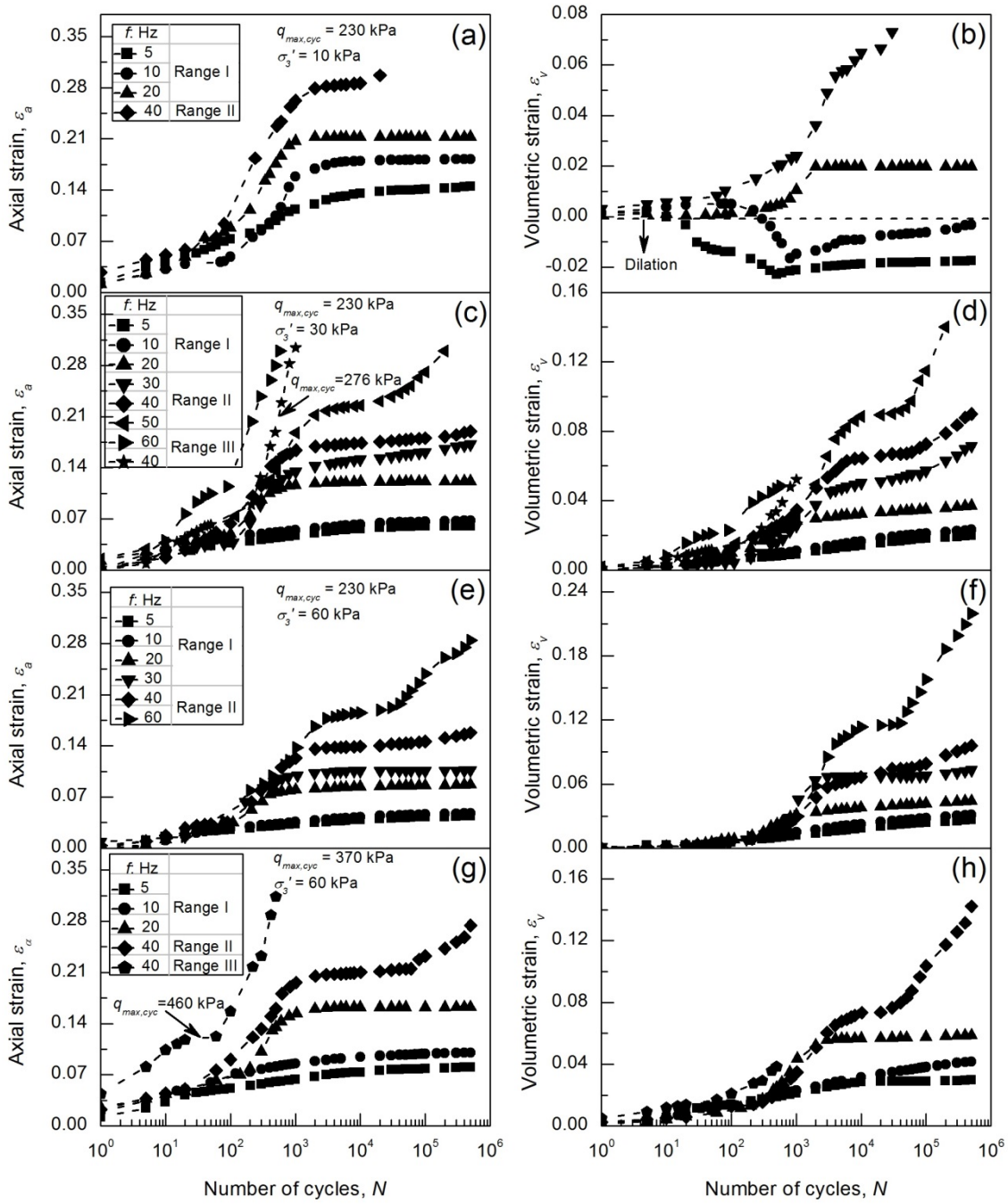

Figure 3.12 Strain response under cyclic loading: (a, c, e & g) axial strain ε_a versus number of cycles *N*; (b, d, f & h) volumetric strain ε_v versus *N*

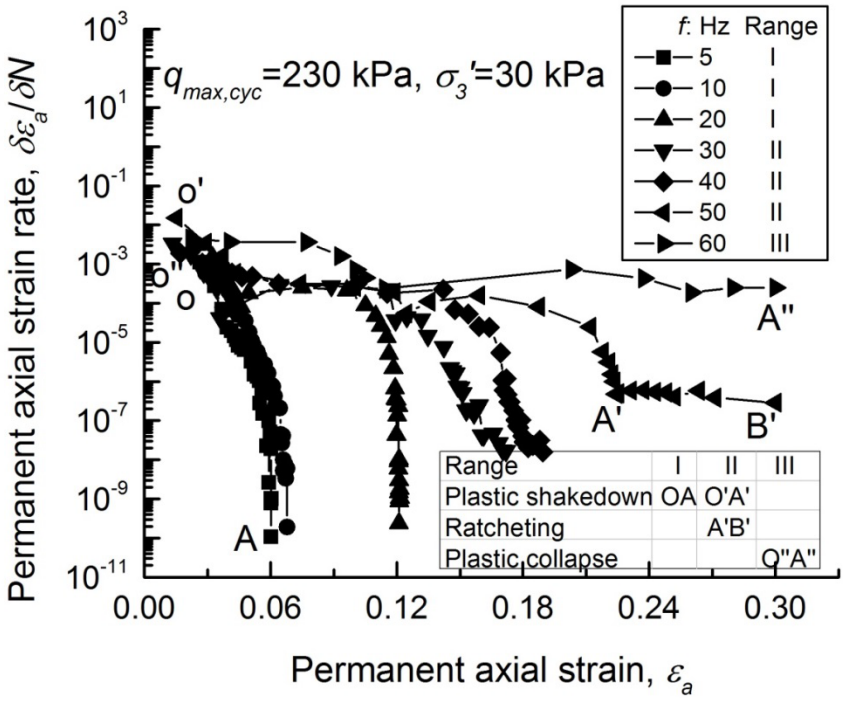

Figure 3.13 Permanent axial strain rate versus permanent axial strain for selected specimens

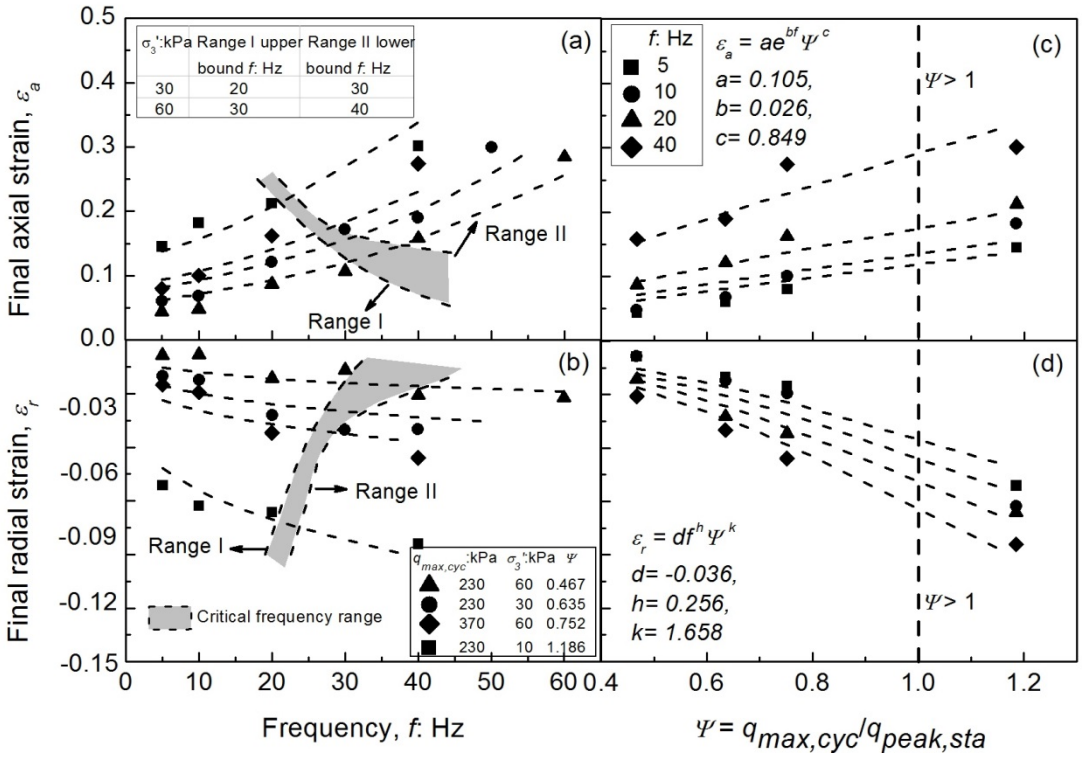

Figure 3.14 Final strain values after 500,000 cycles: (a) axial strain ε_a as a function of *f*; (b) radial strain ε_r as a function of *f*; (c) ε_a as a function of Ψ; (d) ε_r as a function of Ψ

Large vertical train loads ($q_{max,cyc}$) combined with relatively minor horizontal confining stresses (σ_3') can induce significant shear strains in ballast during cyclic loading. A lateral spread of particles can reduce the residual horizontal stresses that confine the layer, but this also reduces the track stability (Selig and Waters, 1994). The radial strain ε_r ($(\varepsilon_v - \varepsilon_a)/2$) can be used to quantify the lateral spread of ballast and to assess the track stability. Hence, the final radial strain ε_r is plotted as a function of *f* in Figure 3.14(b). As expected, the values of ε_r increase with $q_{max,cyc}$ and *f* whereas they decrease with σ_3'. This demonstrates the reduction in track bed stability with increasing axle load and train speed, whereas increased confinement would effectively enhance track stability.

It is more convenient to combine the effects of $q_{max,cyc}$ and σ_3' by using one stress state parameter. Some researchers (e.g. Brown et al., 1975; Raymond and Williams, 1978; Suiker et al., 2005; Lackenby et al., 2007) used the cyclic stress ratio $\Psi = q_{max,cyc}/q_{peak,sta}$ to characterise the cyclic response of materials, where $q_{peak,sta}$ is the static peak deviator stress at failure that can be obtained by monotonic triaxial tests. Figures 3.14(c) and 3.14(d) show the accumulated ε_a and ε_r as a function of Ψ for varied *f*. For a constant Ψ value (i.e. Ψ = 0.635 corresponding to $q_{max,cyc}$ = 230 kPa and σ_3' = 30 kPa), increasing *f* from 5 Hz to 40 Hz generates a larger ε_a and ε_r, whereas for *f* = 5 Hz, ε_a and ε_r increase with Ψ (i.e. Ψ = 0.467 to 1.186). The Ψ value exceeding 1 indicates that specimens are able to sustain significantly greater deviator stress than statically loaded specimens. This observation is also in agreement with the study by Suiker et al. (2005). However, in order to avoid plastic collapse failure in Range III represented in Figures 3.14(c) and 3.14(g) under high frequency loading (i.e. $f \geq 40$ Hz), the Ψ value should be less than 1. Moreover, in a practical sense, empirical relations were readily obtained to predict ε_a and ε_r for given values of *f* and Ψ by Equations (3.6) and (3.7), respectively:

$$\varepsilon_a = a \cdot e^{b \cdot f} \cdot \Psi^c \tag{3.6}$$

$$\varepsilon_r = d \cdot f^h \cdot \Psi^k \tag{3.7}$$

where, *a*, *b*, *c*, *d*, *h* and *k* are the empirical constants.

3.4.2 Empirical Modelling for the Permanent Strain with Number of Cycles

Whilst Equation (3.6) associates ε_a to f and Ψ and can be used to calculate the ballast response after 500,000 load applications, it is more imperative to find a relationship which can predict the accumulation of ε_a with evolving N. Equation (3.6) could be extended to meet such a function by considering the three coefficients (*a*, *b*, and *c*) as a function of *N*. It is shown in Figure 3.12 that rapid development of ε_a occurs within the first 1,000 cycles, and for Range II specimens after the shakedown zone, a ratcheting zone commences around 20,000 cycles. Hence, the relationships between *a*, *b* and *c* with *N* can be broken into two distinct regions for Range I specimens and three for Range II ones. Similarly, Equation (3.7), together with Equation (3.6), can be utilised to calculate the corresponding ε_v. The expressions of *a*, *b*, *c*, *d*, *h* and *k* can be related to *lnN* by a linear function, for instance, $a = \pi \cdot ln(N) + \tau$. The values of empirical constants π and τ are tabulated in Table 3.4. Figure 3.14(a) plots the consistency between the measured and predicted values of ε_a with f = 20 Hz (i.e. Range I) and 60 Hz (i.e. Range II), respectively. It is indicated that Equation (3.6) provides a satisfactory link between the various parameters under investigation, especially the frequency effects. Comparison with other model predictions for the selected specimens is also shown in Figure 3.15(a) and the model regression parameters can be found in Table 3.5. The predictions of ε_v by the current study are shown in Figure 3.15(b) and again the frequency effects are properly reflected by the current models.

Table 3.4 Expressions of coefficients *a*, *b*, *c*, *d*, *h* and *k* with evolving *N*

	a			*b*			*c*			*N*
	π	τ	R^2	π	τ	R^2	π	τ	R^2	
Range I	0.0140	-0.0214	0.94	0.0073	-0.0045	0.62	0.2215	-0.3274	0.97	$N < 1{,}000$
	0.0042	0.0500	0.77	0.0020	0.0560	0.78	-0.0116	1.2830	0.90	$N \geq 1{,}000$
Range II	0.0384	-0.1000	0.81	-0.0025	0.0262	0.71	-0.2143	2.2780	0.93	$N < 1{,}000$
	-0.0036	0.1660	0.49	0.0012	0.0052	0.80	-0.0116	0.8812	0.36	$1{,}000 \leq N \leq 20{,}000$
	-0.0095	0.2275	0.78	0.0042	-0.0245	0.88	0.0751	0.1296	0.57	$N > 20{,}000$
	d			*h*			*k*			
	π	τ	R^2	π	τ	R^2	π	τ	R^2	
Range I	-0.0089	0.0372	0.92	-0.0756	0.09293	0.65	0.4343	-1.326	0.95	$N < 1{,}000$
	-0.0016	-0.0194	0.75	-0.0186	0.4408	0.73	0.0297	1.5710	0.79	$N \geq 1{,}000$
Range II	-0.0081	0.0328	0.57	-0.1750	1.5860	0.67	-0.2364	2.5810	0.28	$N < 1{,}000$
	-0.0043	0.0157	0.37	-0.0705	1.0350	0.40	0.0516	0.6785	0.87	$N \geq 1{,}000$

Table 3.5 Empirical modelling for permanent response

Model	Frequency: Hz	Reference	Regression parameters
$\varepsilon_a = a_1 + a_2 logN$	60	Barksdale (1972)	a_1 = -0.033, a_2 = 0.054
$\varepsilon_a = b_1 N^{b2}$	20	Sweere (1990)	b_1 = 0.032, b_2 = 0.090
$\varepsilon_a = \varepsilon_{a,1}(1 + c_1 logN)$	60	Raymond et al. (1975)	c_1 = 5.364
$\varepsilon_a = \varepsilon_{a,1}(1 + d_1 lnN + 0.5 d_2 lnN^2)$	20	Indraratna and Nimbalkar (2013)	d_1 = 0.189, d_2 = 0.724
$\varepsilon_a = a e^{bf} \Psi^c$	20 & 60	Current study	*a*, *b* and *c* referred in Table 3.4
$\varepsilon_r = d f^h \Psi^k$	20 & 60	Current Study	*d*, *h* and *k* referred in Table 3.4

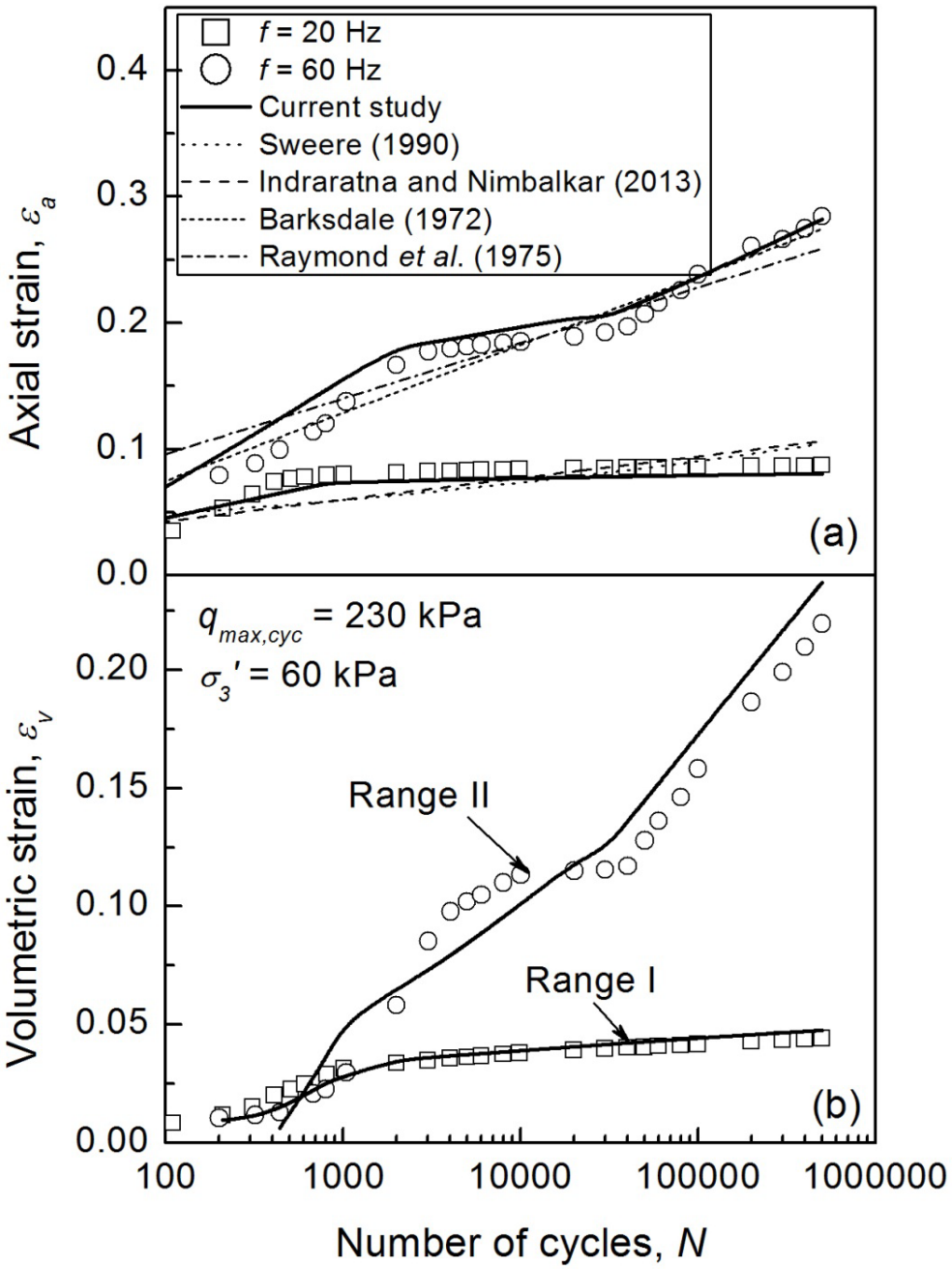

Figure 3.15 Empirical modelling for ballast: (a) axial strain response, (b) volumetric strain response

3.4.3 Cyclic Strain Ratio

When the effect of frequency on ballast deformation is considered, it is useful to compare the cyclic cumulative axial strain $\varepsilon_{a,cyc}$, with the strain $\varepsilon_{a,sta}$ obtained from a monotonic test at the corresponding static load $q_{sta} = q_{max,cyc}$ ($\varepsilon_{a,sta}$=0.018, $\varepsilon_{v,sta}$=0.0035).

The Cyclic Axial Strain Ratio (CASR), $\Phi_a = \varepsilon_{a,cyc}/\varepsilon_{a,sta}$ is therefore defined for this purpose. The data for a series of tests with $q_{max,cyc}$ = 230 kPa and σ_3' = 30 kPa was used as an example. The values of $\varepsilon_{a,cyc}$ at the characteristic N (i.e. N = 20,000 and 500,000) were used to calculate the CASR. Figure 3.16 shows the calculated Φ_a as a function of f, and when $f \leq 20$ Hz, the difference between the values of Φ_a at N = 20,000 and 500,000 was insignificant. This implies that for these specimens the shakedown phase was continued to the end of the test. However, this difference becomes visible when $f \geq$ 30 Hz, which is because the ratcheting zone was reached after a relatively long shakedown zone. A best-fit equation for the data shown in Figure 3.16 can be represented as:

$$\Phi_a = a \cdot e^{b \cdot f} \tag{3.8}$$

where a and b are the empirical coefficients.

By considering a and b as a function of N (Figure 3.16), Equation (3.8) can be extended to capture the permanent deformation under different loading numbers and frequency. Accumulated ε_a can be obtained as:

$$\varepsilon_a = a \cdot \exp(0.138 \cdot b \cdot V) \cdot \varepsilon_{a,sta} \tag{3.9}$$

Like CASR, an empirical relation could be obtained to relate Cyclic Volumetric Strain Ratio (CVSR), Φ_v, with f (i.e. $\Phi_v = c \cdot e^{d \cdot f}$). Figure 3.16 shows that Φ_v was bigger than Φ_a at given values of f and N, which indicates that frequency had more influence on ε_v than ε_a.

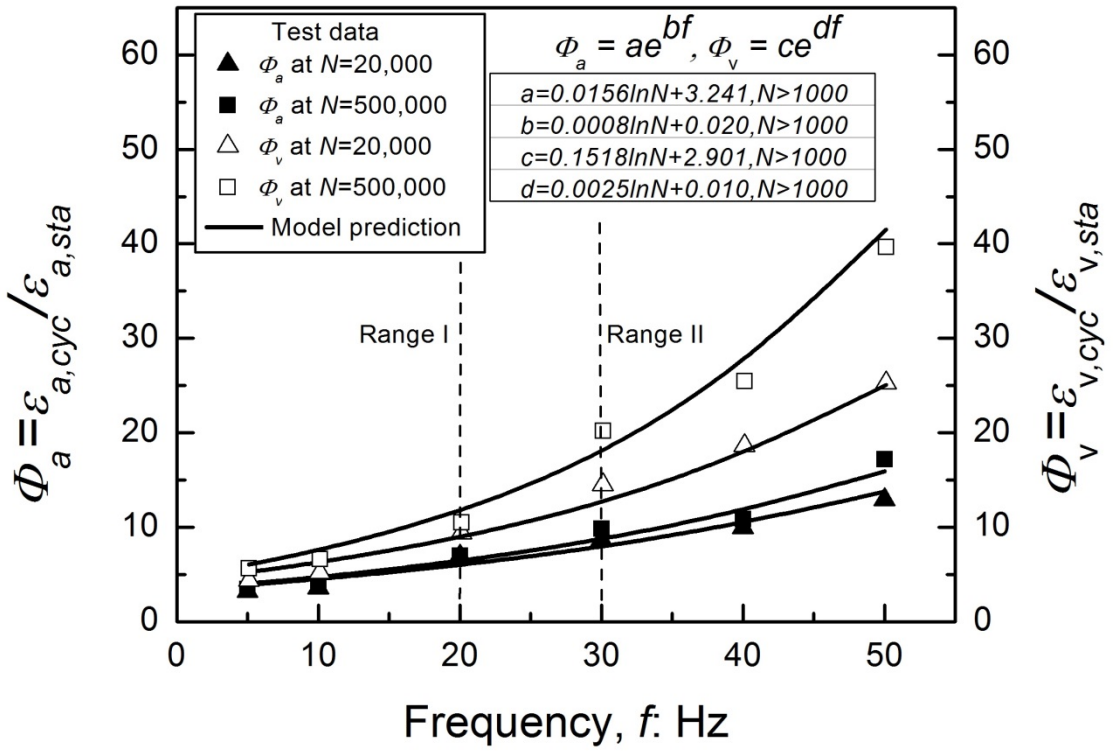

Figure 3.16 Cyclic Axial Strain Ratio and Cyclic Volumetric Strain Ratio as a function of frequency, *f*

3.4.4 Particle Degradation and Its Effect on Permanent Deformation

Indraratna et al. (2005) introduced the Ballast Breakage Index (BBI) to assess the amount of particle degradation. It quantifies the change in the fraction passing a range of sieve sizes. The definition of BBI is shown in Figure 3.17(a), as are the relative PSD curves for selected specimens ($q_{max,cyc}$ = 370 kPa, σ_3' = 60 kPa and f = 10, 20 and 40 Hz). It is illustrated that the area traced out by the shift in the PSD curve increases as f increases. The effect of f on the breakage of ballast at the end of the tests is shown in Figure 3.17(b), and it indicates that BBI increases as f for specific values of $q_{max,cyc}$ and σ_3'. The experiments conducted by Lackenby et al. (2007) on ballast revealed that for a given value of $q_{max,cyc}$, an 'optimum' range of σ_3' exists (i.e. σ_3' = 15-60 kPa for $q_{max,cyc}$ = 230 kPa) such that degradation is minimised. Figure 3.17(b) shows that for those specimens with $q_{max,cyc}$ = 230 kPa, the magnitudes of BBI decreased as σ_3' increased from 10 kPa to 60 kPa at a specific value of f. For those specimens at σ_3' = 60 kPa,

when $q_{max,cyc}$ increased from 230 kPa to 370 kPa, BBI increased in magnitude quite significantly. It can be concluded that the degradation of a particle subjected to compressive forces within a granular medium is not only a function of the applied stresses ($q_{max,cyc}$ and σ_3'), the particle size, the number of cycles, and the coordination number (McDowell and Bolton, 1998), but also of the load frequency.

Distinct ballast degradation behaviours were observed corresponding to different deformation ranges during cyclic testing. For Range I ($f \leq 30$ Hz), the particle degradation was in the form of attrition of asperities and corner breakage (Figure 3.18(a)). As the frequency became higher (30 Hz < f < 60 Hz) in Range II, particle splitting caused by fatigue (Figure 3.18 (c)) and a high degree of attrition resulting from increased vibration became predominant (Figure 3.18(b)). At very high frequency ($f \geq$ 60 Hz) in Range III, the coordination number is greatly reduced, which would induce particle splitting (Figure 3.18(d)). Figure 3.17(b) shows that the critical frequency decreases as the particle breakage increases. Ratcheting failure (Range II) of the specimen would occur with a significant particle breakage (BBI > 0.10) even at a relatively low value of frequency (i.e. f = 25 Hz).

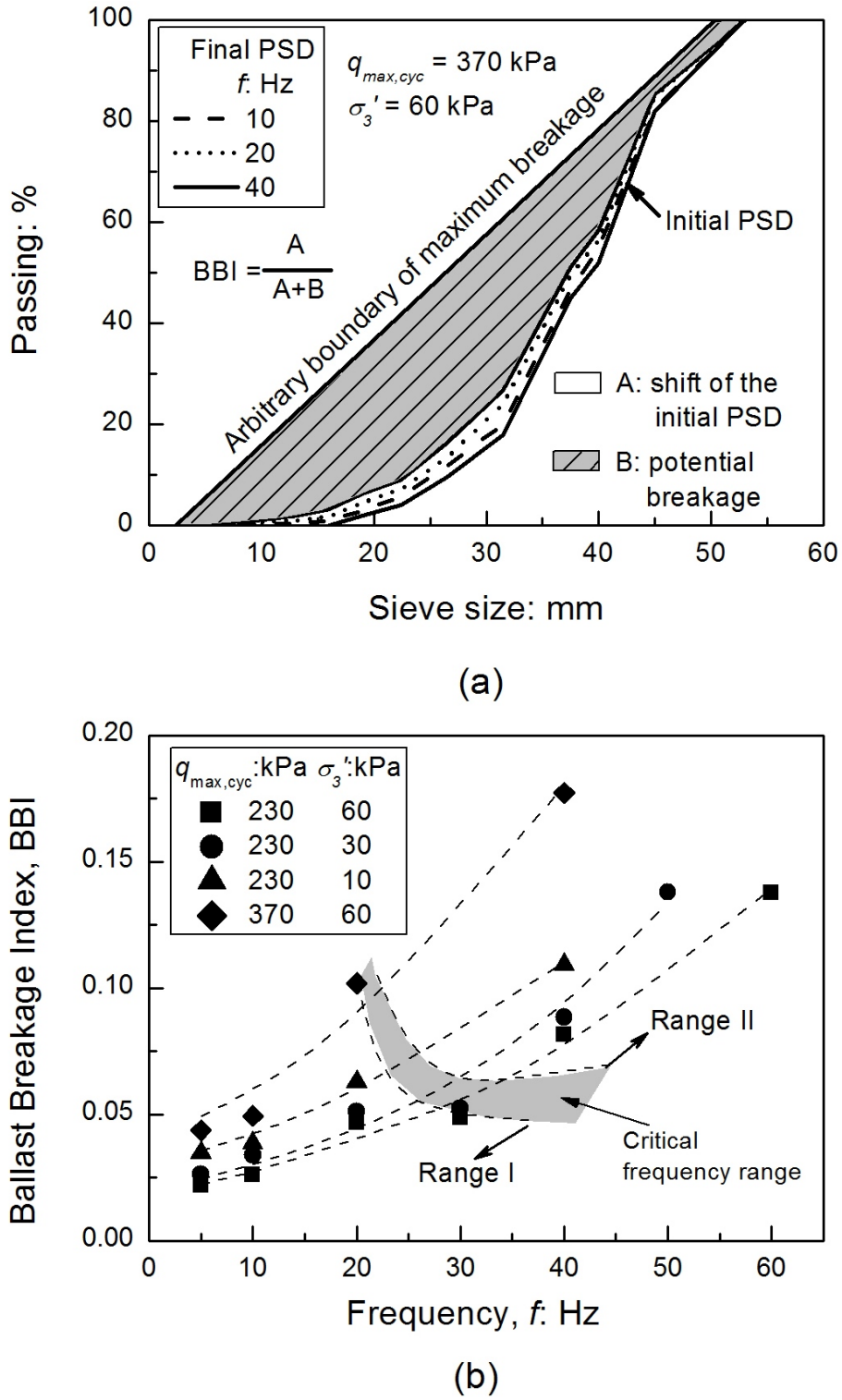

Figure 3.17 (a) Relative particle size distribution curves after loading for selected specimens ($q_{max,cyc}$ = 750 kPa, σ_3' = 60 kPa, f = 10, 20 and 40 Hz respectively); (b) effect of frequency f on ballast breakage index BBI

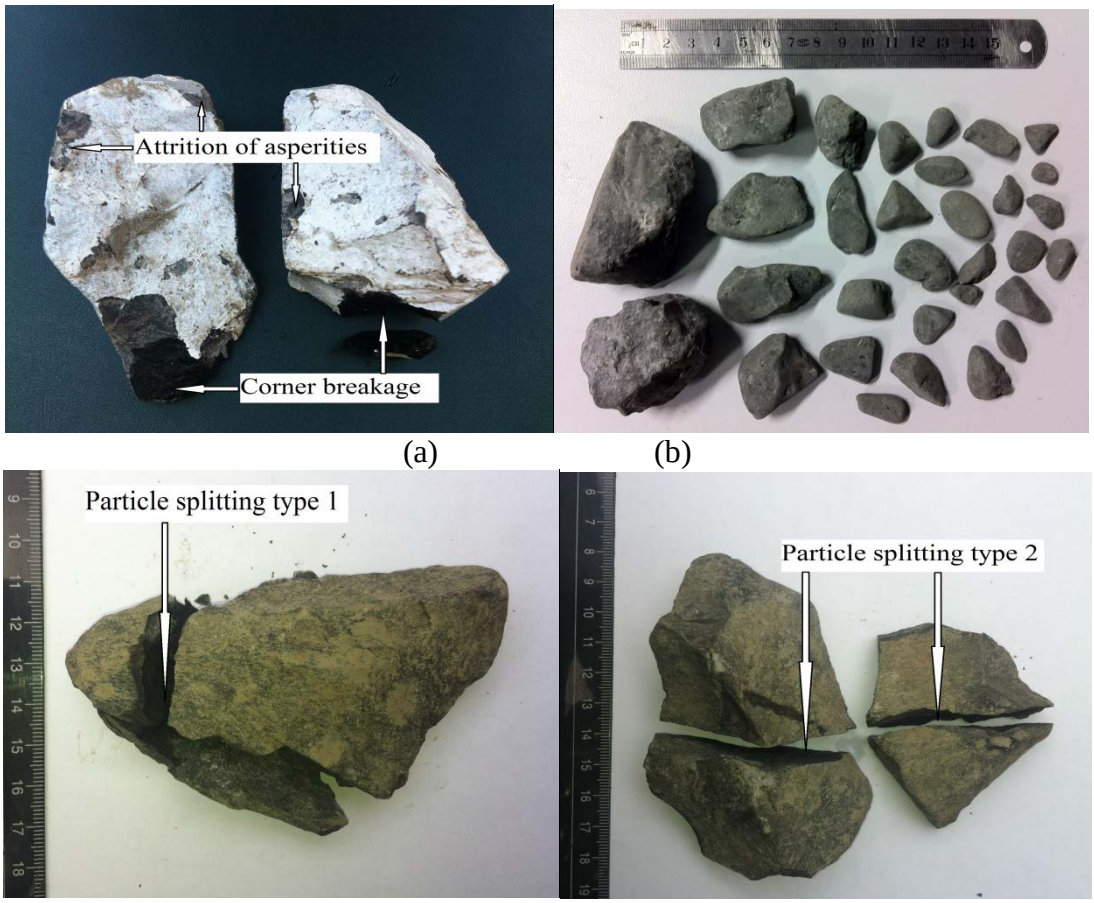

Figure 3.18 Examples of particle degradation: (a) attrition of asperities and corner breakage in Range I, (b) high degree attrition of asperities in Range II, (c) particle splitting type 1 in Range II, and (d) particle splitting type 2 in Range III

Densification is defined in terms of a change in the permanent volumetric strain of granular assemblies that are subjected to dynamic loading (Blazquez and Lopez-Querol, 2006). It is mainly governed by the rearrangement and breakage of particles (Lambe and Whitman 1969). Figure 3.19 presents the variation of accumulated ε_v after 500,000 cycles with final ε_a for different average values of BBI. The results show that the average values of BBI for f = 5, 10, 20 and 40 Hz are found to be 0.027, 0.033, 0.054 and 0.093, respectively. Moreover, the BBI along with f and σ_3' has a profound influence on the magnitude of ε_v, and indeed, an increase in BBI could result in a reduction of the void ratio and a subsequent increase in densification of ballast

assemblies. Increased vibration could lead to higher dynamic stress with repeated shearing and compression, which can also produce greater densification.

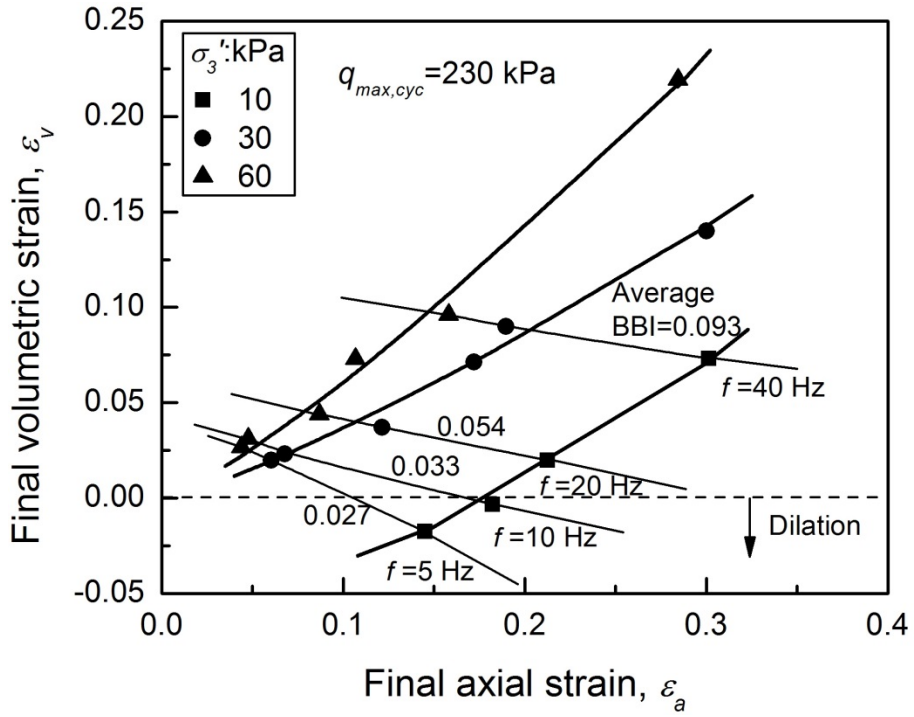

Figure 3.19 Effect of BBI and f on ε_v of ballast

Figure 3.20(a) illustrates the relationship between the particle breakage index BBI and ε_v as a function of f at the end of test ($q_{max,cyc}$ = 230 kPa, σ_3' = 30 kPa). For Range I (i.e. $f \leq 20$ Hz), particle degradation was in the form of attrition of asperities and corner breakage, but for Range II where the frequency was higher (i.e. $f \geq 30$ Hz), particle splitting caused by fatigue and a high degree of attrition became predominant, which contributed to a continual increase of volumetric deformation at a constant rate. In this zone there was a reasonable correlation between ε_v and BBI. The data from Figure 3.20(a) are replotted in Figure 3.20(b) as BBI against ε_v, irrespective of f. The ε_v can be related to BBI by a relationship defined as:

$$\varepsilon_v = me^{n(BBI)} \tag{3.10}$$

where *m* and *n* are the empirical constants (latite basalt, *m* = 0.023 and *n* = 13.37 with regression coefficient R^2 = 0.90).

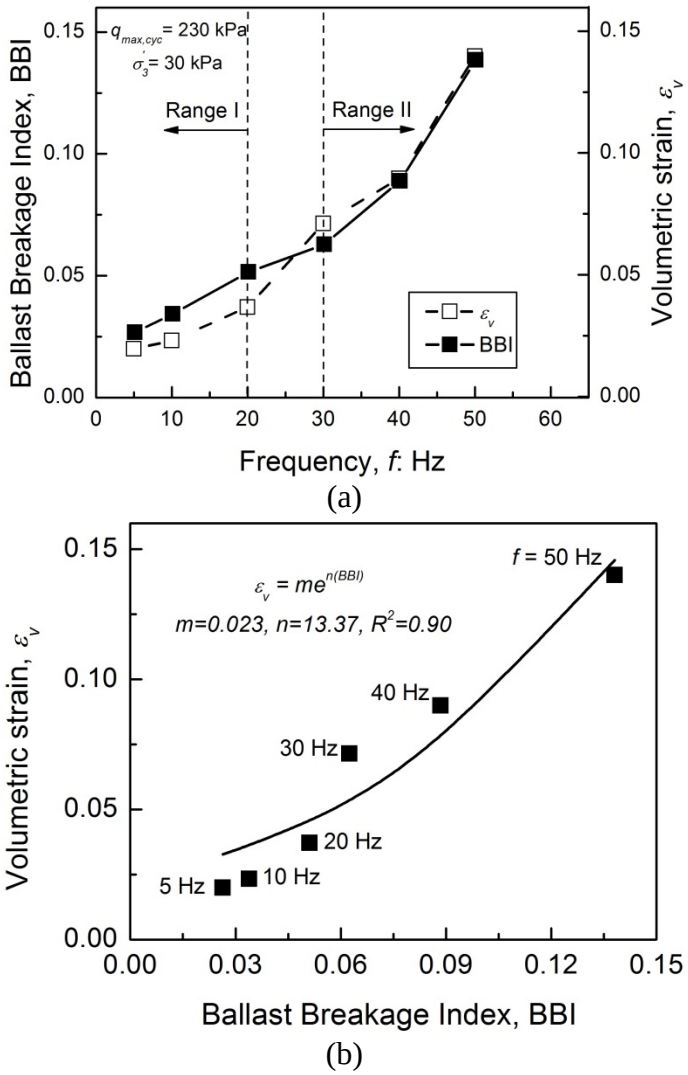

Figure 3.20 Breakage and volumetric strain behaviour at the end of the tests (*N* = 500,000): (a) as a function of frequency *f*, and (b) relationship between ε_v and BBI

3.4.5 Resilient Modulus

The resilient response has traditionally been represented by the resilient modulus M_R and as such, has been widely used in pavement and railway engineering (Lekarp et al., 2000; Lackenby et al., 2007; Indraratna et al., 2009; Thakur et al., 2013). The transient stress-strain measured by data bursting has been used to calculate the values of M_R, defined as $M_R = \Delta q_{cyc}/\varepsilon_{a,rec}$, where Δq_{cyc} is the amplitude of cyclic loading and $\varepsilon_{a,rec}$ is

the resilient axial strain during triaxial unloading, as illustrated in Figure 3.21. Figures 3.22(a) and 3.22(b) show a continual increase in M_R with N, although only a small change is observed beyond 100,000 cycles. The increase in M_R with each successive cycle can be attributed, at least partly, to cyclic densification. As ε_v increases with N (Figures 3.12(b, d, f & h)), leading to a reduction in void ratio and associated increase in stiffness, the progression of M_R with N as shown in Figures 3.22(a) and 3.22(b) is expected. This observation is in agreement with past doctoral studies by Hicks (1970) and Allen (1973) for other granular materials. Figure 3.22(a) also shows a gradual increase in M_R with f, as well as an increase in M_R with σ_3'. A higher frequency along with a higher confining pressure can produce a denser packing of ballast leading to an increased resilient modulus. The effect of $q_{max,cyc}$ on M_R is depicted in Figure 3.22(b) as a function of N, such that the magnitude of M_R increased with $q_{max,cyc}$, which agrees with the study by Lackenby et al. (2007) for a similar rockfill.

Hicks (1970) pointed out that M_R is a function of the bulk stress θ, which is the sum of principal stresses ($\sigma_1' + \sigma_2' + \sigma_3'$). Figures 3.22(c) and 3.22(d) present the variation of resilient modulus M_R after 500,000 cycles with frequency f and bulk stress θ, respectively. It is evident that M_R also increases with f and θ. For a given deviator stress, an increase in f leads to an increased M_R. In view of the above, an empirical relationship between M_R, f and θ could be formulated as:

$$M_R = m \cdot f^n + \theta^t \tag{3.11}$$

where m, n, and t are empirical parameters.

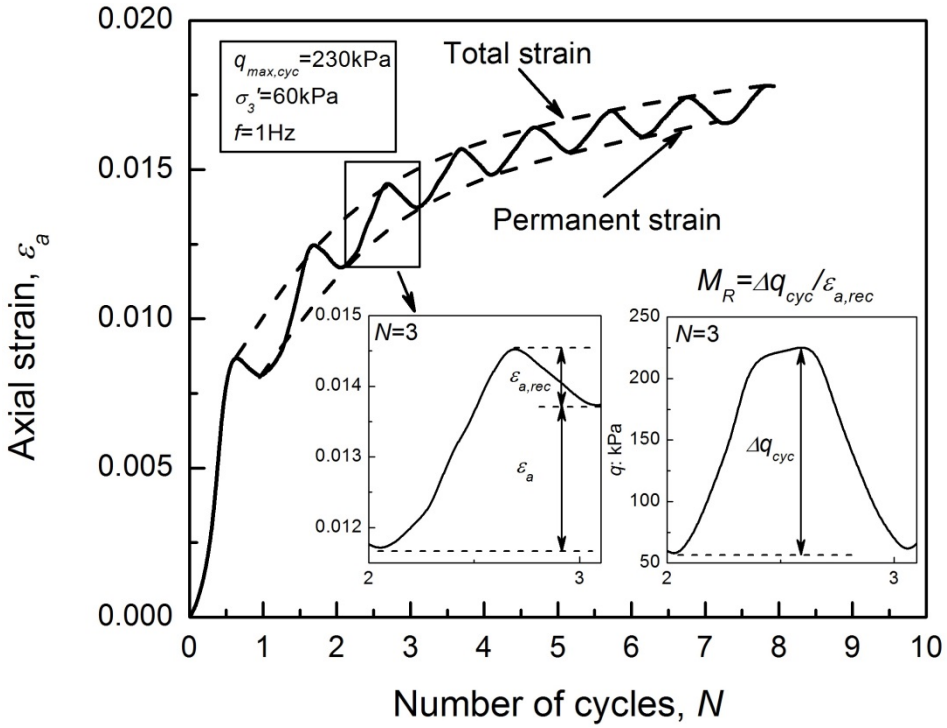

Figure 3.21 Representation of strains during one cycle of load application

Generally, the value of final M_R is larger in Range II than the one in Range I as shown in Figure 3.22(d), which may be caused by the densification resulting from ratcheting behaviour. Within the range of confining pressure used in this study (i.e. σ_3' = 10, 30 and 60 kPa), a higher magnitude of track confinement can effectively increase the resilient modulus as well as the critical train speed (critical frequency). The effect of particle breakage on M_R is also illustrated in Figure 3.22(d), and it shows that increased densification due to particle breakage could result in an increase in the coordination number of the particles, and therefore, an increase of the inter-particle contact area and the magnitude of M_R.

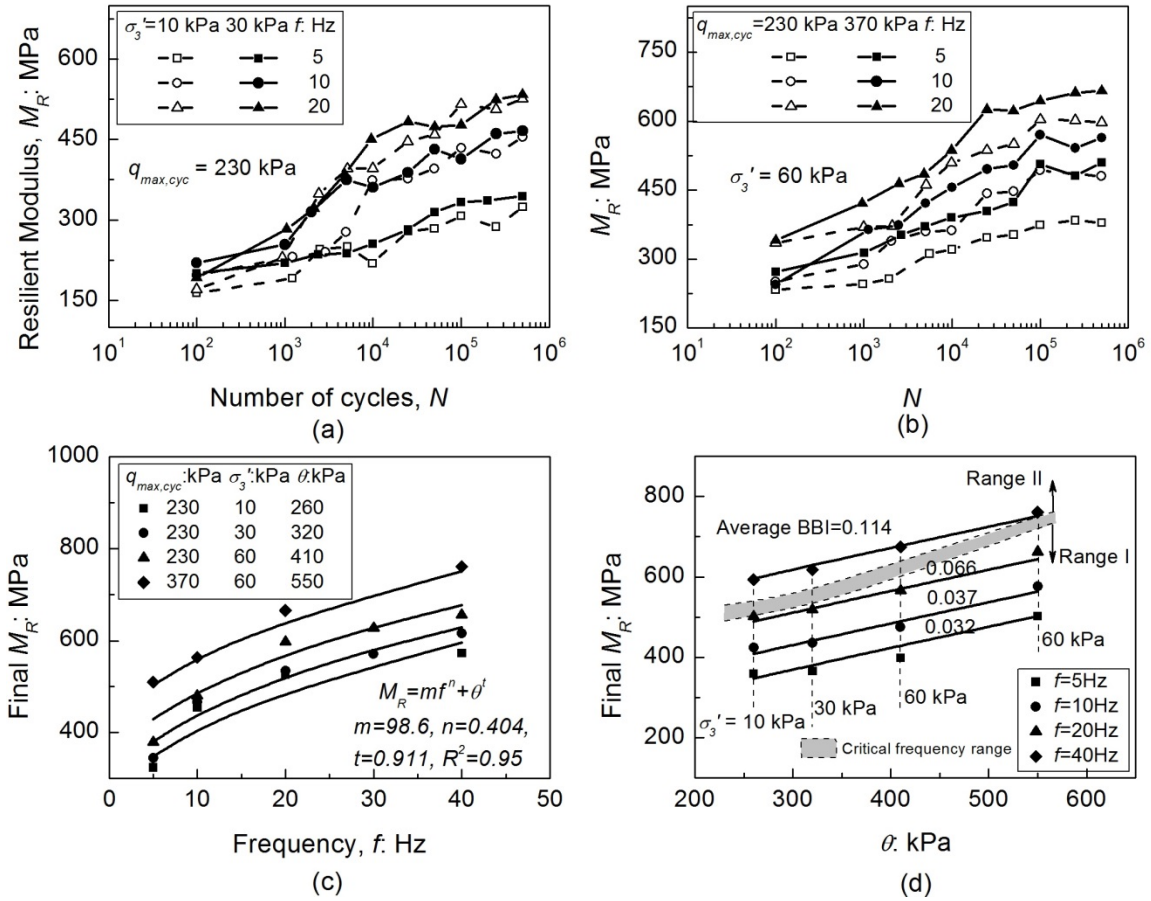

Figure 3.22 Resilient modulus M_R response under cyclic loading: (a) effect of frequency f, confining pressure σ_3' and number of cycles N on M_R; (b) effect of $q_{max,cyc}$ on M_R; (c) final M_R achieved after 500,000 cycles as a function of f; (d) final M_R achieved after 500,000 cycles as a function of θ

There is a note of caution to railway engineers who prefer to use M_R solely as an index of track quality. Interestingly, higher-frequency vibrations do not set larger resilient deformations in the ballast layer, because resilient deformations are primarily governed by the reorientation and rearrangement of particles within the ballast layer which leads to a compacted stable assembly. Particles of granular soils usually respond to different frequencies (vibrations) depending on their size, but when a higher frequency is applied, smaller aggregates move into the voids left by larger aggregates, and this results in a denser packing arrangement (i.e. vibratory compaction). Moreover, a higher train speed can produce a dynamic amplification effect on the deviator load, generating an increase of particle breakage and subsequent densification which also contribute to an increase of

specimen stiffness. For example, in Range II, particle breakage and ratcheting behaviour can contribute to an increase of M_R and subsequent reduction in $\varepsilon_{a,rec}$, however, excessive settlement and degradation may induce track instability.

3.4.6 Dynamic Amplification Factor (DAF) and Practical Significance

In conventional practice, dynamic amplification factor (DAF) is used as a function of static (wheel) load and train velocity to obtain the equivalent dynamic load (Li and Selig, 1998b; Esveld, 2001). In the current study, the same approach is used by replacing the train velocity with the excitation frequency. As the frequency and speed have a distinctly defined linear relationship (Esveld, 2001), the method of calculating DAF using triaxial testing is in accordance with the field practice. In this study, the DAF was calculated by using DAF = $q_d/q_{max,cyc}$, where $q_{max,cyc}$ is the applied deviator stress, and q_d is the dynamic deviator stress measured during the cyclic loading tests as shown in Figure 3.23(a). For a given train load and track confinement (i.e. $q_{max,cyc}$ = 230 kPa, σ_3' = 60 kPa), as f increased from 30 Hz to 40 Hz, q_d varied from 440 kPa to 620 kPa, and the correspondingly permanent deformation behaviour transferred from Range I (i.e. plastic shakedown) into Range II (i.e. plastic shakedown and ratcheting). Figure 3.23(b) illustrates the calculated DAF as a function of train speed V, together with the predictions made from other studies (i.e. Li and selig, 1998b; Esveld 2001). The conventional AREA approach described by Li and Selig (1998b) overestimates the value of DAF when the train speed is smaller than 300 km/h. The alternative approach described by Esveld (2001) also overpredicts the value of DAF within its range of application (i.e. $V \leq$ 200 km/h). This has serious consequences in design rendering it costly, being over-conservative. Irrespective of the applied stresses, the variation of

DAF was confined within a narrow band when plotted against *V*, so a non-linear best-fit equation for the data shown in Figure 3.23(b) could be presented as:

$$DAF = e^{\alpha \cdot V} \tag{3.12}$$

where α is an empirical parameter (= 0.003) obtained through regression analysis having a coefficient of regression R^2 = 0.97. The train speed *V* (km/h) is directly proportional to the frequency *f* (Hz) by *V* = 7.25 *f*, assuming four axle passes under two adjacent bogies from two adjacent cars as one loading cycle for the substructures (see Figure 3.23(a)). The measured data suggests that a modification of Li and Selig's (1998b) model can be applied by using a different coefficient:

$$DAF = 1+0.0048V/D \tag{3.13}$$

where *D* is the wheel diameter.

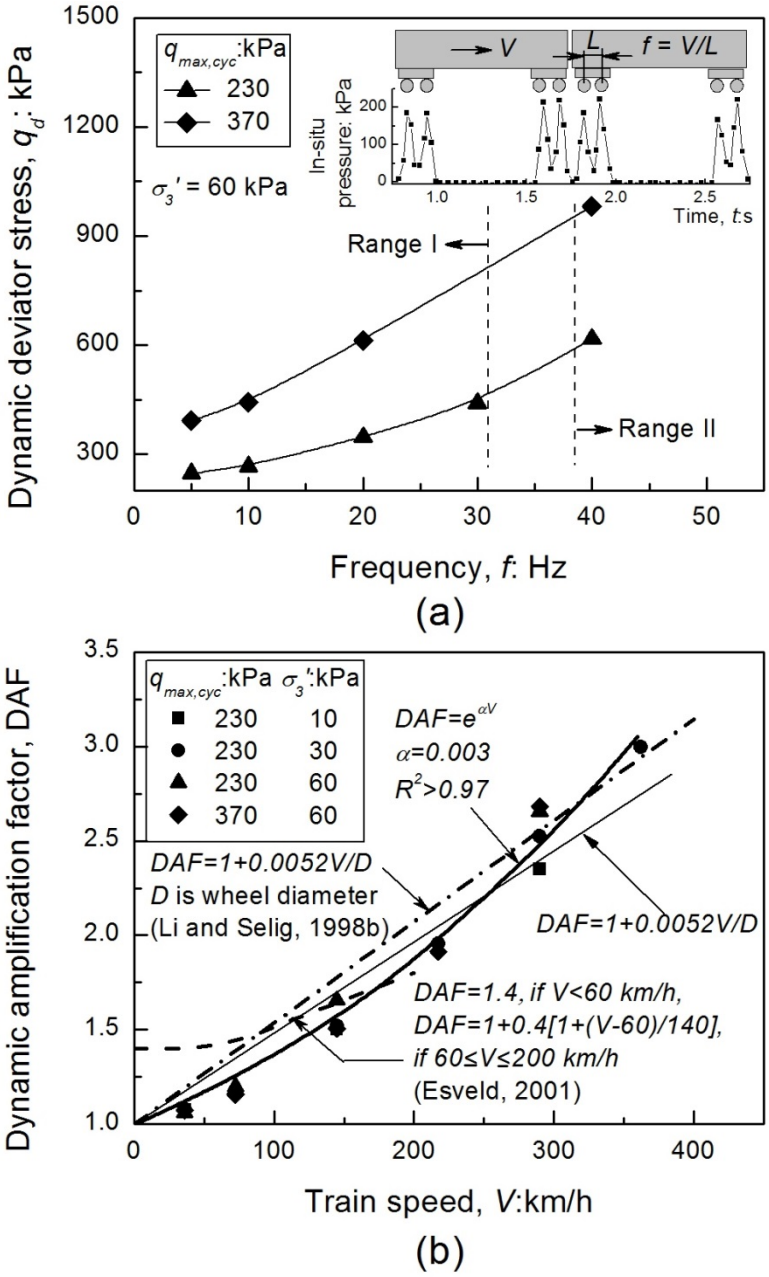

Figure 3.23 (a) Measured dynamic deviator stress q_d; (b) Dynamic amplification factor (DAF) as a function of train speed V

3.4.7 Effect of Train Speed V on the Granular Layer Thickness H

The two most common failures caused by large repetitive stresses on the subgrade are progressive shear failure and excessive plastic deformation (ballast pocket). A sufficiently thick granular layer defined as the combined thickness of the ballast and subballast layers will prevent both types of subgrade failures (Li and Selig, 1998b). The

manual of the American Railway Engineering Association (AREA, 1996) recommends the following method for designing the thickness of granular layers:

$$H = 0.24\left(\frac{p_m}{p_c}\right)^{0.8} \tag{3.14}$$

where H is the thickness of the granular layer (m), p_c is allowable subgrade pressure (with 138 kPa being recommended by the AREA), and p_m is the vertical stress applied onto the ballast. The data plotted in Figure 3.23(a) can be used to represent the sleeper-ballast contact pressure p_m produced by an axle load of 25 t and 40 t, respectively. Figure 3.24 illustrates the calculated H as a function of V, where, as expected, as the axle load increases, a thicker granular layer is required. Given an axle load (i.e. 25 t), when the train speed increases from 50 km/h to 350 km/h, the value of H increases by approximately 120%.

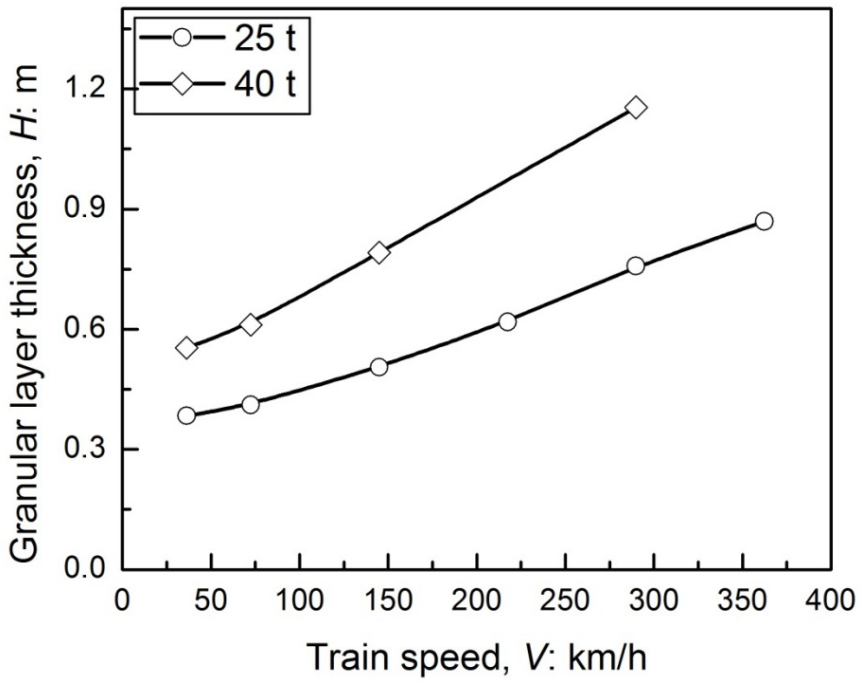

Figure 3.24 Granular layer thickness H as a function of train speed V

3.5 Summary

This chapter described the ballast response under both static and cyclic loading conditions. This study has shown that particle breakage can significantly influence the critical state. At relatively higher confining pressure ($\sigma_3' \geq 180$ kPa), particle breakage is more pronounced and this causes a shift of the location of critical state line on the q-p' and υ-lnp' planes. As particle breakage increases, the critical state stress ratio M_c decreases. The CSL on the υ-lnp' plane is no longer a straight line, and the location of CSL changes as the extent of breakage (BBI) increases. The CSL on the υ-lnp' plane becomes a critical state surface when the extra dimension of BBI is added. Based on the drained compression test data, a hyperbolic relation for the critical state surface was proposed to relate the specific volume with BBI.

Three distinct deformation mechanisms exist in response to the f, $q_{max,cyc}$ and σ_3', namely: Range I: plastic shakedown, Range II: plastic shakedown and ratcheting, and Range III: plastic collapse. Plastic shakedown is tolerable in a track, provided that the accumulated strains are still acceptable. In contrast, either a high value of f or $q_{max,cyc}$ could lead to ratcheting (Range II) or plastic collapse (Range III), which should not be tolerated in design. A range of critical frequency is identified as 20-30 Hz for σ_3' = 30 kPa and 30-40 Hz for σ_3' = 60 kPa, respectively. The reduced axial and radial strain at higher σ_3' results in an increase in critical frequency.

Increase in $q_{max,cyc}$ generates substantial strains leading to a reduction of critical frequency. At higher $q_{max,cyc}$, axial strain are more sensitive to change in f. Therefore, cyclic stress ratio Ψ along with f is necessary to accurately characterise deformation mechanisms. At relatively low f < 10 Hz, ballast specimen undergoes plastic shakedown

at Ψ of 0.45, while further increase in Ψ leads to ratcheting, followed by plastic collapse (i.e. f = 40 Hz, Ψ = 0.93). Thus, $\Psi \leq 1$ should be considered appropriate to avoid failure under high frequency loading.

Particle breakage is found to be more pronounced due to increase in f, σ_3' and $q_{max,cyc}$. Breakage and subsequent recompaction of the grains lead to an associated increase in the resilient modulus (M_R). For practical use, an empirical relationship was established to relate M_R with f and θ, given by $M_R = mf^n + \theta^t$. Moreover, a new expression for the dynamic amplification factor, $DAF = e^{0.003V}$, was proposed to incorporate the effect of train speed (V) on axle load. As the axle load increases, a thicker granular layer is required. Given an axle load (i.e. 25 t), when the train speed increases from 50 km/h to 350 km/h, the value of H increases by approximately 120%.

The triaxial experiments do not always adequately represent the in-situ stress and strain. For example, a conventional triaxial test cannot correctly simulate the train-induced reversal of shear stress in the longitudinal track direction, which occurs as soon as a material point in the track is located directly below the passing train axle. Disregarding the effect of the shear stress reversal in a laboratory experiment naturally yields a different cyclic evolution of the permanent material deformations. Furthermore, the constant geo-static stresses in a railway track are represented in the triaxial tests by means of a constant confining pressure. This is not correct, in sense that geo-static stresses do not have a purely hydrostatic nature. Additionally, the deviation of the intermediate shear stress with respect to the maximum shear stress is not measured in a conventional triaxial test. Despite these limitations the conventional triaxial tests are one of the most versatile and useful laboratory methods for obtaining the deformation and strength properties.

The laboratory data from this chapter has been used to calibrate and validate the ballast model as described in details in Chapter 4.

CHAPTER 4

CONSTITUTIVE MODEL FOR BALLAST

4.1 Introduction

Previous laboratory evidence suggests that the critical state envelope for ballast is non-linear. In order to investigate the implications of this non-linearity and the associated role of particle breakage, static drained triaxial tests were conducted using the large-scale (cylindrical) triaxial apparatus. A non-linear critical state envelope was established in both q-p' and υ-lnp' planes. Mathematical expressions for critical state parameters (i.e. critical state stress ratio and specific volume) were proposed to incorporate the evolution of particle breakage during monotonic shearing, which were reported in Chapter 3.

In this chapter, an elasto-plastic constitutive model based on the critical state soil mechanics framework is presented to capture the salient aspects of stress-strain behaviour and degradation of ballast. Constitutive parameters were conveniently determined from large-scale laboratory tests. The model is able to predict the monotonic shear behaviour of ballast corroborating with the laboratory measurements. The proposed model is further validated using experimental results available from past independent studies. The constitutive model is then extended to capture important aspects of cyclic loading, i.e. load frequency, and predict plastic deformation under repeated traffic loading.

4.2 Formulation of the Constitutive Model

4.2.1 State Parameter

This model is developed based on the critical state concept and introduces a further important feature, in which, as proposed by Muir Wood et al. (1994), the current strength of the sand is not constant but depends on the current specific volume and mean stress, through a state parameter ψ (Been and Jefferies 1985):

$$\psi = \upsilon - \upsilon_c \tag{4.1}$$

where υ is the current specific volume, and υ_c is the critical state volume. Substituting Equations (3.4) and (3.5) into Equation (4.1) gives,

$$\psi = \upsilon - \Gamma_{ref} + a \cdot \exp(b \cdot BBI) + \lambda \ln p' \tag{4.2}$$

Hence, the current state of the sample is linked to the critical state by the introduction of a state parameter. Equation (4.2) also represents the evolution of ψ as a function of BBI.

4.2.2 Modelling of Particle Breakage

Indraratna and Salim (2002) demonstrated with experimental evidence that the particle breakage increases with increasing axial strain, but at a decreasing rate, finally approaching a relatively constant value. The value of breakage index also becomes greater as the confining pressure increases. From these experimental findings, an experimental relationship is proposed to represent the particle breakage during shearing:

$$BBI = \frac{\theta_b \left[1 - \exp\left(-\nu_b \varepsilon_s^p\right)\right]}{\omega_b - \ln p_i'} \tag{4.3}$$

where θ_b, ν_b and ω_b are material constants characterising the breakage of aggregates, and p_i' is the initial effective mean stress.

4.2.3 Elastic Behaviour

The elastic deviatoric strain increment $d\varepsilon_s^e$ can be obtained by:

$$d\varepsilon_s^e = \frac{dq}{3G} \tag{4.4}$$

where G is elastic shear modulus.

The elastic volumetric strain increment $d\varepsilon_v^e$ can be determined by:

$$d\varepsilon_v^e = \frac{3(1-2\nu)dp'}{2(1+\nu)G} \tag{4.5}$$

where ν is the Poisson's ratio.

4.2.4 Plastic Behaviour and Yield Function

Vectors of incremental plastic strain ($\delta\varepsilon_s^p$ and $\delta\varepsilon_v^p$) obtained from the tests have been plotted along the stress paths in Figure 4.1 for constant stress ratios $\eta=q/p'$, varying from 0.6 to 1.5. The plastic strains were derived from the total strains by subtracting the elastic strains computed at the corresponding stress increment. Plastic strains are assumed to develop at the start of the deviatoric stress path. Figure 4.1 indicates that yielding is activated at the initial unloaded state. In the current analysis, the yield surface in q-p' plane is described by the simple linear relationship:

$$f = q/p' - \eta_s = 0 \tag{4.6}$$

where η_s is the hardening law.

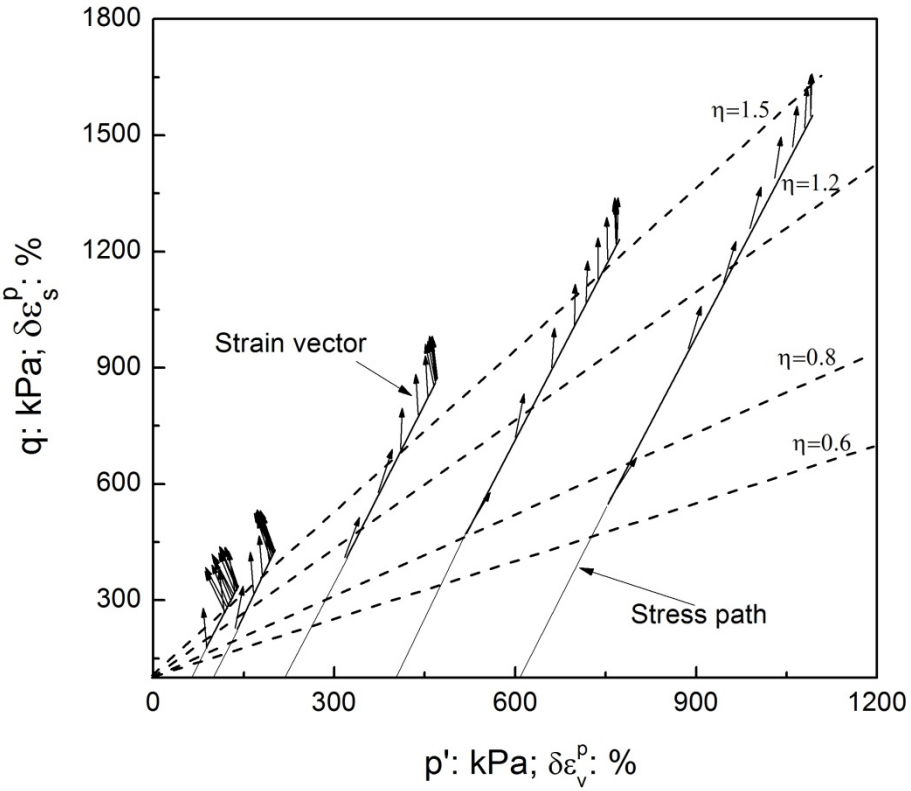

Figure 4.1 Incremental plastic strain vectors along stress paths

The hardening relationship linking the change in location of yield locus (change in stress ratio) to the distortional strain is assumed as:

$$\eta_s = \frac{\varepsilon_s^p}{B_m + \varepsilon_s^p} M_p \tag{4.7}$$

where B_m is a material constant linked to the initial stiffness of the ballast, and M_p is a 'virtual' peak stress ratio attainable at the current state defined by ψ. The idea of having a virtual peak stress ratio is to address the issue of peak stress and subsequent softening of specimens under drained conditions. This is similar to the concept proposed by Muir Wood et al. (1994) considering strain softening for sand modelling. In this study, M_p is related to the state parameter ψ by the following expression:

$$M_p = M_c\left(1 - k_p\psi\right) \tag{4.8}$$

where M_c is critical state stress ratio, and k_p is a constant. M_p is variable with ψ in a way that yields $M_p > M_c$ for $\psi < 0$ (dense states), $M_p < M_c$ for $\psi > 0$ (loose states), and $M_p = M_c$ for $\psi = 0$ (critical states).

Substituting Equations (3.2), (4.2) and (4.8) into Equation (4.7), the hardening function can now be expressed as:

$$\eta_s = \frac{\varepsilon_s^p}{B_m + \varepsilon_s^p}\left[M_{c0} - \left(1 - e^{-\alpha \cdot BBI}\right)\right] \cdot \left[1 - k_p\left(\upsilon - \Gamma_{ref} + a \cdot e^{b \cdot BBI} + \lambda \ln p'\right)\right] \tag{4.9}$$

Equation (4.9) indicates that the hardening of ballast depends on ε_s^p, ψ and BBI.

4.2.5 Dilatancy of Ballast

Figure 4.2 shows that for two specimens of the same bulk unit weight (i.e. γ_b = 15.3 kN/m^3), the ballast specimen initially contracts, then dilates under low confining pressure (i.e. σ_3' = 30 kPa), while it undergoes compression when the confining pressure is considerably higher (i.e. σ_3' = 360 kPa). Furthermore, considering ballast specimens with different bulk unit weights (i.e. γ_b = 15.3 kN/m^3 and 11.2 kN/m^3 separately) subjected to a shear loading increment for the same η (i.e. σ_3' = 60 kPa), the dilation response of the two specimens is different, as shown in Figure 4.2. Both specimens translate from compression to dilation, however, the transformation point for the looser specimen (γ_b = 11.2 kN/m^3) is at a higher deviatoric strain compared to the denser one (γ_b = 15.3 kN/m^3), which confirms the expectation that the looser specimens experience more compression. The separation between the region of compression and the region of

dilation for drained tests on ballast occurs at the phase transformation state at which $\eta = M_d$ and dilatancy $D = 0$, as shown in Figure 4.2.

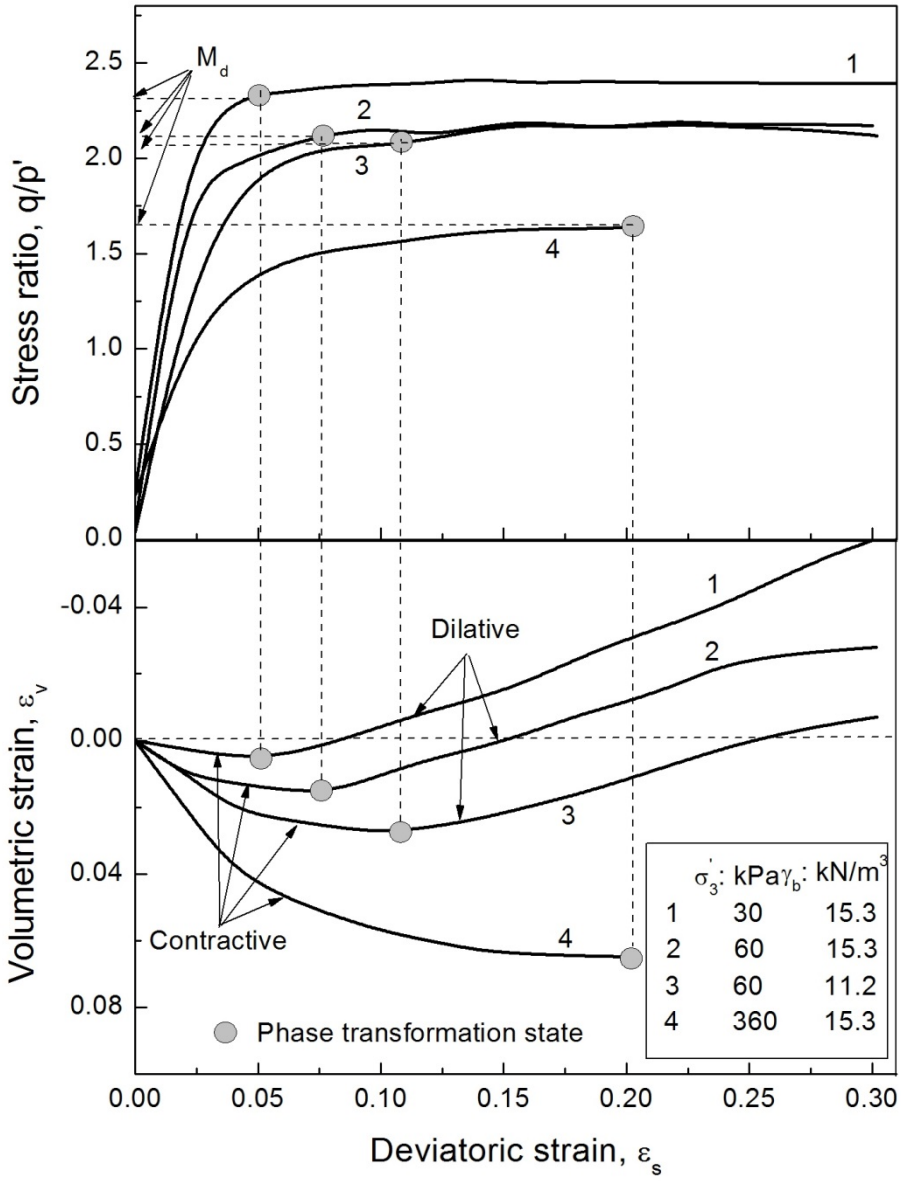

Figure 4.2 Variation in dilatancy with material state

Based on the aforementioned observations and accounting for the critical state constitutive framework, one may propose the following state-dependent dilatancy relationship for ballast:

$$D = \frac{d\varepsilon_v^p}{d\varepsilon_s^p} = A_d\left(M_d - \eta\right) \tag{4.10}$$

where M_d is the phase transformation stress ratio that can be expressed by:

$$M_d = M_c \exp\left(k_d \psi\right) \tag{4.11}$$

In the above equations, A_d and k_d are two characteristic model parameters.

Substituting Equations (3.2), (4.2) and (4.11) into Equation (4.10), the dilatancy term D can be expressed by:

$$D = A_d \left\{ \left[M_{c0} - \left(1 - e^{-\alpha \cdot BBI}\right) \right] \cdot e^{k_d \left[\upsilon - \Gamma_{ref} + a \cdot \exp\left(b \cdot BBI\right) + \lambda \ln p' \right]} - \eta \right\} \tag{4.12}$$

It can be seen that the conventional Cam-clay dilatancy $D = M - \eta$ is a special case of Equation (4.12) (i.e. A_d = 1, k_d = 0 and BBI = 0). Note that at a critical state, ψ = 0 and $\eta = M_c$ simultaneously, Equation (4.12) yields zero dilation, obeying the traditional critical state theory. It can also be observed from Equation (4.12) that the dilatancy depends not only on M_{c0} and η, but also on ψ, as proposed by Manzari and Dafalias (1997) as well as on particle breakage (BBI). At phase transformation points, D = 0, the corresponding stress ratio $\eta = M_d = M_c exp(k_d\ \psi)$ is obtained. It postulates that D depends on the difference of the current stress ratio η from a reference stress ratio $M_c exp(k_d\ \psi)$. This concept is similar to those described by Manzari and Dafalias (1997) and Li and Dafalias (2000).

The phase transformation state and the critical state are very similar, as discussed by Luong (1982). For loose ballast and ballast at high confining pressure, D = 0 is reached at the critical state. The critical state is therefore the same as the phase transformation

state, and it occurs at failure for ballast that compresses during shear. For dense ballast or ballast at low confining pressure, the phase transformation state is reached at small strain magnitudes, as indicated in Figure 4.2, while the critical state is reached at large strains. Hence, the phase transformation state can be used to give an indication of critical state stress ratio M_c for the specimens testing with σ_3' = 30, 60 kPa. The corresponding technique is shown in Appendix A.

4.2.6 Stress-strain Relationship

The incremental elasto-plastic stress-strain relationship is written as:

$$\delta\sigma' = \left(D^e - \frac{D^e m n^T D^e}{H + n^T D^e m} \right) \delta\varepsilon \tag{4.13}$$

where D^e is the elastic compliance matrix, $n=[n_p, n_q]^T$ is the unit vector normal to the loading surface at the current stress state σ', $m = [m_p, m_q]^T$ is the unit direction of plastic flow at σ', and H is the hardening modulus. The derivation of H is given in Appendix B.

4.3 Model Calibration

As summarised in Table 4.1, there are three particle breakage parameters, ten plastic parameters and two elastic parameters in the proposed model. To assess the values of breakage parameters θ_b, ν_b, and ω_b, it is necessary to measure the BBI at various levels of strain. As shown in Figure 4.3, these parameters can be determined by replotting the breakage data as $BBI(\omega_b - lnp_i')$ versus ε_s^p and finding the coefficients of the nonlinear function represented by Equation (4.3).

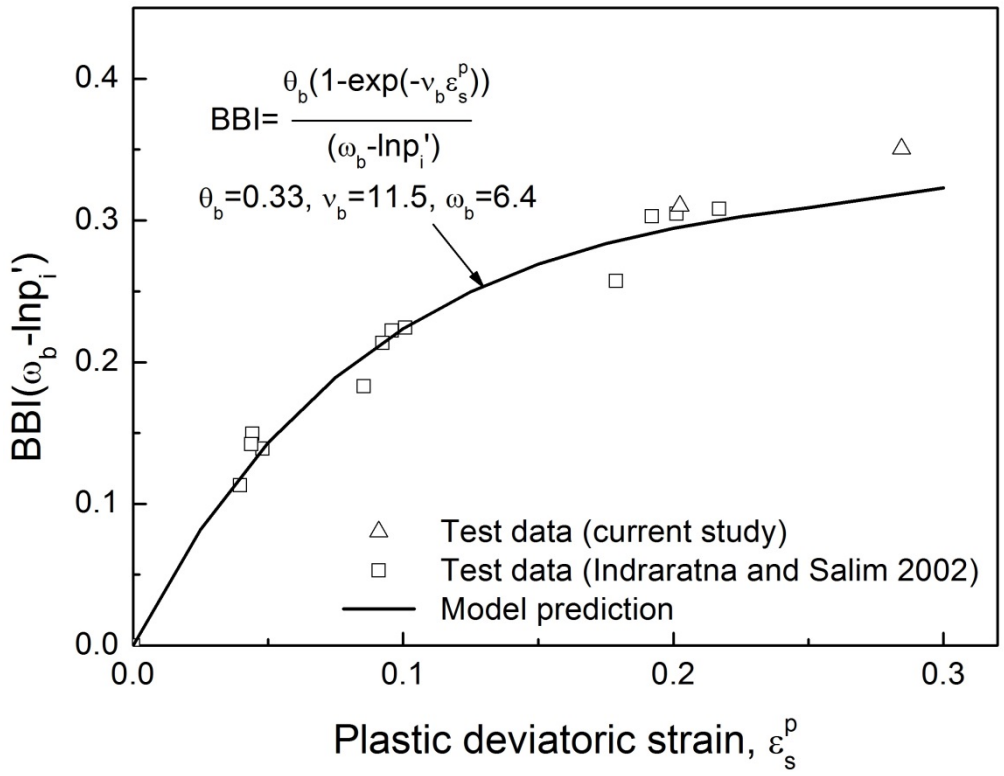

Figure 4.3 Particle breakage parameters (data sourced from Indraratna and Salim, 2002)

The critical state parameters (M_{c0}, Γ_{ref} and λ) can be obtained by conducting a series of drained triaxial compression tests at different effective confining pressures and plotting the test data on the *q-p′* and υ*-lnp′* planes. The slope of the line connecting the critical states under low confining pressures on the *q-p′* plane gives the value of M_{c0}, and that of the υ*-lnp′* plane gives the value of λ. The value of Γ_{ref} is the specific volume of the CSL at p' = 1 kPa on the υ*-lnp′* plane. By plotting the triaxial test results on the *BBI*-M_c plane, the coefficient α can be obtained by applying the least squares method to Equation (3.2), knowing M_{c0}. Similarly, on the *BBI*-Γ plane, parameters *a* and *b* can be obtained by curve fitting Equation (3.5) once Γ_{ref} is known.

The parameter k_d can be determined by Equation (4.10) at a phase transformation state, at which D = 0. Hence,

$$k_d = \frac{1}{\psi_d} \ln \frac{M_d}{M_c} \tag{4.14}$$

where ψ_d and M_d are the values of ψ and η at the phase transformation state, measured from drained test results.

The parameter k_p is determined by Equation (4.8) at a drained peak stress state, thus,

$$k_p = \frac{1}{\psi_p} \left(1 - \frac{M_p}{M_c} \right) \tag{4.15}$$

where ψ_p and M_p are the values of ψ and η at the drained peak stress state, obtained from the laboratory results.

Using Equation (4.12), the parameter A_d is determined from the ε_v-ε_s curves. Parameter B_m is obtained by best-fit regression based on the q/p'-ε_s curves and using Equation (4.8).

Shear modulus G is calibrated from the initial small strain response of the drained triaxial compression tests. This procedure is illustrated in Appendix C. The Poisson's ratio was assumed to be constant (i.e. ν = 0.3). Using G and ν, the elastic strains can be readily computed, while the plastic increments are then obtained by subtracting the elastic component from the total strains.

Table 4.1 Model parameters used for the validation

Model properties	Parameters	Current study		Indraratna et al. (1998)	Indraratna et al. (2013)	Salim and Indraratna (2004)	Suiker et al. (2005)	Anderson and Fair (2008)	Aursudkij et al. (2009)	Varadarajan et al. (2003)	Varadarajan et al. (2003)	Chavez and Alonso (2003)
		With breakage	Without breakage									
Material type	------	Basalt		Basalt	Basalt	Basalt	Basalt	Granite	Limestone	Sedimentary rock	Metamorphic rock	Cambric slate
Test details	σ_3' (kPa) e_i	60/180 0.732/0.75		30/120 0.79/0.70	30/60 0.78/0.75	100/200/300 0.685/0.658/0.646	10.3/41.3/68.9 0.53/0.70/0.70	40/140 0.84/0.82	10/30/60 0.63/0.63/0.63	350/700 0.6/0.6	600/900 0.6/0.6	100/300 0.599/0.594
Gradation characteristics	d_{50} (mm) C_u	39.5 1.53		38.9 1.50	38.8 1.55	35 1.60	24.2 1.70	40.4 1.40	40 1.56	12 95	13 13	22 2.9
Elasticity	G (MPa) ν	8/12 0.3		5.27/10.83 0.25	5.33/7.33 0.25	9.33/7.83/14.67 0.3	4.17/26.67/44.67 0.10	23.9/35.2 0.25	3.67/4.17/16.67 0.3	18.75/31.25 0.29	33.3/33.3 0.31	4.67/13.33 0.29
Particle breakage	θ_b ν_b ω_b	0.33 11.5 6.4	0 0 0	0.30 11.2 6.1	0.31 11.4 6.2	0.33 11.5 6.4	0.31 11 6.5	0.35 12.5 6.8	0.01 12 5	0.25 15 7.38	0.21 12 7.3	0.5 13 6.9
Critical state	Γ_{ref} λ M_{c0} α a b	2.41 0.105 2.6 4.287 0.2 1.87	2.41 0.105 2.18/2.0 0 0 0	2.80 0.164 2.52 2.833 0.061 2.267	2.70 0.123 2.45 4.517 0.048 2.716	2.70 0.155 2.24 0.938 0.038 1.127	2.30 0.053 2.15 4.424 0.030 12.36	2.60 0.112 2.43 6.229 0.016 7.937	1.85 0.016 2.4 54.6 0.042 0.8	1.65 0.004 2.36 0.748 0.036 1.844	1.701 0.009 1.9 1.319 0.025 0.518	2.8 0.131 2.426 2.665 0.076 1.868
Dilatancy	A_d k_d	0.80 1.6	1.25 0.8	1.40 1.28	0.90 0.24	0.95 1.20	1.60 1.48	0.80 2.75	0.5 8	0.37 13	1.05 8	1.3 1.2
Hardening	k_p B_m	1.05 0.017	0.8 0.009	0.90 0.017	0.60 0.009	1.20 0.016	0.01 0.002	0.05 0.003	0.4 0.006	0.50 0.0088	0.2 0.009	0.25 0.026

4.4 Model Validation

Independent sets of triaxial test results were used for initial calibration and for subsequent validation of the model. Three types of ballast and three types of rockfill materials giving a total of 23 independent sets of data were adopted (Varadarajan et al., 2003; Chavez and Alonso, 2003; Indraratna et al., 1998, 2013; Salim and Indraratna, 2004; Suiker et al., 2005; Anderson and Fair, 2008; Aursudkij et al., 2009). The parameters used for the model are shown in Table 4.1 and in general, the model predictions are the ones with breakage. Figures 4.4(a and b) show the stress-strain and volume change predictions of ballast behaviour employing the current model, in comparison with laboratory observations, respectively. The model predictions without any breakage are also shown for comparison. Figure 4.4(a) indicates that particle breakage decreases the shear strength of ballast. As the confining pressure increases, the reduction in strength is more pronounced with greater particle breakage. Figure 4.4(b) shows that only a small difference is evident in volumetric strain response between the model prediction with particle breakage and the one without particle breakage for small confining pressure (i.e. σ_3' = 60 kPa). As shown in Figure 4.4(b), particle breakage causes the specimens to be more compressive, and as the confining pressure ($\sigma_3^{'}$) increases, this effect is more pronounced. Figure 4.5(a) shows the model predictions of particle breakage at various values of σ_3', where the BBI values have been obtained at the end of each test. It is evident from Figure 4.5(a) that BBI increases with the increasing σ_3' and ε_s. The breakage data from Indraratna and Salim (2002) were also used to compare with the model predictions. Good agreement is found between the test data and model predictions. Simulations with and without particle breakage for the

variation in void ratio during the shearing are given in Figure 4.5(b), which also shows an acceptable agreement with laboratory data.

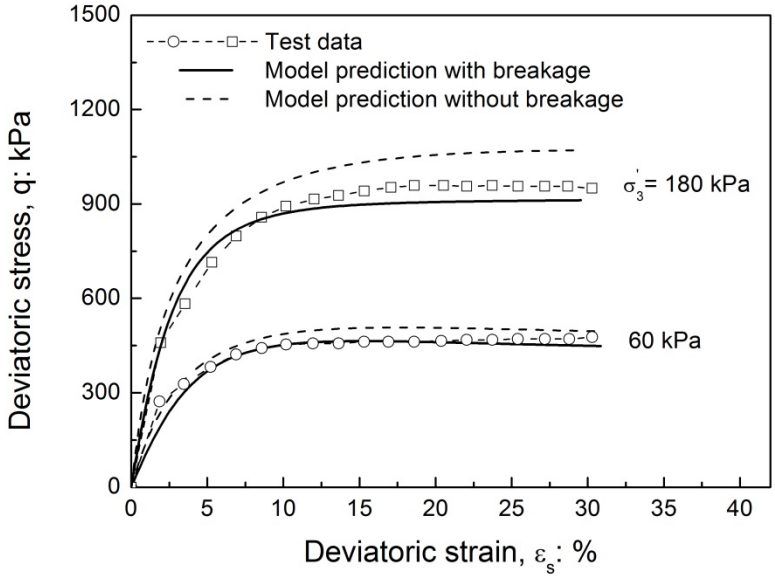

(a)

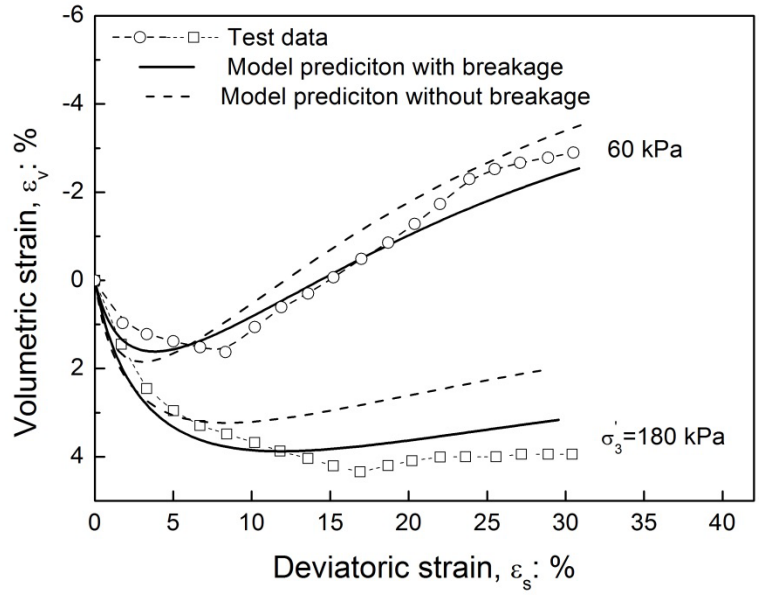

(b)

Figure 4.4 Model predictions compared with experimental results of drained triaxial shearing: (a) stress-strain response and (b) volume change behaviour

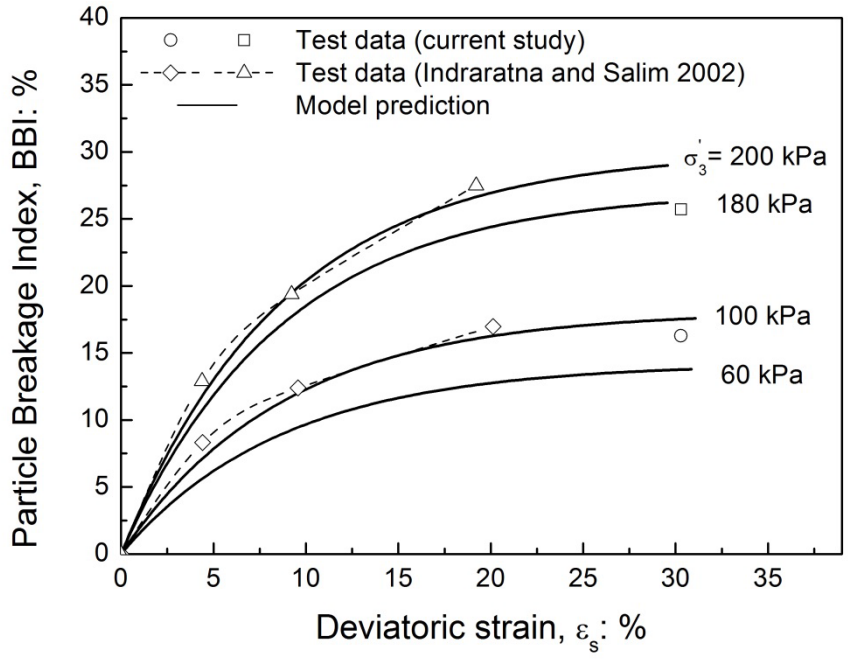

(a)

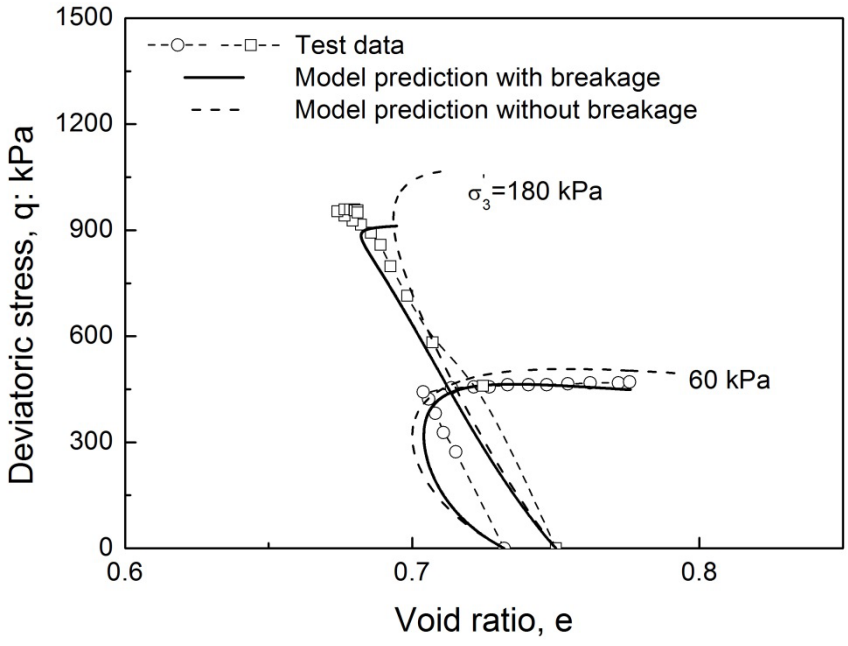

(b)

Figure 4.5 Model predictions compared with experimental results of drained triaxial shearing: (a) particle breakage predictions (data sourced from Indraratna and Salim, 2002) and (b) void ratio

Drained tests from Indraratna et al. (1998) are shown in Figures 4.6(a) and 4.6(b). The pre-shear void ratios (e_i) for the ballast specimens have been determined from weight-volume relationships as summarised in Table 4.1. The critical state was determined by extrapolation of stress-strain data to a most probable value following an approach recommended by Carrera et al. (2011). The BBI values calculated by Equation (4.3) were used to calibrate the model. The stress-strain-volume behaviour is well-captured for the specimen with σ_3' = 120 kPa. For the specimen with lower confining pressure (e.g. σ_3' = 30 kPa), the proposed model fits well with the experimental results considering volumetric strain, even though difference between the simulation and the experimental result can be observed for stress-strain behaviour. Figures 4.7 and 4.8 provide the predictions for drained tests reported by Indraratna et al. (2013) and Salim and Indraratna (2004). The strain-softening behaviours of the specimens are well captured.

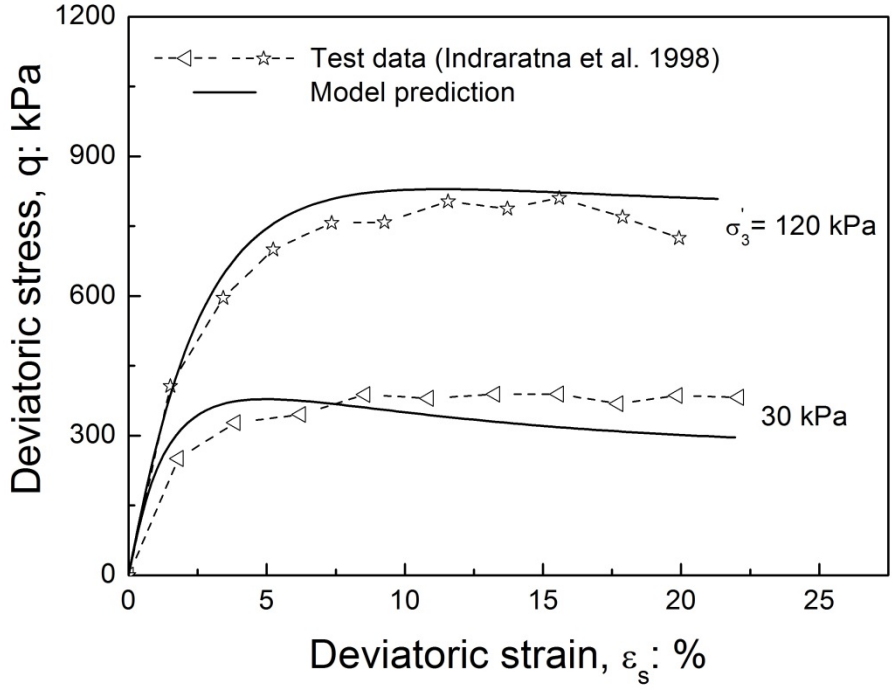

(a)

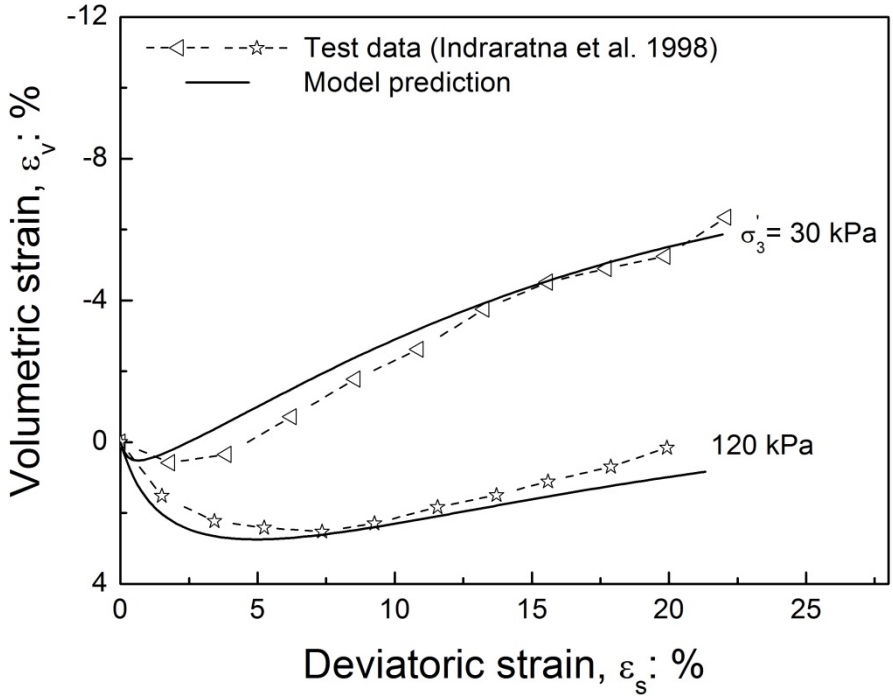

(b)

Figure 4.6 Model predictions compared with experimental results of drained triaxial shearing: (a) stress-strain response and (b) volume change behaviour (data sourced from Indraratna et al., 1998)

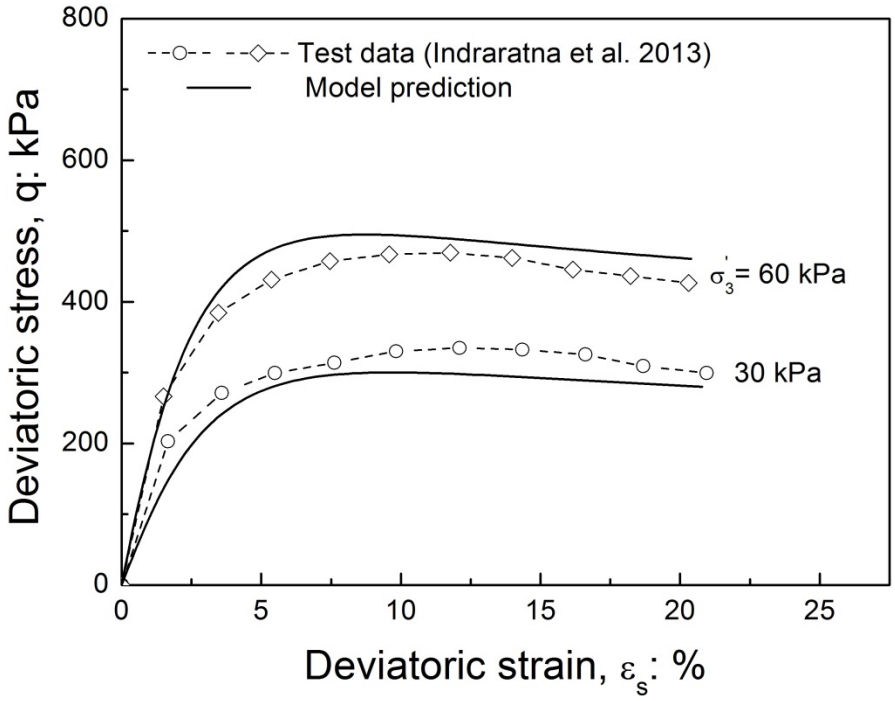

(a)

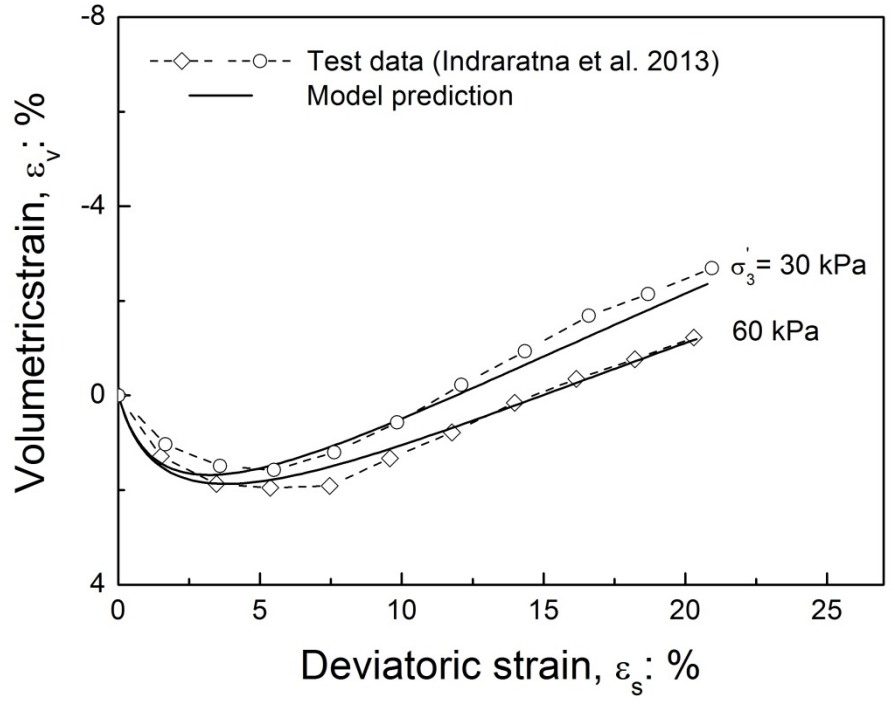

(b)

Figure 4.7 Model predictions compared with experimental results of drained triaxial shearing: (a) stress-strain response and (b) volume change behaviour (data sourced from Indraratna et al., 2013)

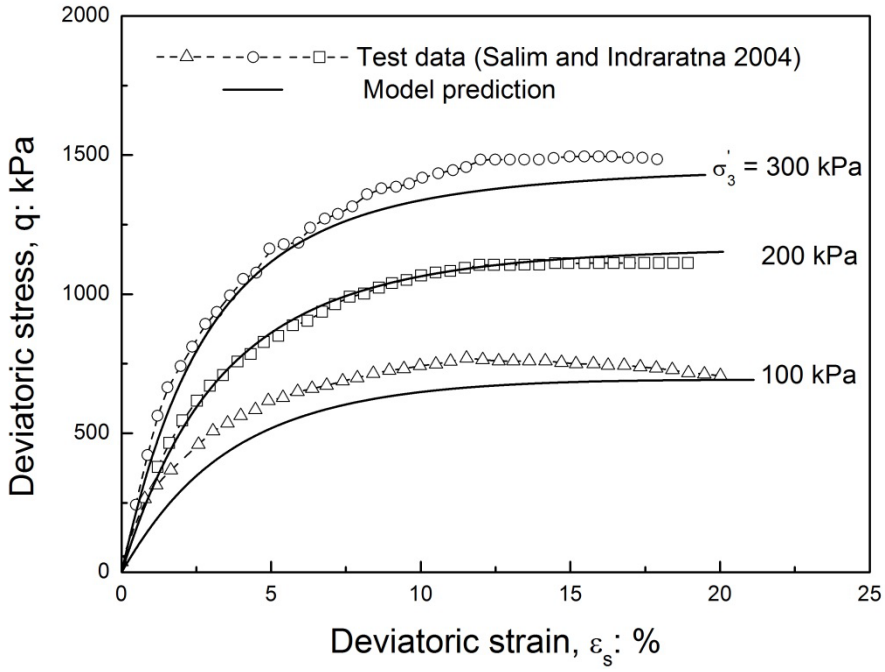

(a)

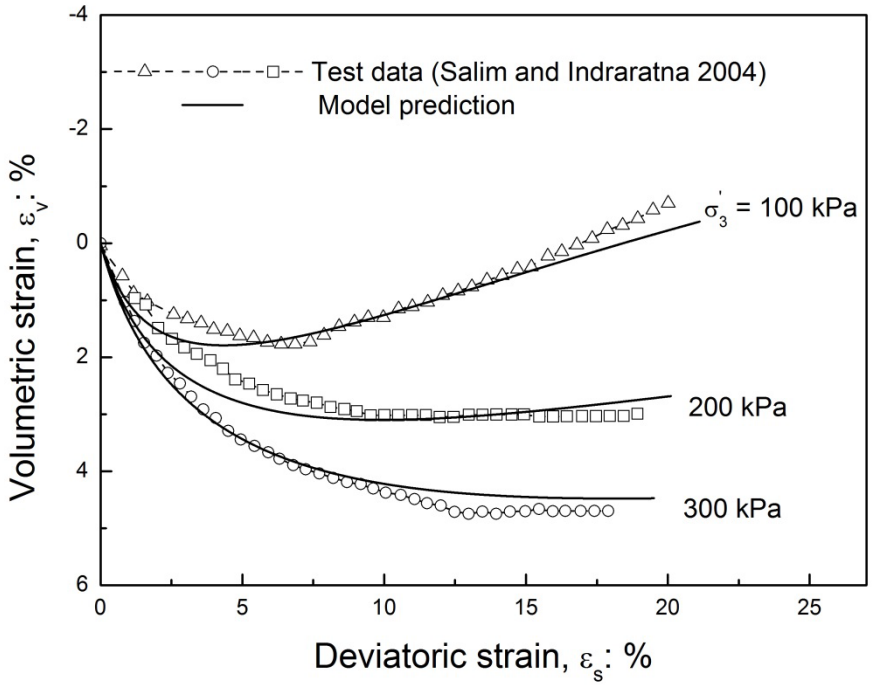

(b)

Figure 4.8 Model predictions compared with experimental results of drained triaxial shearing: (a) stress-strain response and (b) volume change behaviour (data sourced from Salim and Indraratna, 2004)

Comparisons of the observed and computed behaviour of ballast from Suiker et al. (2005) are shown in Figures 4.9(a and b). The peak strength and volumetric strains are reasonably well-represented by the model. It is evident that the analytical formulations of particle breakage and nonlinear critical state envelopes adopted in this study are appropriate. Figures 4.10(a and b) and 4.11(a and b) show the comparisons of drained triaxial compression tests from Anderson and Fair (2008) and Aursudkij et al. (2009). The stress-strain-volumetric behaviour is well-captured for both the specimens. As the studies by Suiker et al. (2005) and Anderson and Fair (2008) did not present the variation of particle breakage against axial strains, the same breakage parameters for latite basalt have been assumed in the analysis. This assumption did not hinder the accuracy of the model predictions as evident from Figures 4.9 and 4.10. This is because similar igneous parent rock types, namely basalt and granite, have been used by Suiker et al. (2005) and Anderson and Fair (2008), respectively.

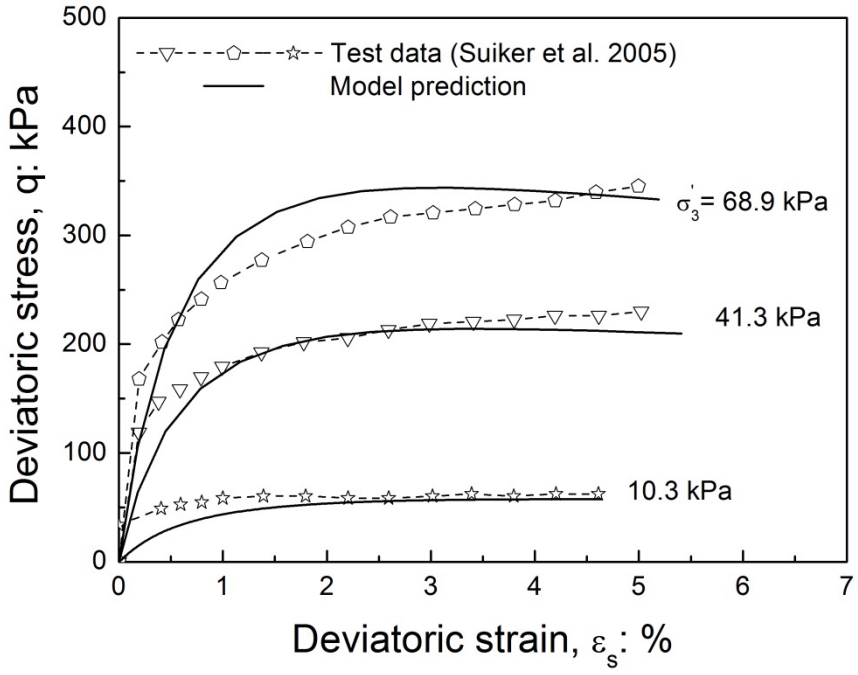

(a)

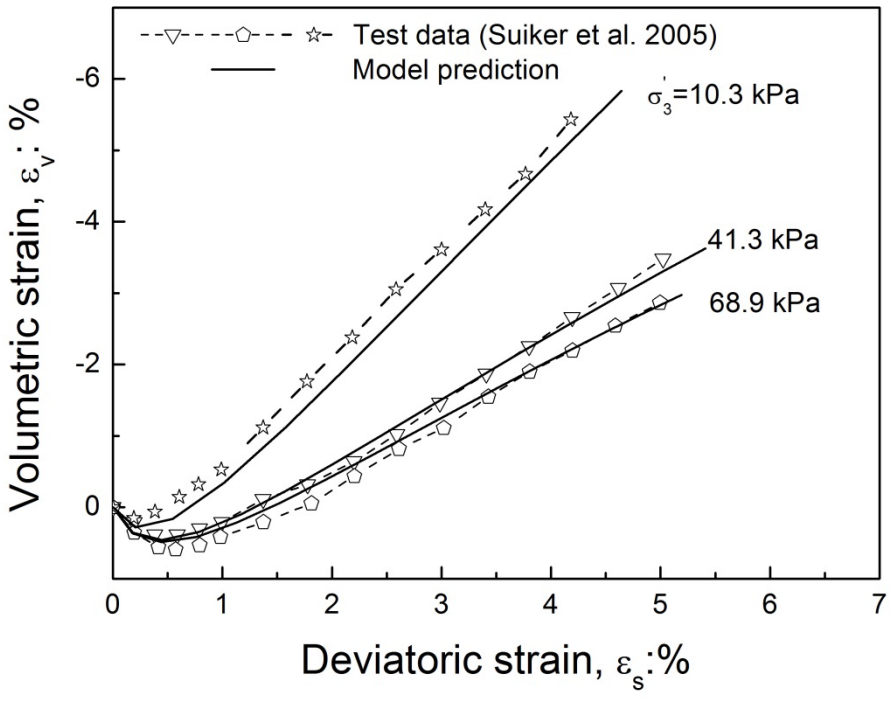

(b)

Figure 4.9 Model predictions compared with experimental results of drained triaxial shearing: (a) stress-strain response and (b) volume change behaviour (data sourced from Suiker et al., 2005)

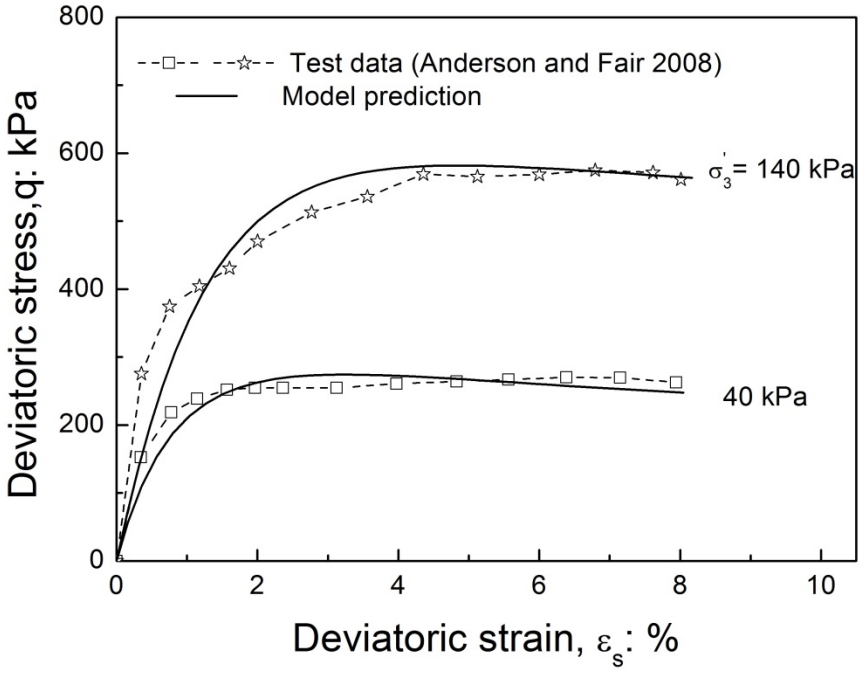

(a)

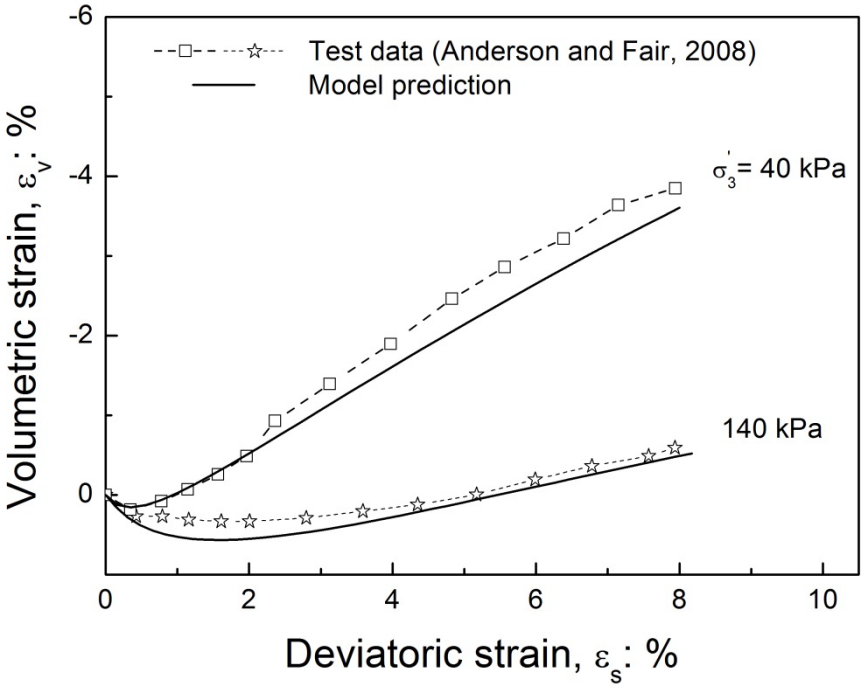

(b)

Figure 4.10 Model predictions compared with experimental results of drained triaxial shearing: (a) stress-strain response and (b) volume change behaviour (data sourced from Anderson and Fair, 2008)

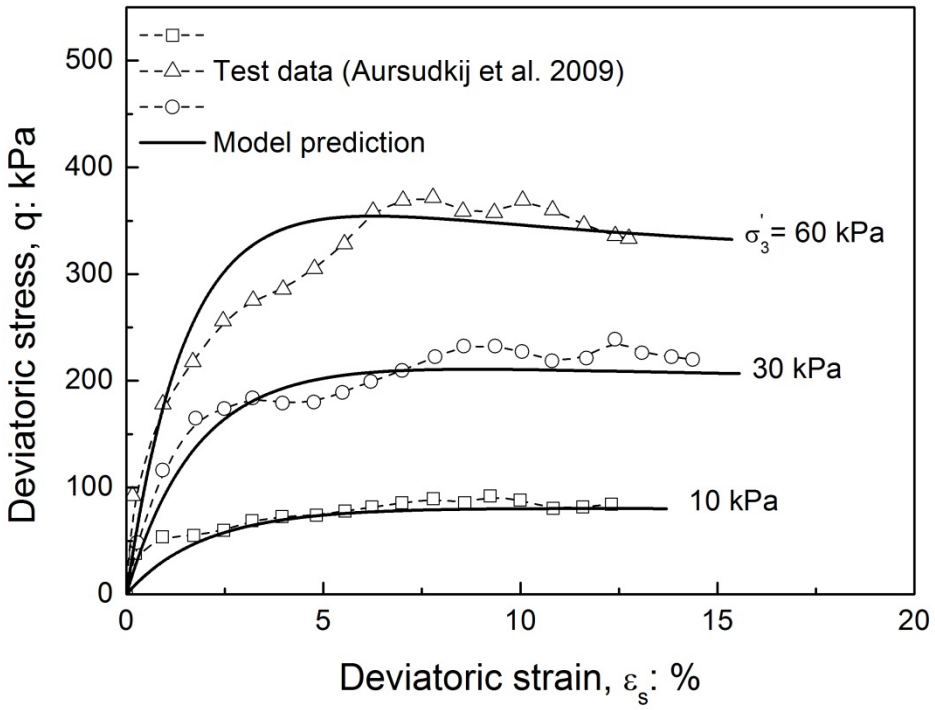

(a)

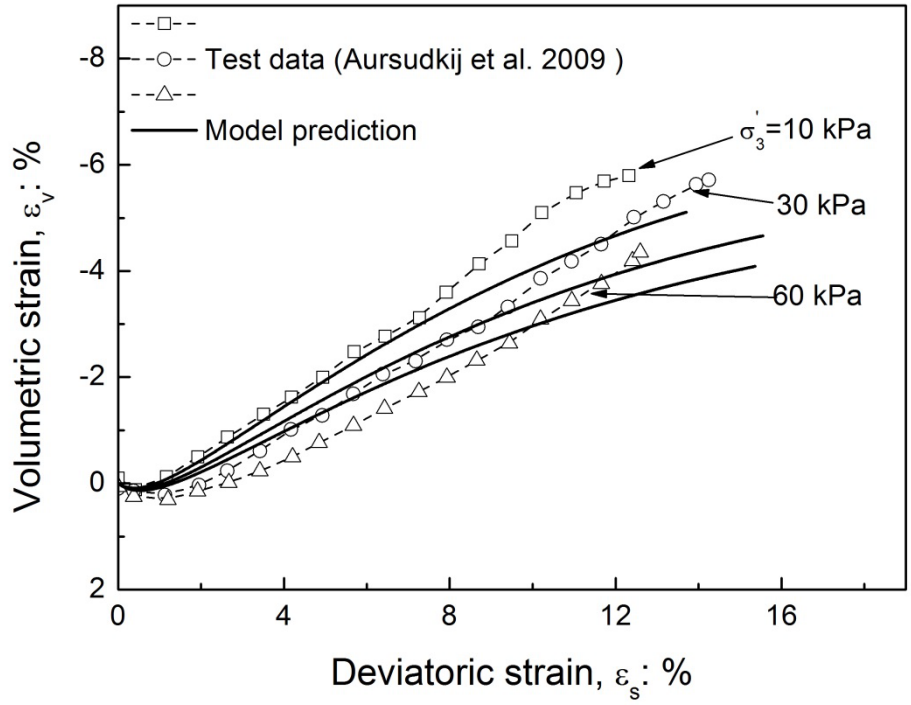

(b)

Figure 4.11 Model predictions compared with experimental results of drained triaxial shearing: (a) stress-strain response and (b) volume change behaviour (data sourced from Aursudkij et al., 2009)

The mechanical response of rockfill is largely dominated by particle breakage. The predictions of the stress-strain-volumetric behaviour for three rockfill materials (Varadarajan, et al., 2003; Chavez and Alonso, 2003) have been made by using the current model as shown in Figures 4.12, 4.13 and 4.14. The predicted and observed results are very close to each other for the selected materials. As such it may be concluded that the model provides satisfactory prediction of the stress-strain-volumetric change behaviour of the three rockfill materials.

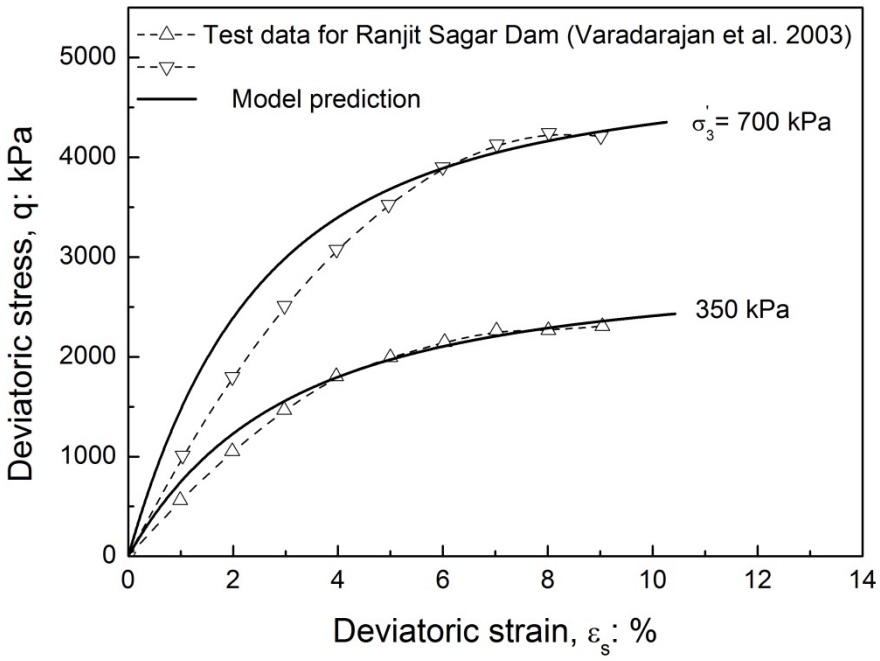

(a)

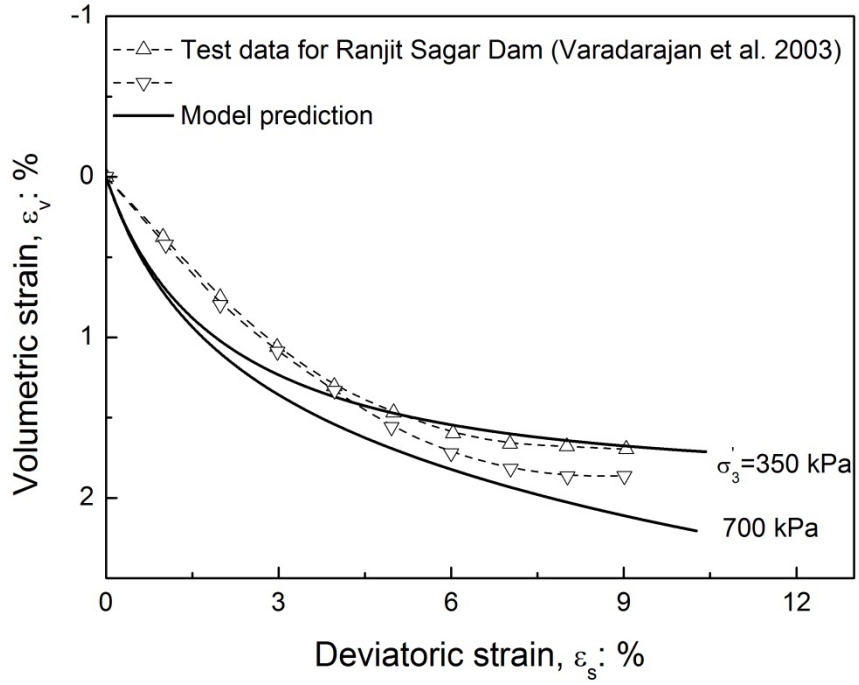

(b)

Figure 4.12 Model predictions compared with experimental results of drained triaxial shearing: (a) stress-strain response and (b) volume change behaviour (data sourced from Varadarajan et al., 2003)

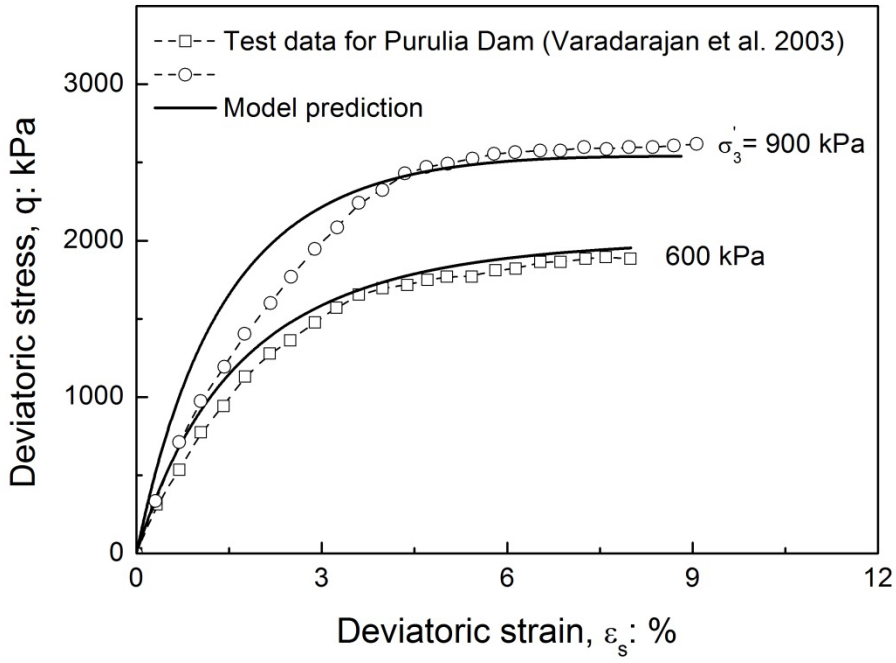

(a)

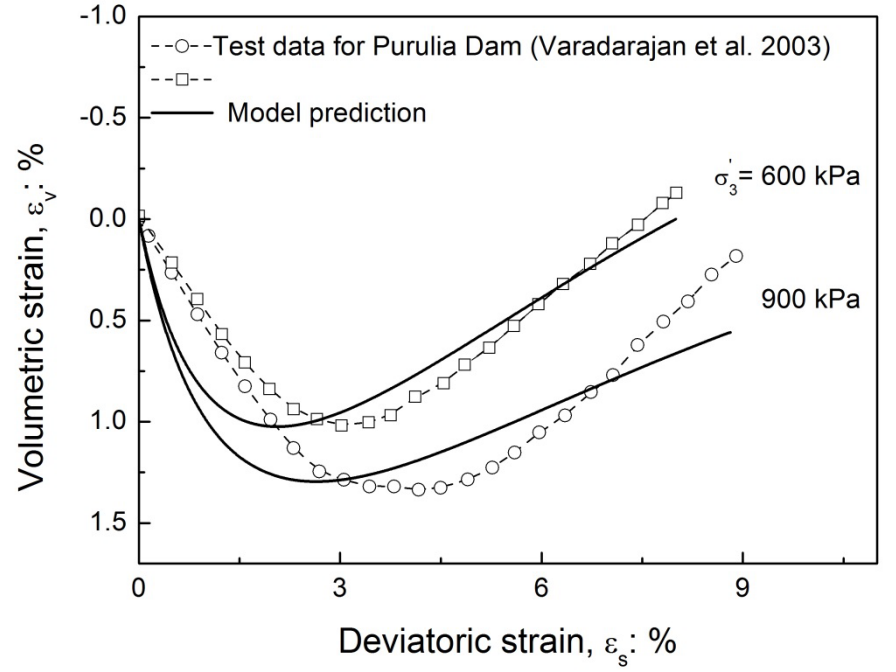

(b)

Figure 4.13 Model predictions compared with experimental results of drained triaxial shearing: (a) stress-strain response and (b) volume change behaviour (data sourced from Varadarajan et al., 2003)

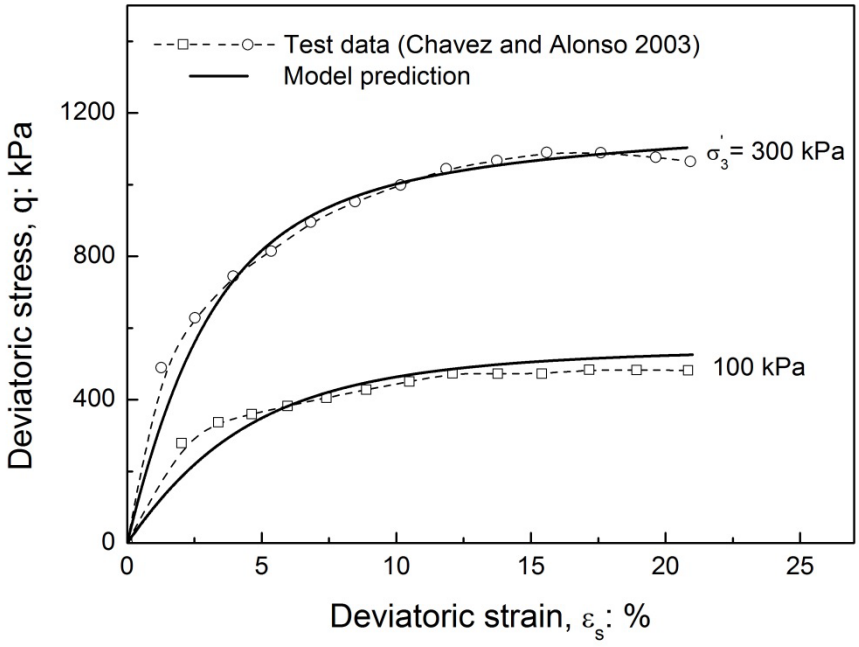

(a)

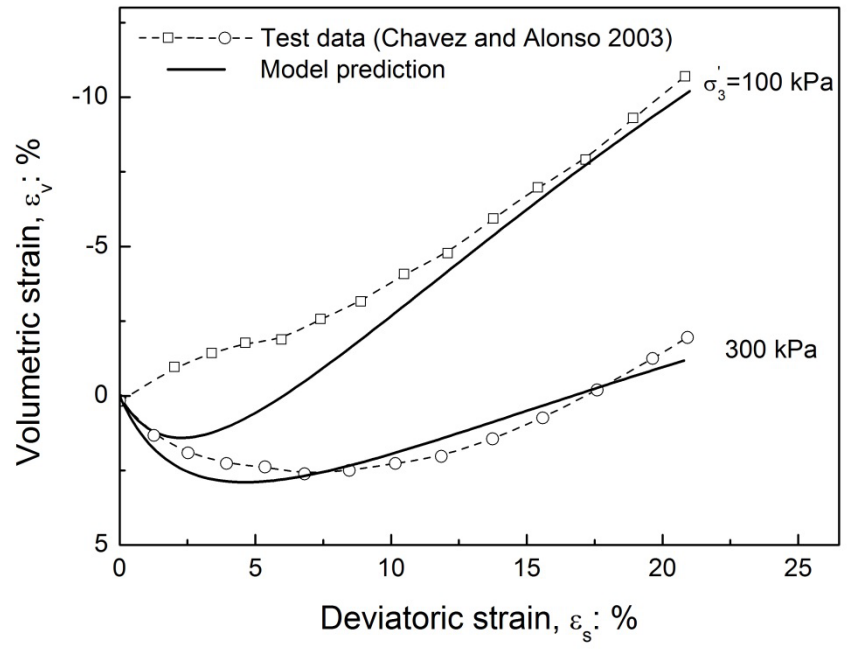

(b)

Figure 4.14 Model predictions compared with experimental results of drained triaxial shearing: (a) stress-strain response and (b) volume change behaviour (data sourced from Chavez and Alonso, 2003)

4.5 Cyclic Model for Ballast

The behaviour of ballast under repeated loading conditions is non-linear, stress-state dependent, and much different from the monotonic behaviour of ballast (Selig and Watters, 1994). Laboratory data for ballast under cyclic loading indicate that during the initial cycles, the axial strain develops rapidly and is partially recovered upon unloading, but each additional cycle contributes to incremental plastic or permanent strains. The magnitude of permanent axial strain increments decreases with the increasing number of cycles. When cyclic loads are applied, the effect of load history appears as a result of gradual material stiffening by each load application, leading to a reduction in the plastic axial strain during subsequent loading cycles.

The development of an accurate model with cyclic loading prediction capacity is essential for solving rail geotechnical problems especially for railway tracks under high speed trains. In the past, many models (Dafalias and Popov, 1975; Bardet, 1986; Manzari and Dafalias, 1997; Khalili et al., 2005) have been developed based on the bounding surface plasticity theory introduced by Dafalias and Popov (1975). These models can produce some of the essential features of granular materials under cyclic loading. However, none of these models can capture the effect of load frequency on the densification and dilation of the materials.

The objective of this section is to extend the static model proposed previously to capture high-frequency cyclic loading response. By applying the bounding surface plasticity theory and having additional experimental-based assumptions on the calculations of the hardening modulus under different loading conditions, the new model is able to produce some of the essential characteristics of ballast under cyclic loading conditions.

4.5.1 Basic Equations in Triaxial Stress Space

The elastic strain increments can be calculated by:

$$d\varepsilon_v^e = \frac{\kappa}{1+e_i}\frac{dp'}{p_i'} \tag{4.16}$$

$$d\varepsilon_s^e = \frac{dq}{3G} \tag{4.17}$$

where $d\varepsilon_v^e$ and $d\varepsilon_s^e$ are incremental elastic volumetric and deviatoric strains, κ is the swelling/recompression constant, e_i is initial void ratio at the start of shearing, and p_i' is the initial effective mean stress. G is the elastic shear modulus that is expressed as:

$$G = \frac{3(1-2\nu)}{2(1+\nu)}\frac{1+e_i}{\kappa}p_i' \tag{4.18}$$

where ν is the Poisson's ratio.

The plastic strain increments are given by:

$$d\varepsilon_s^p = \frac{p'd\eta}{H_C}$$

(4.19)

$$d\varepsilon_v^p = D_C\left|d\varepsilon_s^p\right| \tag{4.20}$$

where $d\varepsilon_s^p$ and $d\varepsilon_v^p$ are incremental plastic deviatoric and volumetric strains, η is stress ratio, H_C is plastic hardening modulus under cyclic loading, D_C is dilatancy under cyclic loading condition.

4.5.2 Loading Surfaces in Triaxial Stress Space

The basic requirement for a cyclic model is that it can describe the response under both monotonic and cyclic loading conditions (i.e. a model which can describe reverse as well as forward loading). Thus, a stress ratio quantity m is introduced into the yield surface (Equation (4.6)) to satisfy this purpose (Manzari and Dafalias, 1997):

$$f = \eta - \eta_s \mp m = 0 \tag{4.21}$$

where $\eta = q/p'$, the scalars m and η_s are tangents of angles related to the opening and the location of the bisector of the yield surface, respectively. Isotropic hardening is neglected by considering m as constant; the kinematic hardening is incorporated via the evolution of η_s. For η inside the wedge only elastic strain is induced by $d\eta \neq 0$. When η satisfies Equation (4.21) and $d\eta$ points 'outward' from the yield surface, i.e., $d\eta > 0$ for loading and $d\eta < 0$ for unloading, plasticity occurs according to Equation (4.19) and (4.20).

Besides the yield surface, this model incorporates the use of three more surfaces: the critical state, bounding and dilatancy surfaces as shown in Figure 4.15. Their shape for triaxial compression is uniquely defined by slopes, M_c, M_p and M_d, respectively. M_p and M_d are continuous functions of M_c and the ever-changing value of the state parameter ψ as given by Equations (4.8) and (4.11), separately.

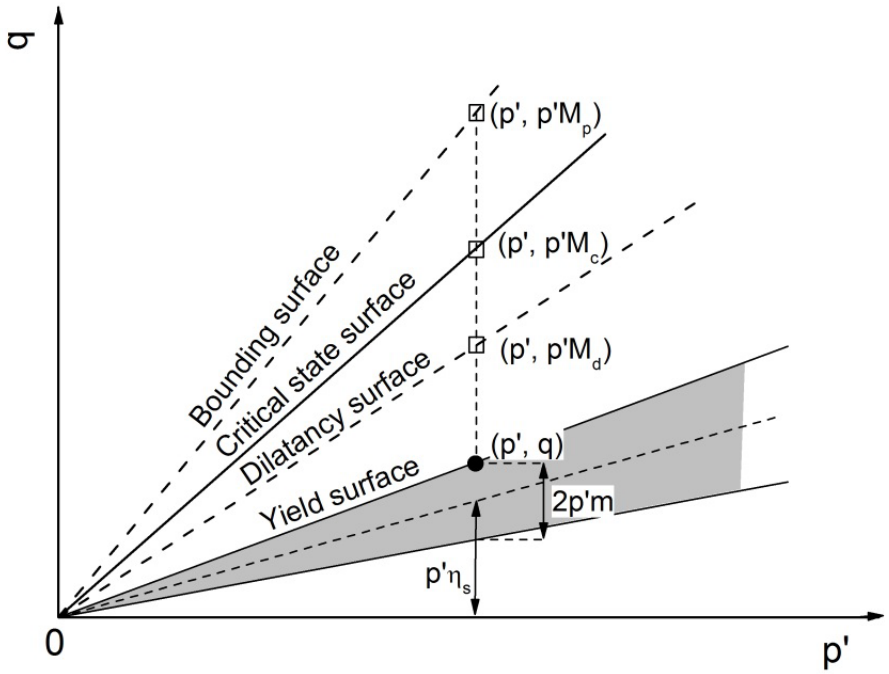

Figure 4.15 Schematic of the yield, critical, dilatancy, and bounding lines in *q*-*p'* space

4.5.3 Cyclic Plastic Modulus

Following the basic concepts of bounding surface plasticity theory (Dafalias and Popov, 1975), the following plastic modulus H_C is proposed, which depends on the 'distance' (M_p - η) in the stress-ratio space.

$$H_C = p' H_f H_k h_0 \left|\eta - \eta_{in}\right| \left(M_p - \eta\right) \tag{4.22}$$

where h_0 is a model parameter, η_{in} is the value of η at initiation of a loading process. The scalar parameters h_0, p', H_f, H_k are non-negative, so that the sign of H is governed by the sign of ($M_p - \eta$).

The scalar function H_f in Equation (4.22) is used to capture the effect of frequency f on the plastic modulus H_C and, in turn, on both the deviatoric and volumetric components of plastic strain. In particular, H_f is defined as:

$$H_f = \frac{p_i'}{\exp\left(\alpha_f \cdot f\right)} \tag{4.23}$$

where α_f is the model parameter.

It is well known that shakedown is an intrinsic property of granular material and is exhibited under repeated loading conditions. Once the material attains shakedown, there is no more accumulation of plastic strain. The scalar parameter H_k is proposed to control the shakedown behaviour of ballast:

$$H_k = \left(1 + \varepsilon_{s0}^p\right)^k \tag{4.24}$$

where ε_{s0}^p is the accumulated plastic deviatoric strain at the current state. k is a model parameter, and it is believed that k is dependent upon a number of factors, which include the initial void ratio, the stress history as well as the current stress level of the ballast. It is noteworthy that three different deformation mechanisms were observed for ballast in response to $q_{max,cyc}$, f and σ_3', namely, plastic shakedown, plastic shakedown and ratcheting and plastic collapse. For simplicity, only shakedown property is reflected in this study.

If m is fixed, it follows from Equation (4.21) that $df = d\eta - d\eta_s = 0$, thus, one obtains hardening law from Equation (4.19) and (4.22) that:

$$d\eta_s = H_f H_k h_0 \left|\eta - \eta_{in}\right| \left(M_p - \eta\right) d\varepsilon_s^p \tag{4.25}$$

If loading reversal occurs from $\eta=\eta_s+m$, Equation (4.21) determines that at $\eta=\eta_s-m$, $d\eta < 0$ will induce plastic deformation in the reverse sense according to Equation (4.19), hence, Equation (4.22) needs to be appropriately modified. A corresponding bounding

stress ratio M_p in extension can be defined and it is assumed to be identical to M_p in compression, so that instead of (M_p–η) one has (M_p+η), which measures the distance of η from M_p in extension. Simultaneously, η_{in} is updated to the value of η at the point of reversal. Thus, while during loading with $d\eta > 0$ one has $H_C=p'H_fH_kh_0|\eta-\eta_{in}|(M_p-\eta)$, for reverse loading with $d\eta < 0$ it changes to $H_C =p'H_fH_kh_0|\eta-\eta_{in}|(M_p+\eta)$.

4.5.4 Cyclic Dilatancy

Based on large-scale monotonic triaxial test data, a state dependent dilatancy relationship for ballast was proposed as Equation (4.10), which can accurately capture the dilatancy behaviour under monotonic loading. However, the dilatancy is different for ballast under high frequency cyclic loading from the one under monotonic loading. At a relatively lower level of confining pressure, the specimens could experience an overall volumetric dilation when frequency is also low (Figure 3.11(b)). As there is an increase of frequency, the particle breakage increases, which results in a reduction of the void ratio and a subsequent increase in compressibility. Hence, the following relationship is proposed for ballast to consider the dilatancy behaviour under high frequency cyclic loading:

$$D_C = \frac{d\varepsilon_v^p}{d\varepsilon_s^p} = A_d\left[\left(1 + d_f \cdot f\right)\cdot M_d - \eta\right] \tag{4.26}$$

where A_d is dilatancy parameter, and d_f is a model parameter reflecting the effect of frequency on dilatancy. Similar to the cyclic hardening modulus, when loading reversal is considered, a corresponding M_p in extension is introduced, such that Equation (4.26) reads $D_C=A_d[(1+d_f\cdot f)M_d+\eta]$. The concept of introducing a bounding stress ratio in extension is similar to the one addressed in Manzari and Dafalias (1997), where the

different values of M_p were used for compression and extension, respectively.

4.5.5 Parametric Study

For simplicity, the effect of particle breakage on the cyclic response of ballast is not considered here. There are six additional parameters introduced in the cyclic model compared with the monotonic model proposed earlier in this chapter. They are κ, m, h_0, α_f, k and d_f. The roles of each of the parameters are listed in Table 4.2 below:

Table 4.2 New parameters introduced in the cyclic model

Parameter	Role
κ	Swelling/recompression constant
m	Isotropic hardening parameter
h_0	Hardening parameter controlling the slope of the stress-strain curve
k	Controlling the rate at which shakedown occurs
α_f	Capturing the effect of frequency on the plastic modulus
d_f	Reflecting the effect of frequency on dilatancy

The parameter κ can be determined from the isotropic (hydrostatic) loading-unloading with complete drainage and measuring the volume change of the specimen. The slope of the unloading part of the *e-lnp'* plot is κ. For the material used in this study, the value of κ can be obtained in the study (Salim and Indraratna, 2004) as 0.007. Only kinematic hardening is considered, hence, a constant m (no isotropic hardening) is usually set equal to about $0.05M_c$ as suggested by Manzari and Dafalias (1997). Values of h_0, k, α_f

and d_f can be obtained by a trial-and-error procedure. By comparison of the model prediction with experimental data, the values of these parameters can be easily obtained within the first three trials.

To investigate the effect of the parameters (h_0, k, α_f and d_f) on the performance of the model, a set of drained cyclic triaxial tests was analysed. The cell pressure was kept constant at 30 kPa while a deviatoric stress of 230 kPa was loaded and then unloaded back to 45 kPa (one way cyclic loading). The load frequency is used as 20 Hz.

The model parameters relevant to ballast used in this parametric study are listed in Table 4.1. Three out of the four new parameters were kept constant in each of the studies. The fourth parameter was varied so that its effect on the model's performance could be seen. The ranges over which the new parameters vary were chosen so that they would clearly affect the performance of the model for its particular ballast.

(1) Effect of h_0 (k=25, α_f=0.1 and d_f=0.08)

Figures 4.16-4.18 show the effect h_0 has on the performance of the cyclic model. This parameter is used to control the magnitude of the strains. The smaller the value of h_0, the more permanent strains (both deviatoric and volumetric) the model will produce. This can be explained as follows: a bigger value of h_0 leads to the ballast being softer during loading and unloading and hence, larger amounts of strains are recovered.

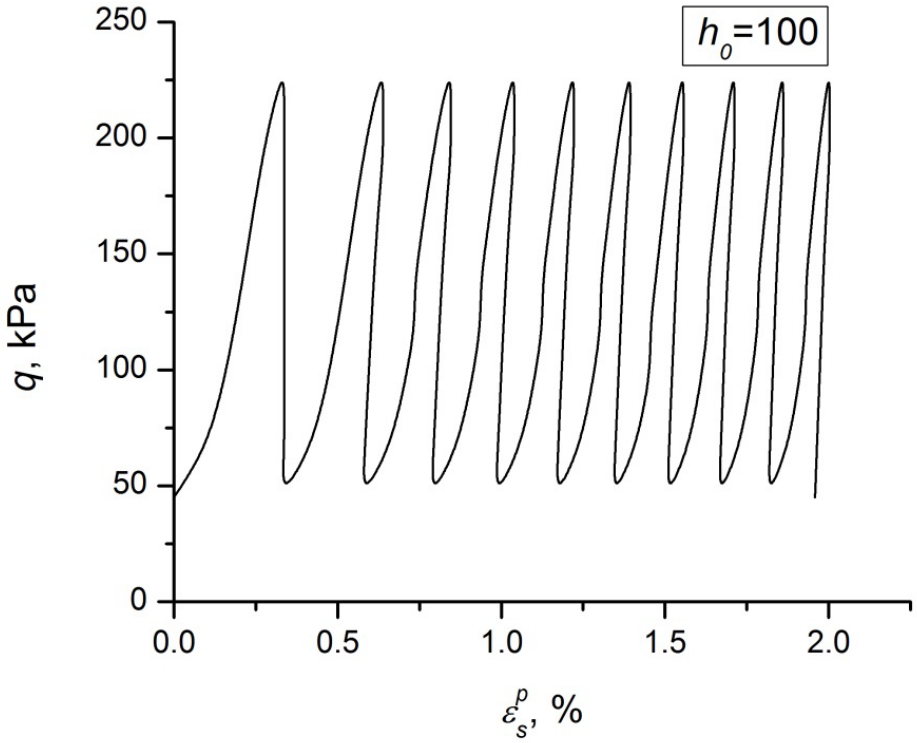

(a)

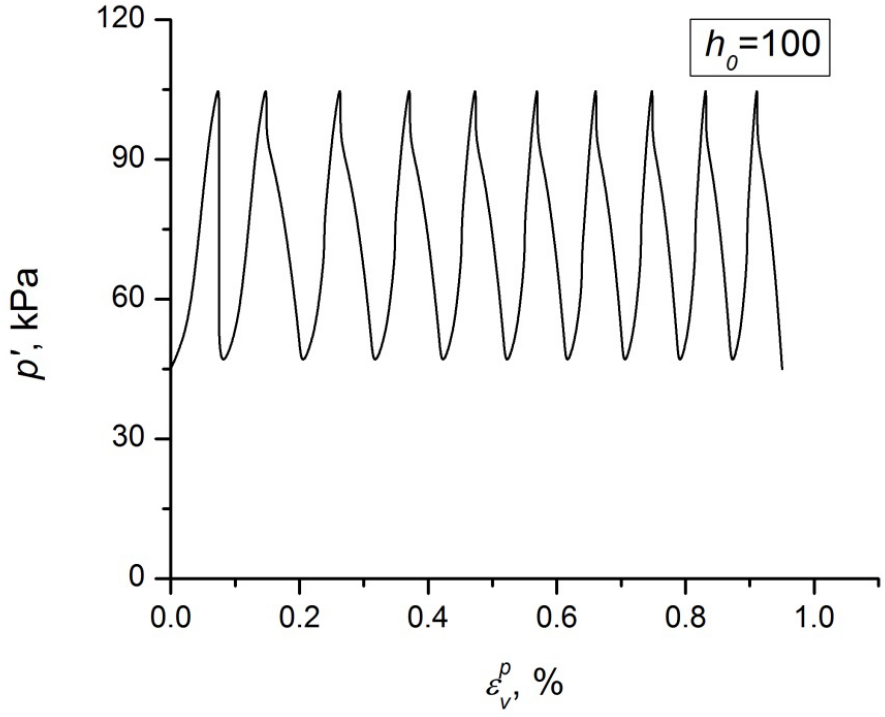

(b)

Figure 4.16 Stress-strain response at h_0=100

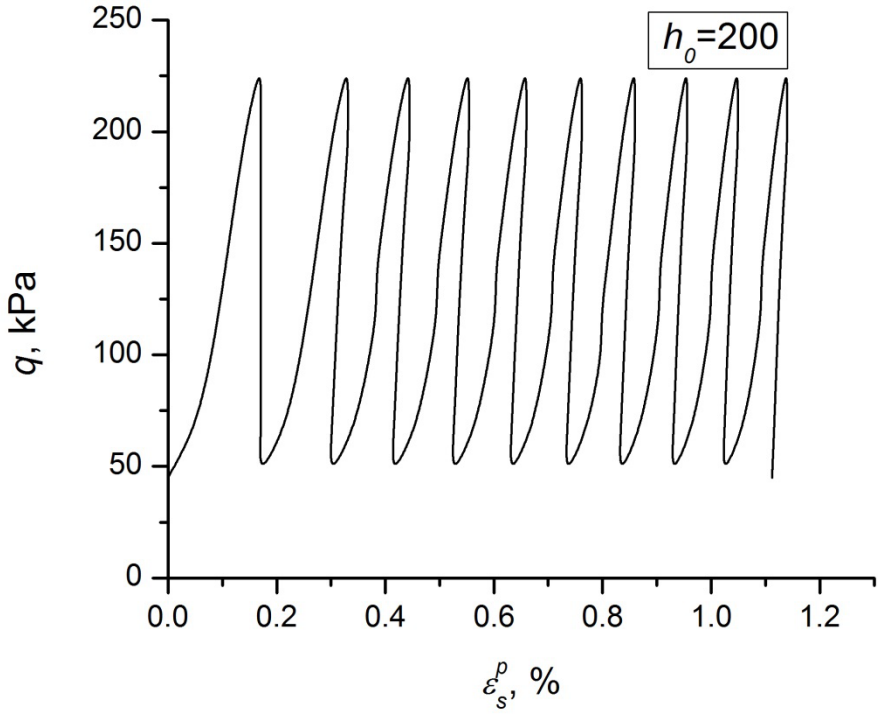

(a)

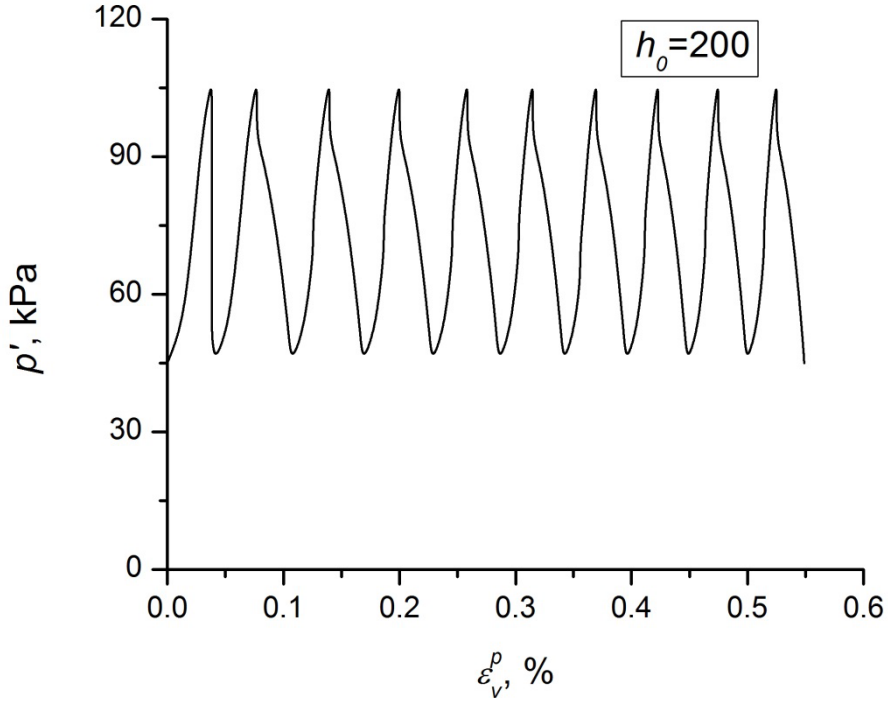

(b)

Figure 4.17 Stress-strain response at h_0=200

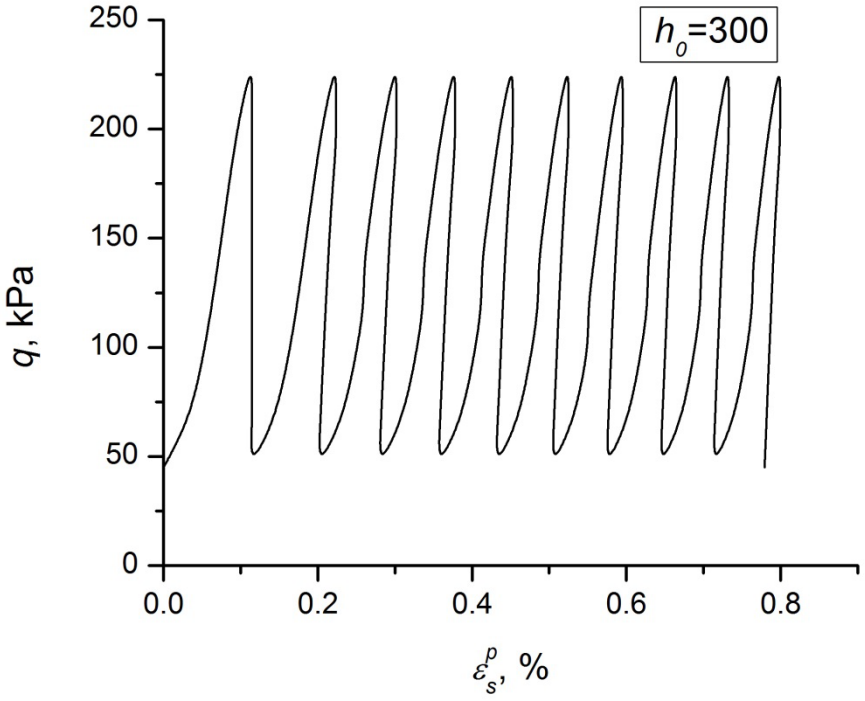

(a)

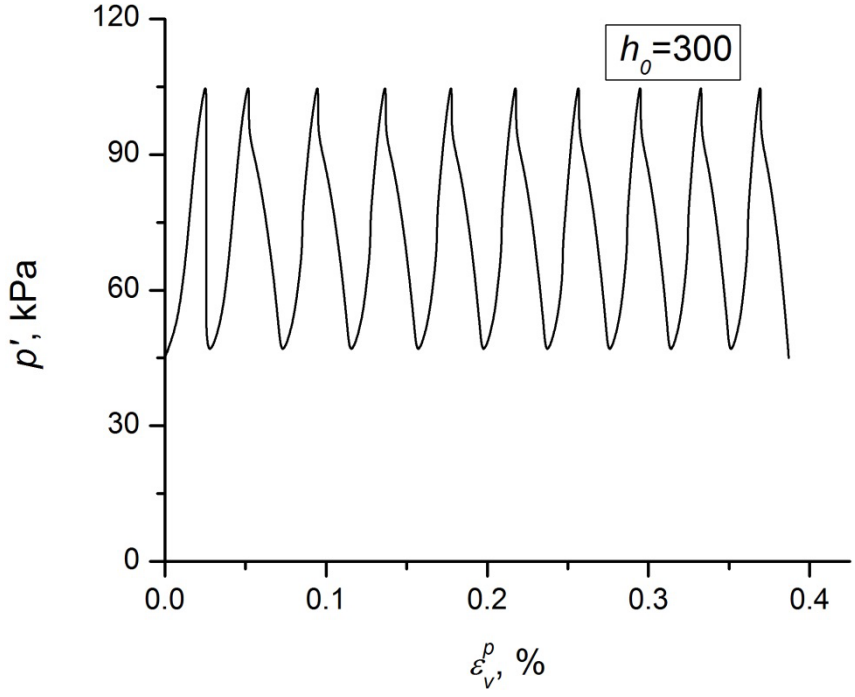

(b)

Figure 4.18 Stress-strain response at h_0=300

(2) effect of k (h_0=200, α_f=0.1 and d_f=0.08)

k is the parameter that controls the rate at which shakedown behavior of the ballast occurs. Figures 4.19-4.21 show the results where the values of k were assumed. It can be seen that a bigger value of k will make the ballast shakedown faster. This can be easily explained by looking at Equation (4.24): a bigger value of k will make the ballast become harder during loading and unloading. Also, the ballast becomes harder faster if the plastic deviatoric strain is bigger. As a result of all these, less strain and shakedown behaviour occurs.

It is to be noted that k depends upon many factors, its value is expected to be very much different from one ballast specimen to another as well as from one analysis to another. A more comprehensive investigation of this parameter is needed in future studies.

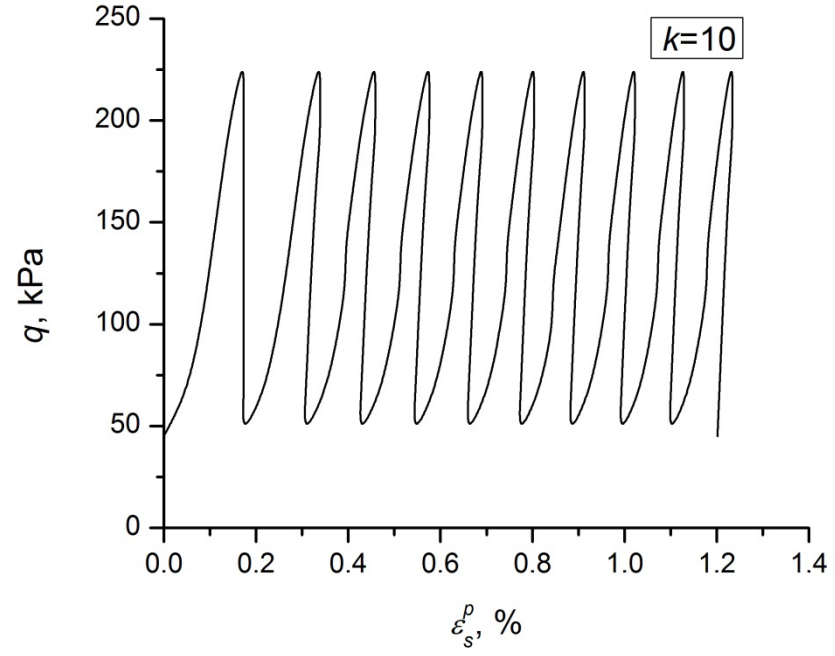

(a)

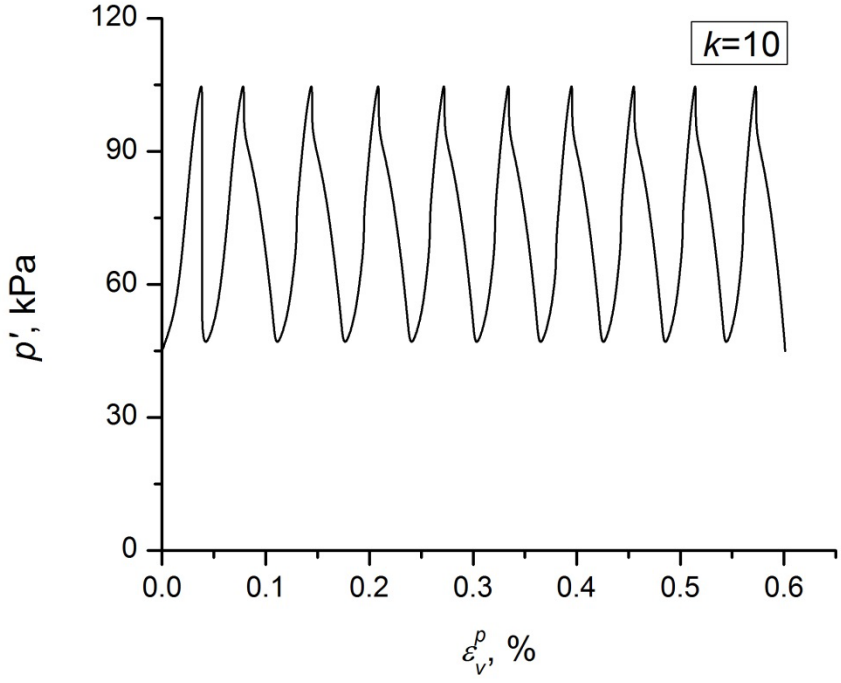

(b)

Figure 4.19 Stress-strain response at k=10

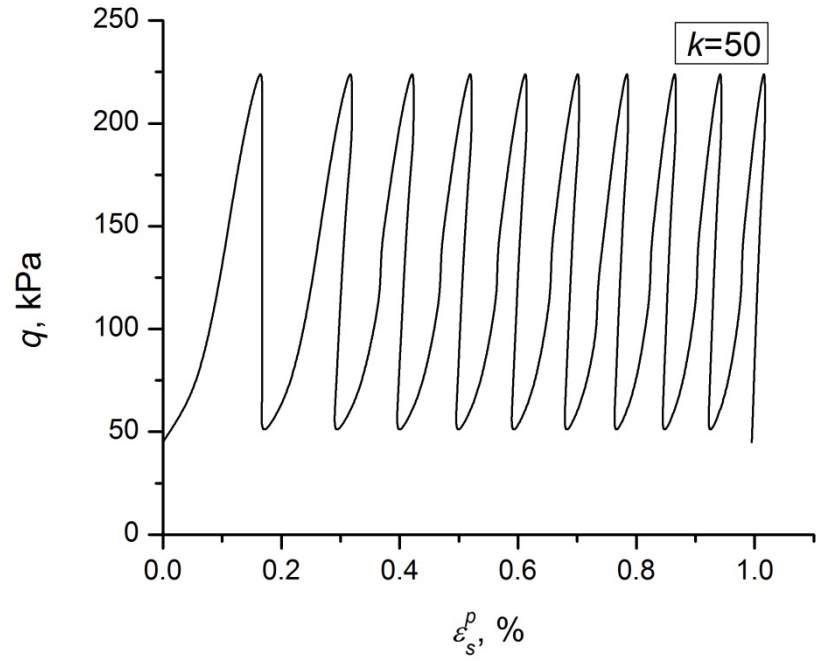

(a)

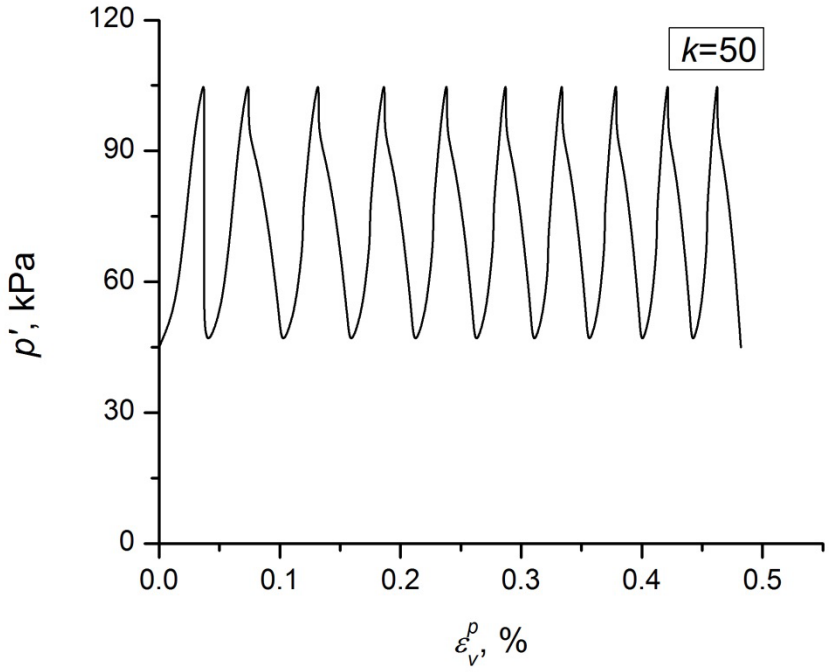

(b)

Figure 4.20 Stress-strain response at k=50

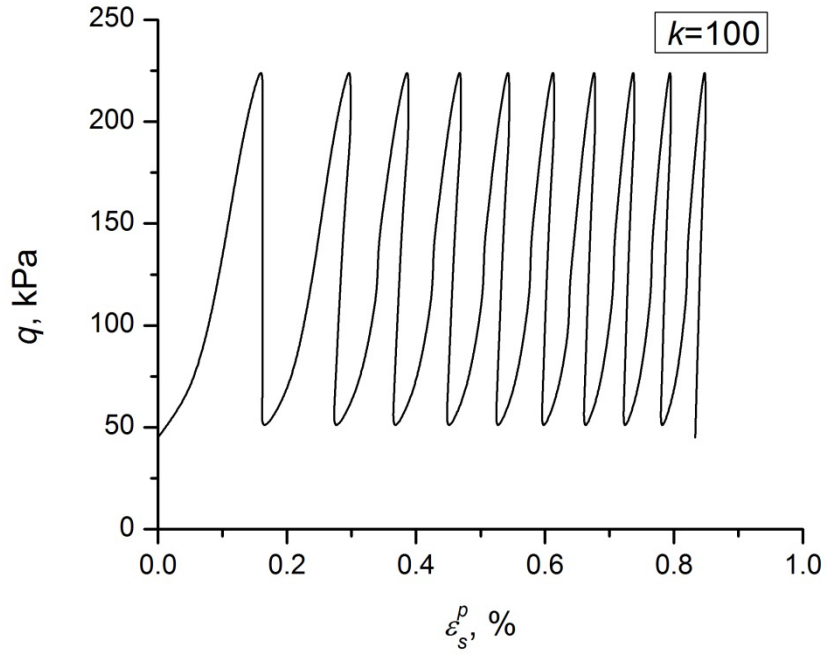

(a)

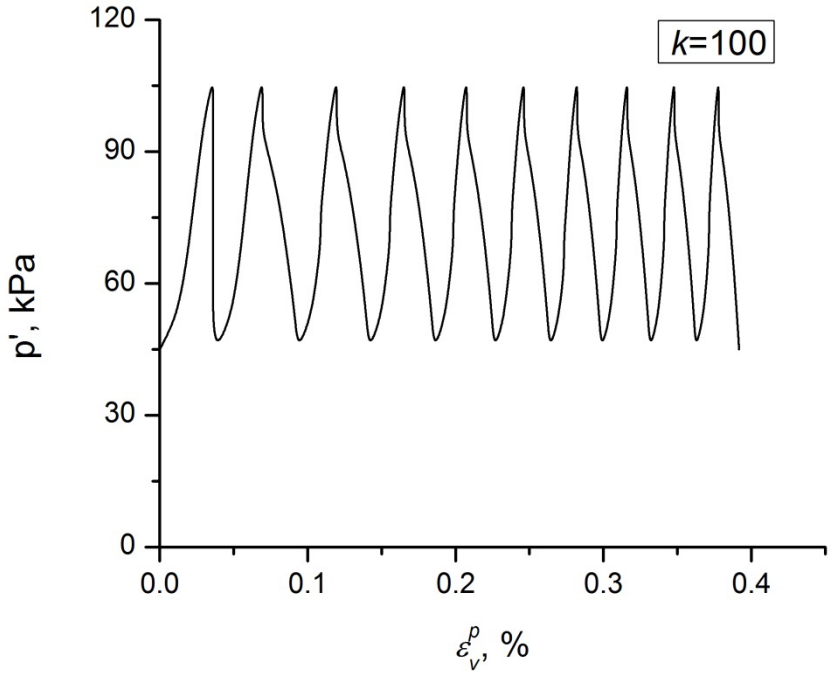

(b)

Figure 4.21 Stress-strain response at *k*=100

(3) Effect of α_f (h_0=200, k=25 and d_f=0.08)

The effect of the parameter α_f is investigated, where it is used to control the effect of load frequency on both plastic deviatoric and volumetric strain components. It can be seen in Figures 4.22-4.24 that permanent strains (both deviatoric and volumetric) increase as the value of α_f increases. It can be concluded that the higher the load frequency, the larger the plastic strains produced by the model.

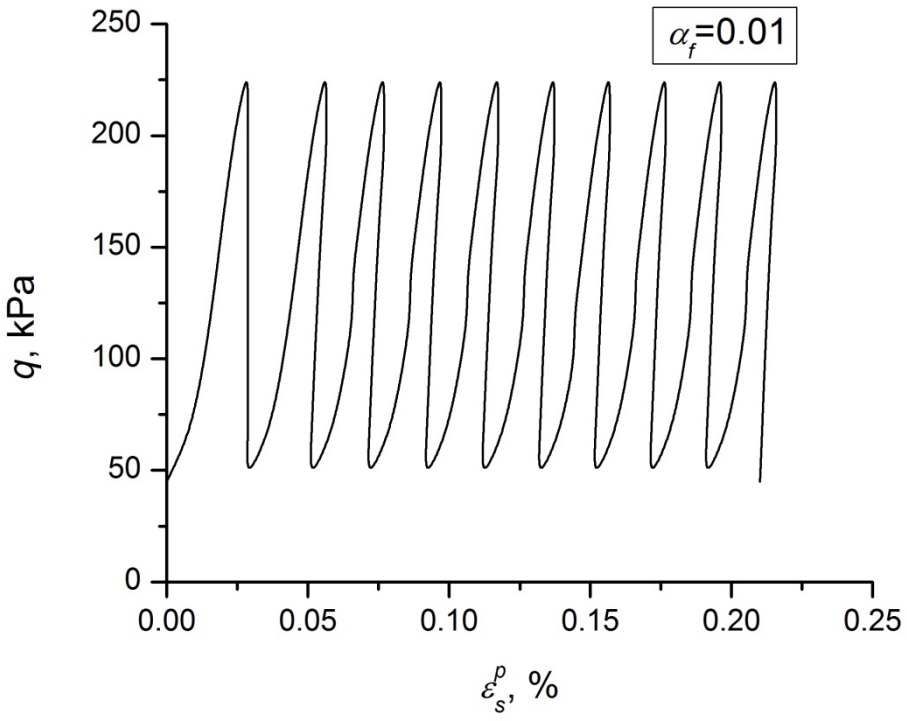

(a)

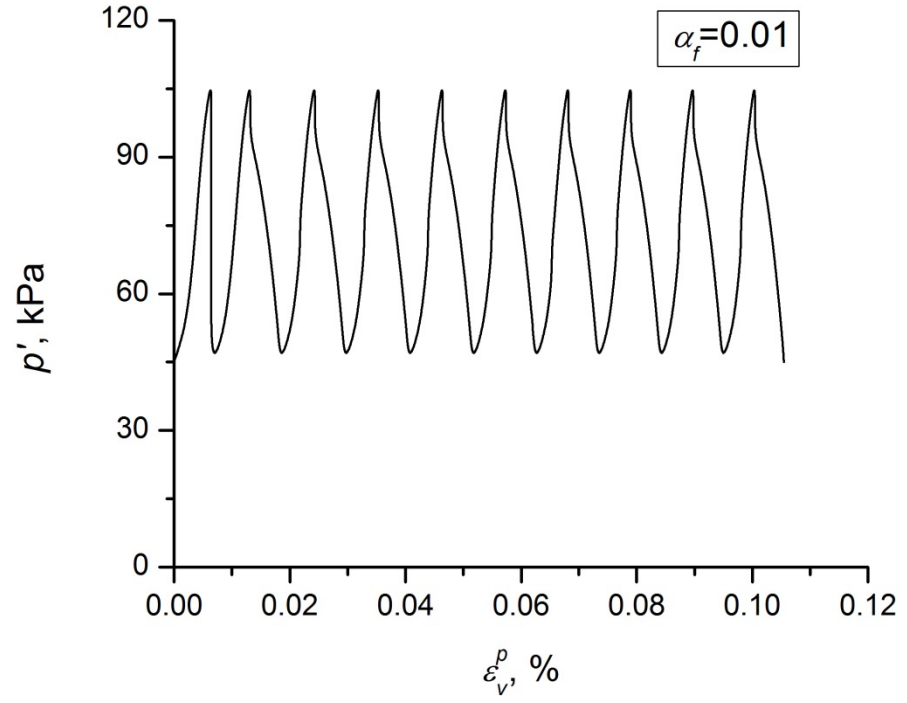

(b)

Figure 4.22 Stress-strain response at α_f=0.01

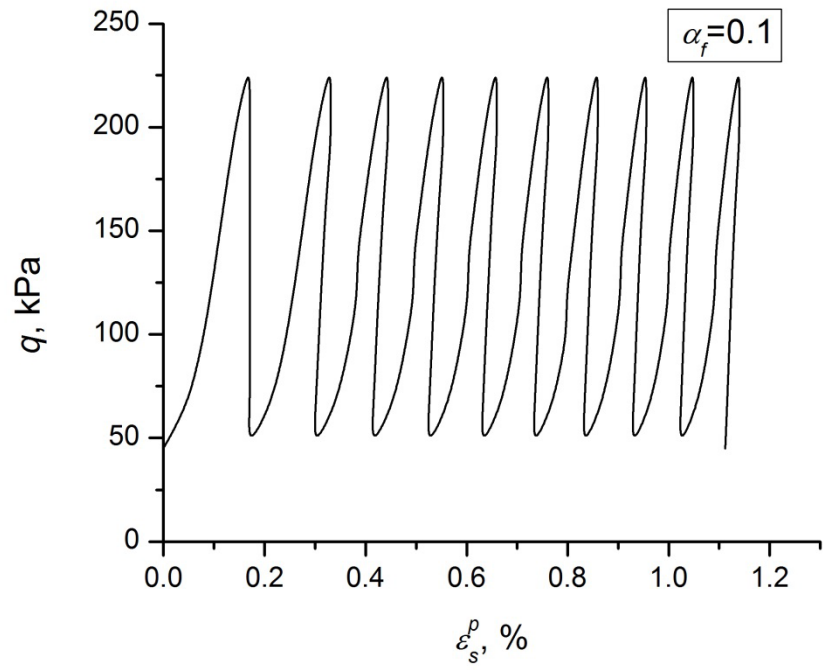

(a)

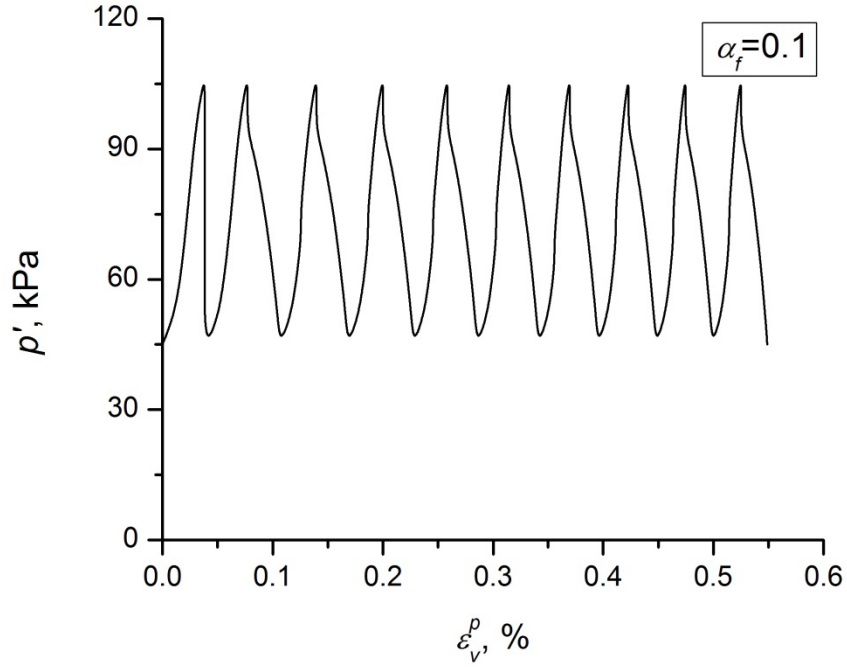

(b)

Figure 4.23 Stress-strain response at α_f=0.1

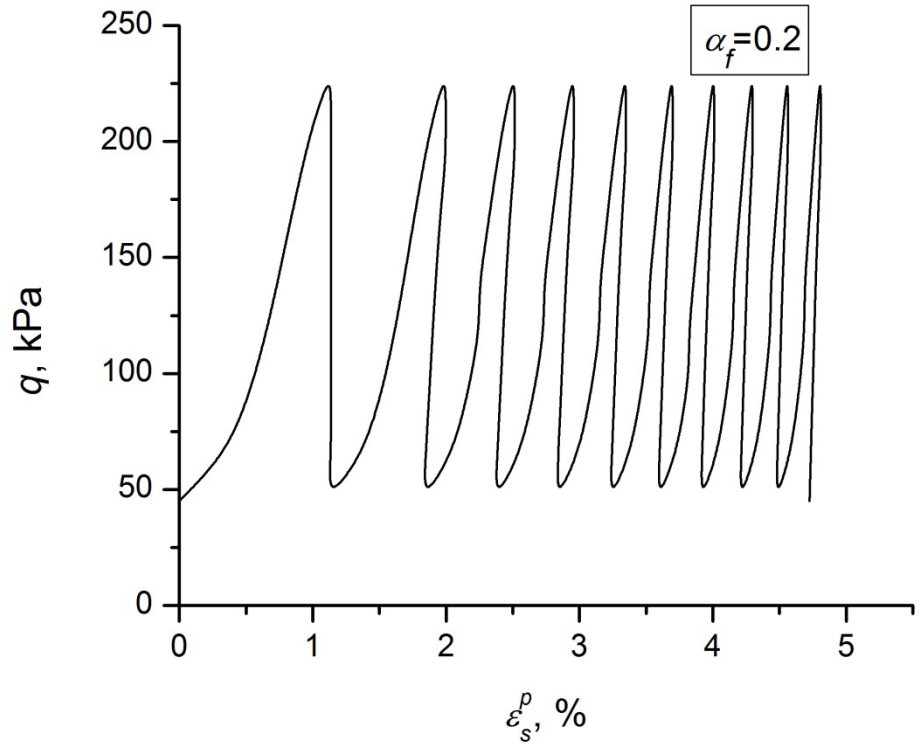

(a)

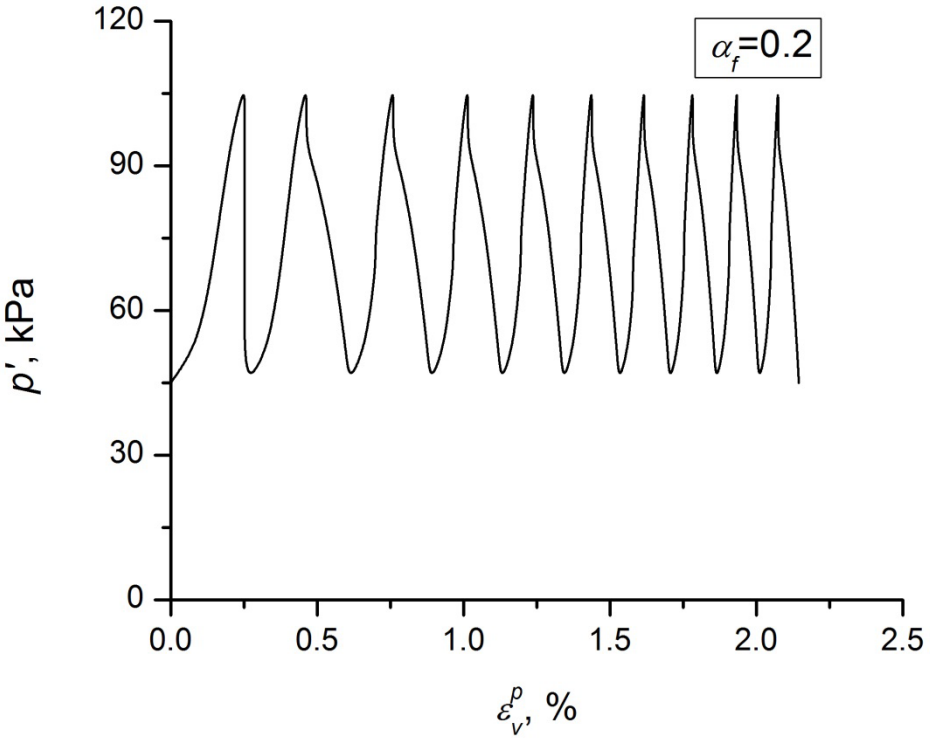

(b)

Figure 4.24 Stress-strain response at α_f=0.2

(4) Effect of d_f (h_0=200, α_f=0.1 and d_f=0.08)

Figures 4.25-4.27 show the effect of d_f on the performance of the model. This parameter is used to reflect the effect of the frequency on the dilatancy of ballast. The parameter d_f has no effect on deviatoric strain prediction of the model. It is shown in Figure 4.25 that when the value of d_f is small, the plastic volumetric strain prediction is dilation in the initial loading cycles and then compression in the following load cycles. As the value of d_f increases, the plastic volumetric strain prediction becomes compression (as shown in Figure 4.26 and 4.27). Cyclic triaxial tests data given earlier in Chapter 3 showed that at relatively lower frequency, the ballast specimens experienced dilation. As the frequency increased, the ballast response became compression. This model can properly reflect this behaviour of ballast.

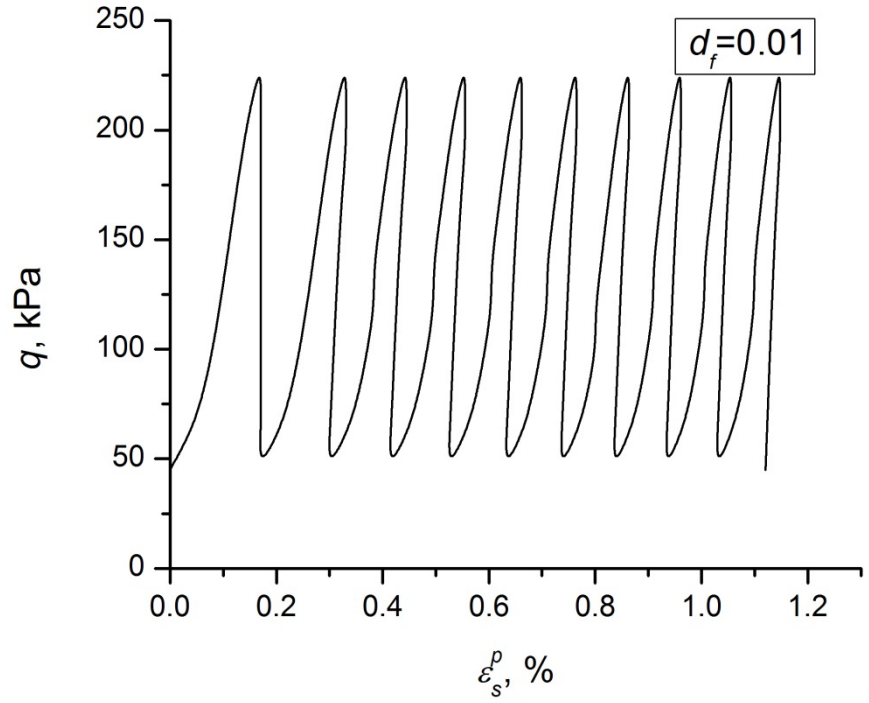

(a)

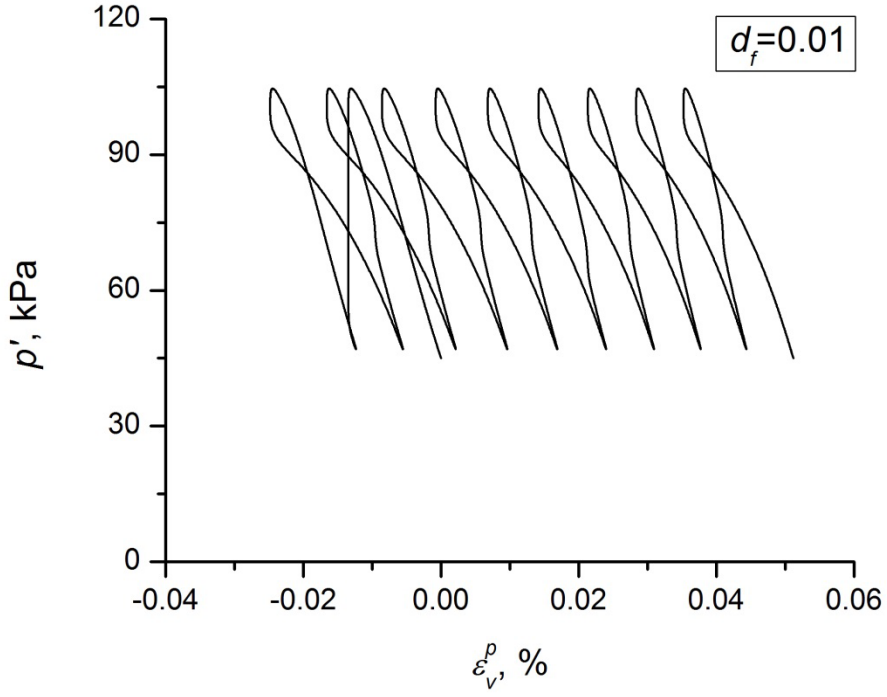

(b)

Figure 4.25 Stress-strain response at d_f=0.01

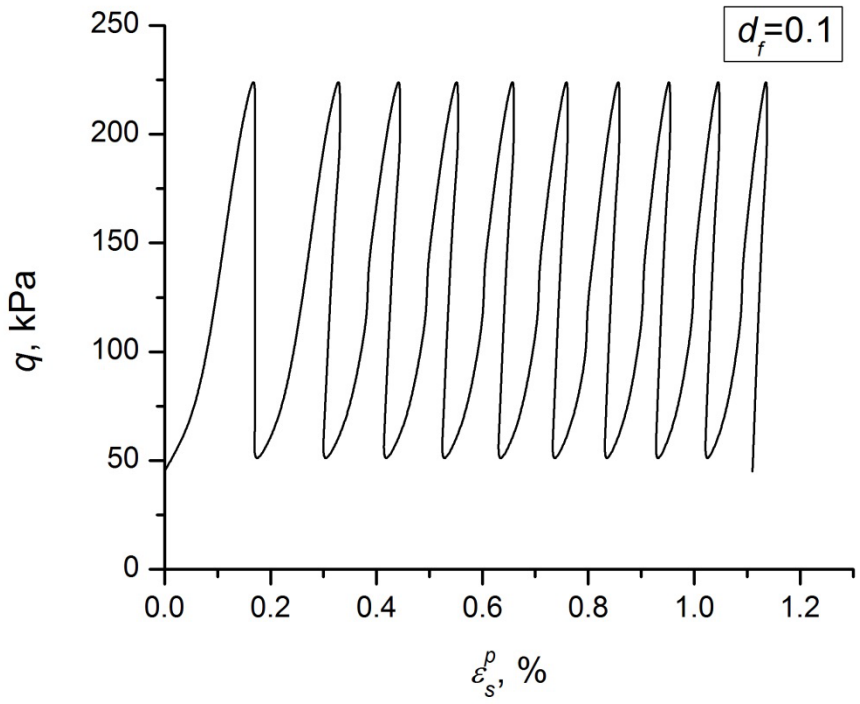

(a)

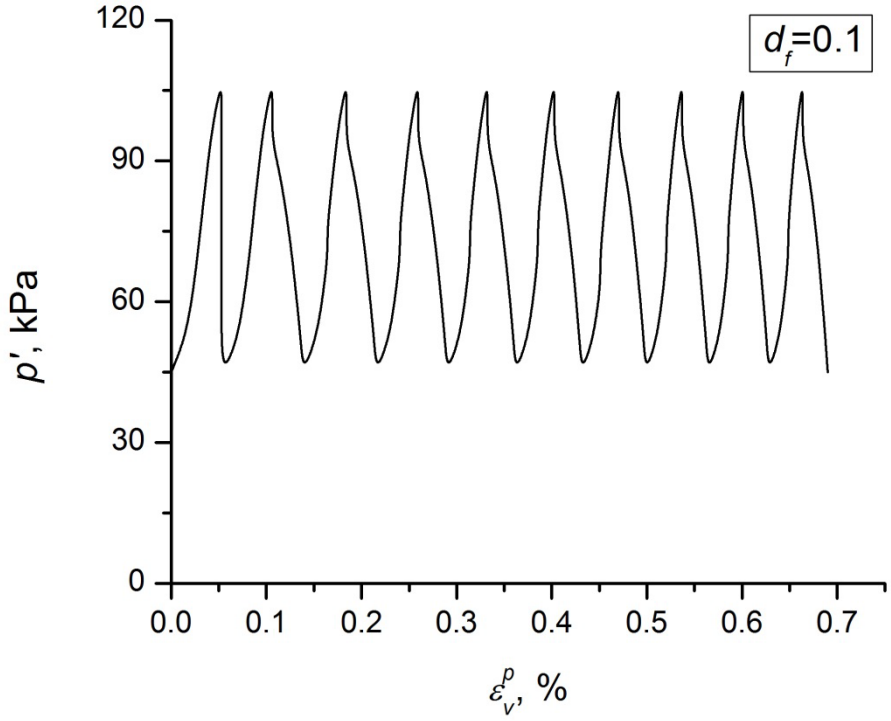

(b)

Figure 4.26 Stress-strain response at d_f=0.1

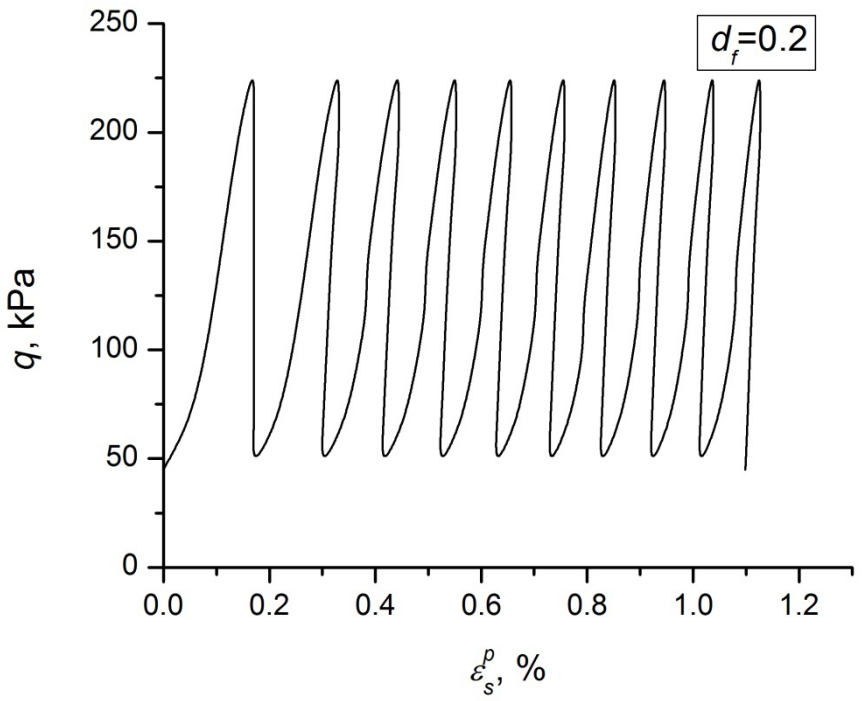

(a)

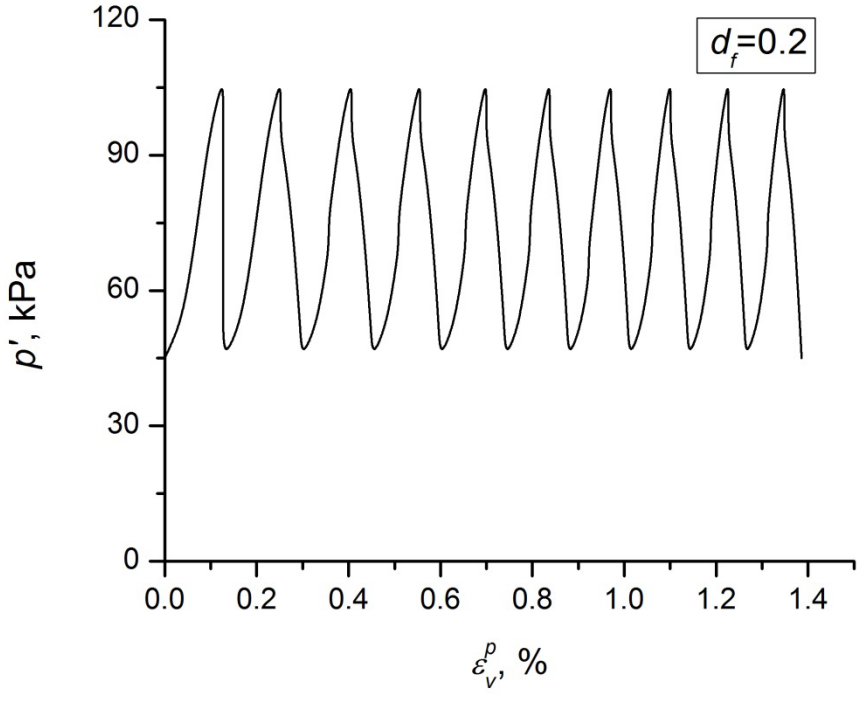

(b)

Figure 4.27 Stress-strain response at d_f=0.2

4.5.6 Comparison with Experimental Data

After examining the behaviour of the cyclic model, the next logical step is to validate it by comparing the model predictions with some experimental data in Chapter 3. This comparison is carried out in this section.

(1) Effect of load frequency

Figures 4.28(a) and 4.28(b) show the results of the cyclic tests on ballast specimen where the axial strain ε_a and volumetric strain ε_v are plotted against the number of load cycles N, respectively. The specimens were applied a confining pressure of σ_3' = 30 kPa and then loaded cyclically between a maximum deviatoric stress $q_{max,cyc}$ = 230 kPa and a minimum one $q_{min,cyc}$ = 45 kPa. The model parameters which are the same as the monotonic model were referred from Table 4.1. The new parameters were chosen by the author: κ = 0.007, m = 0.08, h_0 = 1000, k = 35, α_f=0.05 and d_f = 0.08. The simulations by the cyclic model are shown in Figure 4.28 as well. It can be seen that the model overestimates the volumetric strain under high load frequency. However, it shows that the overall behaviour of the ballast under various cyclic loading frequencies can be reproduced by the cyclic model.

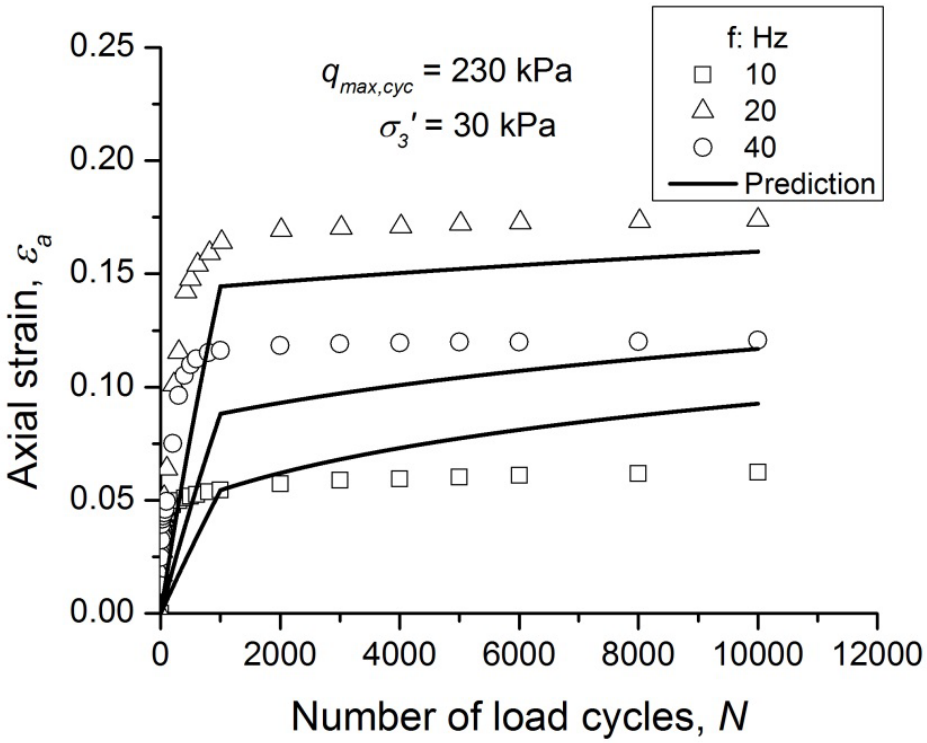

(a)

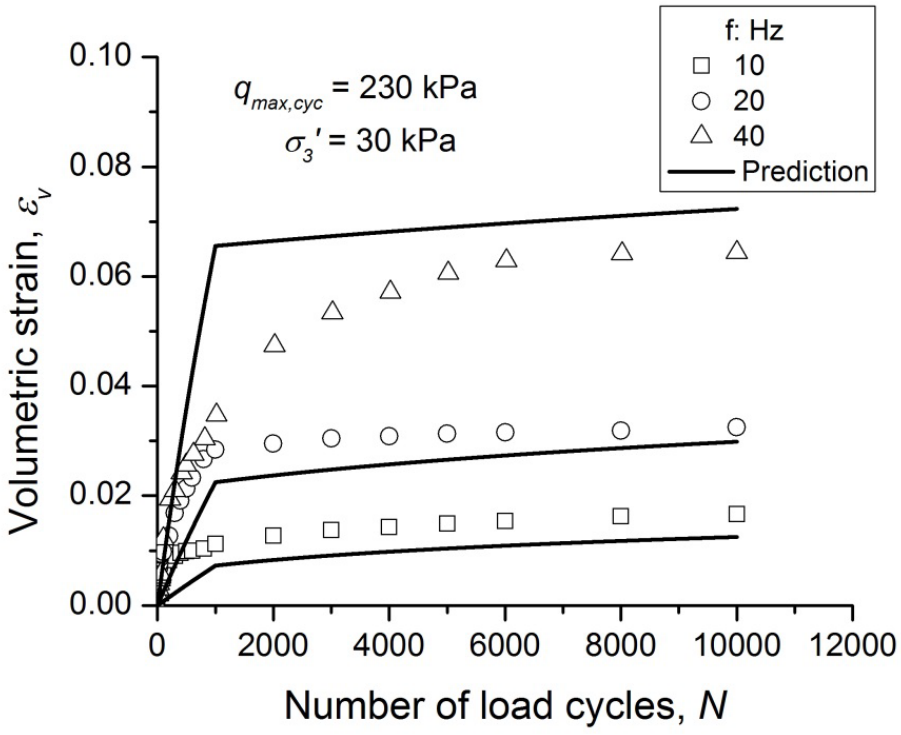

(b)

Figure 4.28 Model prediction versus experimental data: (a) axial strain and (b) volumetric strain

(2) Effect of confining pressure

The cyclic model was also used to simulate the test results of ballast specimens under different confining pressures as shown in Figure 4.29. Three different confining pressures were used (i.e. σ_3' = 10, 30 and 60 kPa). The $q_{max,cyc}$ was used as 230 kPa and the frequency f was applied as 20 Hz. The new parameters were chosen by the writer as: κ = 0.007, m = 0.08, h_0 = 1800, k = 50, α_f=0.1 and d_f = 0.06. Figure 4.29(a) shows that the model underestimates the axial strain when the confining pressure is low. The model could not capture the volumetric response promisingly in this case. However, the overall magnitude of the prediction for volumetric strain is acceptable.

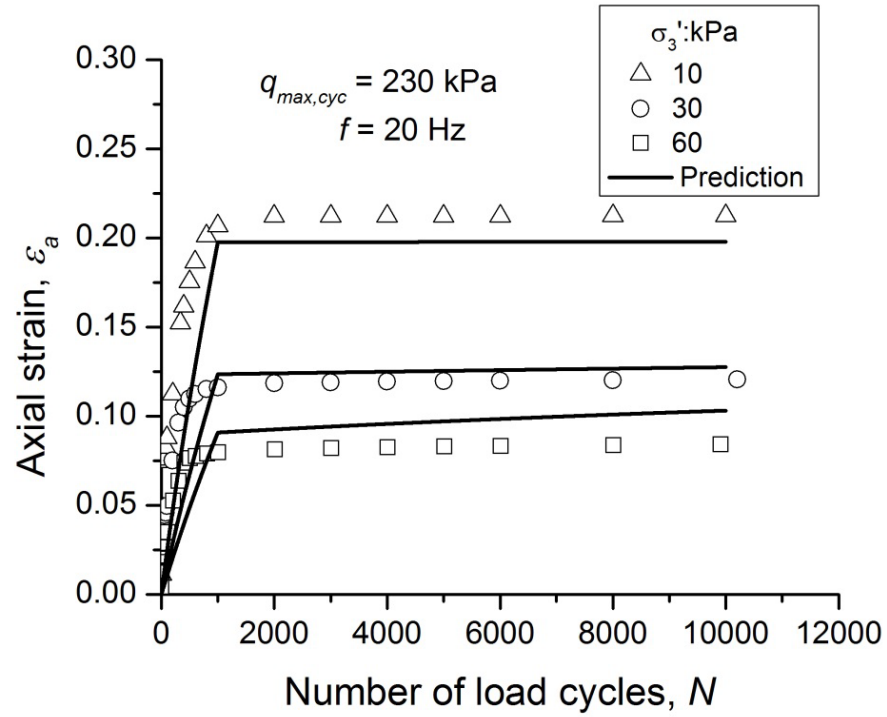

(a)

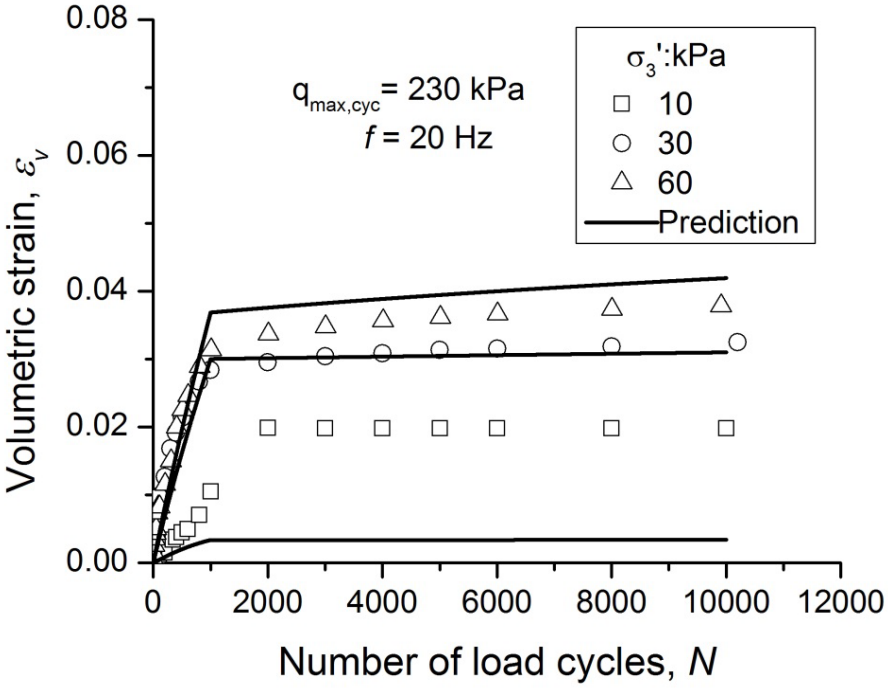

(b)

Figure 4.29 Model prediction versus experimental data: (a) axial strain and (b) volumetric strain

4.6 Summary

This chapter presented a constitutive model for ballast under monotonic loading, which was proposed based on the laboratory findings from Chapter 3. During triaxial shearing, the hardening of ballast depends on ε_s^p, ψ and BBI, and this can be reflected by a hyperbolic hardening relationship. Dilatancy for ballast depends not only on η, and ψ but also on BBI. The present study reveals that effects of particle breakage and their implications on the nonlinearity of CSL are successfully captured in the constitutive equations, and the model predictions are encouraging when compared with the laboratory data.

In the end, the static model was extended into a cyclic one, based on the bounding surface plasticity theory. The features of the cyclic model include: the ability to predict the behaviour of ballast under drained conditions; the effects of frequency on the densification and dilation of ballast; and the plastic shakedown during cyclic loading process.

According to the cyclic tests, it can be concluded that the degradation of a particle subjected to compressive forces within a granular medium is not only a function of the applied stresses, the particle size, the number of cycles, and the coordination number, but also of the load frequency. Distinct ballast degradation behaviours were observed corresponding to different deformation ranges during cyclic testing. For Range I plastic shakedown (f $\leqslant$ 30 Hz), the particle degradation was in the form of attrition of asperities and corner breakage. As the frequency became higher (30 Hz < f < 60 Hz) in Range II (plastic shakedown and ratcheting), particle splitting caused by fatigue and a high degree of attrition resulting from increased vibration became predominant. At very

high frequency ($f \geq 60$ Hz) in Range III (plastic collapse), the coordination number is greatly reduced, which would induce particle splitting. The particle breakage along with frequency and confining pressure has a profound influence on the magnitude of ε_v, and indeed, an increase in particle breakage could result in a reduction of the void ratio and a subsequent increase in densification of ballast assemblies. In the model aspect, in order to understand the development of the particle breakage during the cyclic triaxial loading procedure, it is necessary to measure the magnitude of breakage at different loading stages. For simplicity seek, in this study the effect of particle breakage is not considered.

In Chapter 5, the static model is incorporated in the Finite Element Method (FEM) by using a user-defined material model (or UMAT) in ABAQUS. FEM model is thus established for a railway track and the associated behaviour is studied.

CHAPTER 5

FINITE ELEMENT ANALYSIS OF BALLASTED RAIL TRACK

5.1 Introduction

This chapter describes the finite element modelling implementation of the constitutive model proposed in Chapter 4 to capture the drained monotonic behavior of ballast. A numerical integration of this constitutive model was carried out by using a fully implicit Euler-backward algorithm and an iterative solution procedure. The model was calibrated with the experimental results presented earlier in Chapter 3. A finite element case study is also given, where the settlement of a railway track under the passage of a train is simulated. The results of the finite element analysis revealed a successful validation against the field data.

5.2 Overview of Elasto-plastic Constitutive Relations

This thesis uses matrix-vector notations, where the matrices are designated by bold uppercase symbols and the vectors are designated by bold lowercase symbols. An incremental strain can be deduced as:

$$d\boldsymbol{\varepsilon} = d\boldsymbol{\varepsilon}^{e} + d\boldsymbol{\varepsilon}^{p} \tag{5.1}$$

where $d\boldsymbol{\varepsilon}$ is the total strain increment, and $d\boldsymbol{\varepsilon}^{e}$ and $d\boldsymbol{\varepsilon}^{p}$ are the increments of elastic and plastic strain, respectively. For linear elasticity, the following classical equation can be applied to define stress tensor $\boldsymbol{\sigma}$ as:

$$\boldsymbol{\sigma} = \boldsymbol{C}^{e} : \boldsymbol{\varepsilon}^{e} \tag{5.2}$$

where $\boldsymbol{C}^e$ is the fourth order elasticity tensor and double dots indicate the products defined as $\boldsymbol{A:B=A_{ij}B_{ij}}$.

The yield function involves the first and second invariants of the stress tensor and is given by (Indraratna et al., 2015)

$$f = q - p'\eta_s = 0 \tag{5.3}$$

where η_s is the hardening law given in Chapter 4, and p' is the mean effective stress defined as:

$$p' = \frac{1}{3}\boldsymbol{\sigma : I} \tag{5.4}$$

and where $\boldsymbol{I}$ is the second order identity tensor. q is the deviatoric stress and is called:

$$q = \left(\frac{3}{2}\boldsymbol{s : s}\right)^{1/2} \tag{5.5}$$

where $\boldsymbol{s}$ is the stress deviator. The function f is defined such that whenever $f < 0$ the response is purely elastic.

The flow rule is written as:

$$d\boldsymbol{\varepsilon}^p = d\boldsymbol{\Lambda}\frac{\partial g}{\partial \sigma} \tag{5.6}$$

where $d\boldsymbol{\Lambda}$ is a positive scalar and $g = g(p',q,\eta_s)$ is the flow potential. For the rate independent materials, $d\boldsymbol{\Lambda}$ is determined by the kinematic solution at a given point. Using equation (5.4) and (5.5), the flow rule becomes:

$$d\boldsymbol{\varepsilon}^{p} = d\Lambda\left(\frac{1}{3}\frac{\partial g}{\partial p'}\boldsymbol{I} + \frac{\partial g}{\partial q}\boldsymbol{n}\right) \tag{5.7}$$

where $\boldsymbol{n}$ is the flow direction vector expressed as:

$$\boldsymbol{n} = \frac{3}{2q}\boldsymbol{s} \tag{5.8}$$

Thus, the stress tensor can be written as:

$$\boldsymbol{\sigma} = p\boldsymbol{I} + \frac{2}{3}q\boldsymbol{n} \tag{5.9}$$

The plasticity model is formulated in terms of the evolution of the hardening law η_s that was described previously in Chapter 4.

5.3 Numerical Integration of the Ballast Model

To predict the behaviour of a railway track substructure accurately, the finite element method (FEM) is used to capture the constitutive model proposed in Chapter 4. In FEM, the strain inside the element is evaluated at one or more sample points that are commonly named ‘integration points’. At each integration point, the strain relates to the stress via a constitutive relationship that is now defined by the constitutive model described in Chapter 4. The numerical integration of these constitutive relations is described in the following section.

The elasto-plastic response of ballast has non-linear characteristics, and therefore to determine the actual stress, strain, and hardening variables, an iterative solution procedure must be used where the stress, strain, and hardening variable are expressed as:

$$\left\{\boldsymbol{\sigma}_t, \boldsymbol{\varepsilon}_t, \boldsymbol{\varepsilon}^p_{s,t}\right\} \rightarrow \left\{\boldsymbol{\sigma}_{t+\Delta t}, \boldsymbol{\varepsilon}_{t+\Delta t}, \boldsymbol{\varepsilon}^p_{s,t+\Delta t}\right\} \tag{5.10}$$

where the subscript t designates the material state at time step t, and the subscript $t+\Delta t$ designates the new state that has yet to be determined at time step $t+\Delta t$. Equation (5.10) can be expressed in terms of the time increment of total strain as:

$$\boldsymbol{\varepsilon}_{t+\Delta t} = \boldsymbol{\varepsilon}_t + \Delta\boldsymbol{\varepsilon} \tag{5.11}$$

where $\Delta\boldsymbol{\varepsilon}$ is the incremental total strain that is related to the incremental nodal displacement by means of a strain-displacement operator.

The stress and strain vectors are given in Equation (5.10) and generally consist of six components:

$$\boldsymbol{\sigma} = \left[\sigma_{11}, \sigma_{22}, \sigma_{33}, \sigma_{12}, \sigma_{23}, \sigma_{31}\right]^T \tag{5.12}$$

$$\boldsymbol{\varepsilon} = \left[\varepsilon_{11}, \varepsilon_{22}, \varepsilon_{33}, 2\varepsilon_{12}, 2\varepsilon_{23}, 2\varepsilon_{31}\right]^T \tag{5.13}$$

Equation (5.10) was implemented using a fully implicit Euler backward algorithm (Simo and Taylor, 1986), but for the behavior of elasto-plastic material, the solution to the corresponding non-linear equations is obtained by using a Newton-Raphson iteration procedure. The consistent tangent operator reflects the actual tangential relationship between the increment in stress and the increment in strain, and it is computed by consistent linearisation of the updated stress (Simo and Taylor, 1985). In this section the numerical integration procedure outlined above to capture the elastic and elasto-plastic behaviour was specified successfully.

5.3.1 Update of Elasto-Plastic Response

During the constitutive calculations, where the stresses and state variables were updated, the total strain $\boldsymbol{\varepsilon}$ was known. The elasticity equations give:

$$\boldsymbol{\sigma}_{t+\Delta t} = \boldsymbol{C}^{e} : \boldsymbol{\varepsilon}^{e}_{t+\Delta t} \tag{5.14}$$

where,

$$\boldsymbol{\sigma}^{e} = \boldsymbol{C}^{e} : \left(\boldsymbol{\varepsilon}^{e}_{t} + \Delta\boldsymbol{\varepsilon}\right) \tag{5.15}$$

is the elastic predictor. In Equation (5.15), $\boldsymbol{\varepsilon}^{e}_{t}$ is the elastic strain at the start of the increment.

The yield function and the flow rule are written as

$$f = q_{t+\Delta t} - \eta_s p'_{t+\Delta t} = 0 \tag{5.16}$$

and

$$\Delta\varepsilon^{p} = \frac{1}{3}\Delta\varepsilon^{p}_{v}\boldsymbol{I} + \Delta\varepsilon^{p}_{s}\boldsymbol{n}_{t+\Delta t} \tag{5.17}$$

where $\Delta\varepsilon^{p}_{v} = \Delta\boldsymbol{\Lambda}\left(\frac{\partial g}{\partial p'}\right)_{t+\Delta t}$ and $\Delta\varepsilon^{p}_{s} = \Delta\boldsymbol{\Lambda}\left(\frac{\partial g}{\partial q}\right)_{t+\Delta t}$.

Elimination of $\Delta\boldsymbol{\Lambda}$ gives,

$$\Delta\varepsilon^{p}_{v}\left(\frac{\partial g}{\partial q}\right)_{t+\Delta t} - \Delta\varepsilon^{p}_{s}\left(\frac{\partial g}{\partial p'}\right)_{t+\Delta t} = 0 \tag{5.18}$$

Equation (5.9) is written as:

$$\boldsymbol{\sigma}_{t+\Delta t} = p'_{t+\Delta t}\boldsymbol{I} + \frac{2}{3} q_{t+\Delta t}\boldsymbol{n}_{t+\Delta t} \tag{5.19}$$

and the updated hardening law is given by,

$$\eta_{s,t+\Delta t} = \frac{\varepsilon_{s,t}^{p} + \Delta\varepsilon_{s}^{p}}{B_m + \varepsilon_{s,t}^{p} + \Delta\varepsilon_{s}^{p}} M_{p,t+\Delta t} \tag{5.20}$$

Using Equation (5.17), we can rewrite Equation (5.14) as:

$$\boldsymbol{\sigma}_{t+\Delta t} = \boldsymbol{\sigma}^{e} - K\Delta\varepsilon_{v}^{p}\boldsymbol{I} - 2G\Delta\varepsilon_{s}^{p}\boldsymbol{n}_{t+\Delta t} \tag{5.21}$$

where G and K are the elastic shear and bulk moduli, respectively, and they can relate to each other by $K=2G(1+v)/[3(1-2v)]$.

The above equation shows that in a deviatoric stress space, the 'return' to the yield surface is along $\boldsymbol{n}_{t+\Delta t}$ which means that $\boldsymbol{s}^{e}$ and $\boldsymbol{s}_{t+\Delta t}$ are co-axial, and therefore $\boldsymbol{n}_{t+\Delta t}$ can be simply determined from the elastic predictor $\boldsymbol{\sigma}^{e}$ as,

$$\boldsymbol{n}_{t+\Delta t} = \frac{3}{2q^{e}}\boldsymbol{s}^{e} \tag{5.22}$$

The above observation simplifies the calculations considerably and also reduces the number of unknowns. With a 3-D problem, all 6 independent stress components must be solved at $t+\Delta t$; but Equation (5.19) shows that with $\boldsymbol{n}_{t+\Delta t}$ being known, the two scalar variables $p_{t+\Delta t}$ and $q_{t+\Delta t}$ fully define the stress tensor at the end of the increment. Similarly, Equation (5.17) shows that $\Delta\boldsymbol{\varepsilon}^{p}$ is determined in terms of the two scalars $\Delta\varepsilon_{v}^{p}$ and $\Delta\varepsilon_{s}^{p}$.

Projecting the elasticity Equation (5.14) onto $\boldsymbol{I}$ and $\boldsymbol{n}$, and using Equation (5.19), we

find

$$p'_{t+\Delta t} = p^e - K\Delta\varepsilon_v^p \tag{5.23}$$

and

$$q_{t+\Delta t} = q^e - 3G\Delta\varepsilon_s^p \tag{5.24}$$

The problem of integrating the elasto-plastic equations is reduced to the solution of the following set of non-linear equations:

$$\Delta\varepsilon_v^p \left(\frac{\partial g}{\partial q}\right)_{t+\Delta t} - \Delta\varepsilon_s^p \left(\frac{\partial g}{\partial p}\right)_{t+\Delta t} = 0 \tag{5.18}$$

$$f = q_{t+\Delta t} - \eta_{s,t+\Delta t} p'_{t+\Delta t} = 0 \tag{5.16}$$

$$p'_{t+\Delta t} = p^e - K\Delta\varepsilon_v^p \tag{5.23}$$

$$q_{t+\Delta t} = q^e - 3G\Delta\varepsilon_s^p \tag{5.24}$$

$$\eta_{s,t+\Delta t} = \frac{\varepsilon_{s,t}^p + \Delta\varepsilon_s^p}{B_m + \varepsilon_{s,t}^p + \Delta\varepsilon_s^p} M_{p,t+\Delta t} \tag{5.20}$$

with

$$\left(\frac{\partial g}{\partial q}\right)_{t+\Delta t} = 1 \tag{5.25}$$

$$\left(\frac{\partial g}{\partial p'}\right)_{t+\Delta t} = A_d \left(M_{c,t+\Delta t} exp\left(k_d \cdot \Psi_{t+\Delta t}\right) - q_{t+\Delta t} / p'_{t+\Delta t}\right) \tag{5.26}$$

$$M_{c,t+\Delta t} = M_{c0} - \left(1 - exp\left(-\alpha BBI_{t+\Delta t}\right)\right) \tag{5.27}$$

$$BBI_{t+\Delta t} = \theta_b \left[1 - exp\left(-v_b \varepsilon^p_{s,t+\Delta t} \right) \right] / \left(\omega_b - lnp'_i \right) \tag{5.28}$$

$$\Psi_{t+\Delta t} = v_{t+\Delta t} - \left(\Gamma - a \cdot exp\left(b \cdot BBI_{t+\Delta t} \right) - \lambda log p'_{t+\Delta t} \right) \tag{5.29}$$

$$v_{t+\Delta t} = v_t + v_0 \Delta \varepsilon_v \tag{5.30}$$

$$M_{p,t+\Delta t} = M_{c,t+\Delta t} \left(1 - k_p \Psi_{t+\Delta t} \right) \tag{5.31}$$

These equations were solved using Newton-Raphson's iteration process where $\Delta\varepsilon_v^p$ and $\Delta\varepsilon_s^p$ were the primary unknowns. The values of $p'_{t+\Delta t}$ and $q_{t+\Delta t}$ were updated using Equations (5.23) and (5.24), and $\boldsymbol{\sigma}_{t+\Delta t}$ can be updated by Equation (5.21). The iteration commences by using an elastic predictor that is commonly known as the trial state, but it must be determine in advance if elaso-plastic is active, which corresponds to

$$f = q_{t+\Delta t} - \eta_{s,t} p'_{t+\Delta t} > 0 \tag{5.32}$$

otherwise the material response is elastic. The above strategy is similar to that proposed by Aravas (1987).

5.3.2 Consistent Tangent Operator for Elasto-Plastic Response

A definition of the tangent stiffness operator at the level of the integration point plays a crucial role in the robustness and performance of the iterative procedure. As first discussed by Simo and Taylor (1985), the consistent tangent stiffness matrix follows the consistent linearisation of the stress update $\boldsymbol{\sigma}_{t+\Delta t}$. To begin, the contributions from the deviatoric stress and hydrostatic stress are linearised separately,

$$\frac{d\boldsymbol{\sigma}_{t+\Delta t}}{d\varepsilon_{t+\Delta t}} = \frac{d\boldsymbol{s}_{t+\Delta t}}{d\varepsilon_{t+\Delta t}} + \boldsymbol{I}\frac{dp_{t+\Delta t}}{d\varepsilon_{t+\Delta t}} \tag{5.33}$$

The term $\frac{d\boldsymbol{s}_{t+\Delta t}}{d\varepsilon_{t+\Delta t}} = \frac{\partial \boldsymbol{s}_{t+nt}}{\partial \Delta\gamma}\cdot\frac{\partial \Delta\gamma}{\partial \varepsilon_{t+nt}}$ with $\boldsymbol{s}_{t+\Delta t} = \frac{q_{t+\Delta t}}{q_{t+\Delta t} + 3G\Delta\varepsilon_s^p}\left(\boldsymbol{s}_t + 2G\boldsymbol{R}^{-1}\Delta\gamma\right)$ resulting in following expression:

$$\frac{\partial \boldsymbol{s}_{t+\Delta t}}{\partial \Delta\gamma} = \frac{2Gq_{t+\Delta t}\boldsymbol{R}^{-1}}{q_{t+\Delta t} + 3G\Delta\varepsilon_s^p} \tag{5.34}$$

where $\boldsymbol{R} = diag[1,1,1,2,2,2]$

The second term in expression $\frac{d\boldsymbol{s}_{t+\Delta t}}{d\varepsilon_{t+\Delta t}}$ yields:

$$\frac{\partial \Delta\boldsymbol{\gamma}}{\partial \varepsilon_{t+nt}} = \boldsymbol{Q} \tag{5.35}$$

where the matrix follows from the relationship $\boldsymbol{\gamma}_{t+\Delta t} = \boldsymbol{Q}\cdot\boldsymbol{\varepsilon}_{t+\Delta t}$ where $\boldsymbol{Q}$ is defined as below:

$$Q = \begin{bmatrix} \frac{2}{3} & -\frac{1}{3} & -\frac{1}{3} & & & \\ -\frac{1}{3} & \frac{2}{3} & -\frac{1}{3} & 0 & 0 & 0 \\ -\frac{1}{3} & -\frac{1}{3} & \frac{2}{3} & & & \\ 0 & 0 & 0 & 1 & 0 & 0 \\ 0 & 0 & 0 & 0 & 1 & 0 \\ 0 & 0 & 0 & 0 & 0 & 1 \end{bmatrix} \tag{5.36}$$

Combining $\frac{\partial \boldsymbol{s}_{t+\Delta t}}{\partial \Delta\gamma}$ with $\frac{\partial \Delta\gamma}{\partial \varepsilon_{t+nt}}$, leads to

$$\frac{d\boldsymbol{s}_{t+\Delta t}}{d\varepsilon_{t+\Delta t}} = \frac{2Gq_{t+\Delta t}\boldsymbol{R}^{-1}\boldsymbol{Q}}{q_{t+\Delta t} + 3G\Delta\varepsilon_s^p} \tag{5.37}$$

To determine the term $\frac{dp_{t+\Delta t}}{d\varepsilon_{t+\Delta t}}$, we start from

$$p'_{t+\Delta t} = p'^{e} - K\Delta\varepsilon_v^p = p'_t + K\Delta\varepsilon_v - K\Delta\varepsilon_v^p \tag{5.38}$$

Hence,

$$\frac{dp'_{t+\Delta t}}{d\varepsilon_{t+\Delta t}} = K\frac{\partial\Delta\varepsilon_v}{\partial\varepsilon_{t+\Delta t}} = K\boldsymbol{I} \tag{5.39}$$

The consistent tangent operator now becomes

$$\frac{d\boldsymbol{\sigma}_{t+\Delta t}}{d\varepsilon_{t+\Delta t}} = \frac{2Gq_{t+\Delta t}\boldsymbol{R}^{-1}\boldsymbol{Q}}{q_{t+\Delta t} + 3G\Delta\varepsilon_s^p} + \boldsymbol{K}\cdot\boldsymbol{I}\cdot\boldsymbol{I}^T \tag{5.40}$$

Further details regarding the consistent tangent operator can be found in Suiker (2002).

5.3.3 Update of Elastic Response and Consistent Tangent Operator

The update of the elastic response can be conducted using Equation (5.17), where

$$p'_{t+\Delta t} = p'^{e} \tag{5.41}$$

$$q_{t+\Delta t} = q^e \tag{5.42}$$

Substituting Equations (5.41) and (5.42) into Equation (5.19) leads to

$$\boldsymbol{\sigma}_{t+\Delta t} = p'^{e}\boldsymbol{I} + \frac{2}{3}q^e\boldsymbol{n}_{t+\Delta t} \tag{5.43}$$

The consistent tangent operator for the elastic response is expressed as:

$$C^e = \begin{bmatrix} \lambda^e + 2G & \lambda^e & \lambda^e & 0 & 0 & 0 \\ \lambda^e & \lambda^e + 2G & \lambda^e & 0 & 0 & 0 \\ \lambda^e & \lambda^e & \lambda^e + 2G & 0 & 0 & 0 \\ 0 & 0 & 0 & G & 0 & 0 \\ 0 & 0 & 0 & 0 & G & 0 \\ 0 & 0 & 0 & 0 & 0 & G \end{bmatrix} \tag{5.44}$$

5.4 Finite Element Modelling of Static Triaxial Test

In this section, a subroutine was used to predict the ballast observed during the triaxial tests, and these tests can be analysed using a 2-D axisymmetric approach. A 2D 8-node axisymmetric quadrilateral element (CAX8R) was used in this simulation. The shaded area of the specimen shown in Figure 5.1(a) was numerically simulated in ABAQUS. Figure 5.1 (b) shows the discretised mesh of this ballast specimen along with the prescribed boundary conditions. The left boundary represents the central axis, which does not move laterally (i.e. vertical degree of freedom only), while the boundary condition at the bottom of the specimen is fixed vertically and radially. The top base of the specimen was fixed in a radial direction but remained unrestricted in a vertical direction. Detailed descriptions of the relevant parameters used for the ballast model can be found in Chapter 4. When simulating the monotonic triaxial test procedure, two loading steps were applied; in the first load step the boundary conditions were activated and the cell pressure was applied, and in the second load step the cell pressure and boundary conditions of the specimen were held, and then the specimen was forced to shear.

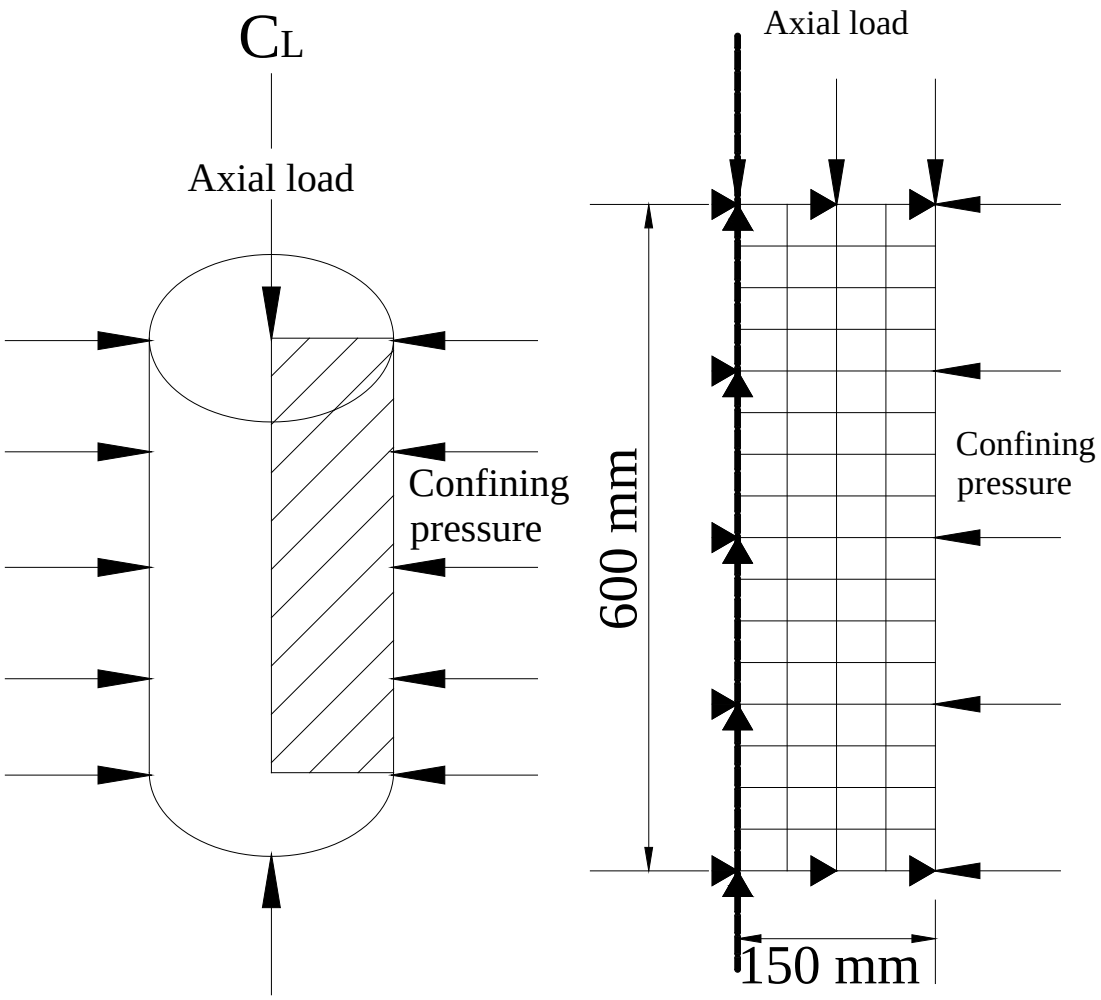

Figure 5.1 (a) The ballast specimen in the triaxial test, (b) Boundary conditions and mesh in the triaxial test simulation

A comparison between the simulated and experimental results is shown in Figure 5.2, and it indicates that the stress-strain response from the simulation and experiment broadly matched each other (Figure 5.2(a)). The change in volume is presented in Figure 5.2(b), and indicates that the predicted changes in volume match the test data quite well. The developed subroutine provides a promising representation of how the ballast behaved. The predictions of the FEM model by adopting an elastic approach are also included in Figure 5.2 to better represent the limitations of elasticity based approaches. Figures 5.3 (a) and (b) show how the Y and X components were distributed

in the triaxial test with a confining pressure σ_3' = 30 kPa. Note that the FEM model captured the specimen 'bulging' after triaxial shearing.

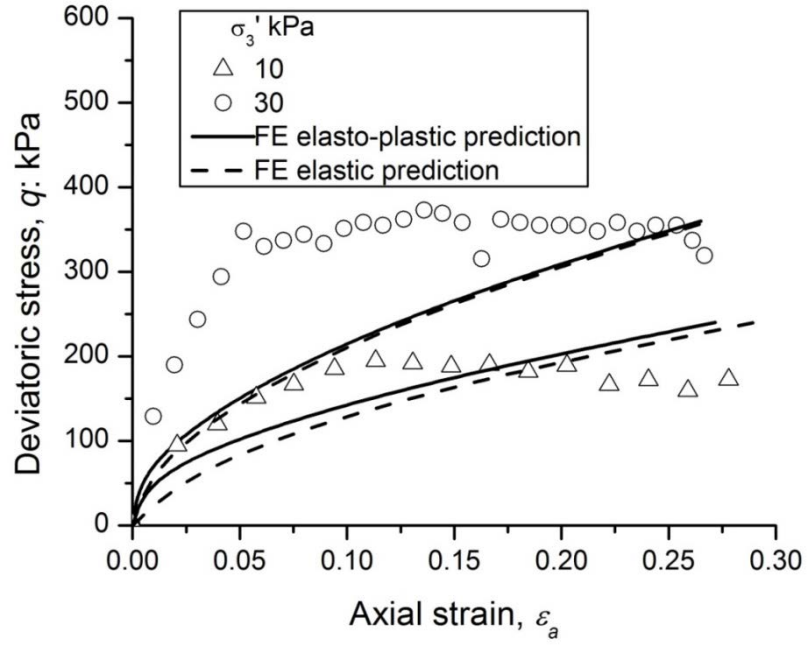

(a)

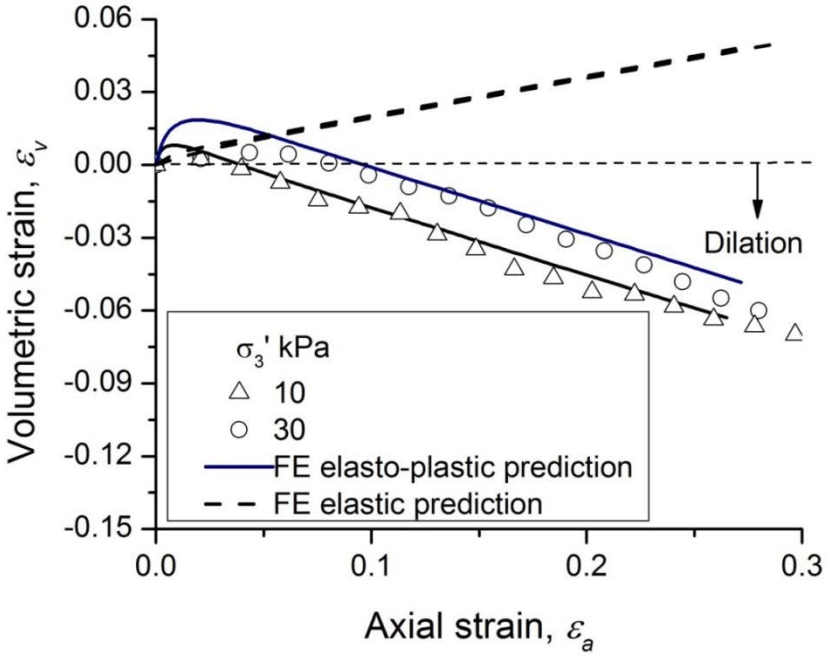

(b)

Figure 5.2 Comparison of the triaxial monotonic tests and the simulation results: (a) the stress-strain behaviour and (b) the volume change behaviour

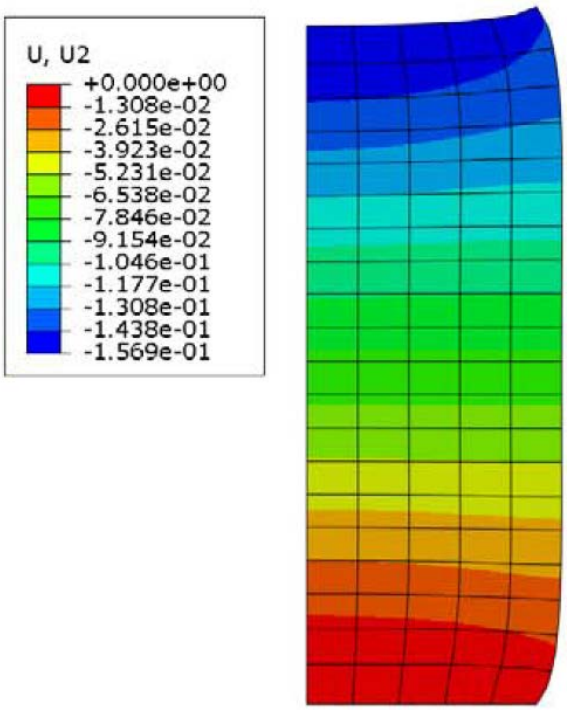

(a)

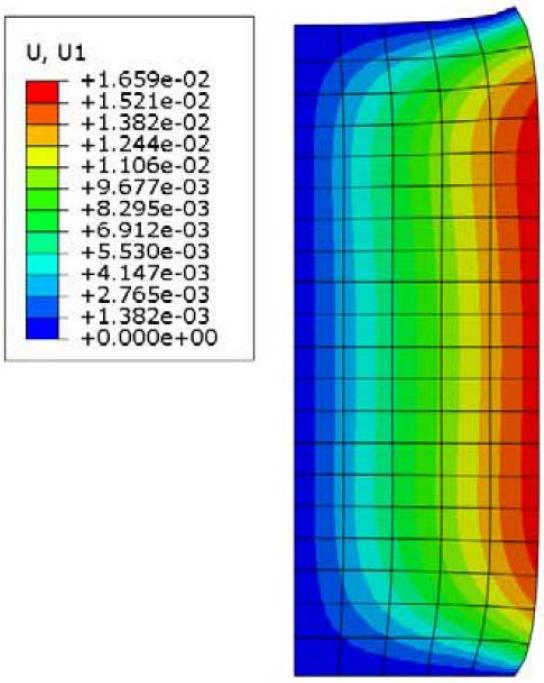

(b)

Figure 5.3 Deformation contours from FEM: (a) vertical displacement U2 (m); (b) lateral displacement U1 (m)

5.5 Finite Element Modelling of Ballasted Railway Track

5.5.1 Railway Substructure Geometry

In this section the ballast model will be used to study the deformation of a ballasted railway track under a train axle passage in FEM. In a traditional railway track system, the steel rails are supported on concrete sleepers that are typically spaced at 650 mm centres. The sleepers are embedded into a layer of coarse granular aggregate (ballast) that is 300 mm thick, below which a 150 mm thick layer of subballast may be placed. The dimension of the natural ground was chosen to be 15 m deep × 15 m wide, which should be sufficiently large to eliminate any boundary effects. The typical track structure shown in Figure 5.4 (a) was modelled in FEM (Figure 5.4 (b)).

5.5.2 Material Models and Properties

The rail and sleeper were modelled as linear elastic materials, the ballast was modelled as a non-associative elasto-plastic material, the subballast was represented by the Mohr-Coulomb model, and subgrade materials was considered as elasto-plastic material by Modified Cam-Clay model. The parameters for the materials are shown in Table 5.1.

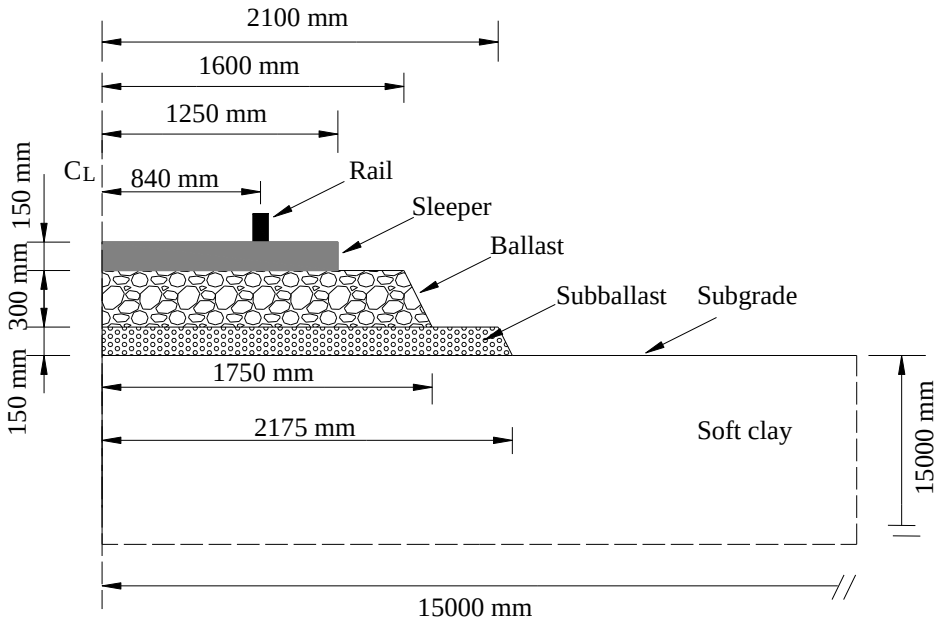

(a)

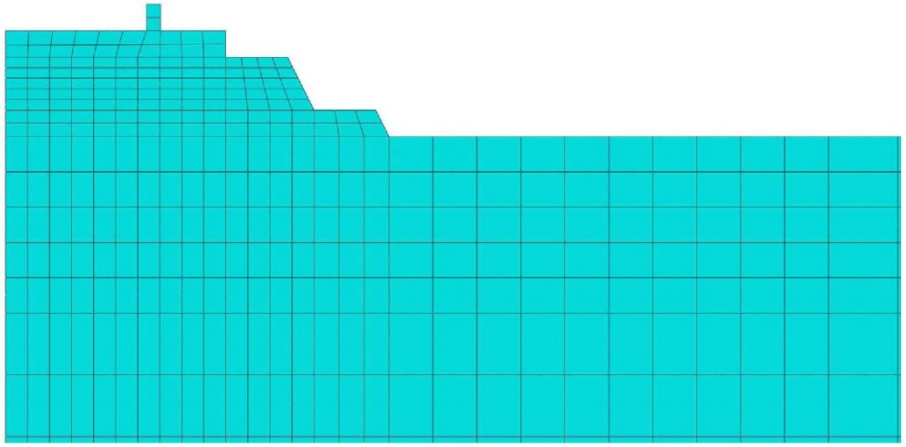

(b)

Figure 5.4 Dimensions and finite element configuration of track model: (a) Schematic cross section of a typical track structure (mm); (b) 2D finite element mesh density

Table 5.1 Finite model material properties

Properties	Ballast	Subballast	Subgrade	Rail	Sleeper
Model type	Model in Chapter 4	Mhor-Coulomb	Modified Cam-Clay	Linear Elastic	Linear Elastic
ρ (kg/m^3)	1520	1520	1700	2000	2000
E (MPa)	50	10	20	200,000	30,000
v	0.3	0.35	0.25	0.3	0.25
θ_b	0.33	--	--	--	--
v_b	11.5	--	--	--	--
ω_b	6.4	--	--	--	--
Γ_{ref}	2.41	--	2.51	--	--
λ	0.105	--	0.15	--	--
M_{c0}	2.6	--	1.02	--	--
α	4.287	--	--	--	--
a	0.2	--	--	--	--
b	1.87	--	--	--	--
A_d	0.80	--	--	--	--
k_d	1.6	--	--	--	--
k_p	1.05	--	--	--	--
B_m	0.017	--	--	--	--
c (kN/m^3)	--	5	--	--	--
ϕ (degrees)	--	35	26	--	--
κ	--	--	0.06	--	--
N	--	--	2.57	--	--
v_0	--	--	2.8	--	--

5.5.3 Finite Element Mesh and Boundary Conditions

A plane strain (2D) finite element analysis was carried out. By taking advantage of symmetry, only half of the embankment and foundations were modelled. The model consisted of 2241 elements and 6931 nodes (Figure 5.4 (b)). Most of these elements were placed in the railway substructure because its behavior was of utmost interest and where deformation was expected to be concentrated. The track was meshed with an 8-node biquadratic plane strain quadrilateral and reduced integration (CPE8R). The vertical boundary under the centreline of the railroad was restrained in the x- and y-directions, and the vertical boundary along the outer edge of the foundation was constrained from being displaced in the x-direction. The constraint was fixed to the bottom boundary to prevent displacement in the y-direction.

5.5.4 Loading Conditions

The USACE railroad design manual (2000) assumes that the point load attained from the wheel of a railcar is distributed between 5 sleepers (Figure 5.5), while emphasizing that the highest load is on the sleeper directly below the wheel (approximately 40% of the wheel load). The wheel load for this analysis was 25 t, so the equivalent load was 98 kN (= 0.4 × 25000 kg × 9.8 m/s^2 / 1000), and it was used to represent the approximate point-loading of a wheel on a rail. For design purposes, the DAF was used to calculate the dynamic axle load under high speed train loading, and equation (3.12) was used to calculate the values of DAF under different train speeds. Three different train speeds were considered (Table 5.2), and the loading was applied monotonically above the central sleeper in the FEM model.

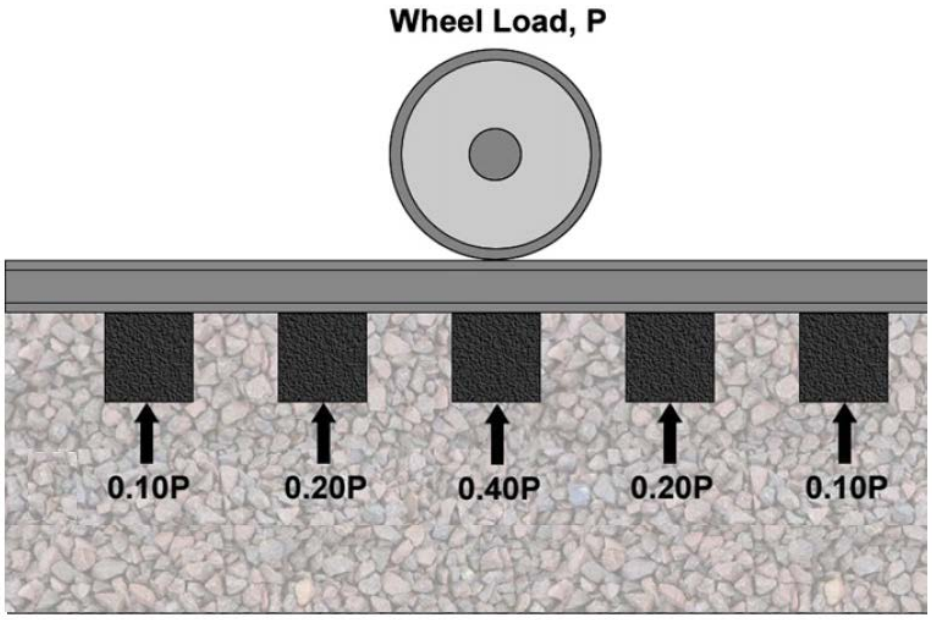

Figure 5.5 Assumed ballast-tie reaction from wheel load (USACE railroad design manual, 2000)

Table 5.2 Values of DAF corresponding to different train speeds

V (km/h)	100	200	300
$DAF=e^{0.003V}$	1.35	1.82	2.46
Dynamic load (kN)	132	178	241

5.5.5 Application of the Initial Ground Stress

It is noteworthy that the application of initial ground stress for geotechnical problems in ABAQUS is important because it uses the initial stresses specified by the user as an initial guess (or to start the progress of getting converged stresses to begin the analysis). This initial stress has a big impact on the subsequent steps, because, Figure 5.6 shows that after the initial ground stress was applied, the soil displacement U2 in ODB (Output Data Base) at the GEOSTATIC STEP became very small (almost equivalent to 0), which means the initial ground stress was successfully applied to the FEM model.

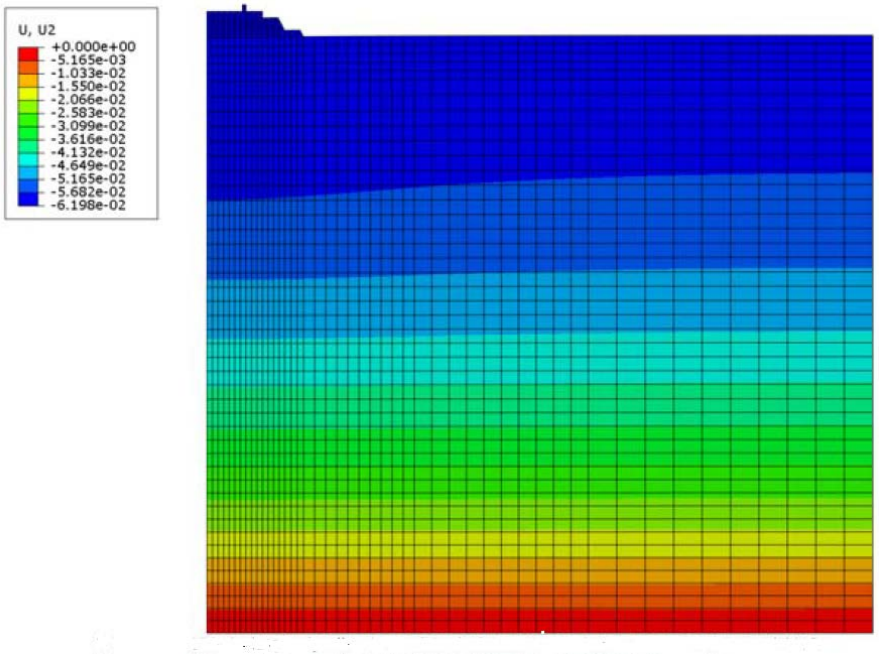

(a)

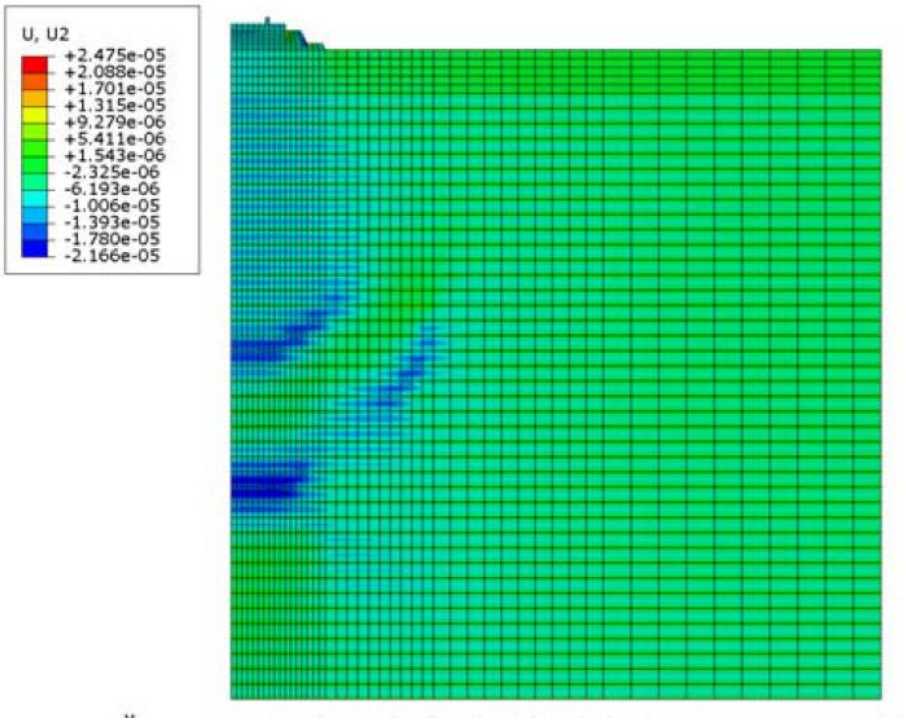

(b)

Figure 5.6 Comparison of displacement component U2 before and after application of initial ground stress; (a) Before and (b) After

5.5.6 Model Predictions and Discussion

In order to validate the findings of this finite element analysis, a comparison was made between the model predictions and the field data (Indraratna et al., 2010b), as shown in Figure 5.7. Here the 2D FEM model predicted more vertical stress and displacement along the depth than were obtained in the actual field measurements. This is possible because (i) difficulty of simulation the appropriate in-situ initial state, (ii) material parameters derived from the triaxial experiments alone do not always adequately represent the in-situ stress and deformation states, e.g. train-induced reversal of shear stress in the longitudinal track direction and (iii) simplifications/approximations adopted in the modelling procedure. Considering the limitations of the FEM model, this prediction is still acceptable for preliminary design practices. Moreover, the present work is compared with another study by Indraratna and Nimbalkar (2011). The comparison of results highlights the fact that the use of innovative constitutive algorithm capturing ballast displacements is promising in predicting the railway track behaviour.

The effect of train speed on the deformation of ballasted rail track was studied using the FEM model. Figure 5.8 shows the pattern of deformation for the upper part of the finite-element configuration computed after quasi-dynamic vertical load that corresponded to a train speed V = 300 km/h was applied, but to make such a comparison, the case for V = 100 km/h was also included. The train speed had a profound influence on the deformation of the ballasted railway track because as the speed of the train increased, the vertical deformation at the ground surface also increased as expected. The maximum displacements at top of ballast and subgrade are plotted against the train speeds in Figure 5.9. Table 5.3 shows the variation of vertical strain ε for ballast with different a

V, so when the train speed increased from 100 to 200 and 300 km/h respectively, the vertical strain on the ballast increased by 34 % and 80% respectively. This proposed FEM model can capture the response of railway tracks under different train speeds and may also be used for further track analysis.

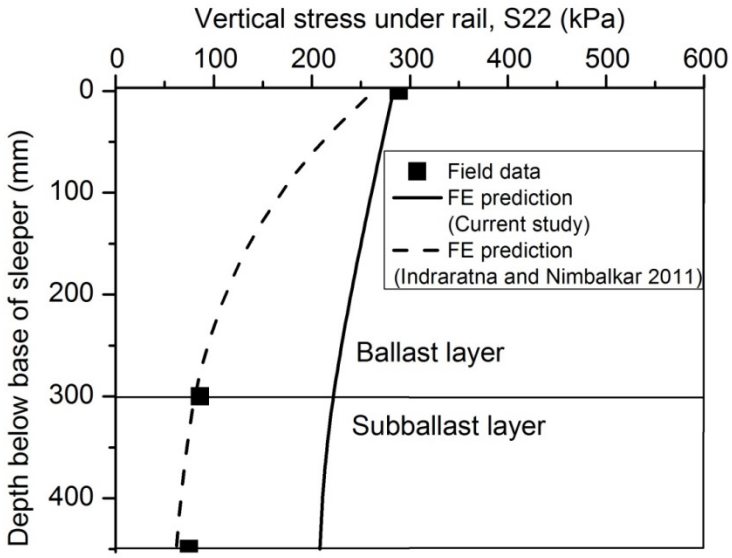

(a)

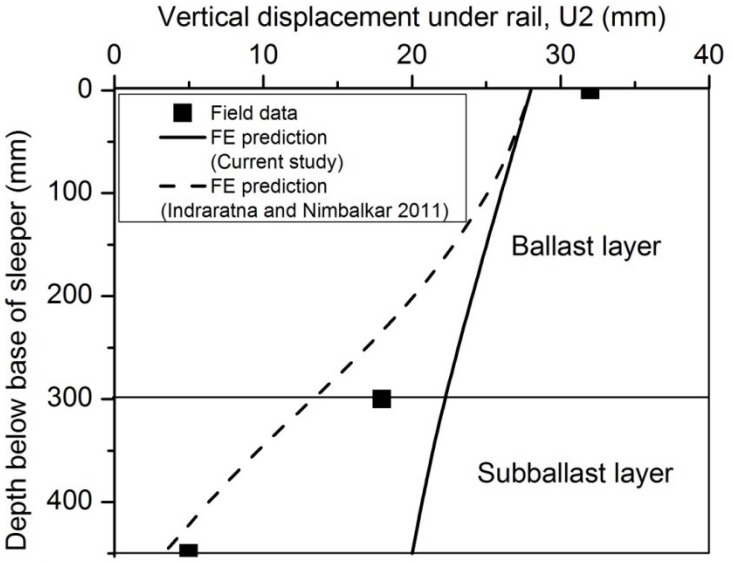

(b)

Figure 5.7 Comparisons of field data with FE predictions: (a) vertical maximum cyclic stresses and (b) vertical displacement (Field data sourced form Indraratna et al., 2010b)

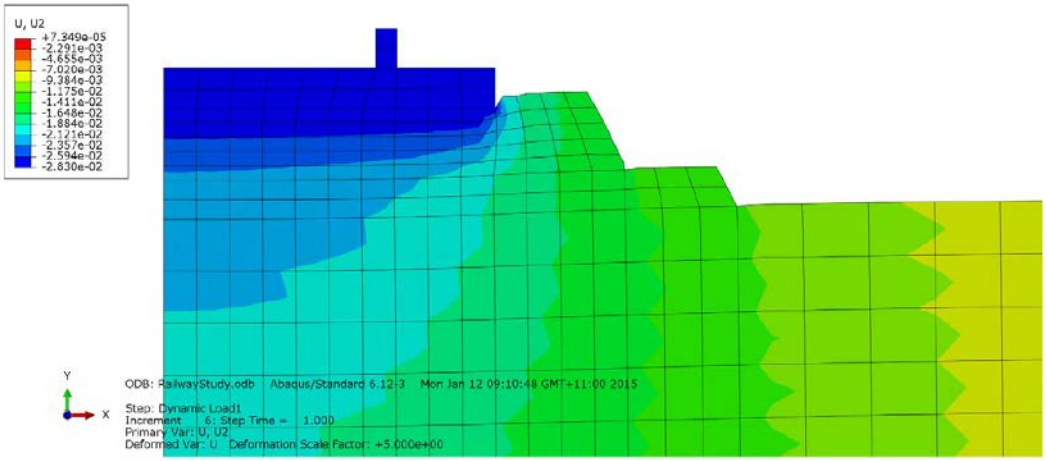

(a)

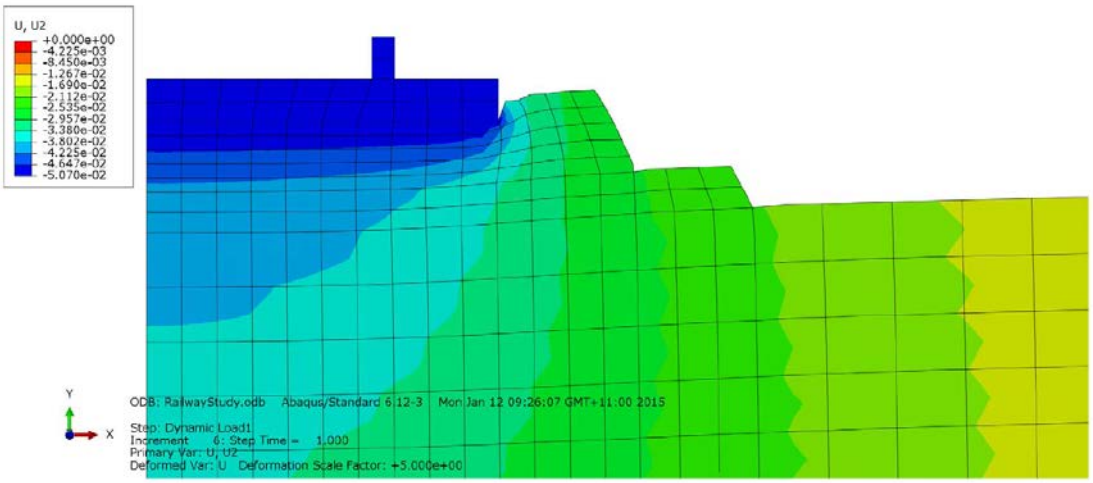

(b)

Figure 5.8 Pattern of deformation (deformation scale factor is 5) for the upper part of finite-element configuration after the application of vertical loads with different train speeds V: (a) V = 100 km/h and (b) V = 300 km/h

Table 5.3 vertical strain ε for ballast with different train speeds V

V (km/h)	100	200	300
U2 (m)	-0.0283	-0.0378	-0.0507
ε (%)	9.4	12.6	16.9

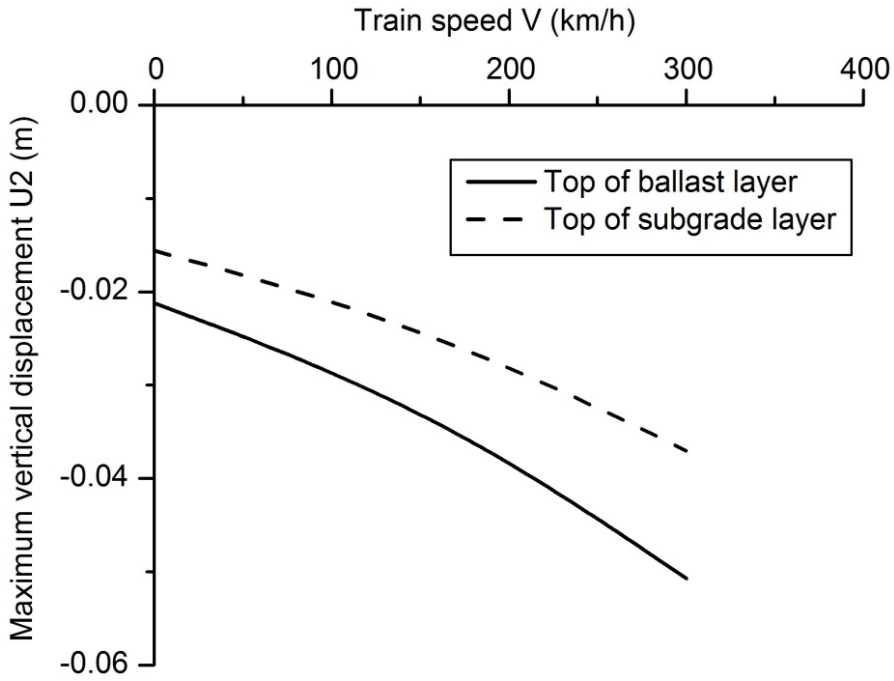

Figure 5.9 Maximum displacements at the ground surface for different train speeds

5.6 Summary

The response of ballasted track can be modelled via an elasto-plastic model that is based on the properties of ballast under traffic loading, and this model was applied successfully in FEM. In accordance with this concept, a ballast model that captures the effect of particle breakage was proposed in Chapter 4.

In this chapter the model was integrated into the FEM software ABAQUS using a fully implicit Euler-backward algorithm that was based on an elastic stress predictor. The tangent operator was derived by consistent linearisation of the updated stress. A 2-D axisymmetric approach was also used to analyse the triaxial test. It was found that the stress and strain from the simulation and the experiment broadly matched each other, so the developed subroutine was a promising representation of the behavior of ballast. The initial ground stress was successfully applied in the FEM model in this study. The rail track FEM model was further validated by a comparison between the simulation and

field data that indicated the predictions were acceptable for preliminary design. The effect of train speed on the deformation of a ballasted rail track was studied using the FEM model, and the results showed that train speed had a profound influence on the deformation of ballasted railway track; as the train speed increased the vertical deformation at the ground surface also increased, as expected. The proposed FEM model could capture the response of railway track under different train speeds very well, and therefore it may be used for further track analysis.

CHAPTER 6

CONCLUSIONS AND RECOMMENDATIONS

6.1 Introduction

This research focussed on large-scale laboratory testing and the development and implementation of analytical models within a finite element (FE) framework to predict the overall behaviour of track structure. A constitutive model for ballast inspired by its response to static large-scale triaxial tests was developed, calibrated, validated, and then numerically integrated into FEM. In order to understand the deformation and degradation of ballast under traffic loading, high frequency cyclic tests were also conducted. The following sections provide the major conclusions obtained from this research into the response of ballast under static and cyclic loading, and the modelling and numerical simulation of ballasted rail track. Recommendations for future study are included at the end of this chapter.

6.2 Ballast Response under Static Loading

The deformation and degradation of ballast was assessed using consolidated drained monotonic loading tests by large-scale cylindrical triaxial apparatus. The salient findings of these tests are summarised below:

(1) It was observed that the deviatoric stress q initially increased with increasing deviator strain until it reached a peak value. At a higher confining pressure the peak value of q became higher. At a relatively low confining pressure ($\sigma_3' \leq 60$ kPa), the volumetric strain was initially compressive but it swiftly became dilative as the

deviatoric strain increased, and as expected, the confining pressure increased as the rate of dilation decreased. At an elevated confining pressure ($\sigma_3' \geq 240$ kPa), the overall volumetric response was compressive.

(2) The CSL in the *q-p'* plane is non-linear. The extent of breakage was greater with increasing *p'*, and the drop in *q* was more pronounced as *p'* increased. The CSL in *q-p'* plane can be expressed as: $q = \omega \cdot p'^{\mu}$ (ω and μ are material constants). The critical state stress ratio $M_c = (q/p')_c$ was not a constant for ballast. The changes in the critical state stress ratio (M_c) with confining stress can be attributed to particle breakage. As particle breakage increased, M_c decreased and it can be represented by the expression: $M_c = M_{c0} - [1 - \exp(-\alpha \cdot BBI)]$ (α is the model parameter and M_{c0} = critical state stress ratio for BBI = 0).

(3) The CSL for ballast was no longer a straight line and its location would change in the compression plane with an increase of BBI. The CSL in the *υ-lnp'* plane becomes a critical state surface when the extra dimension of BBI is added. It was proposed that the critical state surface in the *υ-lnp'-BBI* space would be: $\upsilon_c = \Gamma(BBI) - \lambda \ln p'$, where $\Gamma(BBI)$ decreases as BBI increases. Based on the drained compression test data, a hyperbolic relation could be derived for $\Gamma(BBI)$ as: $\Gamma(BBI) = \Gamma_{ref} - a \cdot \exp(b \cdot BBI)$ (Γ_{ref} is the reference value to $\Gamma(BBI)$, and *a* and *b* are material constants controlling the evolution rate of the CSL with particle breakage).

6.3 Ballast Response under Cyclic Loading

The findings from cyclic testing on ballast are as follows:

(1) Three distinct deformation mechanisms exist in response to the *f*, $q_{max,cyc}$ and σ_3', namely Range I: plastic shakedown, Range II: plastic shakedown and ratcheting, and Range III: plastic collapse. Plastic shakedown is acceptable in a track provided the accumulated strains are small enough, but a high value of *f* or $q_{max,cyc}$ could lead to ratcheting (Range II) or plastic collapse (Range III), which should not be tolerated in design.

(2) A range of critical frequencies were identified as 20-30 Hz for σ_3' = 30 kPa and 30-40 Hz for σ_3' = 60 kPa, respectively. The critical train speed decreases as the deformation accumulates. For a track with heavy haul trains, the critical train speed is lower than passenger trains, and an increase in confinement would increase the critical train speed.

(3) For the same *f* and σ_3', a larger $q_{max,cyc}$ generates a higher axial strain. For a constant σ_3', the differences between the values of axial strain under different load magnitudes increase with *f*. Frequency had a more profound effect on axial strain for the specimen with a higher load magnitude. For given values of *f* and $q_{max,cyc}$, an increasing σ_3' produced a smaller axial strain. Distinct deformation mechanisms (i.e. Range I and II) exist with a specific stress states while varying *f* from 5 Hz to 60 Hz.

(4) Large vertical train loads ($q_{max,cyc}$) combined with relatively minor horizontal confining stresses (σ_3') can induce significant shear strains in ballast during cyclic loading, although the values of ε_r increase with $q_{max,cyc}$ and *f* and decrease with σ_3'. Track bed stability decreases as the axle load and train speed increased, whereas

increased confinement would effectively enhance track stability.

(5) The effects of $q_{max,cyc}$ and σ_3' were combined by using the cyclic stress ratio $\Psi = q_{max,cyc}/q_{peak,sta}$. For a constant Ψ value, increasing f from 5 Hz to 40 Hz generated a larger ε_a and ε_r, whereas for f = 5 Hz, ε_a and ε_r increased with Ψ. The Ψ value exceeding 1 indicated that specimens can sustain a much greater deviator stress than statically loaded specimens, but to avoid plastic collapse failure in Range III under high frequency loading, the Ψ value should be less than 1. In a practical sense, empirical relations were readily obtained to predict ε_a and ε_r for given values of f and Ψ by $\varepsilon_a = a \cdot e^{b \cdot f} \cdot \Psi^c$ and $\varepsilon_r = d \cdot f^h \cdot \Psi^k$ respectively (a, b, c, d, h and k are the empirical constants).

(6) The Cyclic Axial Strain Ratio (CASR), $\Phi_a = \varepsilon_{a,cyc}/\varepsilon_{a,sta}$ was defined to consider the effect of frequency on ballast deformation. The Φ_a can be related to f by: $\Phi_a = a \cdot e^{b \cdot f}$. a and b are the empirical coefficients. An accumulated ε_a can be obtained by $\varepsilon_a = a \cdot \exp(0.138 \cdot b \cdot V) \cdot \varepsilon_{a,sta}$ which can be extended to capture the permanent deformation under different loading numbers and frequency by considering a and b as a function of N.

(7) BBI increased as f for specific values of $q_{max,cyc}$ and σ_3'. The degradation of a particle subjected to compressive forces within a granular medium is not only a function of the applied stresses ($q_{max,cyc}$ and σ_3'), so too is the particle size, the number of cycles, the coordination number, and also the load frequency.

(8) Distinct ballast degradation that corresponded to different deformation ranges occurred during cyclic testing. At range I ($f \leq 30$ Hz), particle degradation was in the form of the attrition of asperities and corner breakage, but as the frequency increased

(30 Hz < f < 60 Hz) in Range II, particle splitting caused by fatigue and a high degree of attrition resulting from increased vibration became predominant. At a very high frequency ($f \geq$ 60 Hz) in Range III, the coordination number decreased considerably which would induce particle splitting; indeed the critical frequency decreased as the particle breakage increased. Ratcheting failure (Range II) of the specimen would occur with a significant particle breakage (BBI > 0.10) even at a relatively low frequency.

(9) The BBI, along with f and σ_3' had a profound influence on the magnitude of ε_v, and indeed, an increase in BBI could cause a reduction in the void ratio and a subsequent increase in compressibility of the ballast assemblies. Increased vibration could lead to higher dynamic stress with repeated shearing and compression which could also produce greater densification.

(10) A higher frequency and a higher confining pressure can cause the ballast to become denser, which leads to an increased resilient modulus M_R. The magnitude of M_R increased with $q_{max,cyc}$ and θ. An empirical relationship between M_R, f and θ could be formulated by: $M_R = m \cdot f^n + \theta^t$ (m, n, and t are empirical parameters).

(11) The dynamic amplification factor (DAF) can be used to calculate the dynamic axle load in design. Irrespective of the applied stresses, the variation of DAF was confined within a narrow band when plotted against V and a non-linear best-fit equation for the data in this study could be presented by: $DAF = e^{\alpha \cdot V}$ (α is an empirical parameter). As the axle load increases, a thicker granular layer is required. Given an axle load (i.e. 25 t), when the train speed increases from 50 km/h to 350 km/h, the value of H increases by approximately 120%.

6.4 Ballast Modelling

The theoretical work considering monotonic and cyclic models for ballast are summarised as:

(1) During triaxial shearing, the hardening of ballast depends on ε_s^p, ψ and BBI and this can be reflected by a hyperbolic relationship. The dilatancy of ballast depends not only on η, and ψ but also on BBI. The present study reveals that particle breakage and its implications on the nonlinearity of CSL were successfully captured in the constitutive equations, and the model predictions were encouraging compared to the laboratory data.

(2) The static model proposed in this study can be extended to a cyclic model. By applying the bounding surface plasticity theory and having additional experimental based assumptions on the calculations of the hardening modulus under different loading conditions, the new model can produce some of the essential characteristics of ballast under cyclic loading conditions, such as the effect of cyclic load frequency on densification and dilation, and the effect of shakedown during cyclic loading. The effect of confining pressure on the axial and volumetric strains can also be captured by the cyclic model.

6.5 Numerical Simulation of the Ballasted Rail Track

The numerical investigation for ballasted rail track can be summarised as:

(1) A 2-D axisymmetric approach was used to analyse the triaxial test. It was found that the stress strain response from FEM simulation and laboratory tests matched each other, so the developed subroutine provided a promising representation of ballast behaviour.

Moreover, the FEM model for rail track was validated by a comparison between a numerical simulation and field data, which indicated that the predictions were acceptable for preliminary design.

(2) FEM model found that train speed had a profound influence on the deformation of ballasted railway track, such that as the train speed increased, the vertical deformation at the ground surface increased. The proposed FEM model could capture the response of the railway track under different train speeds and therefore it could be used for further track analysis.

6.6 Recommendations for Further Study

For a more complete understanding of the behaviour of ballasted rail track under heavier axle loads and higher train speeds, the following topics require more attention:

(1) The experiments reported in this thesis were limited to only one type of aggregate, namely latite basalt. Further tests should be conducted to extend the theories introduced in this study to other types of materials. Moreover, only one particle size degradation (PSD) was used in this test program, so another study could focus on different PSDs in order to identify the optimal PSD. Investigating the effect of the degree of compaction or initial density on the performance of ballast would be useful, especially if increased track compaction were to be used to enhance the substructure.

(2) The mechanical response of ballast is largely dominated by particle breakage, which is mainly controlled by the level of stress, but the prevailing relative humidity (RH) in large ballast voids could also influence breakage, so a series of suction-controlled triaxial tests might help us understand the effect of suction on the mechanical behaviour of ballast, and further effort might focus on the development of a relative constitutive

model.

(3) The cyclic model proposed in this study could capture the effect of load frequency on dilation of ballast, but the effect of particle breakage on the deformation of ballast under cyclic loading should be captured in another version.

(4) In the FEM model, the wheel loading was approximately represented by an equivalent dynamic plane strain analysis, the real cyclic nature of wheel loading needs to be considered in order to improve the accurate simulation of the overall behavior of track.

(5) The track model proposed in this study was 2D, which represents a railway track that is homogeneous in the longitudinal direction. To simulate differential settlements induced by the inhomogeneities present in the longitudinal track direction, a 3D cyclic track model is needed to simulate the deformation and degradation of track under traffic loading.

REFERENCES

Al-Hussaini, M. (1983). Effect of particle size and strain on the strength of crushed rock. *5th International Congress on Rock Mechanics*, Melbourne, Australia, 239-243.

Allen, J. (1973). The effect of non-constant lateral pressures of the resilient response of granular materials. Ph.D. thesis, University of Illinois at Urbana-Champaign.

Alonso-Marroquín, F., García-Rojo, R. & Herrmann, H. J. (2004). Micro-mechanical investigation of the granular ratcheting. *Proc. Int. Conf. on Cyclic behaviour of Soils and Liquefaction Phenomena*, Bochum, Germany, 3-10.

Alva-Hurtado, J. E. (1980). A methodology to predict the elastic and inelastic behaviour of railroad ballast. Report No. OUR80-240D. Department of Civil Engineering, University of Massachusetts, Massachusetts, USA.

American Railway Engineering Association (AREA). (1996). Manual for railway engineering, 1, Washington, D. C.

Anandarajah, A. (1994). A constitutive model for granular materials based on associated flow rule. *Soils and Foundations* **34** No. 3, 81-98.

Anderson, W. F. & Key, A. J. (2000). Model testing of two layer railway track ballast. *Journal of Geotechnical and Geoenvironmental Engineering* **126**, No. 4, 317-323.

Anderson, W. F., and Fair, P. (2008). Behaviour of railroad ballast under monotonic and cyclic loading. *Journal of Geotechnical and Geoenvironmental Engineering, ASCE* **134,** No. 3, 316-327.

Aravas, N. (1987). On the numerical integration of a class of pressure dependent plasticity models. *International Journal for Numerical Methods in Engineering*

24, No. 7, 1395-1416.

Armstrong, P. J. & Frederick, C. O. (1966). A mathematical representation of the multiaxial bauscinger effect. *CEGB Report* No. RD/B/N 731.

Aursudkij, B., McDowell, G. B., Collop, A. C. (2009). Cyclic loading of railway ballast under triaxial conditions and in a railway test facility. *Granular Matter* **11,** No. 6, 391-401.

Bandini, P. M. & Pham, S. M. (2011). Bearing capacity of embedded strip footings in two-layered clay soil. *Geo-Frontiers ASCE*, 332-341.

Bandini, V. & Coop, M. R. (2011). The influence of particle breakage on the location of the critical state line of sands. *Soil and Foundations* **51,** No.4, 591-600.

Banimahd, M. & Woodward, P. K. (2006). Load-displacement and bearing capacity of foundations on granular soils using a multi-surface kinematic constitutive soil model. *Int. J. Numer. Anal. Meth. Geomech*. **30**, 865-886.

Banimahd, M., Woodward, P., Kennedy, J. & Medero, G. (2013). Three-dimensional modelling of high speed ballasted railway tracks. *Proc. Inst. Civ. Eng. Transp.* **166**, 113-123.

Bardet, J. P. (1985). Application of bounding surface plasticity to cyclic sand behaviour. *Proceedings of the Second International Conference on Soil Dynamics and Earthquake Engineering*, 2-16.

Bardet, J. P. (1986). A bounding surface plasticity model for sands. *Journal of Engineering Mechanics, ASCE* **112**, No. 11, 1198-1217.

Bardet, J. P. (1995). A scaled memory model for the undrained behaviour of anisotropic clays. *Journal of Geotechnical Engineering, ASCE* **121,** No. 1, 755-764.

Barksdale, R. D. (1972). Laboratory evaluation of rutting in basecourse materials. *Proc., 3rd Int. Conf. on Struct. Des. of Asphalt Pavements*, 161-174.

Barton, N. & Kjaernsli, B. (1981). Shear strength of rockfill. *Journal of the Geotechnical Engineering Division, ASCE* **107**, No. GT7, 873-891.

Bedin, J., Schnaid, F., Da Fonseca, A. V. and De M. Coasta Filho, L. (2012). Gold tailings liquefaction under critical state soil mechanics. *Géotechnique* **62**, No.3, 263-267.

Been, K. & Jefferies, M. G. (1985). A state parameter for sands. *Géotechnique* **35**, No. 2, 99-112.

Been, K., Jefferies, M. G., and Hachey, J. (1991). The critical state of sands. *Géotechnique* **41,** No. 3, 365-381.

Belytschko, T., Guo, Y., Liu, W. K. & Xiao, S. P. (2000). A unified stability analysis of meshless particle methods. *International Journal for Numerical Methods in Engineering* **48**, No. 9, 1359-1400.

Billam, J. (1971). Some aspects of the behaviour of granular materials at high pressures. *Stress-strain behaviour of soils, Proceedings of the Roscoe Memorial Symposium*, 69-79.

Bishop, A. W. (1966). The strength of soils as engineering materials. *Géotechnique* **16**, 91-128.

Blazquez, R. and Lopez-Querol, S. (2006). Generalized densification law for dry sand subjected to dynamic loading. *Soil Dyn. Earthq Engng.* **26**, No. 9, 888-898.

Brown, S. F. (1974). Repeated load testing of a granular material. *Journal of the Geotechnical Engineering Division, ASCE* **100**, No. GT7, 825-841.

Brown, S. F., Lashine, A. K. F. and Hyde, A. F. L. (1975). Repeated load triaxial testing of silty clay. *Géotechnique* 25, No. 1, 95-114.

Calladine, C. R. (2000). Plasticity for engineers: theory and applications. Horwood Publishing, Chichester.

Carrera, A., Coop, M. R. and Lancellotta, R. (2011). The Influence of grading on the mechanical behaviour of Stava tailings. *Géotechnique* **61**, No. 11, 935–946.

Charles, J. A. & Watts, K. S. (1980). Drained permanent deformation of sand due to cyclic loading. *Journal of Geotechnical Engineering* **114**, No. 10, 1164-1179.

Charles, J. A. and Watts, K. S. (1980). The influence of confining pressure on the shear strength of compacted rockfill. *Géotechnique* **30**, No. 4, 353-367.

Chavez, C., and Alonso, E. F. (2003). A constitutive model for crushed granular aggregates which includes suction effects. *Soils and Foundations* **43**, No. 4, 215-227.

Chen, W. F. & Han, D. J. (1988). Plasticity for structural engineers. Springer Verlag, New York.

Cheng, Y. P., Bolton, M. D. and Nakata, Y. (2005). Grain crushing and critical states observed in DEM simulations. *Powers and Grains 2005-Proceedings of the 5th International Conference on Micromechanics of Granular Media* **2,** 1393-1397.

Coop, M. R. (1990). The mechanics of uncemented carbonate sands. *Géotechnique* **40**, No. 4, 607-626.

Coop, M. R., Sorensen, K. K., Bodas Freitas, T. & Georgoutsos, G. (2004). Particle breakage during shearing of a carbonate sand. *Géotechnique* **54,** No. 3, 157-163.

Dafalias, Y. F. & Herrmann, L. R. (1980). A bounding surface soil plasticity model. *Proc. Int. Symp. On Soils under Cyclic and Transient Loading*, Swansea, U. K., 335-345.

Dafalias, Y. F. & Herrmann, L. R. (1982). Bounding surface formulation of soil plasticity. *In: Soil Mechanics-Transient and Cyclic Loads* (edited by Pande and Zienkiewicz). John Wiley & Sons, 253-282.

Dafalias, Y. F. & Popov, E. P. (1975). A model of nonlinearly hardening materials for

complex loadings. *Acta Mech.* **21**, 173-192.

Daouadji, A., Hicher, P. Y., and Rahma, A. (2001). An elastoplastic model for granular materials taking into account grain breakage. *European Journal of Mechanics A-Solids* **20**, No. 1, 113-137.

Desai, C. S. (1974). A consistent finite element technique for work softening behaviour. *Proc. Int. Conf. on Computer Methods in Nonlinear Mechanics*, University of Texas, Austin, TX.

Desai, C. S. (2007). Unified DSC constitutive model for pavement materials with numerical implementation. *International Journal of Geomechanics, ASCE* **7** No. 2, 83-101.

Eisenmann, J., Leykauf, G. & Mattner, L. (1994). Recent development in German railway track design. *Proc. Inst. Civ. Eng. Transp.* **105**, 91-96.

Esveld, C. (2001). Modern railway track. Zaltbommel, MRT Productions, Zaltbommel, Netherlands.

Ge, Y. N. (2003). Cyclic constitutive modelling of granular materials. PhD thesis, University of Colorado at Boulder, USA.

Griffiths, D. V. (1982). Computation of bearing capacity factors using finite elements. *Géotechnique* **32**, No. 3, 195-202.

Han, J. & Jiang, G. (2011). Influence of inclined bedrock on undrained bearing capacity of shallow strip foundations. *Geo-Frontiers ASCE*, 322-331.

Han, W. & Reddy, B. D. (1999). Plasticity: mathematical theory and numerical analysis. Springer, New York.

Hardin, B. O. (1985). Crushing of soil particles, *Journal of Geotechnical Engineering* **111** No. 10, 1177-1192.

Henkel, D. J. and Gilbert, G. D. (1952). The effect of the rubber membrane on the

measured triaxial compression strength of clay samples. *Géotechnique* **3**, No. 1, 20-29.

Hicks, R. G. (1970). Factors influencing the resilient properties of granular materials. Ph.D. thesis, University of California.

Hill, R. (1950). The mathematical theory of plasticity. Oxford University Press, Oxford, UK.

Indraratna, B, Ionescu, D. & Christie, H. D. (1998). Shear behaviour of railway ballast based on large-scale triaxial tests. *Journal of Geotechnical and Geoenvironmental Engineering* **124** No. 5, 439-449.

Indraratna, B. & Nimbalkar, S. (2011). Implications of ballast breakage on ballasted railway track based on numerical modelling. *Proceedings of 13th International Conference of International Association for Computer Methods and Advances in Computational Mechanics (IACMAG 2011)*, Melbourne, Australia, 1085-1092.

Indraratna, B. & Nimbalkar, S. (2013). Stress-strain degradation response of railway ballast stabilized with geosynthetics. *Journal of Geotechnical and Geoenvironmental Engineering* **139**, No. 5, 684-700.

Indraratna, B. & Salim, W. (2002). Modelling of particle breakage of coarse aggregates incorporating strength and dilatancy. *Proceedings of Institute of Civil Engineers*, London **155**, No. 4, 243-252.

Indraratna, B. Wijewardena, L. S. S. & Balasubramaniam, A. S. (1993). Large-scale triaxial testing of grey wacke rockfill. *Géotechnique* **1**, No. 1, 37-51.

Indraratna, B., Ionescu, D. & Christie, H. D. (1998). Shear behaviour of railway ballast on large-scale triaxial tests. *J. of Geotech. Geoenviron. Engng ASCE* **124**, No. 5, 439-449.

Indraratna, B., Lackenby, J. & Christie, D. (2005). Effect of confining pressure on the

degradation of ballast under cyclic loading. *Géotechnique* **55**, No. 4, 325-328.

Indraratna, B., Nimbalkar, S. & Rujikiatkamjorn, C. (2014b). Enhancement of rail track performance through utilisation of geosynthetic inclusions. *Geotech. Engng J. SEAGS & AGSSEA* **45**, No. 1, 17-27.

Indraratna, B., Nimbalkar, S. & Rujikiatkamjorn, C. (2014c). From theory to practice in track geomechanics - Australian perspective for synthetic inclusions. *Transport Geotech* **1**, No. 4, 171-187.

Indraratna, B., Nimbalkar, S., Christie, D., Rujikiatkamjorn, C. and Vinod, J. S. (2010b). Field assessment of the performance of a ballasted rail track with and without geosynthetics. *J. Geotech. Geoenviron. Engng ASCE* **136**, No. 7, 907-917.

Indraratna, B., Nimbalkar, S., Coop, M. and Sloan, S. W. (2014a). A constitutive model for coal-fouled ballast capturing the effects of particle degradation. *Computers & Geotechnics* **61**, 96-107.

Indraratna, B., Salim, W., and Rujikiatkamjorn, C. (2011). Advanced Rail Geotechnology-Ballasted Track. CRC Press.

Indraratna, B., Sun, Q. D. and Nimbalkar, S. (2015). Observed and predicted behaviour of rail ballast under monotonic loading capturing particle breakage. *Canadian Geotechnical Journal* **52** (1), 73-86.

Indraratna, B., Thakur, P. K. & Vinod, J. S. (2010a). Experimental and numerical study of railway ballast behaviour under cyclic loading. *Int. J. Geomech*. **10**, No. 4, 136-144.

Indraratna, B., Vinod, J. S. and Lackenby, J. (2009). Influence of particle breakage on the resilient modulus of railway ballast. *Géotechnique* **59**, No. 7, 643-646.

Iwan, W. D. (1967). On a class of models for the yielding behaviour of continuous and composite systems. *Journal of Applied Mechanics* **34** No. 3, 612-617.

Jefferies, M. G. (1993). Nor-sand: a simple critical state model for sand. *Géotechnique* **43**, No. 1, 91-103.

Jeffs, T. (1989). Towards ballast life cycle costing. *The 4th International Heavy Haul Railway Conference*, Brisbane, Australia, 439-445.

Karg, C. & Haegeman, W. (2009). Elasto-plastic long-term behaviour of granular soils: Experimental investigation. *Soil Dyn. Earthq Engng.* **29**, No. 1, 155-172.

Kempfert, H. G. & Hu, Y. (1999). Measured dynamic loading of railway underground. *Proc. 11th Pan-American Conf. on Soil Mechanics and Geotechnical Engineering*, Brazil, 843-847.

Khalili, N., Habte, M. A. & Valliappan, S. (2005). A bounding surface plasticity model for cyclic loading of granular soils. *International Journal for Numerical Methods in Engineering* **63**, No. 14, 1939-1960.

Kim, D. S., Kweon, G. C. and Lee, K. H. (2001). Alternative method of determining resilient modulus of subgrade soils using static triaxial test. *Can. Geotech. J.* **38**, No. 1, 107-116.

Klisinski, M. (1988). Plasticity theory based on fuzzy sets. *Journal of Engineering Mechanics, ASCE* **114**, No. 4, 563-582.

Koiter, W. T. (1953). Stress-strain relations, uniqueness and variational theorems for elastic-plastic materials singular yield surface. *Quart. Appl. Math.* **11**, 350-354.

Krieg, R. D. (1975). A practical two surface plasticity theory. *J. of Applied Mechanics, ASME* **42**, 641-646.

Lackenby, J. (2006). Triaxial behaviour of ballast and the role of confining pressure under cyclic loading. PhD thesis, Department of Civil Engineering, University of Wollongong, NSW, Australia.

Lackenby, J., Indraratna, B., McDowell, G. & Christie, D. (2007). Effect of confining

pressure on ballast degradation and deformation under cyclic triaxial loading. *Géotechnique* **57**, No. 6, 527-536.

Lade, P. V. (1977). Elasto-plastic stress-strain theory for cohesionless soil with curved yield surfaces. *International Journal of Solids and Structures* **13**, 1019-1035.

Lade, P.V., Yamamuro, J. A., and Bopp, P. A. (1996). Significance of particle crushing in granular materials. *Journal of Geotechnical Engineering, ASCE* **122**, No. 4, 309-316.

Lambe, T. W. and Whitman, R. V. (1969). Soil mechanics, John Wiley & Sons, Inc., London.

Lee, K. L. & Seed, H. B. (1967). Drained strength characteristics of sands. *Journal of the Soil Mechanics and Foundation Division, ASCE* **93**, No. 6, 117-141.

Lee, K. L. and Farhoomand, I. (1967). Compressibility and crushing of granular soil in anisotropic triaxial compression. *Canadian Geotechnical Journal* **4**, No. 1, 69-86.

Lekarp, F., Isacsson, U. and Dawson, A. (2000). State of the art. I: Resilient response of unbound aggregates. *J. Transp. Eng.* **126**, No. 1, 66-75.

Leshchinsky, B. & Ling, H. (2013). Effects of geocell confinement on strength and deformation behaviour of gravel. *J. Geotech, Geoenviron, Eng*. **139**, No. 2, 340-352.

Li, D. Q. and Selig, E. T. (1998a). Method for Railroad track foundation design. I: Development. *J. Geotech. Geoenviron. Engng ASCE* **124**, No. 4, 316-322.

Li, D. Q. and Selig, E. T. (1998b). Method for Railroad track foundation design. II: Applications. *J. Geotech. Geoenviron. Engng ASCE* **124**, No. 4, 323-329.

Li, X. S., and Dafalias, Y. F. (2000). Dilatancy for cohesionless soils. *Géotechnique* **50**, No. 4, 449-460.

Liu, J. K. & Xiao, J. H. (2010). Experimental study on the stability of railroad silt subgrade with increasing train speed. *J. Geotech Geoenviron Eng*, **136**, No. 6, 833-841.

Lubliner, J. (1990). Plasticity theory. Macmillan, New York.

Luo, Y., Yin, H. & Hua, C. (1996). Dynamic response of railway ballast to the action of trains moving at different speeds. *Proc. IMechE, Part F: J. of Rail and Rapid Transit* **210**, No. 2, 95-101.

Luong, M. P. (1982). Stress-strain aspects of cohesionless soils under cyclic and transient loading. *International Symposium on Soil under Cyclic and Transient Loading*, A. A Balkema, Rotterdam, 315-324.

Maeda, K. & Miura, K. (1999). Confining stress dependency of mechanical properties of sand. *Soils and Foundations* **39,** No. 1, 53-67.

Maniharan, N. & Dasgupta, S. P. (1995). Bearing capacity of surface footings by finite elements. *Computers and Structures* **54**, No. 4, 563-586.

Manzari, M. T., and Dafalias, Y. F. (1997). A critical state two-surface plasticity model for sands. *Géotechnique* **47**, No. 2, 255-272.

Marachi, N. D., Chan, C. K. and Seed, H. B. (1972). Evaluation of properties of rockfill materials. *Journal of the Soil Mechanics and Foundations Division, ASCE* **98**, No. 1, 95-114.

Marsal, R. J. (1967). Large-scale testing of rockfill materials. *Journal of the Soil Mechanics and Foundations Division, ASCE* **93**, No. 2, 27-43.

Marsal, R. J. (1973). Mechanical properties of rockfill. *Embankment Dam Engineering*, New, York, 109-200.

Marschi, N. D., Chan, C. K. & Seed, H. B. (1972). Evaluation of properties of rockfill materials. *Journal of the Soil Mechanics and Foundation Division, ASCE* **98**,

No. 1, 95-114.

McDowell, G. R. & Bolton, M. D. (1998). On the micromechanics of crushable aggregates. *Géotechnique* **48**, No. 5, 667-679.

McDowell, G. R. & Daniell, C. M. (2001). Fracture compression of soil. *Géotechnique* **51**, No. 2, 173-176.

McDowell, G. R., Bolton, M. D. and Robertson, D. (1996). The fractal crushing of granular materials. *J. Mech. Phys. Solids* **44**, No. 12, 2079-2102.

Merifield, R. S. & Nguyen, V. Q. (2006). Two and three dimensional bearing capacity solutions for footings two layered clays. *Geomechanics and Geoengineering: An International Journal* **1**, No. 2, 151-162.

Mirghasemi, A. A., Rothenburg, L & Matyas, E. L. (1997). Numerical simulations of assemblies of two-dimensional polygon-shaped particles and effects of confining pressure on shear strength. *Soils and Foundations* **37**, No. 3, 43-52.

Miura, N. & O'Hara, S. (1979). Particle crushing of a decomposed granite soil under shear stresses. *Soil and Foundations* **19**, No. 3, 1-14.

Mooney, M. A., Finno, R. J. & Viggiani, M. G. (1998). A unique critical state for sand? *Journal of Geotechnical and Geoenvironmental Engineering ASCE* **124**, No. 11, 1100-1108.

Morz, Z. & Norris, V. A. (1982). Elastoplastic and viscoplastic constitutive models for soils with application to cyclic loading. *In: Soil Mechanics-Transient and Cyclic Loads* (edited by Pande and Zienkiewicz). John Wiley & Sons, 173-217.

Mroz, Z. (1967). On the description of anisotropic hardening. *Journal of Mechanics and Physics of Solids* **15**, 163-175.

Mroz, Z., Norris, V. A. & Zienkiewicz, O. C. (1978). An anisotropic hardening model for soils and its application to cyclic loading. *International Journal of Numerical*

and Analytical Methods in Geomechanics **2**, 203-221.

Muir Wood, D., Belkheir, K. & Liu, D. F. (1994). Strain softening and state parameter for sand modelling. *Géotechnique* **44**, No. 2, 335-339.

Muir Wood. D. & Maeda, K. (2008). Changing grading of soil: effect on critical states. *Acta Geotechnica* **3**, No. 1, 3-14.

Nayak, G. C. & Zienkiewicz, O. C. (1972). Elasto-plastic stress and analysis: a generalization for various constitutive relations including strain softening. *Int. J. Num. Meth. Engng.* **5**, 113-135.

Ni, J., Indraratna, B., Geng, X. Y., Carter, J. P. & Rujikiatkamjorn, C. (2013). Radial consolidation of soft soil under cyclic loads. *Couput Geotech*, **50**, No. 1, 1-5.

Nimbalkar, S., Indraratna, B., Dash, S. K. & Christie, D. (2012). Improved performance of railway ballast under impact loads using shock mats. *Journal of Geotechnical and Geoenvironmental Engineering, ASCE* **138**, No. 3, 281-294.

Owen, D. R. J. & Hinton, E. (1980). Finite elements in plasticity. Pineridge Press Limited, Swansea, U. K.

Ozel, M. R. & Mohajerani, A. (2001). Resilient modulus of a stabilised fine grained subgrade soil. *Australian Geomechanics* **36**, No. 3, 75-86.

Pender, M. J. (1978). A model for the behaviour of overconsolidated soil. *Géotechnique* **28**, No. 1, 1-25.

Penman, A. D. M. (1978). The behaviour of rockfill dams. *Geotechnical Engineering* **9**, 105-122.

Ponce, V. M. & Bell, J. M. (1971). Shear strength of sand at extremely low pressures. *Journal of Soil Mechanics and Foundation Engineering, ASCE* **97**, No. SM4, 625-637.

Powrie, W., Yang, L. A. & Clayton, C. R. I. (2007). Stress changes in the ground below

ballasted railway track during train passage. *Proc. IMechE. Part F: J. of Rail and Rapid Transport* **211** No. F2, 247-261.

Prevost, J. H., Cuny, B., Hughes, T. J. R. & Scott, R. F. (1981). Offshore gravity structures: analysis. *Journal of Geotechnical Engineering, ASCE* **107**, 143-165.

Priest, J. A. & Powrie, W. (2009). Determination of dynamic track modulus from measurement of track velocity during train passage. *J. Geotech. Geoenviron. Engng ASCE* **135**, No. 11, 1732-1740.

Provest, J. H. & Hoeg, K. (1975). Soil mechanics and plasticity analysis of strain softening. *Géotechnique* **25**, No. 2, 279-297.

Provest, J. H. (1977). Mathematical modelling of monotonic and cyclic undrained clay behaiviour. *International Journal for Numerical and Analytical Methods in Geomechanics* **1**, No. 2, 195-216.

Raymond, G. P. & Davies, J. R. (1978). Triaxial tests on dolomite railroad ballast. *Journal of the Soil Mechanics and Foundation Division, ASCE* **104**, No. 6, 737-751.

Raymond, G. P., Gaskin, P. N. & Svec, O. (1975). Selection and performance of railroad ballast. *Railroad track mechanics and technology*, Kerr, R., ed., Princeton, NJ, 369-385.

Raymond, G. P. & Williams, D. R. (1978). Repeated load triaxial tests on dolomite ballast. *J. Geotech. Engng Div. ASCE* **104**, No. GT7, 1013-1029.

Roscoe, K. H. & Burland, J. B. (1968). On the generalized stress-strain behaviour of wet clay. *Engineering Plasticity*, 535-609.

Roscoe, K. H., Schofield, A. N. & Thurairajah, A. (1963). Yielding of clays in states wetter than critical. *Géotechnique* **13**, No. 3, 211-240.

Roscoe, K. H., Schofield, A. N. & Wroth, C. P. (1958). On yielding of soils.

Géotechnique **8**, No. 1, 22-53.

Russell, A. R. & Khalili, N. (2004). A bounding surface plasticity model for sands exhibiting particle crushing. *Canadian Geotechnical Journal* **41**, No. 6, 1179-1192.

Sadrekarimi, A. & Olson, S. M. (2011). Critical state friction angle of sands. *Géotechnique* **61**, No. 9, 771-783.

Salim, W. & Indraratna, B. (2004). A new elastoplastic constitutive model for coarse granular aggregates incorporating particle breakage. *Canadian Geotechnical Journal* **41**, No. 4, 657-671.

Schofield, A. N. & Wroth, C. P. (1968). Critical state soil mechanics. McGraw Hill.

Selig, E. T. & Waters, J. M. (1994). *Track geotechnology and substructure management*. Thomas Telford, London.

Shao, C. & Desai, C. S. (2000). Implementation of DSC model and application for analysis of field pile tests under cyclic loading. *International Journal of Numerical and Analytical Methods in Geomechanics* **24**, No. 6, 601-624.

Simo, J. C. & Hughes, T. J. R. (1998). Computational inelasticity. Springer, New York.

Simo, J. C. & Taylor, R. L. (1985). A unified approach to finite deformation elastoplascit analysis based on the use of hyper-elastic constitutive equations. *Computer Methods in Applied Mechanics and Engineering* **49**, 221-245.

Simo, J. C. & Taylor, R. T. (1986). A return mapping algorithm for plane stress elastoplasticity. *International Journal for Numerical Methods in Engineering* **22**, No. 3, 649-670.

Sitharam, T. G. (1999). Micromechanical modelling of granular materials: effect of confining pressure on mechanical behaviour. *Mechanics of Materials* **31**, 653-665.

Sloan, S. W., Krabbenhøft, K. & Lyamin, A. V. (2008). Lower bound shakedown analysis in geotechnics. *Proc. 12th Int. Conf. of International Association for Computer Methods and Advances in Geomechanics (IACMAG)*. Goa, India, 328-335.

Standards Australia. (1996). Aggregates and rock for engineering purposes. 7: Railway ballast. AS 2758.7, New South Wales, Australia, 1996.

Stewart, H. E. (1986). Permanent strains from cyclic variable-amplitude loadings. *Journal of Geotechnical Engineering* **112**, No. 6, 646-660.

Sture, S. Mould, J. C. & Ko., H.-Y. (1982). Modelling of elastic-plastic anisotropic hardening constitutive model and prediction of behaviour of dry quartz sand. *In: Constitutive Relations for Soils*, A. A. Balkema, Rotterdam, Netherlands, 227-248.

Suiker, A. S. J. & de Borst, R. (2003). A numerical model for the cyclic deterioration of railway tracks. *Int. J. Numer. Meth. Engng.* **57**, No. 4, 441-470.

Suiker, A. S. J. (2002). The mechanical behaviour of ballasted railway tracks. PhD thesis, Delft University, Netherlands.

Suiker, A. S. J., Selig, E. T. & Frenkel, R. (2005). Static and cyclic triaxial testing of ballast and subballast. *J. Geotech. Geoenviron. Engng ASCE* **131,** No. 6, 771-782.

Sun, Q. D., Indraratna, B. & Nimbalkar, S. (2014). Effect of cyclic loading frequency on the permanent deformation and degradation of railway ballast. *Géotechnique* **64**, No. 9, 746-751.

Sweere, G. T. H. (1990). Unbound granular bases for roads. PhD thesis, University of Delft, Delft, The Netherlands.

Thakur, P. K., Vinod, J. S. & Indraratna, B. (2013). Effect of confining pressure and

frequency on the deformation of ballast. *Géotechnique* **63**, No. 9, 786-790.

Ueng, T. S. & Chen, T. J. (2000). Energy aspects of particle breakage in drained shear of sands. *Géotechnique* **50**, No. 1, 65-72.

US Army Corps of Engineers Track Design Manual. (2000). TI-850-02, AIR FORECE AFMAN 32-1125(1).

Varadarajan, A., Sharma, K. G., Venkatachalam, K. & Gupta, A. K. (2003). Testing and modeling two rockfill materials. *Journal of Geotechnical and Geoenvironmental Engineering, ASCE* **129**, No. 3, 206-218.

Vermeer, P. A. (1982). A five-constant model unifying well-established concepts. *In: Constitutive Relations for Soils*, A. A. Balkema, Rotterdam, Netherlands, 175-198.

Vesic, A. S. & Clough, G. W. (1968). Behaviour of granular materials under high stresses. *Journal of the soil mechanics and foundation division, ASCE* **94**, No. 3, 661-688.

Werkmeister, S., Dawson, A. R. & Wellner, F. (2001). Permanent deformation behaviour of granular materials and the shakedown concept. *Transportation Research Record* **1757**, 75-81.

Wichtmann, T., Niemunis, A. & Triantafyllidis, T. (2005). Strain accumulation in sand due to cyclic loading: drained triaxial tests. *Soil Dyn. Earthq Engng.* **25**, No. 12, 967-979.

Yamamuro, J. A. & Lade, P. V. (1996). Drained sand behaviour in axisymmetric tests at high pressures. *Journal of Geotechnical Engineering* **122**, No. 2, 109-119.

Yang, L. A., Powrie, W. & Priest, J. A. (2009). Dynamic stress analysis of a ballasted railway track bed during train passage. *J. Geotech, Geoenviron, Eng*. **135**, No. 5, 680-689.

Youd, T. L. (1972). Compaction of sands by repeated shear straining. *J. Soil Mech. Found. Div. ASCE* **98**, No. SM7, 709-734.

Zaman, M., Chen, D-H & Laguros, J. (1994). Resilient moduli of granular materials. *Journal of Transportation Engineering* **120,** No. 6, 967-988.

Zhou, J. & Gong, X. N. (2001). Strain degradation of saturated clay under cyclic loading. *Can Geotech J*, **38**, No. 1, 208-212.

Zhu, M. (2004). Bearing capacity of strip footings on two-layer clay soil by finite element method. *Proceeding of ABAQUS User's Conference*, 777-787.

Zienkiewicz, O. C., Valliapan, S. & King, I. P. (1969). Elasto-plastic solutions of engineering problems: Initial stress finite element approach. *Int. J. Numer. Methods Engrg.* **1**, 75-100.

APPENDIX A

EXAMPLE OF ESTIMATION OF CRITICAL STATE

Figure A1(a) shows an example of a test (σ_3' = 60 kPa) that was stopped when the volumetric strain was still changing slightly. The value of stress ratio at the critical state, $(q/p')_{cs}$, has been predicted from the stress-dilatancy graph (Figure A1(b)) for the test, extending the last part of the curve to the point of intersection with the zero dilatancy axis (Carrera et al. 2011). The rate of volumetric strain, $\delta\varepsilon_v/\delta\varepsilon_s$, plotted against the stress ratio was used to assess dilatancy, where ε_v is volumetric strain and ε_s is deviatoric strain. The $(q/p')_{cs}$ value was determined as 2.17.

The separation between the region of compression and the region of dilation for drained tests on ballast occurs at the phase transformation state at which dilatancy $\delta\varepsilon_v/\delta\varepsilon_s = 0$, as shown in Figure A1(a). The phase transformation state and the critical state are very similar, as discussed by Luong (1982). For dense ballast or ballast at low confining pressure, the phase transformation state is reached at small strain magnitudes, as indicated in Figure A1(a), while the critical state is reached at large strains. Hence, the phase transformation state can be used to give the most appropriate value of $(q/p')_{cs}$ which was determined as 2.15.

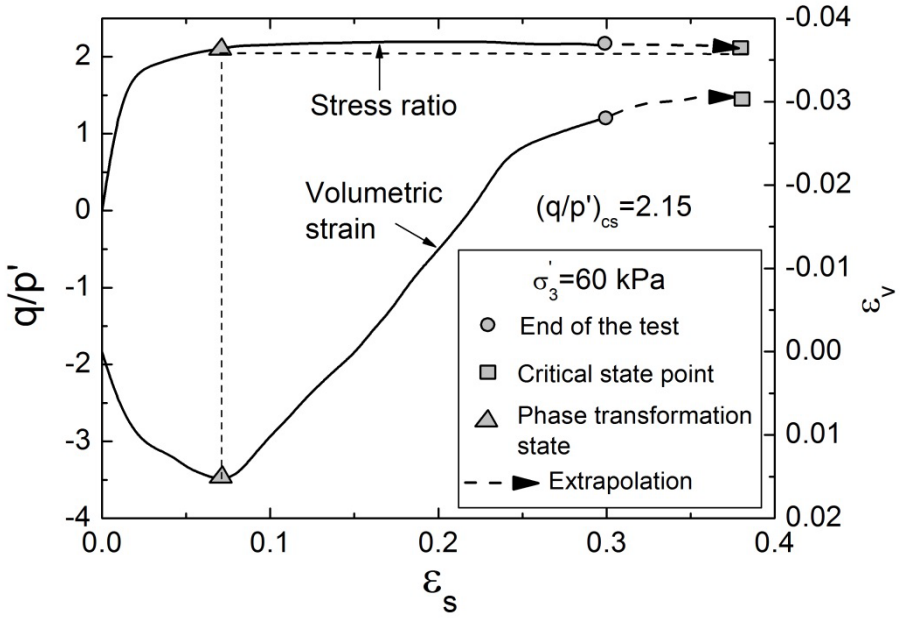

(a)

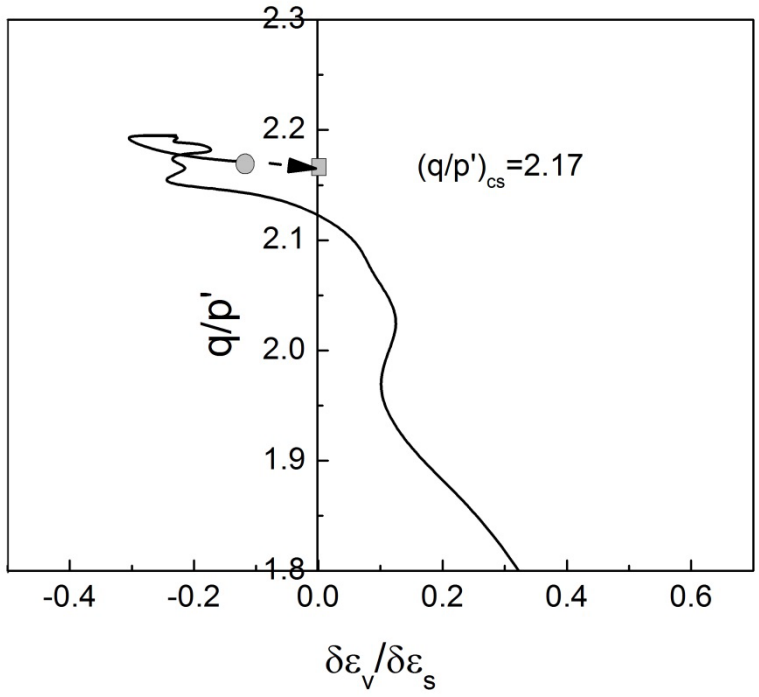

(b)

Figure A1. (a) An example of test (σ_3' = 60 kPa) that ended before reaching the critical state; (b) estimation of the critical state stress ratio by means of stress-dilatancy based approach

REFERENCES

Carrera, A., Coop, M. R. and Lancellotta, R. (2011). The Influence of grading on the mechanical behaviour of Stava tailings. *Géotechnique* **61**, No. 11, 935–946.

Luong, M. P. (1982). Stress-strain aspects of cohesionless soils under cyclic and transient loading. *International Symposium on Soil under Cyclic and Transient Loading*, A. A Balkema, Rotterdam, 315-324.

APPENDIX B

DERIVATION OF HARDENING MODULUS H

According to generalized plasticity, hardening modulus is defined as:

$$H = -\frac{\partial f}{\partial \eta_s}\frac{\partial \eta_s}{\partial \varepsilon_s^p}\frac{\partial g}{\partial q} \tag{B1}$$

The linear yield function is expressed as:

$$f = q / p' - \eta_s = 0 \tag{B2}$$

where,

$$\eta_s = \frac{\varepsilon_s^p}{B_m + \varepsilon_s^p} M_c \left(1 - k_p \psi\right) \tag{B3}$$

Partial differentiation of Equation (B2) yields:

$$\partial f / \partial \eta_s = -1 \tag{B4}$$

Partial differentiation of Equation (B3) gives:

$$\frac{\partial \eta_s}{\partial \varepsilon_s^p} = \partial\left(\frac{\varepsilon_s^p}{B_m + \varepsilon_s^p}\right) \Big/ \partial \varepsilon_s^p \; M_c\left(1 - k_p\psi\right) + \frac{\varepsilon_s^p}{B_m + \varepsilon_s^p}\frac{\partial M_c}{\partial \varepsilon_s^p}\left(1 - k_p\psi\right) + \frac{\varepsilon_s^p}{B_m + \varepsilon_s^p} M_c \frac{\partial\left(1 - k_p\psi\right)}{\partial \varepsilon_s^p} \tag{B5}$$

with,

$$\partial\left(\frac{\varepsilon_s^p}{B_m+\varepsilon_s^p}\right)\Big/\partial\varepsilon_s^p=\frac{B_m}{\left(B_m+\varepsilon_s^p\right)^2} \tag{B6}$$

Critical state stress ratio can be expressed:

$$M_c=M_{c0}-\left\{1-\exp\left[-\alpha\frac{\theta_b\left(1-\exp\left(-\nu_b\varepsilon_s^p\right)\right)}{\omega_b-\ln p_i^{'}}\right]\right\} \tag{B7}$$

Partial differentiation of Equation (B7) gives:

$$\frac{\partial M_c}{\partial\varepsilon_s^p}=-\frac{\alpha\theta_b\nu_b}{\omega_b-\ln p_i^{'}}\exp\left(-\nu_b\varepsilon_s^p\right)\exp\left\{-\alpha\frac{\theta_b\left[1-\exp\left(-\nu_b\varepsilon_s^p\right)\right]}{\omega_b-\ln p_i^{'}}\right\} \tag{B8}$$

The state parameter is expressed as:

$$\psi=\upsilon-\Gamma_{ref}+a\cdot\exp\left\{b\cdot\frac{\theta_b\left[1-\exp\left(-\nu_b\varepsilon_s^p\right)\right]}{\omega_b-\ln p_i^{'}}\right\}+\lambda\ln p^{'} \tag{B9}$$

Substituting Equation (B9) into expression $1-k_p\psi$ and taking partial differentiation of it give:

$$\frac{\partial\left(1-k_p\psi\right)}{\partial\varepsilon_s^p}=-\frac{k_pab\theta_b\nu_b}{\omega_b-\ln p_i^{'}}\exp\left(-\nu_b\varepsilon_s^p\right)\exp\left\{b\frac{\theta_b\left[1-\exp\left(-\nu_b\varepsilon_s^p\right)\right]}{\omega_b-\ln p_i^{'}}\right\} \tag{B10}$$

Third term in Equation (B1) can be expressed as:

$$\frac{\partial g}{\partial q}=1 \tag{B11}$$

where g is the plastic potential function.

Substituting Equations (B4), (B5) and (B11) into eq. (B1), H is expressed as:

$$H = \frac{1}{\left(B_m + \varepsilon_s^p\right)}\left\{\frac{B_m M_c\left(1-k_p\psi\right)}{B_m+\varepsilon_s^p} - \frac{\varepsilon_s^p \theta_b \nu_b}{\omega_b - \ln p_i^{'}}\exp\left(-\nu_b\varepsilon_s^p\right)\left\{\alpha\left(1-k_p\psi\right)\exp\left\{-\frac{\alpha\theta_b\left[1-\exp\left(-\nu_b\varepsilon_s^p\right)\right]}{\omega_b-\ln p_i^{'}}\right\}\right.\right.$$

$$\left.\left.\left. + M_c\exp\left\{\frac{b\theta_b\left[1-\exp\left(-\nu_b\varepsilon_s^p\right)\right]}{\omega_b-\ln p_i^{'}}\right\}\right\}\right\} \qquad \text{(B12)}$$

APPENDIX C

DETERMINATION OF ELASTIC SHEAR MODULUS *G*

The elastic shear modulus *G*, can be evaluated from stress-strain data of triaxial shearing, as shown in Figure C1. The initial small q-ε_s plot gives the value of *3G*. Shear modulus *G* can be determined by:

$$G = \frac{\delta q}{3 \cdot \delta \varepsilon_s} \tag{C1}$$

where δq and $\delta \varepsilon_s$ are increments of stress and strain separately.

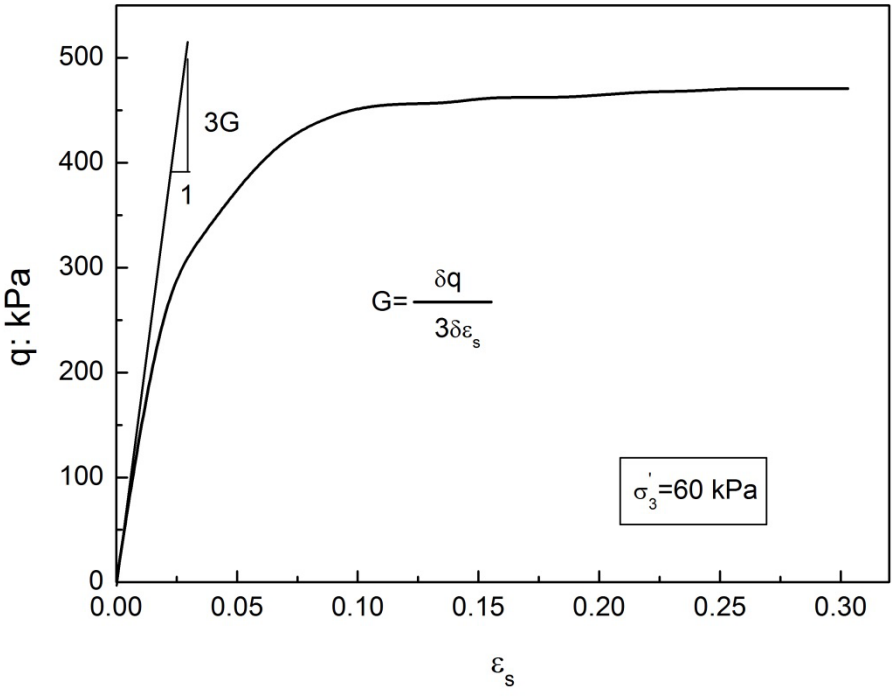

Figure C1 Determination of shear modulus *G*